

A foundation model for atomistic materials chemistry

Ilyes Batatia^{†1}, Philipp Benner^{†2}, Yuan Chiang^{†3,4}, Alin M. Elena^{†17}, Dávid P. Kovács^{†1}, Janosh Riebesell^{†4,13}, Xavier R. Advincula^{12,13}, Mark Asta^{3,4}, Matthew Avaylon³⁰, William J. Baldwin¹, Fabian Berger¹², Noam Bernstein¹¹, Arghya Bhowmik²⁵, Samuel M. Blau¹⁰, Vlad Cărară^{1,13}, James P. Darby¹, Sandip De¹⁸, Flaviano Della Pia¹², Volker L. Deringer¹⁶, Rokas Elijošius¹, Zakariya El-Machachi¹⁶, Fabio Falcioni³¹, Edvin Fako¹⁸, Andrea C. Ferrari²⁶, Annalena Genreith-Schriever¹², Janine George^{2,6}, Rhys E. A. Goodall¹⁵, Clare P. Grey¹², Petr Grigorev²⁷, Shuang Han¹⁸, Will Handley^{13,19}, Hendrik H. Heenen⁹, Kersti Hermansson²³, Christian Holm²², Stephan Hofmann¹, Jad Jaafar¹, Konstantin S. Jakob⁹, Hyunwook Jung⁹, Venkat Kapil^{12, 21}, Aaron D. Kaplan⁴, Nima Karimitari²⁰, James R. Kermode²⁸, Namu Kroupa^{13,19,1}, Jolla Kullgren²³, Matthew C. Kuner^{3,4}, Domantas Kuryla¹², Guoda Liepuoniute^{1,26}, Johannes T. Margraf⁸, Ioan-Bogdan Magdău²⁴, Angelos Michaelides¹², J. Harry Moore¹, Aakash A. Naik^{2,6}, Samuel P. Niblett¹², Sam Walton Norwood²⁵, Niamh O'Neill^{12,13}, Christoph Ortner⁵, Kristin A. Persson^{3,4,7}, Karsten Reuter⁹, Andrew S. Rosen^{3,4}, Lars L. Schaaf¹, Christoph Schran¹³, Benjamin X. Shi¹², Eric Sivonxay¹⁰, Tamás K. Stenczel¹, Viktor Svahn²³, Christopher Sutton²⁰, Thomas D. Swinburne²⁷, Jules Tilly³¹, Cas van der Oord¹, Santiago Vargas²⁹, Eszter Varga-Umbrich¹, Tejs Vegge²⁵, Martin Vondrák^{8,9}, Yangshuai Wang⁵, William C. Witt¹⁴, Fabian Zills²², and Gábor Csányi^{*1}

¹Engineering Laboratory, University of Cambridge, Trumpington St and JJ Thomson Ave, Cambridge, UK

²Federal Institute of Materials Research and Testing (BAM), Berlin, Germany

³Department of Materials Science and Engineering, University of California, Berkeley, CA 94720, USA

⁴Materials Sciences Division, Lawrence Berkeley National Laboratory, Berkeley, CA 94720, USA

⁵Mathematics Department, University of British Columbia, 1984 Mathematics Rd, Vancouver, BC V6T 1Z2, Canada

⁶Institute of Condensed Matter Theory and Solid State Optics, Friedrich Schiller University Jena, Germany

⁷Molecular Foundry, Lawrence Berkeley National Laboratory, Berkeley, California 94720, USA

⁸University of Bayreuth, Bavarian Center for Battery Technology (BayBatt), Bayreuth, Germany

⁹Fritz-Haber-Institute of the Max-Planck-Society, Berlin, Germany

¹⁰Energy Technologies Area, Lawrence Berkeley National Laboratory, Berkeley, CA 94720, USA

¹¹U. S. Naval Research Laboratory, Washington DC 20375, USA

¹²Yusuf Hamied Department of Chemistry, University of Cambridge, Lensfield Road,

[†]These authors, ordered alphabetically, contributed equally. All others, except for the corresponding author, are also ordered alphabetically.

*Corresponding author: gc121@cam.ac.uk

Cambridge, UK

¹³Cavendish Laboratory, University of Cambridge, J. J. Thomson Ave, Cambridge, UK

¹⁴Department of Materials Science and Metallurgy, University of Cambridge, 27 Charles Babbage Road, CB3 0FS, Cambridge, United Kingdom

¹⁵Chemix, Inc., Sunnyvale, CA 94085, USA

¹⁶Inorganic Chemistry Laboratory, Department of Chemistry, University of Oxford, Oxford OX1 3QR, UK

¹⁷Scientific Computing Department, Science and Technology Facilities Council, Daresbury Laboratory, Keckwick Lane, Daresbury WA4 4AD, UK

¹⁸BASF SE, Carl-Bosch-Straße 38, 67056 Ludwigshafen, Germany

¹⁹Kavli Institute for Cosmology, University of Cambridge, Madingley Road, Cambridge CB3 0HA, UK

²⁰Department of Chemistry and Biochemistry, University of South Carolina, South Carolina 29208, USA

²¹Lennard-Jones Centre, University of Cambridge, Trinity Ln, Cambridge, CB2 1TN, UK

²²Institute for Computational Physics, University of Stuttgart, 70569 Stuttgart, Germany

²³Department of Chemistry–Ångström, Uppsala University, Box 538, S-751 21, Uppsala, Sweden

²⁴School of Natural and Environmental Science, Newcastle University, Newcastle upon Tyne, NE1 7RU, UK

²⁵Department of Energy Conversion and Storage, Technical University of Denmark, Anker Engelunds Vej 301, 2800 Kgs. Lyngby, Denmark

²⁶Cambridge Graphene Centre, University of Cambridge, Cambridge, CB3 0FA, UK

²⁷Aix-Marseille Université, CNRS, CINaM UMR 7325, Campus de Luminy, 13288 Marseille, France

²⁸Warwick Centre for Predictive Modelling, School of Engineering, University of Warwick, Coventry CV4 7AL, United Kingdom

²⁹Department of Chemistry and Biochemistry, University of California – Los Angeles, 607 Charles E. Young Drive East, Los Angeles, CA, 90095 USA

³⁰Computing Sciences Area, Lawrence Berkeley National Laboratory, Berkeley, CA 94720, USA

³¹InstaDeep, London, W2 1AY, United Kingdom

March 4, 2024

Machine-learned force fields have transformed the atomistic modelling of materials by enabling simulations of *ab initio* quality on unprecedented time and length scales. However, they are currently limited by: (i) the significant computational and human effort that must go into development and validation of potentials for each particular system of interest; and (ii) a general lack of transferability from one chemical system to the next. Here, using the state-of-the-art MACE architecture we introduce a single general-purpose ML model, trained on a public database of 150k inorganic crystals, that is capable of running stable molecular dynamics on molecules and materials. We demonstrate the power of the MACE-MP-0 model — and its qualitative and at times quantitative accuracy — on a diverse set problems in the physical sciences, including the properties of solids, liquids, gases, chemical reactions, interfaces and even the dynamics of a small protein. The model can be applied out of the box and as a starting or “foundation model” for any atomistic

system of interest and is thus a step towards democratising the revolution of ML force fields by lowering the barriers to entry.

1 Introduction

Atomic-scale simulation based on density functional theory (DFT) is an enormously successful component of materials modeling (1–7). However, the computational cost of such *ab initio* methods, which use electronic structure theory directly, becomes prohibitive for many important cases (e.g., amorphous solids, condensed phase liquids, nanostructured materials, and more). Although fast analytical models in the form of empirical interatomic potentials (or force fields) have existed for decades, having varying levels of accuracy and applicability (8), they generally fail to achieve DFT accuracy, particularly when describing reactive events and phase transitions. As a result, they have been unable to displace DFT for most applications. More recently, machine learning (ML)-based interatomic potentials, custom-trained for a particular material or system, have improved the achievable accuracy considerably, albeit at a moderate increase in cost relative to empirical force fields (9–17). Yet, such custom-trained potentials require significant computational and human effort for the generation of DFT training data, as well as model training and validation (18).

A pinnacle achievement of ML potentials would be to accurately describe the potential energy surface (PES) across all possible chemical and structural spaces without incurring the high computational cost of *ab initio* electronic structure methods. By enabling robust, accurate molecular dynamics (MD) simulations for any material, such a potential would enable immediate study of arbitrary systems at a scale currently inaccessible even via the largest available computational resources. (Here, by robustness we mean that the trajectory should not irreversibly end up in unphysical configurations, a frequently observed behaviour for current-generation ML potentials, especially in long multi-nanosecond simulations (20).) Particularly desirable applications would include complex chemical reaction processes in both solid and liquid phases, at solid-fluid interfaces, or under pressure.

A key advance towards this goal was made by the MEGNet (21) model, which provided property prediction for inorganic crystals, and was trained on minimum energy configurations in the Materials Project (MP) (19) that includes most elements of the periodic table (89) and electronic structure calculations using the Perdew-Burke-Enzerhof (PBE) exchange-correlation functional (22). More recently, models using graph neural network architectures with the capacity to compute forces were also trained on MP-based datasets, including M3GNet (23) and CHGNet (24), which were both trained on snapshots from DFT relaxations of MP structures, with CHGNet using the MPtrj dataset introduced at the same time (24). The ALIGNN-FF model (25) was also trained on a database of inorganic crystals, JARVIS-DFT (26), that covers 89 elements and uses the optB88vdW exchange-correlation functional (27). The proprietary GNoME (28) (NequIP architecture (16)) model also starts from MP, but uses a complex active learning workflow to generate and train on a dataset of inorganic crystals nearly two orders of magnitude larger than MPtrj. The above models were created primarily for the purpose of “materials discovery”, i.e. predicting thermodynamic stability of hypothetical inorganic crystals. In addition, they were capable of molecular dynamics for such crystals, and indeed both CHGNet and GNoME were used to study alkali metal ion diffusion in battery materials. The DPA models (DPA-1 (29) and DPA-2 (30)) were trained to a wide variety of datasets (with 56 and 73 elements, respectively), a combination of some previously available and some released with the models (altogether 4M configurations). The second paper reports MD results for versions of the baseline model fine-tuned separately to specific systems (e.g. water, solid state electrolytes, ferroelectric oxide). To date, the most general and transferable force field for molecular dynamics is the PFP model (31) (TeaNet architecture (32)), also proprietary (including its training set that covered 45 elements originally, recently updated to 72 elements (33), and is significantly larger than MP and also covers molecules and surfaces). PFP was demonstrated for running simulations on solid-state ionic conductors, and a molecular adsorption and a heterogeneous catalysis example. There are also ML force fields specialized for organic molecules (with a much more limited number of elements) such as the ANI (and later AimNET) series of models (34–36) and the MACE-OFF23 model (37), as well as for metal alloys (38). However, there has yet to be a comprehensive demonstration that a single ML potential can describe solid, liquid, and gaseous systems of materials and molecules across the periodic table and well beyond the distribution of the underlying training set.

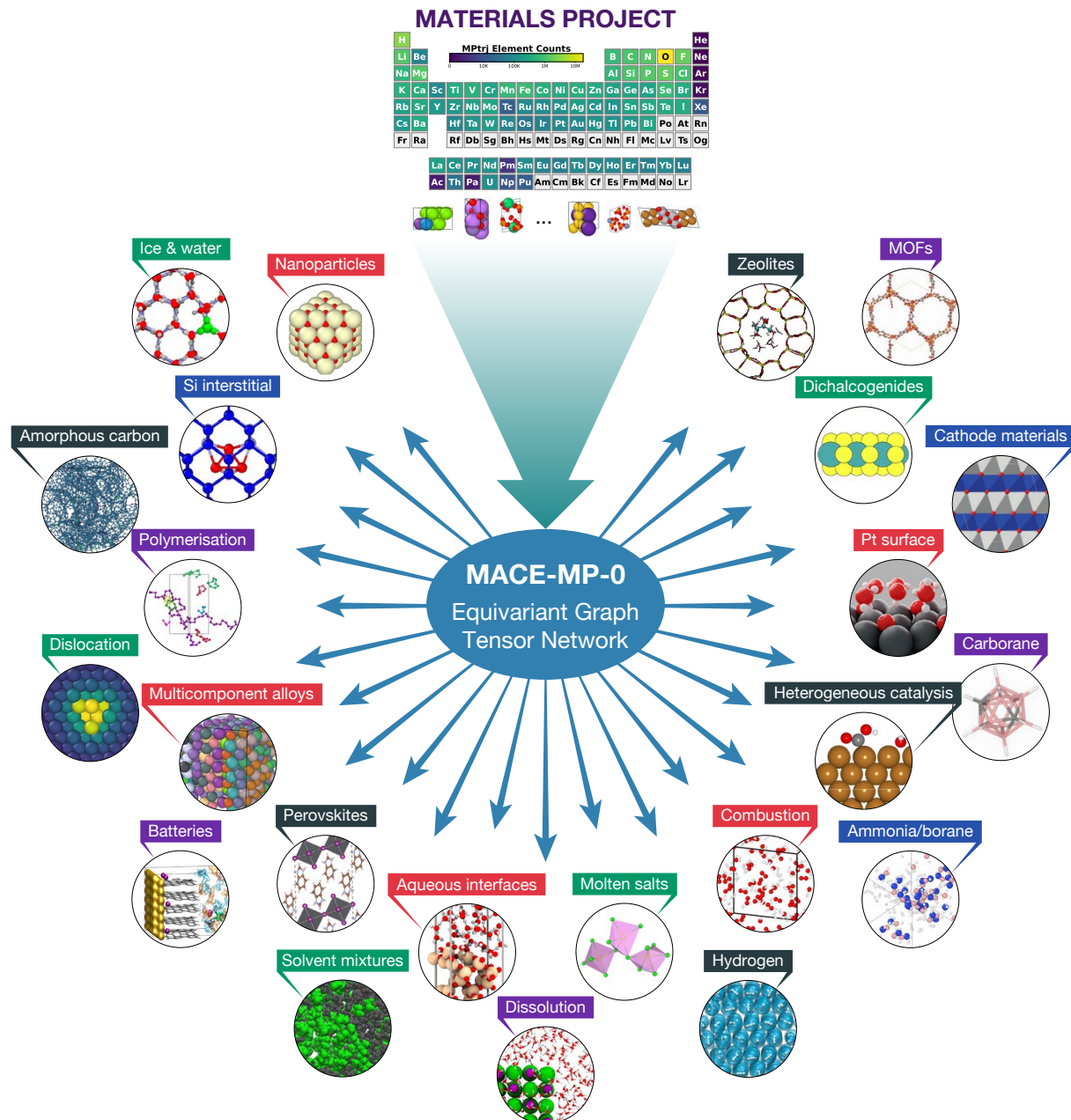


Figure 1: A foundation model for materials modelling. Trained only on Materials Project data (19) which consists primarily of inorganic crystals and is skewed heavily towards oxides, MACE-MP-0 is capable of molecular dynamics simulation across a wide variety of chemistries in the solid, liquid and gaseous phases.

Here, we present MACE-MP-0, a new interatomic potential using the MACE architecture (39) that is trained just on the MPtrj dataset, and demonstrate its capabilities on an unprecedented range of qualitative and quantitative examples drawn from computational chemistry and materials science, including running stable molecular dynamics simulations in a wide variety of chemistries, predicting phonon spectra, calculating activation energies for point defect and dislocation motion, simulating solvent mixtures, combusting hydrogen gas, modelling a complete rechargeable battery cell, and much more; several of these are illustrated in Fig. 1. We find that this pre-trained *foundation model* shows remarkable out-of-distribution performance.

The MACE architecture, which extends the atomic cluster expansion (ACE) (14, 40–43), was designed to keep only what appear to be essential components of equivariant graph neural networks (43): the element embedding with tensor decomposition (44) and the higher order equivariant messages constructed through the tensor product operation. Its unique innovations are that (i) it uses high body order equivariant features in each layer (4-body in the present case), and consequently only two layers of message passing are sufficient; (ii) it is only mildly nonlinear, as the only nonlinear activations are in the radial basis and the final readout layer, hence its classification as a graph tensor network. Its computational cost for evaluation is broadly in line with other graph neural networks, presently allowing simulations of around a thousand atoms for nanoseconds per day on a GPU.

In the following, we highlight three classes of application examples: solid and liquid water, heterogeneous catalysis, and metal–organic frameworks. The SI contains additional examples in 30 separate sections demonstrating the wide-ranging transferability of MACE-MP-0 in predicting properties and dynamic processes of both molecules and materials, as well as benchmarks and graphical exploration of the training data.

2 Applications

2.1 Water and aqueous systems

Water is ubiquitous in nature and technology and has long been a major focus of computational work. Driven by the delicate balance between directional hydrogen bonding and primarily non-directional van der Waals interactions, aqueous systems remain a challenge for simulations (50). For example, the study of proton transfer in water, a fundamental process characterized by the continuous breaking and forming of covalent bonds, has long required using *ab initio* molecular dynamics for detailed atomistic insight (51–53). We demonstrate in this section how MACE-MP-0 describes various aqueous systems.

We start by examining the structure of liquid water and hexagonal ice (ice Ih). The oxygen–oxygen radial distribution function, depicted in Fig. 2a, shows reasonable agreement with reference simulations. The infrared vibrational spectra of both phases, shown in panel Fig. 2b, align well with experimental observations, albeit with a notable red shift in the stretching vibrations indicating a softer description of the O–H bond as is well-known for PBE-D3 (50). In panel Fig. 2d, the relative stabilities of 12 ice polymorphs with respect to ice Ih, used in a recent benchmark (54), show excellent agreement with respect to PBE-D3 with a MAE of around 4 meV. Proton defects (OH^- and H_3O^+) in ice Ih and liquid water were simulated, revealing robust descriptions of proton transfer, as shown in Fig. 2c. The proton transfer barrier for hydroxide is higher than for hydronium in liquid water, consistent with experimental diffusion trends.

Next, we evaluate MACE-MP-0 for describing solid–liquid interfaces. First, we focus on NaCl in water in two cases: a NaCl(001) interface in contact with water and a small nanocrystal surrounded by water. Simulations were performed at 400 K to promote dissolution, and compared to simulations with a custom-trained ML potential based on revPBE-D3 from Ref. (49). As expected, for the flat surface the model predicts no dissolution events on the timescale of the simulation (0.5 ns). Meanwhile, for the nanocrystal surrounded by water, MACE-MP-0 captures a dissolution mechanism resembling that in Ref. (49) as shown in Fig. 2e. The dissolution proceeds via a crumbling mechanism, where an initial steady loss of ions is followed by the rapid disintegration of the crystal. As ions dissolve from the crystal, they are hydrated by water. The dissolution process is stochastic, leading to an intrinsic variation between independent simulations. The final structure of the dissolved ions in water also displays the expected orientation of the water molecules with respect to the ions.

We then model the SiO_2 /water interface, Fig. 2f, revealing the expected density modulations in the first few contact layers. As before, the liquid phase is found to be overstructured, a common characteristic of the PBE functional (50) used by MP and therefore by MACE-MP-0. SiO_2 is known for its dissociative water adsorption, which we observe in our simulations. Deprotonation of water is evidenced by the shoulder in the water density plot and can also be seen in the inset of a snapshot of this system in Fig. 2f.

Finally, we investigate nanoconfined water in graphene-like nanocapillaries (55, 56), which exhibits dramatically different properties from bulk water. MACE-MP-0 proved robust in simulating nanoconfined water. Stable simulations were conducted at 4 GPa and 600 K, conditions under which a superionic phase with high ionic conductivity was previously predicted (57) using a custom-trained ML potential. The MACE-MP-0 model accurately captured the dynamical characteristics of this phase, including extensive proton transfer on the ten pico-seconds timescale, as illustrated in the inset of Fig. 2g. Comparing the free energy profile associated with the O–H distance [Fig. 2g] against the PBE-D3 reference, MACE-MP-0 shows an overall good description, albeit underestimating the proton transfer barrier by 1–2 kcal/mol. This tendency towards autoprotolysis is consistent with the soft description of the O–H bond observed in bulk phases.

2.2 Catalysis

The study of heterogeneous (64–66) and electrocatalysis (67–69) is another major area where DFT excels. It provides atomistic insight into the underlying reaction mechanisms and enables the prediction of the properties of new catalytic materials, (70) including reaction barriers and rates, in turn used to predict turnover frequencies (71). The latter is essential for the computational discovery of new solid catalysts for overcoming the dependence on rare and toxic elements and improving the efficiency of critical processes for energy conversion. However, the computational cost of DFT is a serious impediment. Empirical interatomic potentials are typically inadequate for catalysis applications as they rarely describe chemical reactions accurately. Machine learning has already had strong impact in computational catalysis (61, 72, 73), e.g., enabling

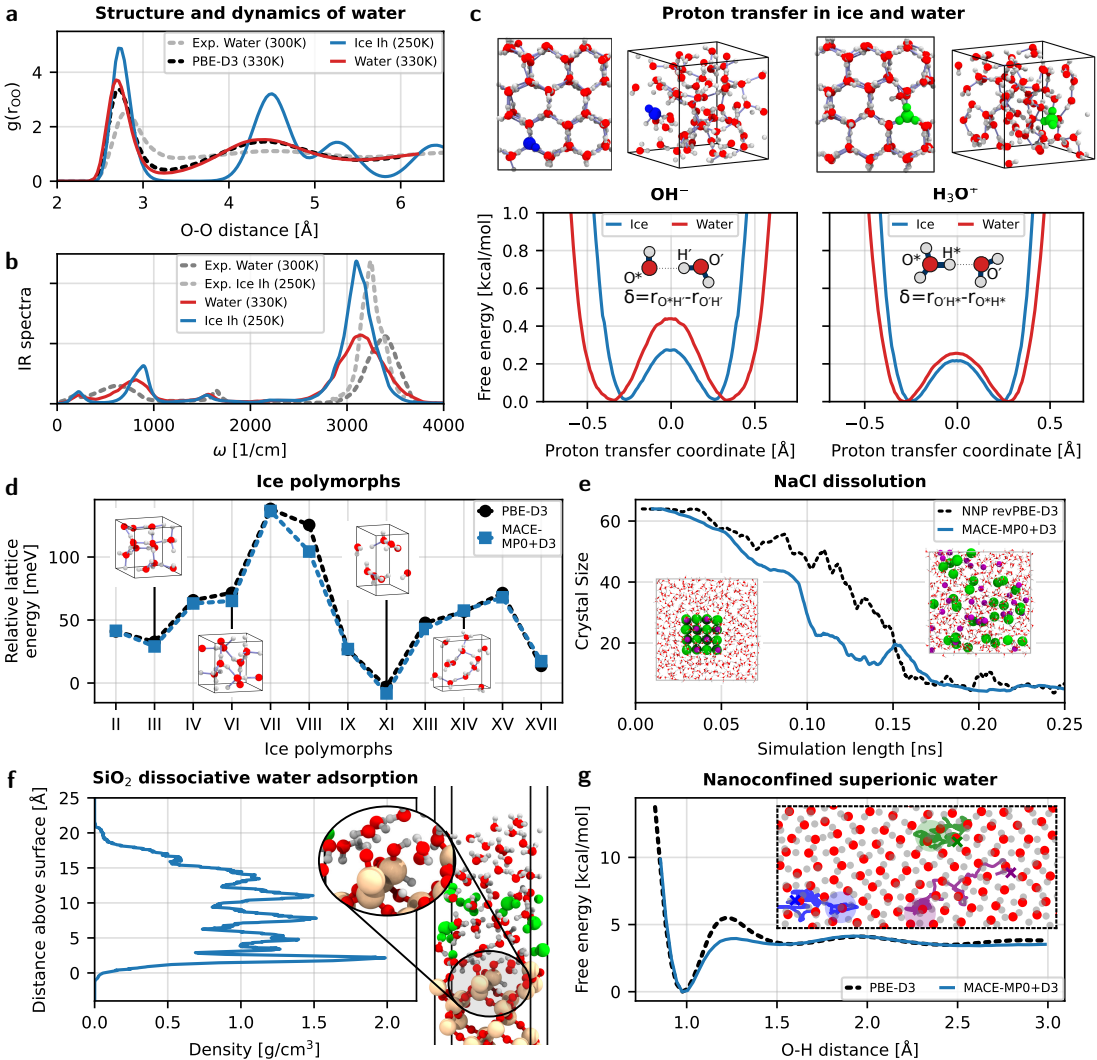


Figure 2: MACE-MP-0 performance for aqueous systems. (a) Oxygen–oxygen radial distribution function for bulk water (experimental result from Ref. (45)) and ice Ih. (b) Experimental (Ref. (46, 47)) and computed infrared spectra of bulk water and ice Ih. (c) Free energy profiles as a function of the proton transfer barrier for a hydroxide ion and excess proton in ice Ih at 250 K and bulk water at 330 K. Snapshots at the top show the simulation cells. (d) Performance of MACE-MP-0 (blue squares) on the relative lattice energies of the DMC-ICE13 dataset, compared to the reference method, PBE-D3 (48) (black circles). (e) Dissolution of a $4 \times 4 \times 4$ unit-cell NaCl nanocrystal in water at 400 K, monitoring the extent of dissolution over the simulation time via the crystal size. Performance of the MACE-MP-0 (blue line) is compared to a neural network potential (49) trained explicitly to capture NaCl dissolution (black dashed line). (f) SiO_2 /water interface simulation showing density modulations and dissociative water adsorption, with an inset highlighting the deprotonation of water as indicated by a shoulder in the water density plot. H_3O^+ defects in the liquid are highlighted in green. (g) The free energy profile of the O–H distance in the superionic phase of monolayer water in a confining potential. The inset shows a snapshot of the monolayer superionic phase with lines indicating the 50 ps-long trajectory of randomly chosen hydrogen atoms with “ \times ” indicating their initial positions.

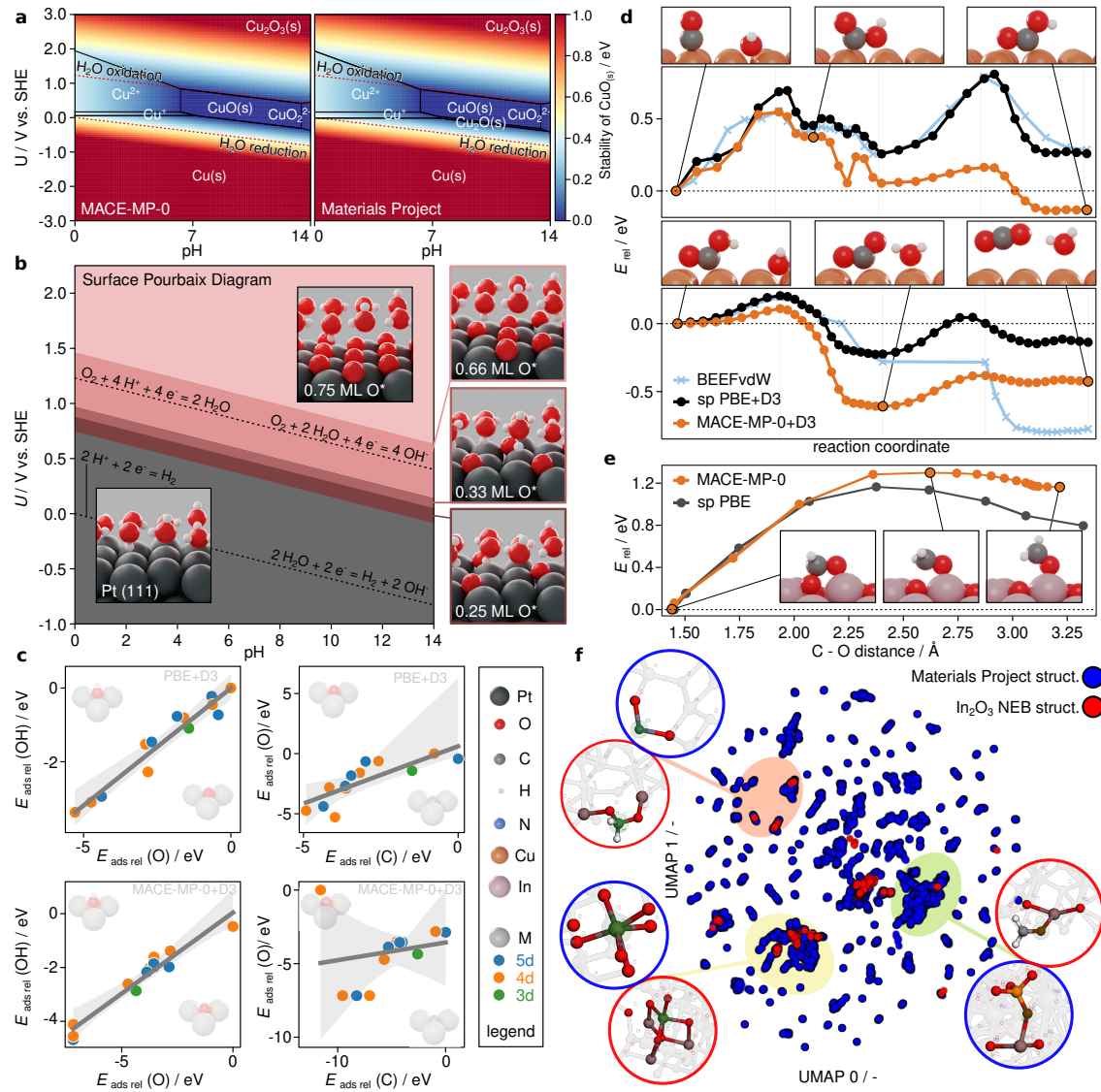


Figure 3: **MACE-MP-0 performance for catalytic applications.** (a) Pourbaix diagrams of CuO bulk systems constructed with MACE-MP-0 (left) and Materials Project reference data (right). (b) MACE-MP-0+D3-calculated Pt(111) surface Pourbaix diagram, in overall good agreement with the literature (58). (c) The relative adsorption energy scaling relation between O and OH on transition metal surfaces is captured correctly by MACE-MP-0+D3, as is the lack of linear scaling between C and O (59). Metals are colored according to rows in the Periodic Table as 3d, 4d and 5d. (d) Reaction profile of multistep electrochemical CO oxidation on Cu. CO–OH coupling and dehydrogenation reactions are characterised in the upper and lower panel, respectively. Energy profiles from MACE-MP-0+D3 nudged elastic band (NEB) calculations, along with PBE+D3 single-point calculations and independent BEEF-vdW profiles from a previous study (60). (e) MACE-MP-0 reaction profile for a key reaction step ($\text{CH}_2\text{O}_2 \rightarrow \text{CH}_2 + \text{O}$) in the CO_2 -to-methanol conversion on In_2O_3 (61). (f) Comparison of the atomic environments in the training data (blue) and in the In_2O_3 NEB images (red) in the form of a UMAP plot (62, 63). Insets show local environments with similar MACE features (inset frames in blue for training data and in red for NEB configurations), exemplifying which bulk training environments influence predictions for the out-of-domain catalytic test case.

fast screening of materials spaces (74–76), and free energy calculations beyond the harmonic approximation (61, 77, 78). However, developing such accurate potentials from scratch still requires significant human and computational effort. We now test the performance of MACE-MP-0 for different catalysis applications and summarise the results in Fig. 3.

Potential-pH Pourbaix diagrams are central to understanding the aqueous stability of solid materials in an electrochemical environment (79, 80), and thus allow predicting the active phase of an electrocatalyst under given conditions. Within the computational hydrogen electrode (CHE) framework (81), these diagrams can be computed without an explicit electrostatic model. Figure 3a–b show the MACE-MP-0+D3-calculated Pourbaix diagrams for bulk CuO and a Pt(111) surface. The Pourbaix diagrams are constructed via the formalism described in (82, 83), where only the energies of the relevant solids are calculated while corrected experimentally-derived energies are used for the aqueous ions. In both cases, the MACE-MP-0 results show remarkably good agreement with DFT (58), predicting the correct sequence of stable phases (with the exception of a very narrow region of Cu₂O stability) and corresponding pH and potential ranges. While this accuracy may be expected for the bulk CuO system that is represented in the training set, the electrosorption at the Pt(111) surface is also well described despite being out of domain.

In Fig. 3c, adsorption energy scaling relations between atomic and hydrogenated adsorbates on transition-metal surfaces are shown for MACE-MP-0+D3 and PBE+D3 (see SI for more examples). Such scaling relations are central to understanding the activity of heterogeneous catalysts (84, 85). MACE-MP-0+D3 captures these trends well, and the slopes of the linear fits are in reasonable agreement with DFT (*e.g.* 0.6 for O vs. OH, compared to 0.64 for PBE+D3). Importantly, the lack of correlation between O and C adsorption energies is also captured, indicating that the model is not merely sorting metals according to their general reactivity (59, 86). Figure 3d–e show reaction energy profiles for CO oxidation on Cu (60) and a key step in CO₂ conversion to methanol on In₂O₃ (61, 87), respectively. While these are not quantitatively accurate when compared to DFT, MACE-MP-0 nevertheless captures the location and magnitude of the barriers surprisingly well. Figure 3f illustrates how MACE-MP-0 generalizes to out-of-domain catalysis tasks from bulk training configurations. To this end, the high-dimensional MACE-MP-0 features are projected to 2D using a Uniform Manifold Approximation Projection (UMAP) (62), with local atomic environments in the training set shown in blue and those found in the In₂O₃ transition path shown in red. Representative environments with similar MACE-MP-0 features are highlighted, indicating that the internal representation of the atomic environments in the NEB configurations is similar to the representation of under-coordinated environments and metal–organic systems in the training set.

While MACE-MP-0 is not always quantitatively accurate for the most challenging catalysis applications, its stability in MD and exploring reactive pathways is remarkable and provides a starting point for further optimisations. Relevant configurations or phase space regions thus identified may subsequently be validated either by first-principles calculations or serve to initiate active-learning for refining the model. Even at its current foundation level, MACE-MP-0 already allows a statistical sampling far beyond the present DFT-based state of the art which is still largely thermochemistry-centered, whereas MACE-MP-0 will pave the way for true kinetic modeling by explicit evaluations of reaction profiles and the reactive flux along them.

2.3 Metal–organic frameworks

Metal–organic frameworks (MOFs) are a class of nanoporous materials comprised of metal cations or clusters connected by organic linkers arranged in a periodic lattice (94). Due to their large surface areas, tunable building blocks, and permanent porosity, MOFs hold substantial promise for various applications, including but not limited to catalysis, energy storage, gas adsorption and separations, and optoelectronic devices (94). We tested our pre-trained model directly against version 14 of the Quantum MOF (QMOF) database, which contains DFT-computed properties at several levels of theory for 20,000+ MOFs and structurally related coordination polymers (88, 89). MACE-MP-0 was not trained on any data from the QMOF database, making this a challenging test of its transferability to largely unseen chemistries.

As shown in Fig. 4a, MACE-MP-0 performs very well in predicting the absolute energies of MOFs, achieving an MAE of 0.033 eV/atom despite the pronounced difference between the inorganic crystals of the MPtrj training set and the MOF structures that make up the QMOF database. This accuracy spans most of the periodic table, as demonstrated in Figure 4b. When the energy prediction is distributed on a per-atom basis, we note a strong elemental dependence of predicted energy error. The higher-than-average errors for

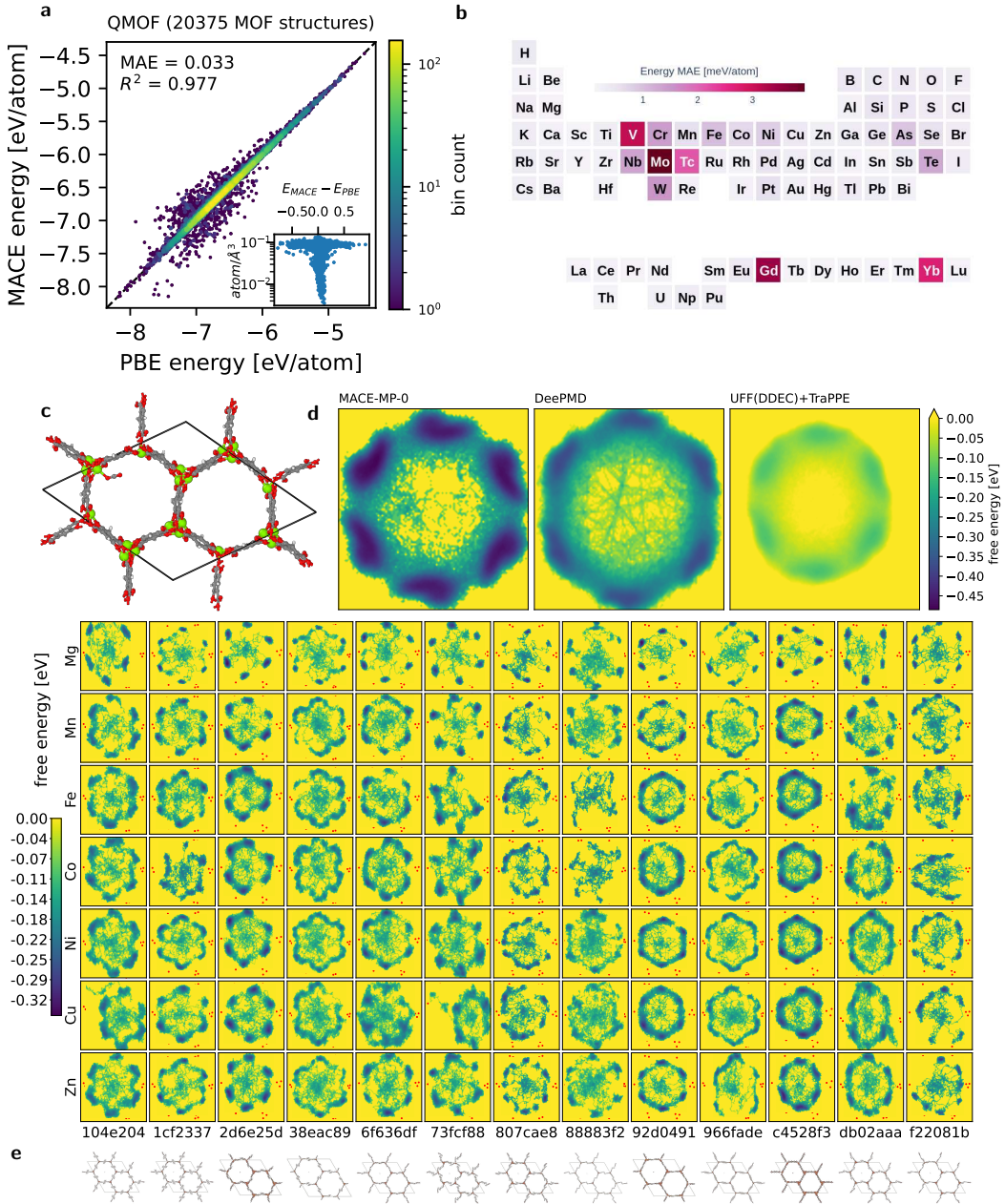


Figure 4: MACE-MP-0 applied to MOFs. (a) Comparison between MACE-MP-0 and DFT (PBE) energies on 20,375 relaxed structures taken from the QMOF database (88, 89). (b) Element-wise mean absolute error (MAE) of MACE-MP-0 predicted energies with respect to PBE energies from the QMOF database. The absolute energy error per atom of each structure is distributed over all constituent elements (see SI). (c) Mg-MOF-74 structure with chemisorbed CO₂ optimized with MACE-MP-0. Color key: Mg (orange), O (red), C (brown), H (white). (d) Left: free energy landscape of CO₂ in Mg-MOF-74. Middle: free energy landscape from Ref. (90) using a custom-trained DeePMD ML force field. Right: free energy landscape using the UFF classical force field (91) with DDEC6 charges (92) for the framework and TraPPE for CO₂ (93). (e) Free energy maps of 91 hypothetical MOF-74 analogues, with the QMOF ID of the parent Mg-containing frameworks indicated at the bottom of each column and the transition metal to the left of each row.

certain elements (Mo, V, Gd, Yb *etc.*) are due to a difference in the chosen pseudopotentials between the MP and QMOF datasets (see SI 2.3).

To validate the use of MACE-MP-0 for capturing dynamic processes, we investigate CO₂ adsorption in a prototypical MOF known as Mg-MOF-74. The MOF-74 family, including the Mg-containing version, has been extensively studied for the selective adsorption of CO₂ (95–97). Of particular note, the coordinatively unsaturated metal sites (98) of Mg-MOF-74 enable chemical bonding interactions between the metal and CO₂ adsorbate (95) that cannot be captured from classical force fields alone. We directly compare the adsorption dynamics against the results presented in Ref. (99), which considered the same system using a custom-trained ML force field generated using DeePMD-Kit (90) and PBE-D3 calculations in CP2K (3).

MACE-MP-0 accurately and efficiently captures the CO₂ adsorption process in Mg-MOF-74. As shown in Fig. 4c, the CO₂ adsorbate favorably binds to the Mg center in a tilted configuration that is in agreement with both experimental neutron diffraction data (96, 100) and the previous custom-trained ML model (99). The mean bond distance between the Mg center and CO₂ adsorbate is predicted to be 2.38 Å from MACE-MP-0 (Figure 43a), in close agreement with the experimental value of 2.27 Å (96) and the value of 2.23 Å from the custom ML model in Ref. (99). The mean Mg–O–C bond angle is predicted to be 133.7° from MACE-MP-0 (Fig. 43a), substantially closer to the experimentally determined bond angle of 131° (96) than the 118.6° value from the ML model in Ref. (99). The projected density map for the CO₂ adsorption site (Fig. 4b) is, again, in excellent agreement with prior work (99, 100) and shows how the adsorbed CO₂ molecules are mobile but largely confined to the vicinity of the Mg binding site due to chemisorption.

To showcase an example of how one might use MACE-MP-0 in a high-throughput setting, we considered 91 hypothetical MOF-74 analogues derived from those in Ref. (101) based on 13 (out of 58) different frameworks and seven different metal cations (M) that have been used to synthesize M-MOF-74 (96). Figure 4e shows the resulting free energy maps, comprising over 357 ns of simulation altogether, displaying diverse and dynamic behaviour of the CO₂ adsorbate across the range of hypothetical MOF-74 analogues.

Given the nature of our foundation model, we anticipate many additional application areas where MACE-MP-0 (or one of its future variants) could be of value in the MOF field. Based on the CO₂ adsorption example, we envision applications in capturing dynamic processes, particularly those that cannot be accurately modeled using classical force fields and are prohibitively expensive to carry out with *ab initio* MD given the large unit-cell size required to describe most MOFs. Foundation models are promising for modeling competitive multi-component physisorption and chemisorption processes, especially across many families of compositionally different MOFs and combinations of gas mixtures, for which training a system-specific, on-the-fly active learning model would be expensive or even prohibitive. In addition to the compositional diversity relevant to high-throughput screening, not all MOFs can be described via a static picture and based on an ideal crystalline structure: in fact, there has been recent interest in liquid and amorphous MOFs (102, 103), and the dynamic behavior of crystalline frameworks (104) — such as in the so-called “flexible” and “breathing” MOFs — has been leveraged for highly selective separation processes (105). This dynamic behavior cannot be completely captured from static DFT calculations alone, and accurate and easily accessible interatomic potentials are expected to accelerate the modeling of spatio-temporal processes in future studies (106).

2.4 Further applications and Supplementary Information

In the Supplementary Information in 32 subsections, we provide further application examples. We also give the results of a comprehensive set of benchmarks, including the performance on calculating phonon dispersions, bulk and shear moduli of crystals, atomisation energies and lattice constants of elemental solids, the cohesive energies of the S66 set (107) of molecular dimers and the X23 set (108) of molecular crystals, the CRBH20 set (109) of reaction barrier heights, and the homonuclear diatomic binding curves. The full set of heteronuclear diatomic curves is provided in the Supplementary Materials.

We also give more details on the training protocol, and a graphical exploration of the data, including histograms of energies, forces, stresses, magnetic moments, and element and composition counts.

3 Current limitations and future outlook

The DFT-quality simulation and stable MD propagation for a wide range of materials across the periodic table that we have shown here are landmark achievements for a single machine-learned interatomic potential. Yet there are a number of limitations of the current version of the MACE-MP-0 model. The exchange-correlation functional used in the MPtrj dataset is PBE (22), which must be augmented with Hubbard U terms to improve electronic correlations for particular element combinations (introducing inconsistencies in the PES that must be compensated (6)), and dispersion corrections, such as D3 (48). Recent developments in DFT are beginning to supersede it by achieving improved accuracy at comparable computational cost (110, 111), and methods beyond DFT such as hybrid functionals (112) and the random phase approximation (113) improve upon this even further but at much larger computational cost. Refitting the model to a more modern functional is expected to increase its predictive power, and will reduce the need for system-dependent corrections such as the use of Hubbard U terms and dispersion.

The MACE model that we used to fit the data does not contain explicit long range interactions (beyond the 12 Å receptive field afforded by two steps of message passing), nor does it take into account magnetic or spin degrees of freedom. Despite the success in describing many different chemistries demonstrated herein, there will be observables, particularly in the context of dilute solutions and at interfaces, that cannot be calculated with a short-range model. There are several approaches to incorporating explicit electrostatic interactions into ML models in the literature (114–117), as well as spin degrees of freedom (24, 118, 119). A subsequent version of our model will undoubtedly benefit from such an extension.

Considering the results for the diverse systems shown in the SI, there are two broad areas where the model clearly needs improvement: (i) describing intermolecular interactions, (ii) high pressure simulations. While the overarching goal of MD stability is achieved for ambient conditions, for many systems there is room for improvement in a quantitative sense. In some cases, e.g. low pressure simulations of ethanol (section appendix A.17), these small quantitative deviations lead to qualitative errors by shifting an important phase transition’s temperature or pressure, thereby changing the equilibrium phase at ambient conditions. In other cases, namely atoms that approach each other at very close distances in random structure search (section appendix A.15) or high pressure hydrogen (section appendix A.22), the energy errors are large, and the simulations become trapped in anomalously low energy, unphysical geometries. These errors are not specific to certain systems, and both can be addressed straightforwardly by extending the existing training data to lower and higher pressures (120) for the former, and using repulsive pair potentials (121) for the latter. In most cases, it is not yet wise to solely rely on ML potentials for all chemical or physical predictions without further validation (122), and the same is true for MACE-MP-0.

Several possible factors may be limiting the model’s accuracy: the size of the model in terms of number of free parameters and the limits this places on its expressivity, the total amount and type of configurations in the training set, or inconsistencies in the quantum-mechanically computed data labels. Exploration of possible improvements to the model and its training data is ongoing to determine which of these are responsible for current limitations. The results will determine in what ways the model and its improved versions will be used in the future.

The most pessimistic, but we think unlikely, possibility is that using MACE-MP-0 as a foundation model that must be fine-tuned to give quantitative accuracy for specific systems will require very large amounts of data and/or training time, and that the pre-trained model will not provide a significant shortcut compared to training models from scratch. In this case, the ability of MACE-MP-0 to produce *reasonable* trajectories will still make it useful as an efficient source of configurations for system-specific fitting databases, perhaps augmented by further active learning.

A more likely scenario is that the current model will at least be able to serve as a starting point that can be efficiently fine-tuned for any particular system. It remains to be seen how much additional data would be needed for such refinement, but based on previous experience we are optimistic; pre-training with cheaply generated data and subsequent fine-tuning has been shown to improve accuracy and stability of ML potentials (30, 123), and transfer-learning approaches can enable such models to fit higher quality reference data (35). This type of refinement will definitely be required for systems where the level of theory that was used to calculate the currently used training dataset are considered to be inadequate. There is good evidence that reaching higher levels of electronic structure theory from a DFT baseline and beyond requires significantly less data than fitting to DFT itself (35, 124, 125).

Finally, we may find that adding only a moderate number of additional configurations computed with essentially the same methodology will be sufficient to achieve quantitative agreement with the target level of theory across the full range of chemistry and structure. If this turns out to be true, future versions of MACE-MP-0 may truly provide a universal model for carrying out material simulations.

4 Methods

4.1 Model

MACE All models trained in the paper use the MACE (39) architecture implemented in PyTorch (126) and employing the *e3nn* library (127). The MACE training and evaluation codes are distributed via GitHub under the MIT license, available at <https://github.com/ACEsuit/mace/>. The models used in this paper are available at <https://github.com/ACEsuit/mace-mp/>. MACE is an equivariant message-passing graph tensor network where each layer encodes many-body information of atomic geometry. At each layer, many-body messages are formed using a linear combination of a tensor product basis (43, 44). This is constructed by taking tensor products of a sum of two-body permutation-invariant polynomials, expanded in a spherical basis. The final output is the energy contribution of each atom to the total potential energy. For a more detailed description of the architecture, see Refs. (39) and (128).

Hyper-parameters All models referred to in this work use two MACE layers, a spherical expansion of up to $l_{\max} = 3$, and 4-body messages in each layer (correlation order 3). All models use a 128-channel dimension for tensor decomposition. We use a radial cutoff of 6 Å and expand the interatomic distances into 10 Bessel functions multiplied by a smooth polynomial cutoff function to construct radial features, in turn fed into a fully-connected feed-forward neural network with three hidden layers of 64 hidden units and SiLU non-linearities. We fit three different size models, which only differ by the maximal message equivariance, $L = 0, 1, 2$ for the small, medium and large models, respectively, and provide different compromises between computational cost and fitting accuracy. The irreducible representations of the messages have alternating parity (in *e3nn* notation, 128x0e for the small model, 128x0e + 128x1o for the medium model, and 128x0e + 128x1o + 128x2e for the large model). All application examples in this paper are run with the medium $L = 1$ model as it offers a good cost-accuracy trade-off.

Normalization To ensure internal normalization of the weights, we divide the atomic basis in each layer by the average number of neighbors in the training dataset, as proposed in (43). This number is fixed at ≈ 62 . The node energy ϵ_a of atom a is shifted by the mean of the atomic energies. Therefore, the prediction of the energy for the whole structure is constructed as

$$\hat{E} = \sum_{a=1}^N \left[\sigma \left(\sum_{k=1}^K \epsilon_a^{(k)} \right) + \mu_{Z_a} \right]$$

where K denotes the total number of message passing layers and $\epsilon_a^{(k)}$ is the energy of atom a at layer k . μ and σ are the mean atomic energies and the mean square of the atomic forces computed on the training set. The predicted forces and stresses are computed as derivatives of the total energy with respect to the atomic positions and the strain tensor, respectively.

Training loss The models were trained using a weighted sum of Huber losses of energy, forces, and stress:

$$\begin{aligned} \mathcal{L} = & \frac{\lambda_E}{N_b} \sum_{b=1}^{N_b} \mathcal{L}_{\text{Huber}} \left(\frac{\hat{E}_b}{N_a}, \frac{E_b}{N_a}, \delta_E \right) \\ & + \frac{\lambda_F}{3 \sum_{b=1}^{N_b} N_a} \sum_{b=1}^{N_b} \sum_{a=1}^{N_a} \sum_{i=1}^3 \mathcal{L}_{\text{Huber}}^* \left(\frac{\partial \hat{E}_b}{\partial r_{b,a,i}}, F_{b,a,i}, \delta_F \right) \\ & + \frac{\lambda_\sigma}{9N_b} \sum_{b=1}^{N_b} \sum_{i=1}^3 \sum_{j=1}^3 \mathcal{L}_{\text{Huber}} \left(\frac{1}{V_b} \frac{\partial \hat{E}_b}{\partial \varepsilon_{b,ij}}, \sigma_{b,ij}, \delta_\sigma \right), \end{aligned} \quad (1)$$

where $\lambda_E, \lambda_F, \lambda_\sigma$ are predetermined weights of energy (E), forces (F), and stress (σ) losses, the symbols under a hat correspond to predicted values, and N_b and N_a are the batch size and the number of atoms in each structure. In the last term involving the stress, ε_b and σ_b correspond to the strain and stress tensors, respectively. We used $(\lambda_E, \lambda_F, \lambda_\sigma) = (1, 10, 100)$ and Huber deltas of $\delta_E = 0.01, \delta_F = 0.01, \delta_\sigma = 0.01$. We

use a conditional Huber loss $\mathcal{L}_{\text{Huber}}^*$ for forces, where the Huber delta δ_F is adaptive to the force magnitude on each atom. The Huber delta δ_F decreases step-wise by a factor from 1.0 to 0.1 as the atomic force increases from 0 to 300 eV/Å. For more details, see the section C.1 in the SI.

Optimization The models are trained with the AMSGrad (129) variant of Adam (130) with default parameters $\beta_1 = 0.9$, $\beta_2 = 0.999$, and $\epsilon = 10^{-8}$. We use a learning rate of 0.001 and a exponential moving average (EMA) learning scheduler with decaying factor of 0.995. We employ a gradient clipping of 100. The training curves for small ($L = 0$), medium ($L = 1$), and large ($L = 2$) models are presented in Fig. 57 in the SI. Models are trained for 200 epochs on 40–80 NVIDIA A100 GPUs across 10–20 nodes. Training the medium-sized model took approx. 2,600 GPU hours. We find that MACE-MP-0 achieves an energy MAE of 20 meV/atom and a force MAE of 45 meV/Å for the medium model. After fine-tuning with higher weights for energies for an additional 50 epochs, the small model is able to achieve an energy MAE of 13 meV/atom (see SI C.1).

Performance The speed of evaluation of the MACE-MP-0 model depends on the atomic density, hardware, floating point precision, size of model, *etc.* (see section SI A.32 for details), but a rough guide is that on a single NVIDIA A100 GPU with 80GB of RAM, it can do several nanoseconds per day for 1000 atoms. When run in parallel using domain decomposition, weak scaling at 0.1 ns/day is perfect up to 32,000 atoms and 64 GPUs for a dense metallic alloy.

Training data The MACE-MP-0 model was trained on the MPtrj dataset which was compiled originally for CHGNet (24). This dataset consists of a large number of static calculations and structural optimization trajectories from the Materials Project (MP) (19). These include approx. 1.5M configurations (roughly ten times the approx. 150k unique MP structures), mainly small periodic unit cells (90% under 70 atoms) describing inorganic crystals with some molecular components. The DFT calculations use the PBE exchange-correlation functional with Hubbard U terms applied to some transition metal oxide systems, but no additional dispersion correction (131).

Since the potential we fit calculates the energy based only on structural information, ideally we would like to use consistent electronic calculation parameters and the lowest energy electronic state for each configuration. One significant source of inconsistency is the application of Hubbard U , which is used in MP calculations only when O or F are present together with any of 8 transition metals (Co, Cr, Fe, Mn, Mo, Ni, V, W) (132). The application of U leads to a shift in energy correlated with the value of U , *i.e.* a few eV, not explicitly accounted for in our fit. Thus, energies from calculations using those 8 elements with and without O or F are inconsistent (in the sense that the energy along a continuous deformation path that removes the O or F atoms from around these metals would be discontinuous). The pre-trained CHGNet fit to MPtrj used energies corrected to account for the presence or absence of U (133). In our fit, this shift only occurs between structures with different compositions and for any given composition the energies should be consistent. As a result, we expect configurations that include local regions of these metals with very different O or F content, *e.g.* an interface between a metal and an oxide, may be poorly described.

In addition, the current fitting database includes a variety of magnetic orders generated as part of a systematic search for the magnetic ground state (134), chosen from the full database only based on calculation type (“GGA Static” and “GGA Structure Optimization”) and energy-difference criteria (24). To quantify the effect of this additional and unaccounted-for degree of freedom, we classify the magnetic order associated with each calculation task into one of four categories: 1) no atomic magnetic moment listed, 2) moment converged to zero on all atoms, 3) converged to ferromagnetic order, and 4) converged to another magnetic order. Of the approx. 150k MP-IDs present, about 48k have more than one magnetic order present in the fitting database. In the vast majority of cases, this includes a calculation where the moments are *unknown* (*i.e.* not recorded) and a single other magnetic order, and we can hope that they are actually consistent. However, for 5186 MP-IDs we find multiple non-trivial magnetic orders. To quantify the effect on the fitting quantities, we calculate the minimum energies of each magnetic order for each material, and analyze the range of minima values seen for each material (distribution is plotted in SI Fig. 61). While the vast majority of materials have negligible variation, there are hundreds with variation >100 meV/atom (*i.e.* an order of magnitude larger than the energy error on the validation set), and a few that vary by <0.5 eV/atom.

Long-range dispersion corrections Dispersion interactions, sometimes called van der Waals interactions, are crucial for describing the weak, long-range interactions between electrons. Common approximations in DFT, such as PBE (22), cannot capture such long-ranged interactions, motivating the use of additive non-local corrections, such as DFT-D3 (48) or rVV10 (135). Inclusion of a dispersion correction to DFT is necessary to describe the dynamics of liquid water (136), the geometries and binding energies of layered solids (137), and stability of metal–organic frameworks (138), among many other examples.

Additive dispersion corrections typically employ a physical model for dispersion interactions with empirical parameters optimized to cut off the correction at interatomic distances where approximate DFT is reliable. DFT-D3 is an interatomic potential which uses tabulated values of atomic polarizabilities to describe two-body and, optionally, three-body Axilrod–Teller (139) dispersion interactions. As MACE-MP-0 is trained to PBE energies, forces, and stresses, it inherits PBE’s lack of long-range dispersion interactions. An optional, additive DFT-D3 dispersion correction can be applied to MACE-MP-0. The PyTorch implementation of DFT-D3 used in this work is described in Ref. (31). The same parameters used in PBE-D3(BJ), i.e., DFT-D3 with a Becke-Johnson damping function (140), are used in the D3 correction to MACE-MP-0.

Author contributions

Model training: YC, PB, IB; **Data/Model analysis:** PB, YC, JR, NB, RE, MCK, ES; **MACE code:** IB, YC, SWN, DPK, PB, WCW, MA, SV, ES; **Application examples:** WJB (CsPbI_3 , appendix A.5); LLS (catalysis: In_2O_3 , section 2.2 and appendix A.24.4); IB (a-C quenches, appendix A.3.1); ZEM (a-C graphitisation, appendix A.3.2); NK (Si interstitials, appendix A.1); EVU, XRA, NON (aqueous interfaces, section 2.1 and appendix A.19); YC (molten salts, appendix A.20); CSc, VK, FDP, XRA (water and ice, section 2.1 and appendix A.16); SPN and AGS (LiNiO_2 , appendix A.12); SWN (lithiated graphite, appendix A.11); AME (zeolites appendix A.10); JJ (transition metal dichalcogenides, appendix A.26); JHM (ethanol/water, appendix A.17, trialanine, appendix A.30); GL (a-Si appendix A.2); DK (carborane, appendix A.25, ammonia-borane, appendix A.23); VC (S polymerisation, appendix A.9); JR, JG and AAN (phonons, appendix B.1); JR, REAG (materials discovery: formation energy, appendix A.29.1); KSJ (materials discovery: stoichiometric substitutions, appendix A.29.2); ADK (materials discovery: highly-coordinated structures, appendix A.29.3); ASR, YC and AME (MOFs, section 2.3 and appendix A.28); MV (solvent mixtures, appendix A.18); DPK, ES, SMB (hydrogen combustion, appendix A.8); NKA, CSu (HOIPs, appendix A.6); FF, JT (protein folding and stability appendix A.7); PG, YW, TDS, JRK and CO (point and extended defects in BCC metals, appendix A.13); BXS, FB (molecule-surface interactions, appendix A.31); WCW (HEA, appendix A.32); EF, SD (catalysis: linear scaling relationships, section 2.2 and appendix A.24.2); HJ, HHH (catalysis: CO oxidation on Cu, section 2.2 and appendix A.24.3); SH, SD (catalysis: Pourbaix diagrams, section 2.2 and appendix A.24.1); MCK (benchmarks: bulk and shear moduli, appendix B.2); FDP (benchmarks: cohesive energies and lattice constants of solids, appendix B.3, atomization energies appendix B.4, and reaction barrier heights, appendix B.5); TKS (Al_2O_3 , appendix A.14, diatomics, appendix B.6); JPD (Arsenic random structure search, appendix A.15); IBM (high-pressure hydrogen, appendix A.22); IBM, CvdO (electrode-electrolyte interface / battery system, appendix A.27); JK, VS and KH (CeO_2 , appendix A.4); FZ (ionic liquids, appendix A.21) **Supervision:** AB, ACF, AM, ASR, CH, CO, CPG, CSu, GC, HHH, JG, JK, JTM, KAP, KH, KR, MA, SD, SMB, TV, VLD, WH, WJB; **Drafted manuscript:** IB, NB, YC, GC, SD, HHH, MCK, JR, ASR, CSc, JTM; **Edited manuscript:** IB, NB, YC, GC, VLD, JG, REAG, JR, MCK, KAP, ASR, LLS, JTM, AM, CO, AME, WCW.

Acknowledgments

Model training made use of resources of the National Energy Research Scientific Computing Center, a DOE Office of Science User Facility supported by the Office of Science of the U.S. Department of Energy under contract no. DE-AC02-05CH11231 using awards BES-ERCAP0023528 and BES-ERCAP0022838. Part of this work was performed using the Cambridge Service for Data-Driven Discovery (CSD3), part of which is operated by the University of Cambridge Research Computing on behalf of the STFC DiRAC HPC Facility (www.dirac.ac.uk). The DiRAC component of CSD3 was funded by BEIS capital funding via STFC capital grants ST/P002307/1 and ST/R002452/1 and STFC operations grant ST/R00689X/1. DiRAC is

part of the National e-Infrastructure. The work of YC, JR, ADK, MCK, MA and KAP was supported by the US Department of Energy, Office of Science, Office of Basic Energy Sciences, Materials Sciences and Engineering Division, under contract no. DE-AC02-05-CH11231 (Materials Project program KC23MP). We could not have done this work without the DFT relaxation trajectories freely provided by the Materials Project and carefully curated into the MPtrj training set by Bowen Deng (24). JR acknowledges support from the German Academic Scholarship Foundation (Studienstiftung). YC acknowledges financial support from UC Berkeley and Taiwan-UC Berkeley Fellowship from the Ministry of Education in Taiwan. MCK acknowledges support by the National Science Foundation Graduate Research Fellowship Program under Grant No. DGE-2146752. Any opinions, findings, and conclusions or recommendations expressed in this work are those of the author(s) and do not necessarily reflect the views of the National Science Foundation. NB was supported by fundamental-research base-program funding from the U.S. Naval Research Laboratory. ASR acknowledges support via a Miller Research Fellowship from the Miller Institute for Basic Research in Science, University of California, Berkeley. LLS acknowledges support from the EPSRC Syntech CDT with grant reference EP/S024220/1. AM and XRA acknowledge support from the European Union under the "n-AQUA" European Research Council project (Grant no. 101071937). SWN, AB, TV acknowledge support from the European Union's Horizon 2020 research and innovation program under the Marie Skłodowska-Curie Actions (Grant Agreement 945357) as part of the DESTINY PhD program. GC, CPG, TV, AB and SWN acknowledge support from the European Union's Horizon 2020 research and innovation program under Grant Agreement 957189 (BIG-MAP). VK acknowledges support from the Ernest Oppenheimer Early Career Fellowship and the Sydney Harvey Junior Research Fellowship, Churchill College, University of Cambridge. V.K. acknowledges computational support from the Swiss National Supercomputing Centre under project s1209. ZEM acknowledges support from the EPSRC Centre for Doctoral Training in Theory and Modeling in Chemical Sciences (TMCS), under grant EP/L015722/1. VLD acknowledges support from the John Fell OUP Research Fund. CH and FZ acknowledge support by the Deutsche Forschungsgemeinschaft (DFG, German Research Foundation) in the framework of the priority program SPP 2363, "Utilization and Development of Machine Learning for Molecular Applications - Molecular Machine Learning" Project No. 497249646 as well as further funding through the DFG under Germany's Excellence Strategy - EXC 2075 - 390740016 and the Stuttgart Center for Simulation Science (SimTech). AME's work used the DiRAC Extreme Scaling service (Tursa) at the University of Edinburgh, which is part of the STFC DiRAC HPC Facility (www.dirac.ac.uk) and scarf cluster (www.scarf.rl.ac.uk/) maintained by Scientific Computing Department STFC. AME's access to DiRAC resources was granted through a Director's Discretionary Time allocation in 2023/24, under the auspices of the UKRI-funded DiRAC Federation Project. AME's work was also supported by Ada Lovelace centre at STFC (<https://adalovelacecentre.ac.uk/>), Physical Sciences Databases Infrastructure (<https://psdi.ac.uk>) and EPSRC under grants EP/W026775/1 and EP/V028537/1. IB, RE and NK were supported by the Harding Distinguished Postgraduate Scholarship. HJ gratefully acknowledges support from the Alexander-von-Humboldt (AvH) Foundation. HHH, JTM and KR acknowledge support from the German Research Foundation (DFG) through DFG CoE e-conversion EXC 2089/1. FB acknowledges the Alexander von Humboldt Foundation for a Feodor Lynen Research Fellowship and the Isaac Newton Trust for an Early Career Fellowship. BXS acknowledges support from the EPSRC Doctoral Training Partnership (EP/T517847/1). IB, DPK, XRA, WJB, FDP, RE, VK, DK, GL, NON, LLS, CSc, TKS, CvdO, EVU, WCW acknowledge access to CSD3 GPU resources through a University of Cambridge EPSRC Core Equipment Award (EP/X034712/1). We acknowledge project/application support by the Max Planck Computing and Data Facility. KH, JK and VS acknowledge the Swedish Research Council (Vetenskapsrådet, project number 2021-06757) and the National Strategic e-Science program eSSENCE for funding, as well as the Swedish National Infrastructure for Computing (SNIC/NAIIS) for providing computer resources used in this project. SW, AB and TV acknowledge the Pioneer Center for Accelerating P2X Materials discovery (CAPeX), DNRF Grant number P3. YW acknowledges support from the Shanghai Jiao Tong University. WCW acknowledges support from the EPSRC (Grant EP/V062654/1). CO acknowledges support from NSERC (Discovery Grant GR019381) and NFRF (Exploration Grant GR022937). JG and AN would like to acknowledge the Gauss Centre for Supercomputing e.V. (<https://www.gauss-centre.eu>) for funding workflow-related developments by providing generous computing time on the GCS Supercomputer SuperMUC-NG at Leibniz Supercomputing Centre (www.lrz.de) (Project pn73da). SH and JJ acknowledge funding from EPSRC (EP/T001038/1, EP/S022953/1). ADK acknowledges the Savio computational cluster resource provided by the Berkeley Research Computing program at the University of California,

Berkeley (supported by the UC Berkeley Chancellor, Vice Chancellor for Research, and Chief Information Officer). ACF acknowledges funding from EU Graphene Flagship, ERC grants Hetero2D, GIPT, EU grants Graph-X, CHARM, EPSRC grants EP/K01711X/1, EP/K017144/1, EP/N010345/1, EP/L016087/1, EP/V000055/1, EP/X015742/1. WB, CSu, and CG thank the US AFRL for partial funding of this project through grant FA8655-21-1-7010. JPD, JRK and GC acknowledge funding from the NOMAD Centre of Excellence (European Commission grant agreement ID 951786). PG and TDS acknowledge the support from the Cross-Disciplinary Program on Numerical Simulation of CEA, the French Alternative Energies and Atomic Energy Commission. PG and TDS used access to the HPC resources of IDRIS under the allocation A0120913455 attributed by GENCI. GC is grateful to Ágnes Borszéki for help with graphics.

References

1. W. Kohn and L. J. Sham, “Self-consistent equations including exchange and correlation effects,” *Phys. Rev.*, vol. 140, pp. A1133–A1138, Nov 1965.
2. P. Giannozzi, O. Baseggio, P. Bonfà, D. Brunato, R. Car, I. Carnimeo, C. Cavazzoni, S. de Gironcoli, P. Delugas, F. Ferrari Ruffino, A. Ferretti, N. Marzari, I. Timrov, A. Urru, and S. Baroni, “Quantum ESPRESSO toward the exascale,” *The Journal of Chemical Physics*, vol. 152, p. 154105, 04 2020.
3. T. D. Kühne, M. Iannuzzi, M. Del Ben, V. V. Rybkin, P. Seewald, F. Stein, T. Laino, R. Z. Khaliullin, O. Schütt, F. Schiffmann, *et al.*, “Cp2k: An electronic structure and molecular dynamics software package-quickstep: Efficient and accurate electronic structure calculations,” *The Journal of Chemical Physics*, vol. 152, no. 19, 2020.
4. G. Kresse and J. Hafner, “Ab initio molecular dynamics for liquid metals,” *Phys. Rev. B*, vol. 47, p. 558, 1993.
5. P. J. Hasnip, K. Refson, M. I. J. Probert, J. R. Yates, S. J. Clark, and C. J. Pickard, “Density functional theory in the solid state,” *Phil. Trans. R. Soc. A.*, vol. 372, p. 20130270, 2014.
6. A. Jain, Y. Shin, and K. A. Persson, “Computational predictions of energy materials using density functional theory,” *Nat Rev Mater*, vol. 1, p. 714, 2016.
7. J. Neugebauer and T. Hickel, “Density functional theory in materials science,” *WIREs Comput Mol Sci*, vol. 3, pp. 438–448, 2013.
8. M. Finnis, *Interatomic forces in condensed matter*, vol. 1. Oxford Series on Materials Mod, 2003.
9. J. Behler and M. Parrinello, “Generalized neural-network representation of high-dimensional potential-energy surfaces,” *Phys. Rev. Lett.*, vol. 98, p. 146401, Apr 2007.
10. A. P. Bartók, M. C. Payne, R. Kondor, and G. Csányi, “Gaussian approximation potentials: The accuracy of quantum mechanics, without the electrons,” *Phys. Rev. Lett.*, vol. 104, p. 136403, Apr 2010.
11. A. Thompson, L. Swiler, C. Trott, S. Foiles, and G. Tucker, “Spectral neighbor analysis method for automated generation of quantum-accurate interatomic potentials,” *Journal of Computational Physics*, vol. 285, pp. 316–330, 2015.
12. K. T. Schütt, H. E. Sauceda, P.-J. Kindermans, A. Tkatchenko, and K.-R. Müller, “SchNet – A deep learning architecture for molecules and materials,” *The Journal of Chemical Physics*, vol. 148, p. 241722, 03 2018.
13. V. L. Deringer, M. A. Caro, and G. Csányi, “Machine Learning Interatomic Potentials as Emerging Tools for Materials Science,” *Advanced Materials*, vol. 31, no. 46, p. 1902765, 2019.
14. R. Drautz, “Atomic cluster expansion for accurate and transferable interatomic potentials,” *Phys. Rev. B*, vol. 99, p. 014104, Jan 2019.

15. O. A. von Lilienfeld and K. Burke, “Retrospective on a decade of machine learning for chemical discovery,” *Nature Communications*, vol. 11, no. 1, p. 4895, 2020.
16. S. Batzner, A. Musaelian, L. Sun, M. Geiger, J. P. Mailoa, M. Kornbluth, N. Molinari, T. E. Smidt, and B. Kozinsky, “E (3)-equivariant graph neural networks for data-efficient and accurate interatomic potentials,” *Nature communications*, vol. 13, no. 1, p. 2453, 2022.
17. T. W. Ko and S. P. Ong, “Recent advances and outstanding challenges for machine learning interatomic potentials,” *Nature Computational Science*, pp. 1–3, 2023.
18. V. L. Deringer, A. P. Bartók, N. Bernstein, D. M. Wilkins, M. Ceriotti, and G. Csányi, “Gaussian process regression for materials and molecules,” *Chemical Reviews*, vol. 121, no. 16, pp. 10073–10141, 2021. PMID: 34398616.
19. A. Jain, S. P. Ong, G. Hautier, W. Chen, W. D. Richards, S. Dacek, S. Cholia, D. Gunter, D. Skinner, G. Ceder, *et al.*, “Commentary: The materials project: A materials genome approach to accelerating materials innovation,” *APL materials*, vol. 1, no. 1, 2013.
20. S. Stocker, J. Gasteiger, F. Becker, S. Günnemann, and J. T. Margraf, “How robust are modern graph neural network potentials in long and hot molecular dynamics simulations?,” *Mach. Learn.: Sci. Technol.*, vol. 3, p. 045010, 2022.
21. C. Chen, W. Ye, Y. Zuo, C. Zheng, and S. P. Ong, “Graph networks as a universal machine learning framework for molecules and crystals,” *Chemistry of Materials*, vol. 31, no. 9, pp. 3564–3572, 2019.
22. J. P. Perdew, K. Burke, and M. Ernzerhof, “Generalized gradient approximation made simple,” *Physical review letters*, vol. 77, no. 18, p. 3865, 1996.
23. C. Chen and S. P. Ong, “A universal graph deep learning interatomic potential for the periodic table,” *Nat Comput Sci*, vol. 2, no. 11, pp. 718–728, 2022. Number: 11 Publisher: Nature Publishing Group.
24. B. Deng, P. Zhong, K. Jun, J. Riebesell, K. Han, C. J. Bartel, and G. Ceder, “CHGNet as a pre-trained universal neural network potential for charge-informed atomistic modeling,” *Nature Machine Intelligence*, vol. 5, no. 9, pp. 1031–1041, 2023.
25. K. Choudhary, B. DeCost, L. Major, K. Butler, J. Thiyyagalingam, and F. Tavazza, “Unified graph neural network force-field for the periodic table: solid state applications,” *Digital Discovery*, vol. 2, no. 2, pp. 346–355, 2023.
26. K. Choudhary, K. F. Garrity, A. C. E. Reid, B. DeCost, A. J. Biacchi, A. R. Hight Walker, Z. Trautt, J. Hattrick-Simpers, A. G. Kusne, A. Centrone, A. Davydov, J. Jiang, R. Pachter, G. Cheon, E. Reed, A. Agrawal, X. Qian, V. Sharma, H. Zhuang, S. V. Kalinin, B. G. Sumpter, G. Pilania, P. Acar, S. Mandal, K. Haule, D. Vanderbilt, K. Rabe, and F. Tavazza, “The joint automated repository for various integrated simulations (jarvis) for data-driven materials design,” *npj Computational Materials*, vol. 6, no. 1, p. 173, 2020.
27. J. Klimeš, D. R. Bowler, and A. Michaelides, “Chemical accuracy for the van der waals density functional,” *Journal of Physics: Condensed Matter*, vol. 22, no. 2, p. 022201, 2010.
28. A. Merchant, S. Batzner, S. S. Schoenholz, M. Aykol, G. Cheon, and E. D. Cubuk, “Scaling deep learning for materials discovery,” *Nature*, pp. 1–6, 2023. Publisher: Nature Publishing Group.
29. D. Zhang, H. Bi, F.-Z. Dai, W. Jiang, L. Zhang, and H. Wang, “Dpa-1: Pretraining of attention-based deep potential model for molecular simulation,” *tbd*, 2023.
30. D. Zhang, X. Liu, X. Zhang, C. Zhang, C. Cai, H. Bi, Y. Du, X. Qin, J. Huang, B. Li, Y. Shan, J. Zeng, Y. Zhang, S. Liu, Y. Li, J. Chang, X. Wang, S. Zhou, J. Liu, X. Luo, Z. Wang, W. Jiang, J. Wu, Y. Yang, J. Yang, M. Yang, F.-Q. Gong, L. Zhang, M. Shi, F.-Z. Dai, D. M. York, S. Liu, T. Zhu, Z. Zhong, J. Lv, J. Cheng, W. Jia, M. Chen, G. Ke, W. E, L. Zhang, and H. Wang, “Dpa-2: Towards a universal large atomic model for molecular and material simulation,” *tbd*, 2023.

31. S. Takamoto, C. Shinagawa, D. Motoki, K. Nakago, W. Li, I. Kurata, T. Watanabe, Y. Yayama, H. Iriguchi, Y. Asano, *et al.*, “Towards universal neural network potential for material discovery applicable to arbitrary combination of 45 elements,” *Nature Communications*, vol. 13, no. 1, p. 2991, 2022.
32. S. Takamoto, S. Izumi, and J. Li, “Teanet: Universal neural network interatomic potential inspired by iterative electronic relaxations,” *Computational Materials Science*, vol. 207, p. 111280, 2022.
33. S. Takamoto, D. Okanohara, Q.-J. Li, and J. Li, “Towards universal neural network interatomic potential,” *Journal of Materomics*, vol. 9, no. 3, pp. 447–454, 2023.
34. J. S. Smith, O. Isayev, and A. E. Roitberg, “ANI-1: an extensible neural network potential with DFT accuracy at force field computational cost,” *Chem. Sci.*, vol. 8, no. 4, pp. 3192–3203, 2017. Publisher: The Royal Society of Chemistry.
35. J. S. Smith, B. T. Nebgen, R. Zubatyuk, N. Lubbers, C. Devereux, K. Barros, S. Tretiak, O. Isayev, and A. E. Roitberg, “Approaching coupled cluster accuracy with a general-purpose neural network potential through transfer learning,” *Nat. Commun.*, vol. 10, no. 1, p. 2903, 2019.
36. R. Zubatyuk, J. S. Smith, J. Leszczynski, and O. Isayev, “Accurate and transferable multitask prediction of chemical properties with an atoms-in-molecules neural network,” *Science Advances*, vol. 5, no. 8, p. eaav6490, 2019.
37. D. P. Kovács, J. H. Moore, N. J. Browning, I. Batatia, J. T. Horton, V. Kapil, I.-B. Magdău, D. J. Cole, and G. Csányi, “Mace-off23: Transferable machine learning force fields for organic molecules,” *arXiv preprint arXiv:2312.15211*, 2023.
38. N. Lopanitsyna, G. Fraux, M. A. Springer, S. De, and M. Ceriotti, “Modeling high-entropy transition metal alloys with alchemical compression,” *Physical Review Materials*, vol. 7, no. 4, p. 045802, 2023.
39. I. Batatia, D. P. Kovacs, G. Simm, C. Ortner, and G. Csányi, “Mace: Higher order equivariant message passing neural networks for fast and accurate force fields,” *Advances in Neural Information Processing Systems*, vol. 35, pp. 11423–11436, 2022.
40. G. Dusson, M. Bachmayr, G. Csányi, R. Drautz, S. Etter, C. van der Oord, and C. Ortner, “Atomic cluster expansion: Completeness, efficiency and stability,” *Journal of Computational Physics*, vol. 454, p. 110946, 2022.
41. Y. Lysogorskiy, C. v. d. Oord, A. Bochkarev, S. Menon, M. Rinaldi, T. Hammerschmidt, M. Mrovec, A. Thompson, G. Csányi, C. Ortner, *et al.*, “Performant implementation of the atomic cluster expansion (pace) and application to copper and silicon,” *npj computational materials*, vol. 7, no. 1, p. 97, 2021.
42. W. C. Witt, C. van der Oord, E. Gelžinytė, T. Järvinen, A. Ross, J. P. Darby, C. H. Ho, W. J. Baldwin, M. Sachs, J. Kermode, *et al.*, “Acepotentials. jl: A julia implementation of the atomic cluster expansion,” *The Journal of Chemical Physics*, vol. 159, no. 16, 2023.
43. I. Batatia, S. Batzner, D. P. Kovács, A. Musaelian, G. N. C. Simm, R. Drautz, C. Ortner, B. Kozinsky, and G. Csányi, “The design space of e(3)-equivariant atom-centered interatomic potentials,” 2022.
44. J. P. Darby, D. P. Kovács, I. Batatia, M. A. Caro, G. L. W. Hart, C. Ortner, and G. Csányi, “Tensor-reduced atomic density representations,” *Phys. Rev. Lett.*, vol. 131, p. 028001, Jul 2023.
45. L. B. Skinner, C. Huang, D. Schlesinger, L. G. M. Pettersson, A. Nilsson, and C. J. Benmore, “Benchmark oxygen-oxygen pair-distribution function of ambient water from x-ray diffraction measurements with a wide Q-range,” *J. Chem. Phys.*, vol. 138, p. 074506, 02 2013.
46. J. E. Bertie and Z. Lan, “Infrared intensities of liquids xx: The intensity of the OH stretching band of liquid water revisited, and the best current values of the optical constants of H₂O(l) at 25°C between 15,000 and 1 cm⁻¹,” *Appl. Spectrosc.*, vol. 50, no. 8, pp. 1047–1057, 1996.

47. D. R. Moberg, S. C. Straight, C. Knight, and F. Paesani, “Molecular Origin of the Vibrational Structure of Ice Ih,” *J. Phys. Chem. Lett.*, vol. 8, no. 12, pp. 2579–2583, 2017. PMID: 28541703.
48. S. Grimme, J. Antony, S. Ehrlich, and H. Krieg, “A consistent and accurate ab initio parametrization of density functional dispersion correction (dft-d) for the 94 elements h-pu,” *The Journal of chemical physics*, vol. 132, no. 15, 2010.
49. N. O’Neill, C. Schran, S. J. Cox, and A. Michaelides, “Crumbling crystals: On the dissolution mechanism of nacl in water,” 2022.
50. M. J. Gillan, D. Alfe, and A. Michaelides, “Perspective: How good is dft for water?,” *The Journal of chemical physics*, vol. 144, no. 13, 2016.
51. D. Marx, M. E. Tuckerman, J. Hutter, and M. Parrinello, “The nature of the hydrated excess proton in water,” *Nature*, vol. 397, pp. 601–604, feb 1999.
52. M. E. Tuckerman, D. Marx, and M. Parrinello, “The nature and transport mechanism of hydrated hydroxide ions in aqueous solution,” *Nature*, vol. 417, pp. 925–929, jun 2002.
53. N. Agmon, H. J. Bakker, R. K. Campen, R. H. Henchman, P. Pohl, S. Roke, M. Thämer, and A. Has-sanalı, “Protons and Hydroxide Ions in Aqueous Systems,” *Chem. Rev.*, vol. 116, pp. 7642–7672, jul 2016.
54. F. Della Pia, A. Zen, D. Alfè, and A. Michaelides, “DMC-ICE13: Ambient and high pressure polymorphs of ice from diffusion Monte Carlo and density functional theory,” *The Journal of Chemical Physics*, vol. 157, p. 134701, 10 2022.
55. G. Algara-Siller, O. Lehtinen, F. C. Wang, R. R. Nair, U. Kaiser, H. A. Wu, A. K. Geim, and I. V. Grigorieva, “Square ice in graphene nanocapillaries,” *Nature*, vol. 519, pp. 443–445, mar 2015.
56. L. Fumagalli, A. Esfandiar, R. Fabregas, S. Hu, P. Ares, A. Janardanan, Q. Yang, B. Radha, T. Taniguchi, K. Watanabe, G. Gomila, K. S. Novoselov, and A. K. Geim, “Anomalously low dielectric constant of confined water,” *Science*, vol. 360, pp. 1339–1342, jun 2018.
57. V. Kapil, C. Schran, A. Zen, J. Chen, C. J. Pickard, and A. Michaelides, “The first-principles phase diagram of monolayer nanoconfined water,” *Nature*, vol. 609, no. 7927, pp. 512–516, 2022.
58. H. A. Hansen, J. Rossmeisl, and J. K. Nørskov, “Surface pourbaix diagrams and oxygen reduction activity of Pt, Ag and Ni(111) surfaces studied by DFT,” *Phys. Chem. Chem. Phys.*, vol. 10, pp. 3722–3730, July 2008.
59. S. Vijay, G. Kastlunger, K. Chan, and J. K. Nørskov, “Limits to scaling relations between adsorption energies?,” *The Journal of Chemical Physics*, vol. 156, June 2022.
60. A. Tiwari, H. H. Heenen, A. S. Bjørnlund, D. Hochfilzer, K. Chan, and S. Horch, “Electrochemical oxidation of co on cu single crystals under alkaline conditions,” *ACS Energy Letters*, vol. 5, no. 11, pp. 3437–3442, 2020.
61. L. L. Schaaf, E. Fako, S. De, A. Schäfer, and G. Csányi, “Accurate energy barriers for catalytic reaction pathways: an automatic training protocol for machine learning force fields,” *npj Computational Materials*, vol. 9, no. 1, p. 180, 2023.
62. L. McInnes, J. Healy, and J. Melville, “Umap: Uniform manifold approximation and projection for dimension reduction,” *arXiv preprint arXiv:1802.03426*, 2018.
63. R. Elijošius, “MACE-MP UMAP analysis,” *github.com*, 2023. 10.5281/zenodo.10426282 - <https://github.com/RokasEl/mace-mp-umap>.
64. J. K. Nørskov, T. Bligaard, J. Rossmeisl, and C. H. Christensen, “Towards the computational design of solid catalysts,” *Nature Chem*, vol. 1, pp. 37–46, 2009.

65. A. J. Medford, A. Vojvodic, J. S. Hummelshøj, J. Voss, F. Abild-pedersen, F. Studt, T. Bligaard, A. Nilsson, and J. K. Nørskov, “From the sabatier principle to a predictive theory of transition-metal heterogeneous catalysis,” *Journal of Catalysis*, vol. 328, pp. 36–42, 2015.
66. A. Bruix, J. T. Margraf, M. Andersen, and K. Reuter, “First-principles-based multiscale modelling of heterogeneous catalysis,” *Nat Catal*, vol. 2, pp. 659–670, 2019.
67. X. Qin, T. Vegge, and H. A. Hansen, “Cation-coordinated inner-sphere co₂ electroreduction at au–water interfaces,” *J. Am. Chem. Soc.*, vol. 145, pp. 1897–1905, 2023.
68. I. C. Man, H. Su, F. Calle-vallejo, H. A. Hansen, J. I. Martínez, N. G. Inoglu, J. Kitchin, T. F. Jaramillo, J. K. Nørskov, and J. Rossmeisl, “Universality in oxygen evolution electrocatalysis on oxide surfaces,” *ChemCatChem*, vol. 3, pp. 1159–1165, 2011.
69. A. Auer, M. Andersen, E.-M. Wernig, N. G. Hörmann, N. Buller, K. Reuter, and J. Kunze-liebhäuser, “Self-activation of copper electrodes during co electro-oxidation in alkaline electrolyte,” *Nat Catal*, vol. 3, pp. 797–803, 2020.
70. Q. Wang, J. Pan, J. Guo, H. A. Hansen, H. Xie, L. Jiang, L. Hua, H. Li, Y. Guan, P. Wang, W. Gao, L. Liu, H. Cao, Z. Xiong, T. Vegge, and P. Chen, “Ternary ruthenium complex hydrides for ammonia synthesis via the associative mechanism,” *Nat Catal*, vol. 4, pp. 959–967, 2021.
71. J. K. Nørskov, F. Studt, F. Abild-Pedersen, and T. Bligaard, *Fundamental Concepts in Heterogeneous Catalysis*. John Wiley & Sons, Inc., 2014.
72. J. T. Margraf, H. Jung, C. Scheurer, and K. Reuter, “Exploring catalytic reaction networks with machine learning,” *Nat Catal*, vol. 6, pp. 112–121, 2023.
73. X. Yang, A. Bhowmik, T. Vegge, and H. A. Hansen, “Neural network potentials for accelerated meta-dynamics of oxygen reduction kinetics at au–water interfaces,” *Chem. Sci.*, vol. 14, pp. 3913–3922, 2023.
74. K. Tran and Z. W. Ulissi, “Active learning across intermetallics to guide discovery of electrocatalysts for co₂ reduction and h₂ evolution,” *Nat Catal*, vol. 1, pp. 696–703, 2018.
75. L. Foppa, C. Sutton, L. M. Ghiringhelli, S. De, P. Löser, S. A. Schunk, A. Schäfer, and M. Scheffler, “Learning design rules for selective oxidation catalysts from high-throughput experimentation and artificial intelligence,” *ACS Catalysis*, vol. 12, no. 4, pp. 2223–2232, 2022.
76. M. Khatamirad, E. Fako, C. Boscagli, M. Müller, F. Ebert, R. Naumann d’Alnoncourt, A. Schaefer, S. A. Schunk, I. Jevtovikj, F. Rosowski, and S. De, “A data-driven high-throughput workflow applied to promoted in-oxide catalysts for co₂ hydrogenation to methanol,” *Catalysis Science & Technology*, vol. 13, no. 9, p. 2656–2661, 2023.
77. S. Stocker, H. Jung, G. Csányi, C. F. Goldsmith, K. Reuter, and J. T. Margraf, “Estimating free energy barriers for heterogeneous catalytic reactions with machine learning potentials and umbrella integration,” *J. Chem. Theory Comput.*, vol. 19, pp. 6796–6804, 2023.
78. R. Tran, J. Lan, M. Shuaibi, B. M. Wood, S. Goyal, A. Das, J. Heras-domingo, A. Kolluru, A. Rizvi, N. Shoghi, A. Sriram, F. Therrien, J. Abed, O. Voznyy, E. H. Sargent, Z. Ulissi, and C. L. Zitnick, “The open catalyst 2022 (oc22) dataset and challenges for oxide electrocatalysts,” *ACS Catal.*, vol. 13, pp. 3066–3084, 2023.
79. M. Pourbaix, *ATLAS of Electrochemical Equilibria in Aqueous Solutions*. Pergamon Press, Oxford, 1966.
80. M. Pourbaix, *Lectures on Electrochemical Corrosion*. Springer Science and Business Media, 1973.

81. J. K. Nørskov, J. Rossmeisl, A. Logadottir, L. Lindqvist, J. R. Kitchin, T. Bligaard, and H. Jónsson, “Origin of the overpotential for oxygen reduction at a fuel-cell cathode,” *J. Phys. Chem. B*, vol. 108, pp. 17886–17892, Nov. 2004.
82. K. A. Persson, B. Waldwick, P. Lazić, and G. Ceder, “Prediction of solid-aqueous equilibria: Scheme to combine first-principles calculations of solids with experimental aqueous states,” *Phys. Rev. B Condens. Matter Mater. Phys.*, vol. 85, June 2012.
83. A. K. Singh, L. Zhou, A. Shinde, S. K. Suram, J. H. Montoya, D. Winston, J. M. Gregoire, and K. A. Persson, “Electrochemical stability of metastable materials,” *Chem. Mater.*, vol. 29, pp. 10159–10167, Dec. 2017.
84. F. Abild-Pedersen, J. Greeley, F. Studt, J. Rossmeisl, T. R. Munter, P. G. Moses, E. Skúlason, T. Bligaard, and J. K. Nørskov, “Scaling properties of adsorption energies for hydrogen-containing molecules on transition-metal surfaces,” *Physical Review Letters*, vol. 99, July 2007.
85. J. Pérez-Ramírez and N. López, “Strategies to break linear scaling relationships,” *Nature Catalysis*, vol. 2, p. 971–976, Oct. 2019.
86. R. García-Muelas and N. López, “Statistical learning goes beyond the d-band model providing the thermochemistry of adsorbates on transition metals,” *Nat. Commun.*, vol. 10, p. 4687, Oct. 2019.
87. S. Dang, B. Qin, Y. Yang, H. Wang, J. Cai, Y. Han, S. Li, P. Gao, and Y. Sun, “Rationally designed indium oxide catalysts for CO₂ hydrogenation to methanol with high activity and selectivity,” *Science advances*, vol. 6, no. 25, p. eaaz2060, 2020.
88. A. S. Rosen, S. M. Iyer, D. Ray, Z. Yao, A. Aspuru-Guzik, L. Gagliardi, J. M. Notestein, and R. Q. Snurr, “Machine learning the quantum-chemical properties of metal–organic frameworks for accelerated materials discovery,” *Matter*, vol. 4, no. 5, pp. 1578–1597, 2021.
89. A. S. Rosen, V. Fung, P. Huck, C. T. O’Donnell, M. K. Horton, D. G. Truhlar, K. A. Persson, J. M. Notestein, and R. Q. Snurr, “High-throughput predictions of metal–organic framework electronic properties: theoretical challenges, graph neural networks, and data exploration,” *npj Computational Materials*, vol. 8, no. 1, p. 112, 2022.
90. J. Zeng, D. Zhang, D. Lu, P. Mo, Z. Li, Y. Chen, M. Rynik, L. Huang, Z. Li, S. Shi, Y. Wang, H. Ye, P. Tuo, J. Yang, Y. Ding, Y. Li, D. Tisi, Q. Zeng, H. Bao, Y. Xia, J. Huang, K. Muraoka, Y. Wang, J. Chang, F. Yuan, S. L. Bore, C. Cai, Y. Lin, B. Wang, J. Xu, J.-X. Zhu, C. Luo, Y. Zhang, R. E. A. Goodall, W. Liang, A. K. Singh, S. Yao, J. Zhang, R. Wentzcovitch, J. Han, J. Liu, W. Jia, D. M. York, W. E. R. Car, L. Zhang, and H. Wang, “DeePMD-kit v2: A software package for deep potential models,” *The Journal of Chemical Physics*, vol. 159, p. 054801, 08 2023.
91. A. K. Rappé, C. J. Casewit, K. Colwell, W. A. Goddard III, and W. M. Skiff, “Uff, a full periodic table force field for molecular mechanics and molecular dynamics simulations,” *Journal of the American chemical society*, vol. 114, no. 25, pp. 10024–10035, 1992.
92. T. A. Manz and N. G. Limas, “Introducing ddec6 atomic population analysis: part 1. charge partitioning theory and methodology,” *RSC advances*, vol. 6, no. 53, pp. 47771–47801, 2016.
93. J. J. Potoff and J. I. Siepmann, “Vapor–liquid equilibria of mixtures containing alkanes, carbon dioxide, and nitrogen,” *AIChE journal*, vol. 47, no. 7, pp. 1676–1682, 2001.
94. O. M. Yaghi, M. J. Kalmutzki, and C. S. Diercks, *Introduction to reticular chemistry: metal-organic frameworks and covalent organic frameworks*. John Wiley & Sons, 2019.
95. D. Britt, H. Furukawa, B. Wang, T. G. Glover, and O. M. Yaghi, “Highly efficient separation of carbon dioxide by a metal-organic framework replete with open metal sites,” *Proceedings of the National Academy of Sciences*, vol. 106, no. 49, pp. 20637–20640, 2009.

96. W. L. Queen, M. R. Hudson, E. D. Bloch, J. A. Mason, M. I. Gonzalez, J. S. Lee, D. Gygi, J. D. Howe, K. Lee, T. A. Darwish, *et al.*, “Comprehensive study of carbon dioxide adsorption in the metal–organic frameworks M 2 (dobdc)(M= Mg, Mn, Fe, Co, Ni, Cu, Zn),” *Chemical Science*, vol. 5, no. 12, pp. 4569–4581, 2014.
97. J. H. Choe, H. Kim, and C. S. Hong, “Mof-74 type variants for co₂ capture,” *Materials Chemistry Frontiers*, vol. 5, no. 14, pp. 5172–5185, 2021.
98. Ü. Kökçam-Demir, A. Goldman, L. Esrafili, M. Gharib, A. Morsali, O. Weingart, and C. Janiak, “Coordinatively unsaturated metal sites (open metal sites) in metal–organic frameworks: design and applications,” *Chemical Society Reviews*, vol. 49, no. 9, pp. 2751–2798, 2020.
99. B. Zheng, F. L. Oliveira, R. Neumann Barros Ferreira, M. Steiner, H. Hamann, G. X. Gu, and B. Luan, “Quantum informed machine-learning potentials for molecular dynamics simulations of CO₂’s chemisorption and diffusion in Mg-MOF-74,” *ACS nano*, vol. 17, no. 6, pp. 5579–5587, 2023.
100. L. Valenzano, B. Civalleri, S. Chavan, G. T. Palomino, C. O. Areán, and S. Bordiga, “Computational and experimental studies on the adsorption of CO, N₂, and CO₂ on Mg-MOF-74,” *The Journal of Physical Chemistry C*, vol. 114, no. 25, pp. 11185–11191, 2010.
101. M. Witman, S. Ling, S. Anderson, L. Tong, K. C. Stylianou, B. Slater, B. Smit, and M. Haranczyk, “In silico design and screening of hypothetical mof-74 analogs and their experimental synthesis,” *Chemical science*, vol. 7, no. 9, pp. 6263–6272, 2016.
102. T. D. Bennett and S. Horike, “Liquid, glass and amorphous solid states of coordination polymers and metal–organic frameworks,” *Nature Reviews Materials*, vol. 3, no. 11, pp. 431–440, 2018.
103. N. Castel and F.-X. Coudert, “Atomistic Models of Amorphous Metal–Organic Frameworks,” *The Journal of Physical Chemistry C*, vol. 126, no. 16, pp. 6905–6914, 2022.
104. J. D. Evans, V. Bon, I. Senkovska, H.-C. Lee, and S. Kaskel, “Four-dimensional metal–organic frameworks,” *Nature Communications*, vol. 11, no. 1, p. 2690, 2020.
105. M. K. Taylor, T. Runcevski, J. Oktawiec, J. E. Bachman, R. L. Siegelman, H. Jiang, J. A. Mason, J. D. Tarver, and J. R. Long, “Near-perfect CO₂/CH₄ selectivity achieved through reversible guest templating in the flexible metal–organic framework co (bdp),” *Journal of the American Chemical Society*, vol. 140, no. 32, pp. 10324–10331, 2018.
106. V. Van Speybroeck, S. Vandenhaut, A. E. Hoffman, and S. M. Rogge, “Towards modeling spatiotemporal processes in metal–organic frameworks,” *Trends Chem.*, vol. 3, pp. 605–619, 2021.
107. J. Řezáč, K. E. Riley, and P. Hobza, “S66: A well-balanced database of benchmark interaction energies relevant to biomolecular structures,” *Journal of Chemical Theory and Computation*, vol. 7, no. 8, pp. 2427–2438, 2011. PMID: 21836824.
108. A. M. Reilly and A. Tkatchenko, “Understanding the role of vibrations, exact exchange, and many-body van der Waals interactions in the cohesive properties of molecular crystals,” *The Journal of Chemical Physics*, vol. 139, p. 024705, 07 2013.
109. T. W. Keal and D. J. Tozer, “Semiempirical hybrid functional with improved performance in an extensive chemical assessment,” *The Journal of Chemical Physics*, vol. 123, p. 121103, 09 2005.
110. J. W. Furness, A. D. Kaplan, J. Ning, J. P. Perdew, and J. Sun, “Accurate and numerically efficient r²SCAN meta-generalized gradient approximation,” *J. Phys. Chem. Lett.*, vol. 11, pp. 8208–8215, 2020.
111. R. Kingsbury, A. S. Gupta, C. J. Bartel, J. M. Munro, S. Dwaraknath, M. Horton, and K. A. Persson, “Performance comparison of r²SCAN and SCAN metaGGA density functionals for solid materials via an automated, high-throughput computational workflow,” *Phys. Rev. Materials*, vol. 6, 2022.

112. T. M. Henderson, J. Paier, and G. E. Scuseria, “Accurate treatment of solids with the HSE screened hybrid,” *physica status solidi (b)*, vol. 248, no. 4, pp. 767–774, 2011.
113. J. Harl, L. Schimka, and G. Kresse, “Assessing the quality of the random phase approximation for lattice constants and atomization energies of solids,” *Phys. Rev. B*, vol. 81, p. 115126, Mar. 2010.
114. S. A. Ghasemi, A. Hofstetter, S. Saha, and S. Goedecker, “Interatomic potentials for ionic systems with density functional accuracy based on charge densities obtained by a neural network,” *Phys. Rev. B*, vol. 92, 2015.
115. A. Grisafi and M. Ceriotti, “Incorporating long-range physics in atomic-scale machine learning,” *J. Chem. Phys.*, vol. 151, p. 12828, 2019.
116. T. W. Ko, J. A. Finkler, S. Goedecker, and J. Behler, “A fourth-generation high-dimensional neural network potential with accurate electrostatics including non-local charge transfer,” *Nat Commun*, vol. 12, p. 585, 2021.
117. M. Vondrák, K. Reuter, and J. T. Margraf, “q-pac: A python package for machine learned charge equilibration models,” *J. Chem. Phys.*, vol. 159, p. 10037, 2023.
118. I. Novikov, B. Grabowski, F. Körmann, and A. Shapeev, “Magnetic moment tensor potentials for collinear spin-polarized materials reproduce different magnetic states of bcc fe,” *npj Computational Materials*, vol. 8, no. 1, p. 13, 2022.
119. M. Rinaldi, M. Mrovec, A. Bochkarev, Y. Lysogorskiy, and R. Drautz, “Non-collinear magnetic atomic cluster expansion for iron,” 2023.
120. I.-B. Magdău, D. J. Arismendi-Arrieta, H. E. Smith, C. P. Grey, K. Hermansson, and G. Csányi, “Machine learning force fields for molecular liquids: Ethylene carbonate/ethyl methyl carbonate binary solvent,” *npj Computational Materials*, vol. 9, no. 1, p. 146, 2023.
121. J. Byggmästar, A. Hamedani, K. Nordlund, and F. Djurabekova, “Machine-learning interatomic potential for radiation damage and defects in tungsten,” *Phys. Rev. B*, vol. 100, p. 144105, Oct 2019.
122. J. D. Morrow, J. L. A. Gardner, and V. L. Deringer, “How to validate machine-learned interatomic potentials,” *J. Chem. Phys.*, vol. 158, p. 121501, Mar. 2023.
123. J. L. A. Gardner, K. T. Baker, and V. L. Deringer, “Synthetic pre-training for neural-network interatomic potentials,” *Mach. Learn.: Sci. Technol.*, pp. in press, DOI: 10.1088/2632-2153/ad1626, 2023.
124. A. P. Bartók, M. J. Gillan, F. R. Manby, and G. Csányi, “Machine-learning approach for one- and two-body corrections to density functional theory: Applications to molecular and condensed water,” *Phys. Rev. B*, vol. 88, p. 054104, Aug 2013.
125. P. O. Dral, A. Owens, A. Dral, and G. Csányi, “Hierarchical machine learning of potential energy surfaces,” *The Journal of Chemical Physics*, vol. 152, p. 204110, 05 2020.
126. A. Paszke, S. Gross, F. Massa, A. Lerer, J. Bradbury, G. Chanan, T. Killeen, Z. Lin, N. Gimelshein, L. Antiga, A. Desmaison, A. Köpf, E. Yang, Z. DeVito, M. Raison, A. Tejani, S. Chilamkurthy, B. Steiner, L. Fang, J. Bai, and S. Chintala, “Pytorch: An imperative style, high-performance deep learning library,” in *Neural Information Processing Systems*, 2019.
127. M. Geiger and T. Smidt, “e3nn: Euclidean neural networks,” 2022.
128. D. P. Kovács, I. Batatia, E. S. Arany, and G. Csányi, “Evaluation of the MACE force field architecture: From medicinal chemistry to materials science,” *The Journal of Chemical Physics*, vol. 159, p. 044118, 07 2023.
129. S. J. Reddi, S. Kale, and S. Kumar, “On the convergence of adam and beyond,” *arXiv preprint arXiv:1904.09237*, 2019.

130. D. P. Kingma and J. Ba, “Adam: A method for stochastic optimization,” *arXiv preprint arXiv:1412.6980*, 2014.
131. “Materials project calculation details.” <https://docs.materialsproject.org/methodology/materials-methodology/calculation-details>. Accessed: 2023-12-18.
132. “Materials project.” <https://docs.materialsproject.org/methodology/materials-methodology/calculation-details/gga+u-calculations/hubbard-u-values>. Accessed: 2023-12-12.
133. A. Jain, G. Hautier, S. P. Ong, C. J. Moore, C. C. Fischer, K. A. Persson, and G. Ceder, “Formation enthalpies by mixing GGA and GGA + U calculations,” *Phys. Rev. B*, vol. 84, p. 045115, July 2011.
134. M. K. Horton, J. H. Montoya, M. Liu, and K. A. Persson, “High-throughput prediction of the ground-state collinear magnetic order of inorganic materials using Density Functional Theory,” *npj Comput Mater*, vol. 5, pp. 1–11, June 2019.
135. R. Sabatini, T. Gorni, and S. de Gironcoli, “Nonlocal van der waals density functional made simple and efficient,” *Phys. Rev. B*, vol. 87, p. 041108, Jan 2013.
136. I.-C. Lin, A. P. Seitsonen, I. Tavernelli, and U. Rothlisberger, “Structure and dynamics of liquid water from ab initio molecular dynamics—comparison of blyp, pbe, and revpbe density functionals with and without van der waals corrections,” *J. Chem. Theory Comput.*, vol. 8, no. 10, pp. 3902–3910, 2012.
137. A. V. Terentjev, L. A. Constantin, and J. M. Pitarke, “Dispersion-corrected pbepsol exchange-correlation functional,” *Phys. Rev. B*, vol. 98, p. 214108, Dec 2018.
138. F. Formalik, M. Fischer, J. Rogacka, L. Firlej, and B. Kuchta, “Benchmarking of GGA density functionals for modeling structures of nanoporous, rigid and flexible MOFs,” *J. Chem. Phys.*, vol. 149, p. 064110, 08 2018.
139. B. M. Axilrod and E. Teller, “Interaction of the van der Waals Type Between Three Atoms,” *J. Chem. Phys.*, vol. 11, pp. 299–300, 12 2004.
140. S. Grimme, S. Ehrlich, and L. Goerigk, “Effect of the damping function in dispersion corrected density functional theory,” *Journal of computational chemistry*, vol. 32, no. 7, pp. 1456–1465, 2011.
141. A. P. Bartók, J. Kermode, N. Bernstein, and G. Csányi, “Machine learning a general-purpose interatomic potential for silicon,” *Physical Review X*, vol. 8, no. 4, p. 041048, 2018.
142. Y. Yoshida and G. Langouche, *Defects and Impurities in Silicon Materials*. Springer, 2015.
143. D. Richie, J. Kim, S. A. Barr, K. R. Hazzard, R. Hennig, and J. W. Wilkins, “Complexity of small silicon self-interstitial defects,” *Physical review letters*, vol. 92, no. 4, p. 045501, 2004.
144. B. Sahli and W. Fichtner, “Ab initio molecular dynamics simulation of self-interstitial diffusion in silicon,” *Physical Review B*, vol. 72, no. 24, p. 245210, 2005.
145. M. Posselt, F. Gao, and D. Zwicker, “Migration of di-and tri-interstitials in silicon,” *Nuclear Instruments and Methods in Physics Research Section B: Beam Interactions with Materials and Atoms*, vol. 228, no. 1-4, pp. 212–217, 2005.
146. Y. A. Du, S. A. Barr, K. R. Hazzard, T. J. Lenosky, R. G. Hennig, and J. W. Wilkins, “Fast diffusion mechanism of silicon tri-interstitial defects,” *Physical Review B*, vol. 72, no. 24, p. 241306, 2005.
147. P. Pichler, *Intrinsic point defects, impurities, and their diffusion in silicon*. Springer Science & Business Media, 2012.
148. F. Dorner, Z. Sukurma, C. Dellago, and G. Kresse, “Melting si: beyond density functional theory,” *Physical Review Letters*, vol. 121, no. 19, p. 195701, 2018.

149. V. L. Deringer, N. Bernstein, G. Csányi, C. Ben Mahmoud, M. Ceriotti, M. Wilson, D. A. Drabold, and S. R. Elliott, “Origins of structural and electronic transitions in disordered silicon,” *Nature*, vol. 589, no. 7840, pp. 59–64, 2021.
150. N. Bernstein, B. Bhattacharai, G. Csányi, D. A. Drabold, S. R. Elliott, and V. L. Deringer, “Quantifying Chemical Structure and Machine-Learned Atomic Energies in Amorphous and Liquid Silicon,” *Angew. Chem. Int. Ed.*, vol. 58, pp. 7057–7061, 2019.
151. J. D. Morrow and V. L. Deringer, “Indirect learning and physically guided validation of interatomic potential models,” *J. Chem. Phys.*, vol. 157, no. 10, p. 104105, 2022.
152. V. L. Deringer, N. Bernstein, A. P. Bartók, M. J. Cliffe, R. N. Kerber, L. E. Marbella, C. P. Grey, S. R. Elliott, and G. Csányi, “Realistic atomistic structure of amorphous silicon from machine-learning-driven molecular dynamics,” *The journal of physical chemistry letters*, vol. 9, no. 11, pp. 2879–2885, 2018.
153. S. Plimpton, “Fast parallel algorithms for short-range molecular dynamics,” *Journal of computational physics*, vol. 117, no. 1, pp. 1–19, 1995.
154. S. Roorda, W. Sinke, J. Poate, D. Jacobson, S. Dierker, B. Dennis, D. Eaglesham, F. Spaepen, and P. Fuoss, “Structural relaxation and defect annihilation in pure amorphous silicon,” *Physical review B*, vol. 44, no. 8, p. 3702, 1991.
155. P. Grigorev, L. Frérot, F. Birks, A. Gola, J. Golebiowski, J. Grießer, J. L. Hörmann, A. Klemenz, G. Moras, W. G. Nöhring, *et al.*, “matscipy: materials science at the atomic scale with python,” *Journal of Open Source Software*, vol. 9, no. 93, p. 5668, 2024.
156. V. L. Deringer and G. Csányi, “Machine learning based interatomic potential for amorphous carbon,” *Phys. Rev. B*, vol. 95, p. 094203, Mar 2017.
157. R. Jana, D. Savio, V. L. Deringer, and L. Pastewka, “Structural and elastic properties of amorphous carbon from simulated quenching at low rates,” *Modeling and Simulation in Materials Science and Engineering*, vol. 27, p. 085009, Oct. 2019.
158. M. Qamar, M. Mrovec, Y. Lysogorskiy, A. Bochkarev, and R. Drautz, “Atomic cluster expansion for quantum-accurate large-scale simulations of carbon,” *Journal of Chemical Theory and Computation*, vol. 19, p. 5151–5167, June 2023.
159. T. K. Stenczel, Z. El-Machachi, G. Liepuoniute, J. D. Morrow, A. P. Bartók, M. I. J. Probert, G. Csányi, and V. L. Deringer, “Machine-learned acceleration for molecular dynamics in CASTEP,” *J. Chem. Phys.*, vol. 159, p. 044803, 07 2023.
160. C. de Tomas, A. Aghajamali, J. L. Jones, D. J. Lim, M. J. López, I. Suarez-Martinez, and N. A. Marks, “Transferability in interatomic potentials for carbon,” *Carbon*, vol. 155, pp. 624–634, 2019.
161. G. A. Marchant, M. A. Caro, B. Karasulu, and L. B. Pártay, “Exploring the configuration space of elemental carbon with empirical and machine learned interatomic potentials,” *npj Comput. Mater.*, vol. 9, p. 131, 2023.
162. M. A. Caro, V. L. Deringer, J. Koskinen, T. Laurila, and G. Csányi, “Growth mechanism and origin of high sp^3 content in tetrahedral amorphous carbon,” *Phys. Rev. Lett.*, vol. 120, p. 166101, Apr 2018.
163. P. Broqvist, J. Kullgren, M. J. Wolf, A. C. van Duin, and K. Hermansson, “Reaxff force-field for ceria bulk, surfaces, and nanoparticles,” *The Journal of Physical Chemistry C*, vol. 119, no. 24, pp. 13598–13609, 2015.
164. T. P. Senftle, S. Hong, M. M. Islam, S. B. Kylasa, Y. Zheng, Y. K. Shin, C. Junkermeier, R. Engel-Herbert, M. J. Janik, H. M. Aktulga, T. Verstraelen, A. Grama, and A. C. T. van Duin, “The reaxff reactive force-field: development, applications and future directions,” *npj Computational Materials*, vol. 2, p. 15011, 2016.

165. J. Kullgren, K. Hermansson, and P. Broqvist, “Supercharged low-temperature oxygen storage capacity of ceria at the nanoscale,” *The journal of physical chemistry letters*, vol. 4, no. 4, pp. 604–608, 2013.
166. A. Marronnier, G. Roma, S. Boyer-Richard, L. Pedesseau, J. M. Jancu, Y. Bonnassieux, C. Katan, C. C. Stoumpos, M. G. Kanatzidis, and J. Even, “Anharmonicity and disorder in the black phases of cesium lead iodide used for stable inorganic perovskite solar cells,” *ACS Nano*, vol. 12, pp. 3477–3486, 4 2018.
167. W. J. Baldwin, X. Liang, J. Klarbring, M. Dubajic, D. Dell’Angelo, C. Sutton, C. Caddeo, S. D. Stranks, A. Mattoni, A. Walsh, and G. Csányi, “Dynamic local structure in caesium lead iodide: Spatial correlation and transient domains,” *Small*, vol. n/a, no. n/a, p. 2303565, 2023.
168. E. Fransson, J. Wiktor, and P. Erhart, “Phase transitions in inorganic halide perovskites from machine-learned potentials,” *The Journal of Physical Chemistry C*, vol. 127, no. 28, pp. 13773–13781, 2023.
169. R. Jinnouchi, J. Lahnsteiner, F. Karsai, G. Kresse, and M. Bokdam, “Phase transitions of hybrid perovskites simulated by machine-learning force fields trained on the fly with bayesian inference,” *Phys. Rev. Lett.*, vol. 122, p. 225701, Jun 2019.
170. D. H. Cao, C. C. Stoumpos, O. K. Farha, J. T. Hupp, and M. G. Kanatzidis, “2d homologous perovskites as light-absorbing materials for solar cell applications,” *Journal of the American Chemical Society*, vol. 137, no. 24, pp. 7843–7850, 2015. PMID: 26020457.
171. T. Wang, X. He, M. Li, B. Shao, and T.-Y. Liu, “Aimd-chig: Exploring the conformational space of a 166-atom protein chignolin with ab initio molecular dynamics,” *Scientific Data*, vol. 10, Aug. 2023.
172. S. Agrawalla and A. C. T. van Duin, “Development and application of a reaxff reactive force field for hydrogen combustion,” *The Journal of Physical Chemistry A*, vol. 115, no. 6, pp. 960–972, 2011. PMID: 21261320.
173. D. L. Baulch, C. T. Bowman, C. J. Cobos, R. A. Cox, T. Just, J. A. Kerr, M. J. Pilling, D. Stocker, J. Troe, W. Tsang, R. W. Walker, and J. Warnatz, “Evaluated Kinetic Data for Combustion Modeling: Supplement II,” *Journal of Physical and Chemical Reference Data*, vol. 34, pp. 757–1397, 07 2005.
174. L. Martínez, R. Andrade, E. G. Birgin, and J. M. Martínez, “Packmol: A package for building initial configurations for molecular dynamics simulations,” *Journal of computational chemistry*, vol. 30, no. 13, pp. 2157–2164, 2009.
175. A. Stukowski, “Visualization and analysis of atomistic simulation data with ovito—the open visualization tool,” *Modeling and simulation in materials science and engineering*, vol. 18, no. 1, p. 015012, 2009.
176. R. Steudel, *Elemental sulfur and sulfur-rich compounds II*, vol. 2. Springer Science & Business Media, 2003.
177. P. Lindgren, G. Kastlunger, and A. A. Peterson, “Scaled and dynamic optimizations of nudged elastic bands,” *Journal of Chemical Theory and Computation*, vol. 15, no. 11, p. 5787–5793, 2019. PMID: 31600078.
178. S. Makri, C. Ortner, and J. R. Kermode, “A preconditioning scheme for minimum energy path finding methods,” *The Journal of Chemical Physics*, vol. 150, p. 094109, 03 2019.
179. M. Trachta, O. Bludský, J. Vaculík, R. Bulánek, and M. Rubeš, “Investigation of brønsted acidity in zeolites through adsorbates with diverse proton affinities,” *Scientific Reports*, vol. 13, p. 12380, Jul 2023.
180. S. Melchionna, G. Ciccotti, and B. L. Holian, “Hoover npt dynamics for systems varying in shape and size,” *Molecular Physics*, vol. 78, no. 3, pp. 533–544, 1993.
181. S. Melchionna, “Constrained systems and statistical distribution,” *Phys. Rev. E*, vol. 61, pp. 6165–6170, Jun 2000.

182. C. S. Cucinotta, A. Ruini, A. Catellani, and A. Stirling, “Ab initio molecular dynamics study of the keto–enol tautomerism of acetone in solution,” *ChemPhysChem*, vol. 7, no. 6, p. 1229–1234, 2006.
183. A. M. Elena, “md driver,” *gitlab.com*, 2023. 10.5281/zenodo.10432005 - <https://gitlab.com/drFaustroll/lavello>.
184. D. A. Stevens and J. R. Dahn, “The mechanisms of lithium and sodium insertion in carbon materials,” *Journal of The Electrochemical Society*, vol. 148, p. A803, jun 2001.
185. J.-X. Huang, G. Csányi, J.-B. Zhao, J. Cheng, and V. L. Deringer, “First-principles study of alkali-metal intercalation in disordered carbon anode materials,” *J. Mater. Chem. A*, vol. 7, pp. 19070–19080, 2019.
186. M. Babar, H. L. Parks, G. Houchins, and V. Viswanathan, “An accurate machine learning calculator for the lithium-graphite system,” *Journal of Physics: Energy*, vol. 3, p. 014005, dec 2020.
187. A. Genreith-Schriever, A. Alexiu, G. Phillips, C. Coates, L. Nagle-Cocco, J. Bocarsly, F. Sayed, S. Dutton, and C. Grey, “Jahn-Teller distortions and phase transitions in LiNiO₂: Insights from *ab initio* molecular dynamics and variable-temperature x-ray diffraction.,” *ChemRxiv preprint*, 2023.
188. P. Hiremath, S. Melin, E. Bitzek, and P. A. Olsson, “Effects of interatomic potential on fracture behaviour in single- and bicrystalline tungsten,” *Computational Materials Science*, vol. 207, 2022.
189. D. Smirnova, S. Starikov, G. D. Leines, Y. Liang, N. Wang, M. N. Popov, I. A. Abrikosov, D. G. Sangiovanni, R. Drautz, and M. Mrovec, “Atomistic description of self-diffusion in molybdenum: A comparative theoretical study of non-Arrhenius behavior,” *Physical Review Materials*, vol. 4, no. 1, p. 13605, 2020.
190. C. Yang and L. Qi, “Modified embedded-atom method potential of niobium for studies on mechanical properties,” *Computational Materials Science*, vol. 161, pp. 351–363, 2019.
191. M. Čák, T. Hammerschmidt, J. Rogal, V. Vitek, and R. Drautz, “Analytic bond-order potentials for the bcc refractory metals Nb, Ta, Mo and W,” *Journal of Physics Condensed Matter*, vol. 26, no. 19, p. 195501, 2014.
192. S. Starikov, P. Grigorev, and P. A. Olsson, “Angular-dependent interatomic potential for large-scale atomistic simulation of w-mo-nb ternary alloys,” *Computational Materials Science*, vol. 233, p. 112734, 2024.
193. P. W. Ma and S. L. Dudarev, “Universality of point defect structure in body-centered cubic metals,” *Physical Review Materials*, vol. 3, no. 1, p. 13605, 2019.
194. L. Ventelon, E. Clouet, and F. Willaime, “Ab initio modeling of dislocation core properties in metals and semiconductors,” *Acta Materialia*, vol. 124, pp. 633–659, 2017.
195. A. M. Goryaeva, J. Dérès, C. Lapointe, P. Grigorev, T. D. Swinburne, J. R. Kermode, L. Ventelon, J. Baima, and M.-C. Marinica, “Efficient and transferable machine learning potentials for the simulation of crystal defects in bcc fe and W,” *Phys. Rev. Materials*, vol. 5, p. 103803, Oct. 2021.
196. L. Ventelon and F. Willaime, “Generalized stacking-faults and screw-dislocation core-structure in bcc iron: A comparison between ab initio calculations and empirical potentials,” *Philosophical Magazine*, vol. 90, 2010.
197. L. Dezerald, L. Ventelon, E. Clouet, C. Denoual, D. Rodney, and F. Willaime, “Ab initio modeling of the two-dimensional energy landscape of screw dislocations in bcc transition metals,” *Physical Review B*, vol. 89, p. 024104, 1 2014.
198. P. Grigorev, A. M. Goryaeva, M.-C. Marinica, J. R. Kermode, and T. D. Swinburne, “Calculation of dislocation binding to helium-vacancy defects in tungsten using hybrid ab initio-machine learning methods,” *Acta Materialia*, vol. 247, p. 118734, 2023.

199. T. D. Swinburne and J. R. Kermode, “Computing energy barriers for rare events from hybrid quantum/classical simulations through the virtual work principle,” *Phys. Rev. B*, vol. 96, p. 144102, Oct 2017.
200. E. Bitzek, P. Koskinen, F. Gähler, M. Moseler, and P. Gumbsch, “Structural relaxation made simple,” *Physical review letters*, vol. 97, no. 17, p. 170201, 2006.
201. P. Grigorev, T. D. Swinburne, and J. R. Kermode, “Hybrid quantum/classical study of hydrogen-decorated screw dislocations in tungsten: Ultrafast pipe diffusion, core reconstruction, and effects on glide mechanism,” *Physical Review Materials*, vol. 4, no. 2, p. 023601, 2020.
202. R. H. Doremus, “Diffusion in alumina,” *Journal of Applied Physics*, vol. 100, p. 101301, 11 2006.
203. E. L. Kolsbjerg, M. N. Groves, and B. Hammer, “An automated nudged elastic band method,” *The Journal of Chemical Physics*, vol. 145, p. 094107, 09 2016.
204. S. Makri, C. Ortner, and J. R. Kermode, “A preconditioning scheme for minimum energy path finding methods,” *The Journal of Chemical Physics*, vol. 150, p. 094109, 03 2019.
205. S. J. Clark, M. D. Segall, C. J. Pickard, P. J. Hasnip, M. I. Probert, K. Refson, and M. C. Payne, “First principles methods using castep,” *Zeitschrift für kristallographie-crystalline materials*, vol. 220, no. 5-6, pp. 567–570, 2005.
206. C. J. Pickard and R. Needs, “Ab initio random structure searching,” *Journal of Physics: Condensed Matter*, vol. 23, no. 5, p. 053201, 2011.
207. N. Bernstein, G. Csányi, and V. L. Deringer, “De novo exploration and self-guided learning of potential-energy surfaces,” *npj Computational Materials*, vol. 5, no. 1, p. 99, 2019.
208. E. V. Podryabinkin, E. V. Tikhonov, A. V. Shapeev, and A. R. Oganov, “Accelerating crystal structure prediction by machine-learning interatomic potentials with active learning,” *Physical Review B*, vol. 99, no. 6, p. 064114, 2019.
209. C. J. Pickard, “Ephemeral data derived potentials for random structure search,” *Physical Review B*, vol. 106, no. 1, p. 014102, 2022.
210. D. Vanderbilt, “Soft self-consistent pseudopotentials in a generalized eigenvalue formalism,” *Physical review B*, vol. 41, no. 11, p. 7892, 1990.
211. M. Hart, J. Chen, A. Michaelides, A. Sella, M. S. Shaffer, and C. G. Salzmann, “One-dimensional arsenic allotropes: Polymerization of yellow arsenic inside single-wall carbon nanotubes,” *Angewandte Chemie*, vol. 130, no. 36, pp. 11823–11827, 2018.
212. D. Schiferl and C. Barrett, “The crystal structure of arsenic at 4.2, 78 and 299 k,” *Journal of Applied Crystallography*, vol. 2, no. 1, pp. 30–36, 1969.
213. P. Smith, A. Leadbetter, and A. Apling, “The structures of orthorhombic and vitreous arsenic,” *Philosophical Magazine*, vol. 31, no. 1, pp. 57–64, 1975.
214. P. Silas, J. R. Yates, and P. D. Haynes, “Density-functional investigation of the rhombohedral to simple-cubic phase transition of arsenic,” *Physical Review B*, vol. 78, no. 17, p. 174101, 2008.
215. M. Southard and D. Green, *Perry’s Chemical Engineers’ Handbook, 9th Edition*. McGraw-Hill Education, 2018.
216. L.-M. Liu, M. Krack, and A. Michaelides, “Density oscillations in a nanoscale water film on salt: Insight from ab initio molecular dynamics,” *Journal of the American Chemical Society*, vol. 130, pp. 8572–8573, 11 2008.
217. Y. Chiang, “Muse: A python package for fast building amorphous solids and liquid mixtures,” *github.com*, Dec. 2023. 10.5281/zenodo.10369245.

218. G. van Oudenaren, J. Ocadiz-Flores, and A. Smith, "Coupled structural-thermodynamic modeling of the molten salt system nacl-ucl3," *Journal of Molecular Liquids*, vol. 342, p. 117470, 2021.
219. D. Andersson and B. W. Beeler, "Ab initio molecular dynamics (aimd) simulations of nacl, ucl3 and nacl-ucl3 molten salts," *Journal of Nuclear Materials*, vol. 568, p. 153836, 2022.
220. L. P. N. Rebelo, V. Najdanovic-Visak, Z. P. Visak, d. P. M. Nunes, J. Szydlowski, C. A. Cerdeiriña, J. Troncoso, L. Romaní, J. M. S. S. Esperança, H. J. R. Guedes, and d. S. H. C., "A detailed thermodynamic analysis of [C4mim][BF4] + water as a case study to model ionic liquid aqueous solutions," *Green Chemistry*, vol. 6, no. 8, pp. 369–381, 2004.
221. E. Perlt, P. Ray, A. Hansen, F. Malberg, S. Grimme, and B. Kirchner, "Finding the best density functional approximation to describe interaction energies and structures of ionic liquids in molecular dynamics studies," *The Journal of Chemical Physics*, vol. 148, no. 19, p. 193835, 2018.
222. E. Gregoryanz, C. Ji, P. Dalladay-Simpson, B. Li, R. T. Howie, and H.-K. Mao, "Everything you always wanted to know about metallic hydrogen but were afraid to ask," *Matter and Radiation at Extremes*, vol. 5, no. 3, 2020.
223. I. B. Magdău, M. Marqués, B. Borgulya, and G. J. Ackland, "Simple thermodynamic model for the hydrogen phase diagram," *Physical Review B*, vol. 95, no. 9, p. 094107, 2017.
224. I. B. Magdău, F. Balm, and G. J. Ackland, "Theory of high pressure hydrogen, made simple," in *Journal of Physics: Conference Series*, vol. 950, 4, p. 042059, IOP Publishing, 2017.
225. C. J. Pickard, M. Martinez-Canales, and R. J. Needs, "Density functional theory study of phase iv of solid hydrogen," *Physical Review B*, vol. 85, no. 21, p. 214114, 2012.
226. I. B. Magdău and G. J. Ackland, "Identification of high-pressure phases iii and iv in hydrogen: Simulating raman spectra using molecular dynamics," *Physical Review B*, vol. 87, no. 17, p. 174110, 2013.
227. R. T. Howie, I. B. Magdău, A. F. Goncharov, G. J. Ackland, and E. Gregoryanz, "Phonon localization by mass disorder in dense hydrogen-deuterium binary alloy," *Physical review letters*, vol. 113, no. 17, p. 175501, 2014.
228. I. B. Magdău and G. J. Ackland, "Infrared peak splitting from phonon localization in solid hydrogen," *Physical review letters*, vol. 118, no. 14, p. 145701, 2017.
229. P. I. Cooke, I. B. Magdău, M. Peña-Alvarez, V. Afonina, P. Dalladay-Simpson, X.-D. Liu, R. T. Howie, E. Gregoryanz, and G. J. Ackland, "Raman signal from a hindered hydrogen rotor," *Physical Review B*, vol. 102, no. 6, p. 064102, 2020.
230. B. Cheng, G. Mazzola, C. J. Pickard, and M. Ceriotti, "Evidence for supercritical behaviour of high-pressure liquid hydrogen," *Nature*, vol. 585, no. 7824, pp. 217–220, 2020.
231. H. Zong, H. Wiebe, and G. J. Ackland, "Understanding high pressure molecular hydrogen with a hierarchical machine-learned potential," *Nature communications*, vol. 11, no. 1, p. 5014, 2020.
232. S. Frueh, R. Kellett, C. Mallory, T. Molter, W. S. Willis, C. King'ondu, and S. L. Suib, "Pyrolytic decomposition of ammonia borane to boron nitride," *Inorganic Chemistry*, vol. 50, pp. 783–792, 2 2011. doi: 10.1021/ic101020k.
233. A. Marfavi, P. Kavianpour, and L. M. Rendina, "Carboranes in drug discovery, chemical biology and molecular imaging," *Nature Reviews Chemistry*, vol. 6, pp. 486–504, 2022.
234. I. B. Sivaev and V. I. Bregadze, "Chemistry of nickel and iron bis(dicarbollides). a review," *Journal of Organometallic Chemistry*, vol. 614-615, pp. 27–36, 2000.
235. C. A. Brown and M. L. McKee, "Rearrangements in icosahedral boranes and carboranes revisited," *Journal of Molecular Modeling*, vol. 12, pp. 653–664, 2006.

236. F. Neese, "Software update: The orca program system—version 5.0," *WIREs Computational Molecular Science*, vol. 12, p. e1606, 9 2022.
237. A. S. Rosen, J. M. Notestein, and R. Q. Snurr, "Comprehensive phase diagrams of mos₂ edge sites using dispersion-corrected dft free energy calculations," *The Journal of Physical Chemistry C*, vol. 122, no. 27, pp. 15318–15329, 2018.
238. D. Kieczka, T. Durrant, K. Milton, K. E. J. Goh, M. Bosman, and A. Shluger, "Defects in ws₂ monolayer calculated with a nonlocal functional: any difference from gga?," *Electronic Structure*, vol. 5, no. 2, p. 024001, 2023.
239. Z. Fang, M. P. Confer, Y. Wang, Q. Wang, M. R. Kunz, E. J. Dufek, B. Liaw, T. M. Klein, D. A. Dixon, and R. Fushimi, "Formation of surface impurities on lithium–nickel–manganese–cobalt oxides in the presence of co₂ and h₂o," *Journal of the American Chemical Society*, vol. 143, no. 27, pp. 10261–10274, 2021.
240. A. H. Larsen, J. J. Mortensen, J. Blomqvist, I. E. Castelli, R. Christensen, M. Dułak, J. Friis, M. N. Groves, B. Hammer, C. Hargus, *et al.*, "The atomic simulation environment—a python library for working with atoms," *Journal of Physics: Condensed Matter*, vol. 29, no. 27, p. 273002, 2017.
241. E. Vanden-Eijnden and G. Ciccotti, "Second-order integrators for langevin equations with holonomic constraints," *Chemical Physics Letters*, vol. 429, no. 1, pp. 310–316, 2006.
242. H.-C. Wang, S. Botti, and M. A. Marques, "Predicting stable crystalline compounds using chemical similarity," *npj Computational Materials*, vol. 7, no. 1, p. 12, 2021.
243. H. Glawe, A. Sanna, E. K. U. Gross, and M. A. L. Marques, "The optimal one dimensional periodic table: A modified Pettifor chemical scale from data mining," *New Journal of Physics*, vol. 18, no. 9, p. 093011, 2016.
244. J. Riebesell, R. E. A. Goodall, Y. Chiang, A. Jain, P. Benner, K. A. Persson, and A. A. Lee, "Matbench Discovery – An evaluation framework for machine learning crystal stability prediction," *arXiv*, 2023.
245. D. Zagorac, H. Müller, S. Ruehl, J. Zagorac, and S. Rehme, "Recent developments in the Inorganic Crystal Structure Database: theoretical crystal structure data and related features," *J. Appl. Crystallography*, vol. 52, pp. 918–925, Oct 2019.
246. H. Pan, A. M. Ganose, M. Horton, M. Aykol, K. A. Persson, N. E. R. Zimmermann, and A. Jain, "Benchmarking coordination number prediction algorithms on inorganic crystal structures," *Inorganic Chem.*, vol. 60, no. 3, pp. 1590–1603, 2021.
247. S. Zhang, R. Schweitzer-Stenner, and B. Urbanc, "Do Molecular Dynamics Force Fields Capture Conformational Dynamics of Alanine in Water?," *Journal of Chemical Theory and Computation*, vol. 16, pp. 510–527, Jan. 2020.
248. J. K. Nørskov, T. Bligaard, J. Rossmeisl, and C. H. Christensen, "Towards the computational design of solid catalysts," *Nat. Chem.*, vol. 1, pp. 37–46, Apr. 2009.
249. Y. S. Al-Hamdani, M. Rossi, D. Alfè, T. Tsatsoulis, B. Ramberger, J. G. Brandenburg, A. Zen, G. Kresse, A. Grüneis, A. Tkatchenko, and A. Michaelides, "Properties of the water to boron nitride interaction: From zero to two dimensions with benchmark accuracy," *J. Chem. Phys.*, vol. 147, p. 044710, July 2017.
250. J. G. Brandenburg, A. Zen, M. Fitzner, B. Ramberger, G. Kresse, T. Tsatsoulis, A. Grüneis, A. Michaelides, and D. Alfè, "Physisorption of water on graphene: Subchemical accuracy from many-body electronic structure methods," *J. Phys. Chem. Lett.*, vol. 10, pp. 358–368, Feb. 2019.
251. C. Ehlert, A. Piras, and G. Gryn'ova, "CO₂ on graphene: Benchmarking computational approaches to noncovalent interactions," *ACS Omega*, vol. 8, pp. 35768–35778, Oct. 2023.

252. T. Tsatsoulis, S. Sakong, A. Groß, and A. Grüneis, “Reaction energetics of hydrogen on Si(100) surface: A periodic many-electron theory study,” *J. Chem. Phys.*, vol. 149, p. 244105, Dec. 2018.
253. T. Tsatsoulis, F. Hummel, D. Usyat, M. Schütz, G. H. Booth, S. S. Binnie, M. J. Gillan, D. Alfè, A. Michaelides, and A. Grüneis, “A comparison between quantum chemistry and quantum Monte Carlo techniques for the adsorption of water on the (001) LiH surface,” *J. Chem. Phys.*, vol. 146, p. 204108, May 2017.
254. H.-Z. Ye and T. C. Berkelbach, “Ab initio surface chemistry with chemical accuracy,” *arXiv preprint arXiv:2309.14640*, 2023.
255. P. G. Lustemberg, P. N. Plessow, Y. Wang, C. Yang, A. Nefedov, F. Studt, C. Wöll, and M. V. Ganduglia-Pirovano, “Vibrational frequencies of cerium-oxide-bound CO: A challenge for conventional dft methods,” *Phys. Rev. Lett.*, vol. 125, p. 256101, Dec. 2020.
256. B. X. Shi, A. Zen, V. Kapil, P. R. Nagy, A. Grüneis, and A. Michaelides, “Many-body methods for surface chemistry come of age: Achieving consensus with experiments,” *J. Am. Chem. Soc.*, vol. 145, pp. 25372–25381, Nov. 2023.
257. N. Hanikel, X. Pei, S. Chheda, H. Lyu, W. Jeong, J. Sauer, L. Gagliardi, and O. M. Yaghi, “Evolution of water structures in metal-organic frameworks for improved atmospheric water harvesting,” *Science*, vol. 374, pp. 454–459, 2021.
258. F. Berger, M. Rybicki, and J. Sauer, “Molecular dynamics with chemical accuracy—Alkane adsorption in acidic zeolites,” *ACS Catal.*, vol. 13, pp. 2011–2024, 2023.
259. F. Berger and J. Sauer, “Dimerization of linear butenes and pentenes in an acidic zeolite (H-MFI),” *Angew. Chem., Int. Ed.*, vol. 60, pp. 3529–3533, 2021.
260. G. Kresse and J. Hafner, “Ab initio molecular-dynamics simulation of the liquid-metal-amorphous-semiconductor transition in germanium,” *Phys. Rev. B*, vol. 49, p. 14251, 1994.
261. G. Kresse and J. Furthmüller, “Efficiency of ab-initio total energy calculations for metals and semiconductors using a plane-wave basis set,” *Comput. Mat. Sci.*, vol. 6, p. 15, 1996.
262. J. K. Nørskov, F. Abild-Pedersen, F. Studt, and T. Bligaard, “Density functional theory in surface chemistry and catalysis,” *Proceedings of the National Academy of Sciences*, vol. 108, pp. 937–943, Jan. 2011.
263. L. Chanussot, A. Das, S. Goyal, T. Lavril, M. Shuaibi, M. Riviere, K. Tran, J. Heras-Domingo, C. Ho, W. Hu, A. Palizhati, A. Sriram, B. Wood, J. Yoon, D. Parikh, C. L. Zitnick, and Z. Ulissi, “Open Catalyst 2020 (OC20) dataset and community challenges,” *ACS Catal.*, vol. 11, pp. 6059–6072, May 2021.
264. R. Tran, J. Lan, M. Shuaibi, B. M. Wood, S. Goyal, A. Das, J. Heras-Domingo, A. Kolluru, A. Rizvi, N. Shoghi, A. Sriram, F. Therrien, J. Abed, O. Voznyy, E. H. Sargent, Z. Ulissi, and C. L. Zitnick, “The Open Catalyst 2022 (OC22) dataset and challenges for oxide electrocatalysts,” *ACS Catal.*, vol. 13, pp. 3066–3084, Mar. 2023.
265. B. Cantor, I. Chang, P. Knight, and A. Vincent, “Microstructural development in equiatomic multi-component alloys,” *Materials Science and Engineering: A*, vol. 375, pp. 213–218, 2004.
266. A. Mazitov, M. A. Springer, N. Lopanitsyna, G. Fraux, S. De, and M. Ceriotti, “Surface segregation in high-entropy alloys from alchemical machine learning,” *arXiv preprint arXiv:2310.07604*, 2023.
267. A. P. Thompson, H. M. Aktulga, R. Berger, D. S. Bolintineanu, W. M. Brown, P. S. Crozier, P. J. in’t Veld, A. Kohlmeyer, S. G. Moore, T. D. Nguyen, *et al.*, “Lammps-a flexible simulation tool for particle-based materials modeling at the atomic, meso, and continuum scales,” *Computer Physics Communications*, vol. 271, p. 108171, 2022.

268. C. R. Trott, D. Lebrun-Grandié, D. Arndt, J. Ciesko, V. Dang, N. Ellingwood, R. Gayatri, E. Harvey, D. S. Hollman, D. Ibanez, N. Liber, J. Madsen, J. Miles, D. Poliakoff, A. Powell, S. Rajamanickam, M. Simberg, D. Sunderland, B. Turcksin, and J. Wilke, “Kokkos 3: Programming model extensions for the exascale era,” *IEEE Transactions on Parallel and Distributed Systems*, vol. 33, no. 4, pp. 805–817, 2022.
269. A. Togo, “First-principles Phonon Calculations with Phonopy and Phono3py,” *Journal of the Physical Society of Japan*, vol. 92, no. 1, p. 012001, 2023.
270. A. Togo, L. Chaput, T. Tadano, and I. Tanaka, “Implementation strategies in phonopy and phono3py,” *Journal of Physics: Condensed Matter*, vol. 35, no. 35, p. 353001, 2023.
271. R. P. Stoffel, C. Wessel, M.-W. Lumey, and R. Dronskowski, “Ab Initio Thermochemistry of Solid-State Materials,” *Angew. Chem. Int. Ed.*, vol. 49, no. 31, p. 5242, 2010.
272. C. J. Bartel, “Review of computational approaches to predict the thermodynamic stability of inorganic solids,” *J Mater Sci*, Feb. 2022.
273. J. George, G. Hautier, A. P. Bartók, G. Csányi, and V. L. Deringer, “Combining phonon accuracy with high transferability in Gaussian approximation potential models,” *J. Chem. Phys.*, vol. 153, p. 044104, July 2020. Publisher: American Institute of Physics.
274. “atomate2.” <https://github.com/materialsproject/atomate2>.
275. A. Dunn, Q. Wang, A. Ganose, D. Dopp, and A. Jain, “Benchmarking materials property prediction methods: the Matbench test set and Automatminer reference algorithm,” *Npj Comput. Mater.*, vol. 6, pp. 1–10, Sept. 2020. Number: 1 Publisher: Nature Publishing Group.
276. M. T. Agne, R. Hanus, and G. J. Snyder, “Minimum thermal conductivity in the context of *diffusion*-mediated thermal transport,” *Energy Environ. Sci.*, vol. 11, no. 3, pp. 609–616, 2018.
277. W. Voigt, *Lehrbuch der kristallphysik: (mit ausschluss der kristalloptik)*. B.G. Teubner, 1910. Google-Books-ID: 9GISAAAAIAAJ.
278. A. Reuss, “Berechnung der fließgrenze von mischkristallen auf grund der plastizitätsbedingung für einkristalle .,” *ZAMM - Journal of Applied Mathematics and Mechanics / Zeitschrift für Angewandte Mathematik und Mechanik*, vol. 9, no. 1, pp. 49–58, 1929. <https://onlinelibrary.wiley.com/doi/10.1002/zamm.19290090104>.
279. R. Hill, “The elastic behaviour of a crystalline aggregate,” *Proc. Phys. Soc. A*, vol. 65, no. 5, p. 349, 1952.
280. J. Riebesell, E. Liu, J. Qi, T. W. Ko, and S. P. Ong, “MatCalc: A Python library for calculating materials properties,” *github.com*, 2023. released July 2023, <https://github.com/materialsvirtuallab/matcalc>.
281. P. J. Huber, “Robust estimation of a location parameter,” in *Breakthroughs in statistics: Methodology and distribution*, pp. 492–518, Springer, 1992.
282. C. M. Bishop, *Neural networks for pattern recognition*. Oxford university press, 1995.
283. A. Wang, R. Kingsbury, M. McDermott, M. Horton, A. Jain, S. P. Ong, S. Dwaraknath, and K. A. Persson, “A framework for quantifying uncertainty in DFT energy corrections,” *Scientific Reports*, vol. 11, p. 15496, July 2021.
284. R. S. Kingsbury, A. S. Rosen, A. S. Gupta, J. M. Munro, S. P. Ong, A. Jain, S. Dwaraknath, M. K. Horton, and K. A. Persson, “A flexible and scalable scheme for mixing computed formation energies from different levels of theory,” *npj Computational Materials*, vol. 8, no. 1, p. 195, 2022.
285. J. Riebesell, “Pymatviz: visualization toolkit for materials informatics,” *github.com*, 2022. 10.5281/zenodo.7486816 - <https://github.com/janosh/pymatviz>.

286. S. De, A. P. Bartók, G. Csányi, and M. Ceriotti, “Comparing molecules and solids across structural and alchemical space,” *Physical Chemistry Chemical Physics*, vol. 18, no. 20, pp. 13754–13769, 2016.
287. G. Fraux, R. K. Cersonsky, and M. Ceriotti, “Chemiscope: Interactive structure-property explorer for materials and molecules,” *Journal of Open Source Software*, vol. 5, no. 51, p. 2117, 2020.
288. L. McInnes, J. Healy, and J. Melville, “UMAP: Uniform Manifold Approximation and Projection for Dimension Reduction,” 2020.

Supplementary Information

The following sections contain a diverse set of examples where the MACE-MP-0 foundation model is applied to a variety of material and chemical systems with each subsection containing one application with one or more related examples.

Similarity statement

Each subsection also contains a statement (both qualitative and quantitative) about the extent to which the training data contains configurations similar to those relevant to the application in that section. This should inform the reader about the degree of extrapolation inherent in the particular example. In order to facilitate further scrutiny, we provide a data file for most applications that can be used in conjunction with the `chemiscope` tool (at chemiscope.org) to explore the chemical environments in the training data and the application example and their relation to one another.

Performance summary

Each subsection also contains a concise statement summarising the performance of the MACE-MP-0 model in the application.

Contents

A Further Applications	38
A.1 Self-interstitials in silicon	38
A.2 Amorphous silicon from melt-quench simulations	40
A.3 Amorphous carbon	42
A.4 Ceria nanoparticles	44
A.5 Inorganic halide perovskite	46
A.6 Hybrid Organic-Inorganic Perovskites (HOIPs)	47
A.7 Protein Dynamics and Stability	48
A.8 Hydrogen combustion	52
A.9 Sulfur polymerisation	54
A.10 Zeolites	56
A.11 Open-circuit voltage of lithiated graphite	58
A.12 Jahn-Teller Distortions in LiNiO ₂	60
A.13 Point and extended defects in BCC metals	62
A.14 Alumina defects and bulk diffusion	66
A.15 Random structure search: Arsenic	67
A.16 Properties of bulk and nanoconfined water	69
A.17 Ethanol-water density-composition curves	70
A.18 Solvent mixtures	71
A.19 Aqueous interfaces	72
A.20 Molten salts	74
A.21 Room temperature ionic liquids	76
A.22 High-pressure hydrogen	77
A.23 Ammonia and borane thermal decomposition	79
A.24 Heterogeneous Catalysis	80
A.25 Carborane rearrangement	84
A.26 Transition Metal Dichalcogenides	85
A.27 Electrode-electrolyte interface / Battery system	87
A.28 Metal-organic frameworks	89
A.29 Combinatorial Materials Discovery	91
A.30 Alanine Tripeptide free energy surface	97
A.31 Molecule-Surface Interactions	98

A.32 Computational efficiency (twenty-element alloy)	101
B Benchmarks	103
B.1 Phonons	103
B.2 Bulk and Shear Moduli	105
B.3 Cohesive energies	106
B.4 Atomization energies and lattice constants of solids	107
B.5 Reaction barrier heights	110
B.6 Homonuclear diatomics	111
C Training Methods and Data Exploration	112
C.1 Training protocol	112
C.2 Exploration of the training data	114
C.3 Similarity analysis	119

A Further Applications

A.1 Self-interstitials in silicon

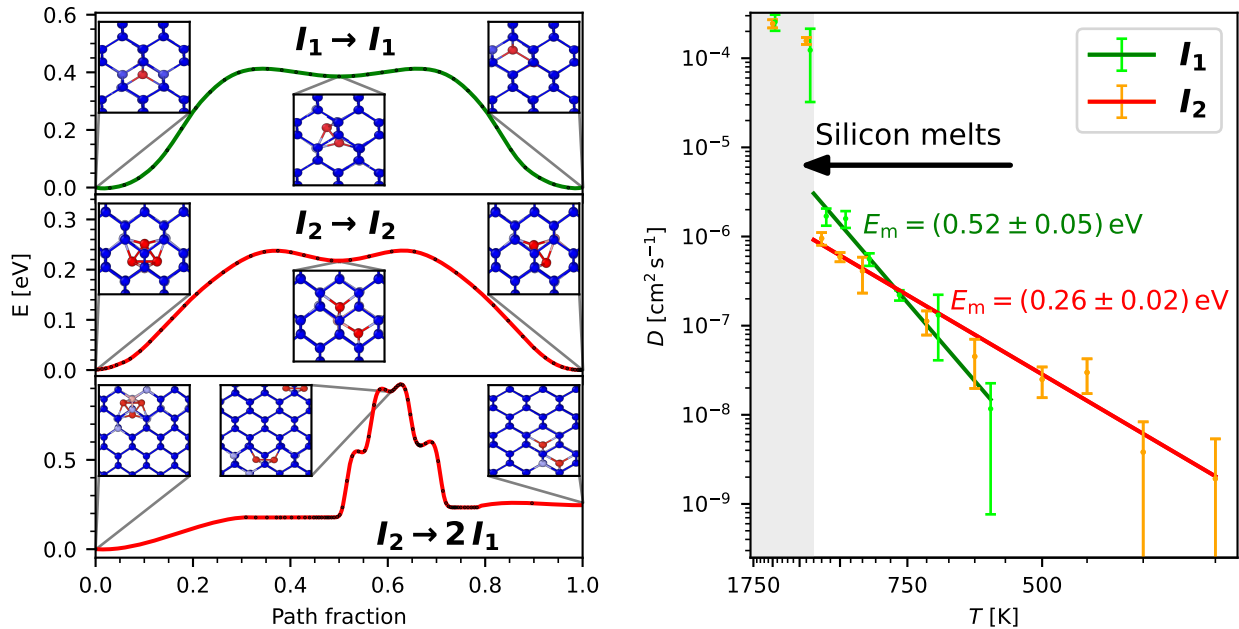


Figure 5: Single- (I_1) and di-interstitial (I_2) defects in silicon. Left: Nudged elastic band paths between two metastable sites with a subset of images shown (black dots). Right: Diffusion coefficient against inverse temperature and Arrhenius laws with migration energy E_m . The barrier heights for $I_1 \rightarrow I_1$ and $I_2 \rightarrow I_2$ agree with the corresponding E_m .

Di-interstitial silicon (I_2) constitutes a test case for the transferability of MACE-MP-0 to point defects in a periodic lattice. In the following, self-diffusion coefficients D and interstitial migration energies E_m are obtained from MD simulations without a D3 dispersion correction. Consistency tests with a (64 + 2)-atom silicon structure from (141) relaxed with the PW91 functional are performed. Relaxing with MACE-MP-0 showed no change in energy at a force tolerance of 0.05 eV/Å.

The I_2 structure was generated by relaxing a (216 + 2)-atom diamond structure with lattice constant 5.4 Å. After running NVT MD, the distance to the closest lattice site for each atom was plotted. The interstitials propagate consistent with the accepted mechanism (142). Isolating the trajectories of the point defect shows a characteristic jump length corresponding to expected jumps between stable sites.

At temperatures below 700 K, the interstitials almost exclusively remain bound in a state corresponding to the ground state with C_{1h} symmetry (143) and transition between symmetry-equivalent ground states. At higher temperatures, higher-energy states are sampled in which the interstitials separate into tetrahedral interstitial states, lying at a higher energy 0.25 eV (Fig. 5). We calculate D from the mean-square-displacement (MSD) of all atoms in the unit cell (144). The fit to the Arrhenius law (Fig. 5) gives a prefactor of $D_0 = (1.3 \pm 0.4) \times 10^{-4} \text{ cm}^2/\text{s}$ and $E_m = (0.26 \pm 0.02)$ eV, in agreement with (145) and (146).

The above calculations were repeated for a single interstitial (I_1) in a 64-atom cell. The interstitial predominantly occupies the tetrahedral state and transitions between symmetry-equivalent states via the split $\langle 110 \rangle$ state. While these states are expected, the occupancy of each state shows larger deviations from those reported in (144). Figure 5 shows a nudged elastic band (NEB) between two tetrahedral interstitial sites via a $\langle 110 \rangle$ split interstitial site, from which an energy barrier of 0.41 eV is calculated. Repeating the MD simulations at several temperatures (Fig. 5) gives $E_m = (0.52 \pm 0.05)$ eV, in agreement with LDA (144). While the prefactor is strongly system-dependent (147), the migration energy is an intrinsic property of the energy landscape and may be compared with other calculations. However, the finite system size and the interaction between interstitials results in the difference between the single- and di-interstitial migration

energies.

MACE-MP-0 underestimates the melting point, this is shown by the fact that the I_1 structure is unstable at 1173 K, whereas (144) observe no melting up to 1473 K (with the LDA functional). For I_2 and a 64-atom diamond structure, the instability is also at about 1200 K. For a 216-atom diamond structure, the phonon instability temperature lies at about 1500 K, in agreement with PBE (148).

Similarity statement

The MP dataset contains 41 pure silicon structures, including the diamond structure but no self-interstitial defects.

Performance summary

Silicon interstitials display the correct set of local minima, while their relative occupancy at finite temperature is not correct. The predicted activation energies for self-diffusion of the single and di-interstitials are consistent with previous force field and DFT calculations. The melting temperature of silicon too low by about 20 %.

A.2 Amorphous silicon from melt–quench simulations

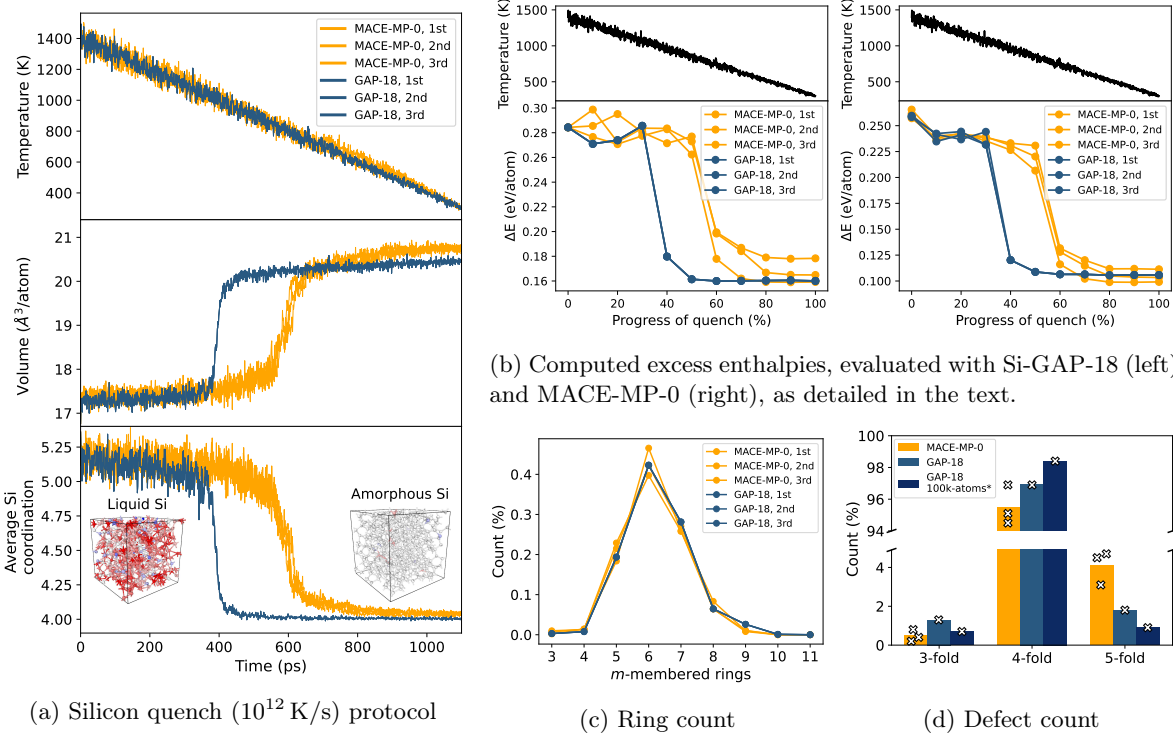


Figure 6: **Amorphous silicon.** We characterise 512-atom structural models of liquid and amorphous silicon simulated using MACE-MP-0 and, for comparison, using the established Si-GAP-18 model (141). (a) Evolution of properties during 1×10^{12} K/s quench simulations. The top panel visualises the temperature reduction from 1400 K to 300 K over 1100 ps. Below, the simulation-cell volume and the average coordination number are presented as a function of simulation time. Inset images in the lower panel visualise the coordination number distribution in simulated liquid and amorphous Si structures. Red (blue) atoms represent coordination numbers higher (lower) than 4, respectively. White atoms are 4-fold coordinated. (b) Excess enthalpies (ΔE) using Si-GAP-18 (left) and MACE-MP-0 (right) as calculated by relaxing snapshots at several points throughout the simulation. (c) Ring-size distribution in relaxed a-Si structures. (d) Coordination defect count in a-Si. Markers indicate values from individual runs and dark blue bars represent a reference 100,000-atom simulation using Si-GAP-18, taken from Ref. (149).

Amorphous silicon (a-Si) is one of the most widely studied disordered materials. It has served as an example of both the physical and chemical insight afforded by machine-learned potentials (149, 150) and as a challenging benchmark for the development of new methodology and potential models (41, 141, 151). In the present example, multiple 512-atom melt–quench simulations (1×10^{12} K/s), describing the change from liquid (1400 K) to amorphous silicon (300 K) were performed to assess the qualitative behaviour and quantitative performance of MACE-MP-0 as compared to an existing, previously validated general-purpose ML potential for silicon (141). The latter, known as “Si-GAP-18”, has been shown to produce a-Si structures in good agreement with experimental observations (149, 152). Quench simulations were carried out using LAMMPS (153) in an NPT ensemble. To test the variability from one run to another, especially given the rather small system size, three independent MD runs were performed using Si-GAP-18 and three with MACE-MP-0.

Changes in temperature profiles, volume per atom, and average Si coordination number (determined using a 2.85 Å bond-length cutoff) are presented in Fig. 6a. When quenched from the liquid state, Si undergoes a vitrification transition that is accompanied by a sudden increase in volume and concomitantly by a decrease in the average atomic coordination number, as the highly-coordinated metallic liquid transforms into the mainly four-fold coordinated semiconducting a-Si. As Fig. 6a indicates, the Si-GAP-18 and MACE-MP-0

models predict the occurrence of this transition at markedly different points in the simulation, and therefore predict different vitrification temperatures. That said, all silicon systems before and after the transition described by both models show comparable volumes per atom and an overall mostly fourfold-connected network of atoms, as expected for a-Si.

Further analysis included comparing excess energies (ΔE) that were calculated relative to crystalline diamond-type silicon. These values were computed by taking structural snapshots throughout the quench and relaxing them either with Si-GAP-18 or MACE-MP-0, similar to Ref. (152). As Fig. 6b indicates, both Si-GAP-18 and MACE-MP-0 show very low energy fluctuations between individual runs for the Si-GAP-18 simulations, while MACE-MP-0 had some minor variability in each run. For 300 K, Si-GAP-18 predicted enthalpies at around 0.16 eV/atom, whereas the relaxation and energy evaluation with MACE-MP-0 predicts a notably lower value of 0.11 eV/atom. Experimentally, the excess enthalpy of a-Si after deposition and annealing is around 0.14 eV/atom (154). This enthalpy compares well with results from a previously reported 4,096-atom 1.0×10^{11} K/s quench using Si-GAP-18 (152). Since our quench is one order of magnitude faster, higher enthalpies than 0.14 eV/atom can be expected, and there is likely more variability in the results due to the small system size. Nonetheless, the excess enthalpies predicted by MACE-MP-0 are qualitatively in the correct ballpark, viz. slightly above the corresponding crystalline phase.

As an additional measure of quality probing more subtle features of the structures, the distribution of shortest-path rings and coordination defects were investigated (Fig. 6c). The ring size distribution was assessed using `matscipy` (155). Whereas diamond-type Si consists of 6-membered ($m = 6$) rings only, a-Si includes some smaller and larger ones. Five- and seven-membered rings are still rather favourable, whereas smaller and larger ring sizes can be considered as topological defects. According to 100k-atom simulations in Ref. (149), well-relaxed a-Si was predicted to contain on the order of 1.5–2% of defects, consistent with the 4,096-atom simulations of Ref. (152). Faster quenching leads to higher defect counts, as seen from the Si-GAP-18 results in Fig. 6d, whereas the overall defect count predicted by MACE-MP-0 is still notably higher than that of Si-GAP-18 at the same quench rate.

Similarity statement

The MP dataset includes 41 different silicon-only structures, however, many of them are very high-density (high coordination number) or crystalline (all 4-fold). There were no cases of wide coordination number distribution, as seen in liquid Si – however, we found 5 unique a-Si structures (with 100 atoms each) with a mix of slightly higher and lower coordination numbers, providing information about a-Si. Based on a UMAP analysis, the closest structures in the training set are mp-1244971, mp-1245242 and mp-1245041. To help with visualization, we provide `amorphous-silicon.json` on chemiscope.org.

Performance summary

The model performs reasonably well for the description of the melt–quench process, leading to good-quality a-Si structures, albeit markedly underestimating the vitrification temperature and the excess enthalpy and overestimating the number of 5-fold coordinated atoms compared to an accurate ML potential.

A.3 Amorphous carbon

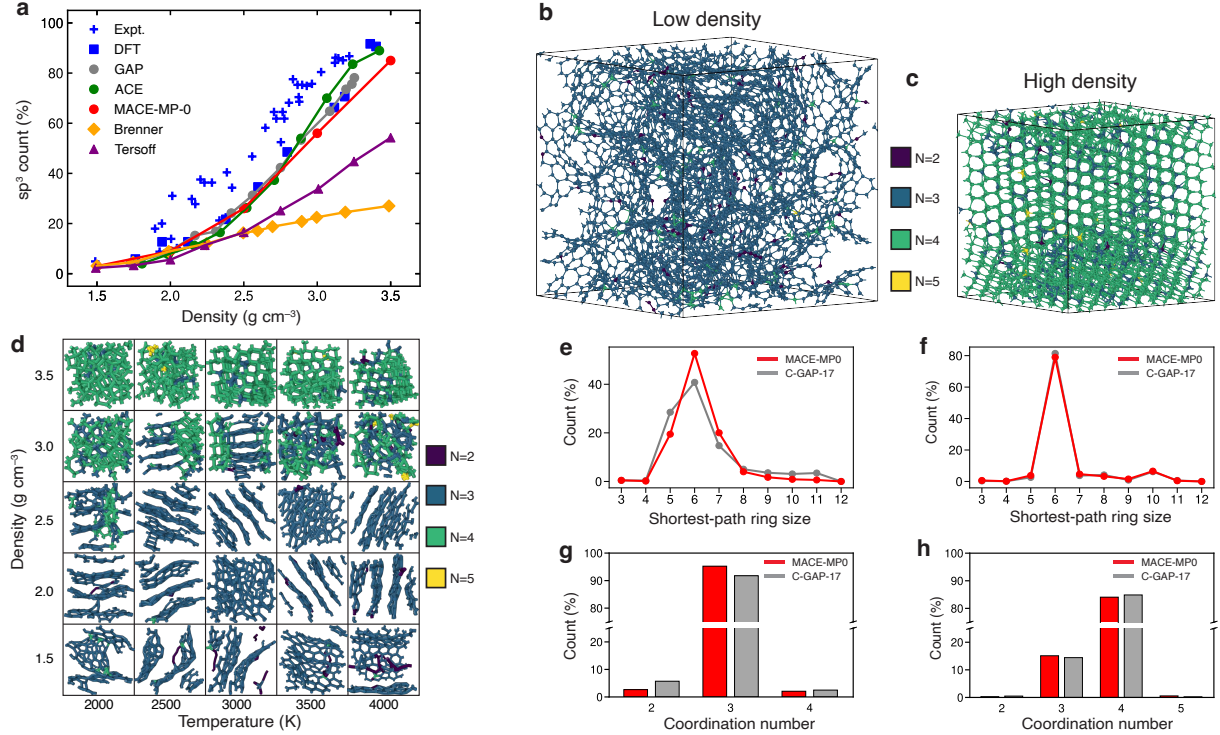


Figure 7: **Amorphous carbon.** (a) Count of sp^3 (fourfold coordinated) carbon atoms in melt-quenched carbon structures as a function of density. The results obtained with the MACE-MP-0 model are compared to computational and experimental data compiled in Ref. (156) and references therein, as well as Refs. (157) and (158). (b,c) 4,096-atom structures generated using the MACE-MP-0 potential within ASE. (d) 25×200 atom graphitisation simulations spanning relevant temperature and density ranges, similar to Ref. (159). The structures in (b-d) are colour-coded according to coordination numbers as indicated in the legends. (e-f) Shortest-path ring size count for 4,096-atom structures as determined using `matscipy` (155). (g-h) Coordination number count for 4,096-atom structures. The results in panels (e-h) are shown for a C-GAP-17-driven simulation (gray) and for a comparable simulation driven by the MACE-MP-0 potential (red).

A.3.1 Melt-quench simulations

Carbon forms many different crystalline and amorphous modifications. The structural diversity of amorphous carbon (a-C), characterised by the simultaneous presence of three-fold coordinated (sp^2) and four-fold coordinated carbon atoms (sp^3), makes it a challenging system for both classical and ML force fields (160, 161). The correct description of its growth mechanism has been among the early successes of ML-driven materials modeling (162).

We assess the accuracy of the MACE-MP-0 model in reproducing the structural complexity of amorphous phases by plotting the concentration of four-fold coordinated atoms (sp^3) as a function of density in Fig. 7. To generate amorphous structures with a given density with the MACE-MP-0 model, we perform melt-quench simulations. We start by melting diamond structures at a given density by running NVT simulations at 8000 K for 3 ps. We then perform a fast quench, reducing the temperature from 8000 K to 300 K at a cooling rate of 1000 K/ps. Finally, we optimize the geometry with LFBGS to obtain the final structure and determine the count of sp^3 atoms using a bond-length cutoff of 1.85 Å. We observe in Fig. 7 that the MACE-MP-0 model predictions reproduce the trend observed in both the DFT (157) and the experimental data extracted from (156). We also see good agreement with results of quenches using the carbon ACE reported

by Qamar et al. in Ref. (158), and using C-GAP-17 reported in Ref. (157), noting that both potentials had been specifically trained on large carbon datasets.

A.3.2 Graphitisation

MACE-MP-0 was used for two graphitisation runs containing 4096 atoms at low density (1.5 g/cm^3) and high density (3.5 g/cm^3). The low-density simulation was run at 2000 K and the high-density simulation was run at 4000 K. Additionally, 25×200 atom graphitisations spanning from 2000 to 4000 K and 1.5 to 3.5 g/cm^3 were conducted. Both 4,096 atom structures were compared to structures generated using C-GAP-17 using the same protocol, which was also used recently for an “on-the-fly” generated GAP potential (159). The protocol has two stages. The goal of the stage I is to prepare the starting configuration for the anneal in stage II, and it begins with a random structure with a hard-sphere constraint of $r_{min} \geq 1 \text{ \AA}$ and equilibrating it at 9000 K for 40 ps, followed by cooling to 5500 K over 40 ps and subsequent quenching to 300 K over 10 ps. The structures are then held at 300 K over 50 ps before being rapidly heated up to the annealing temperature over 10 ps. This concludes stage I. In stage II, the structure is annealed at 2000 K or 4000 K for 350 ps using a time step of 1 fs. We used C-GAP-17 to perform stage I because MACE-MP-0 was found to be unstable at 9000 K.

Figures 7b–c show the final structures generated using MACE-MP-0. Qualitatively, the low-density structure contains graphitic regions along with large pores of a few nm and sp chains, and the high-density structure contains highly ordered diamond-like regions. This is similar to structures generated with C-GAP-17 where similar features are also observed – see, for example, a comprehensive survey by de Tomas et al. (Ref. (160)). The same can be observed for a more comprehensive set of smaller structures (Fig. 7d). Quantitatively, the structures generated by MACE-MP-0 in annealing simulations agree with the predictions of the established C-GAP-17 model in terms of overall trends. For more detailed insight, Fig. 7e shows the shortest-path ring distribution for the low-density structure, indicating that MACE-MP-0 predicts a greater number of 6-membered rings and fewer large rings for the low-density structure compared to C-GAP-17 (thus indicating a higher degree of crystallinity in the MACE-MP-0 prediction) – this might be correlated with the higher relative count of graphite versus amorphous-like structures in the training dataset, although further analysis is required. Figure 7f shows close agreement between MACE-MP-0 and C-GAP-17 in terms of ring count for the high density structure. Finally, Figures 7g–h shows the coordination number for both 4,096 atom structures. MACE-MP-0 contains more sp^2 environments, whereas C-GAP-17 has more sp environments in the low-density structure.

Similarity statement

The MP dataset contains 89 different all-carbon structures, most of which correspond to diamond and related stacking polytypes (lonsdaleite-like and more complex ones, all purely sp^3 -bonded), as well as graphite in various forms. These structures include a range of mixed configurations with sp^2/sp^3 coexistence – the latter is expected to be critical for a correct description of a-C. The dataset also contains a number of compressed and defective fullerene configurations, with one of those cells containing sp-, sp^2 -, and sp^3 -like environments, and a few hypothetical allotropes (notably “T-carbon” and a cubane-motif-based form, representing 3- and 4-membered shortest-path rings, respectively). In essence, the dataset does contain relevant carbon environments but does not contain a significant share of highly disordered carbon configurations. Based on UMAP analysis, we find that the closest structures in the training set are mp-568028 and mp-568806. We provide `amorphous_carbon.json` to help visualize the interactive UMAP on chemiscope.org.

Performance summary

The MACE-MP-0 model correctly captures the sp^3 content as a function of density in melt–quench simulations. Detailed analysis of long annealing simulations shows good agreement with a purpose-trained ML force field for the high-density structures and qualitative agreement for low-density a-C graphitisation.

A.4 Ceria nanoparticles

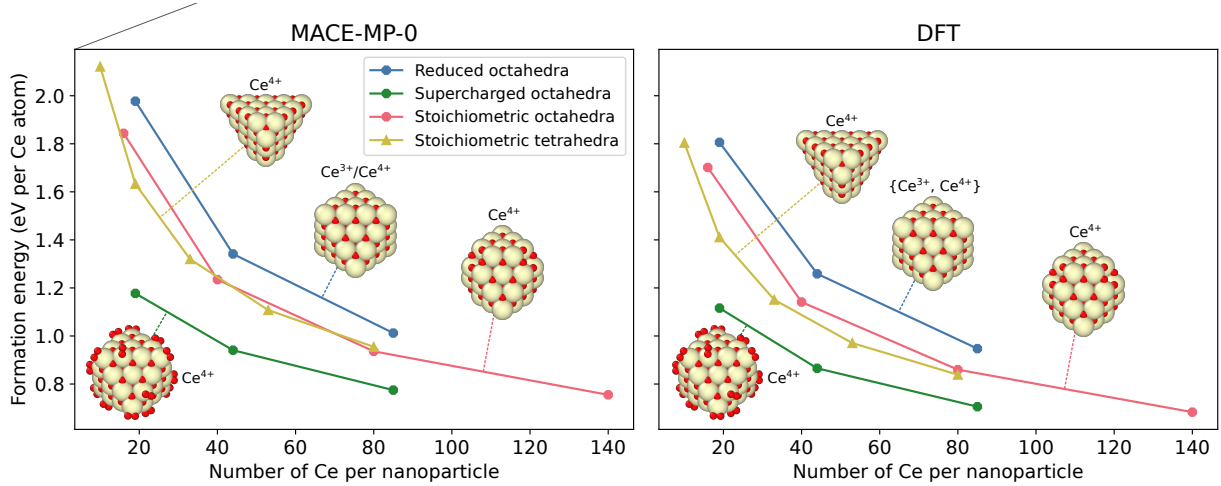


Figure 8: Size-dependent formation energies for different shapes and stoichiometries of ceria nanoparticles (NPs). Left panel: Results calculated with the MACE-MP-0 model, which was not trained on any data from ceria surfaces or NPs. Right panel: Independent validation data from PBE+U calculations. The NP images are just illustrations; the optimized structures from MACE-MP and DFT are compared in more detail in Fig. 9. The formation energy is calculated with respect to stoichiometric bulk CeO_2 (and gas-phase O_2 molecules as needed).

Cerium oxide (ceria, CeO_2) is a reducible metal oxide with intriguing chemical and physical properties, and important technological applications especially for nanostructured ceria. Experiments in the literature have for example shown that the oxygen storage capacity (OSC) of ceria at the nanoscale is strongly shape- and size-dependent.

Behind the versatile usage of ceria lies one overriding feature, namely, its exceptional reduction-oxidation (redox) properties enabled by the duality of the cerium ion ($\text{Ce}^{4+} \longleftrightarrow \text{Ce}^{3+}$). It is generally a formidable task to try to mimic interactions, structure and energetics simultaneously for a compound like ceria without having access to explicit electrons. In earlier work (163), we constructed a reactive interaction model using the ReaxFF modelling framework (164) with the aim of handling stoichiometric and partially reduced ceria bulk, surfaces, and nanoparticles (NPs). The model was based on a training set of DFT calculations for a large number of ceria systems in various forms and configurations (bulk, clusters, surface systems; stoichiometric as well as reduced systems). With some exceptions that model performed very well. In the present study, instead, our forcefield is MACE-MP-0, where the content of ceria in the training set is only bulk structures, namely exactly 18 bulk polymorphs (stoichiometric or partially reduced).

Here we assess the ability of the MACE-MP-0 model to describe small ceria nanoparticles of different shapes, sizes and reduction degrees without the training ever including any ceria NPs or surfaces. The optimized NP structures/shapes as well as their formation energies (with respect to stoichiometric bulk CeO_2 and gas-phase O_2 as needed) will be assessed.

The left panel in Fig. 8 shows the MACE-MP-0 results for optimized particles up to 140 formula units: stoichiometric tetrahedra, stoichiometric truncated octahedra, and perfect octahedra (which are partially reduced by virtue of their shapes). The bottommost curve pertains to “supercharged” NPs, i.e. perfect octahedra that are decorated with oxygen molecules. The right panel shows the corresponding results from independent reference calculations at the DFT (PBE+U) level, taken from Refs. (163, 165).

The agreement between the energetics in the two panels in Fig. 8 is good overall, which is satisfying. However, we note that as far as structures are concerned, the MACE-MP-0 model (leftmost panel of Fig. 9) is unable to distinguish between Ce^{3+} and Ce^{4+} ions, both of which should in fact be present in a partially reduced perfectly octahedral ceria nanoparticle. This deficiency of the MACE-MP-0 structure is evident from a comparison with the independent electronic PBE+U calculations in the rightmost panel of Fig. 8, labelled

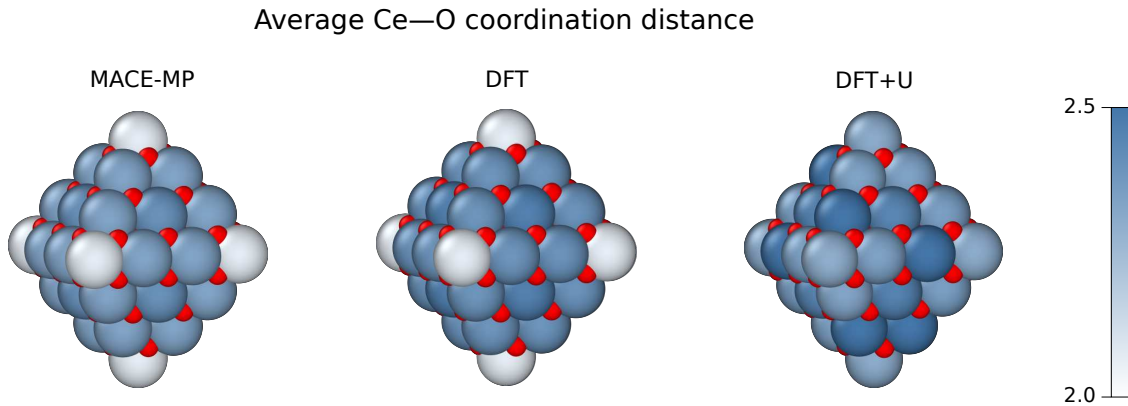


Figure 9: Optimized structures of the perfect $\text{Ce}_{44}\text{O}_{80}$ octahedron with three different methods: MACE-MP, PBE, and PBE+U. The purpose of the figure is to highlight the "pattern of distances" rather than quantitative values. The large spheres are the Ce ions (regardless of charge), and the small red spheres are oxygens. The colour scheme indicates the optimized interatomic distances in the following way: for each Ce atom, the distances to its O neighbours in the coordination figure of nearest-neighbours is measured and the average value is reflected in the colour of the sphere. Light blue indicates a short average Ce–O distance, dark blue indicates a long average Ce–O distance. The distance scale is shown in the colour bar to the right which covers the range from 2.0 Å to 2.5 Å.

"DFT+U". Such calculations involve a Hubbard correction which enforces a stronger and more adequate localization of electrons at Ce^{3+} sites than what is achieved by standard PBE without U, which is the DFT method used in the Materials Project for ceria. The presence of both Ce^{3+} and Ce^{4+} ions in the PBE+U results is seen to lead to local relaxations of the nearest-neighbour oxygen ions around the Ce ions, resulting in symmetry breaking of the NP; see for example the lack of symmetry with respect to the NP edges in the rightmost panel.

Neither the proper local relaxation nor the symmetry breaking, both seen in the PBE+U results, is captured by the MACE-MP-0 model. On the other hand, the middle panel of Fig. 9 shows our PBE-optimized results for the same NP. The structural similarity between the MACE-MP-0 result and the PBE-optimized nanoparticle is evident.

Similarity statement:

There are altogether 18 CeO_2 and CeO_{2-x} bulk structures present in the MP dataset. No examples of stoichiometric or reduced ceria surface structures or ceria nanoparticles are present in MP.

Performance summary

Broadly correct prediction of the energy of nanoparticles as a function of size, including overoxidised particles, with respect to reference DFT results.

A.5 Inorganic halide perovskite

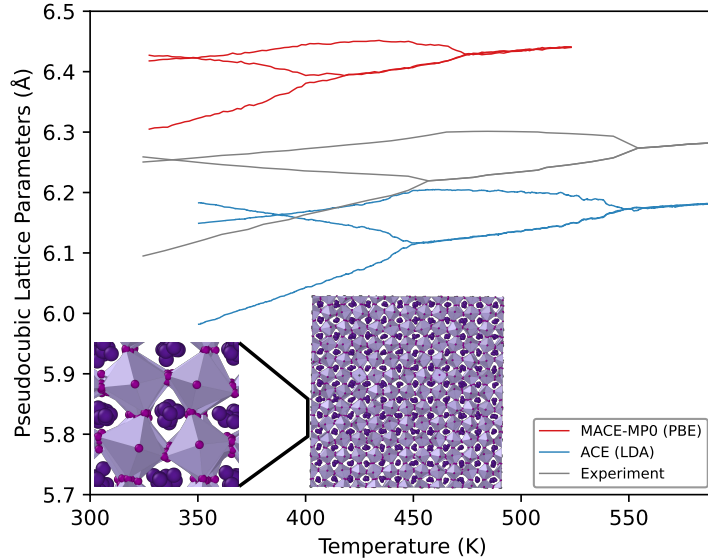


Figure 10: Variation of pseudo-cubic lattice parameters with temperature for CsPbI_3 . The MACE-MP-0 model is compared to experimental data reported by Even and co-workers (166) and an atomic cluster expansion (ACE) model trained for this material (167). Inset shows an illustration of the 8640 atom cell used to calculate the lattice constant dependence on temperature.

Halide perovskites have been shown to exhibit subtle phase transitions and long-range structural correlations. The MACE-MP-0 model has been applied to these systems by predicting phase transitions in the inorganic perovskite CsPbI_3 . This material shows two solid-solid phase transitions between room temperature and 600 K, both of which involve small rotations of the octahedral units and accompanying changes in pseudo-cubic lattice parameters (166).

To analyze these transitions, we ran constant pressure simulations of an 8640 atom supercell (Fig. 10 inset) with a slowly varying temperature. Figure 10 shows the variation in pseudo-cubic lattice parameters with temperature, compared to experimental data. These data were obtained from a 2.5 ns simulation during which the temperature was raised from 325 K to 525 K. The MACE-MP-0 model correctly predicts the qualitative nature of both phase transitions. There is a shift in both the transition temperatures and the average lattice constant, which has also been observed in other studies of these materials with DFT (167). It is also known that the choice of exchange-correlation functional has a large effect on transition temperatures for these materials (168, 169).

Similarity statement

There are 57 structures in the MP dataset containing some combination of Cs, Pb and I, without other elements. Of these, 5 structures contain all three of these elements in different compositions spanning several phases of this material. Based on UMAP analysis, these 5 structures are close to the training dataset. In particular, the cubic and orthorhombic phases which are studied in this example are present. Several similar structures with Br replacing I are also in the training set.

Performance summary

Both structural phase transitions and their transition temperatures well captured, and the 10% discrepancy in the latter with respect to experimental values is likely due to the PBE functional.

A.6 Hybrid Organic-Inorganic Perovskites (HOIPs)

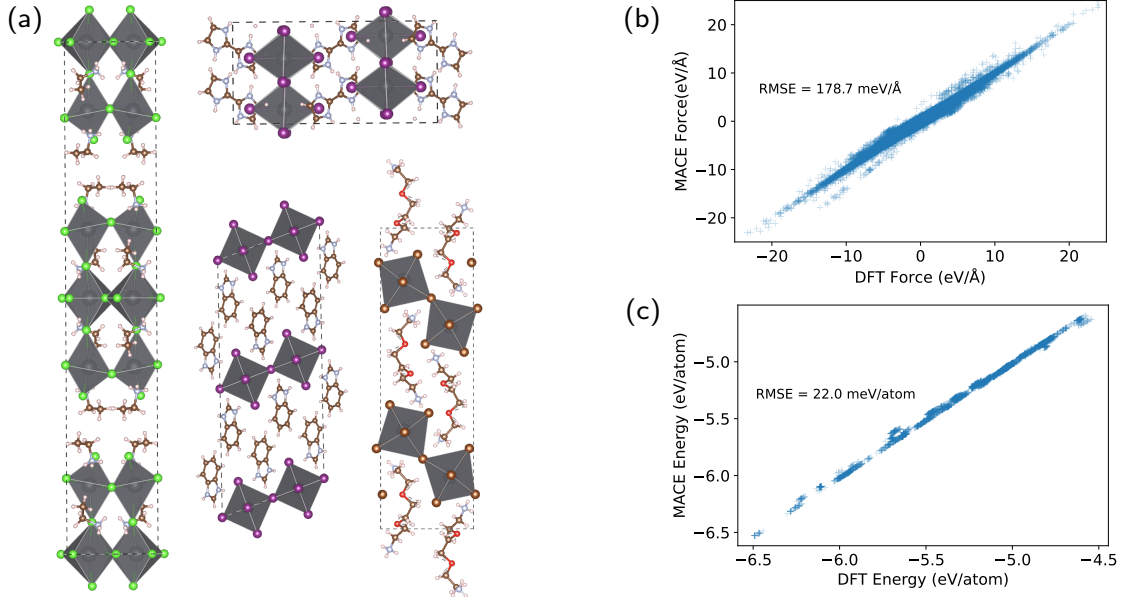


Figure 11: (a) Four emblematic HOIPs structures (b) force parity and (c) energy parity plots, with samples taken from MD trajectories and compared directly with their corresponding DFT values.

Two-dimensional hybrid organic-inorganic perovskites (HOIPs) have the advantages of enhanced stability and structural tunability over three-dimensional halide perovskites, which makes them candidates for promising applications in photoluminescence (PL), solar cells and light emitting diodes (LEDs) (170). However, HOIPs are difficult to examine using DFT because of their complicated unit cells formed when the organic cations separate the inorganic layers in (100) direction, giving the modified general formula $A'^m A_{n-1} B_n X_{3n+1}$, corresponding to n layers of the 3D-parent ABX_3 structure, separated by a layer of A' organic cations that carry either a single charge ($m = 2$) or two charges ($m = 1$); the diversity of these systems can be seen in Fig. 11a.

Using MACE-MP-0, we have investigated a set of 159 experimentally synthesized 2D HOIPs from the Cambridge Structural Database (none are in the MP) with $B = \text{Pb}$ and $X = \text{Cl}, \text{I}$, and Br . The organic cations (A' and A) are comprised of only the elements C, H, N and O, with either a +1 or +2 charge. MD simulations were performed within the NPT ensemble using the MACE-MP-0 with the D3 correction at a temperature of 300 K and pressure of 1 atmosphere. Out of 55 MD simulations, no bond-breaking or surface cleavage between the organic/inorganic layers occurred. Samples were taken every 1 ps and the errors in forces (RMSE = 180 meV/Å) and energies (RMSE = 22 meV/atom) are calculated relative to PBE+D3 (see Fig. 11b and c).

Similarity statement

In the MP training set, there are in total 398 structures with PbX ($X: \text{Cl}, \text{Br}, \text{I}$), and 1627 structures with organics made of the elements C, H, N and O. Based on UMAP analysis, we observe that some have similarities in environments to the MP training set, but only 22 structures have a mixture of PbX and CHNO. From these, there are 14 3D HOIPs in which 12 of them have methylammonium (MA) as the organic cation, 3 0D HOIPs, and 4 cases of non-perovskite systems. In the MP, there is one 2D HOIP, which is the most similar to our dataset (mp-1194995), but this structure was not in the our dataset.

Performance summary

Stable NPT MD at ambient conditions for all 159 2D hybrid perovskite materials.

A.7 Protein Dynamics and Stability

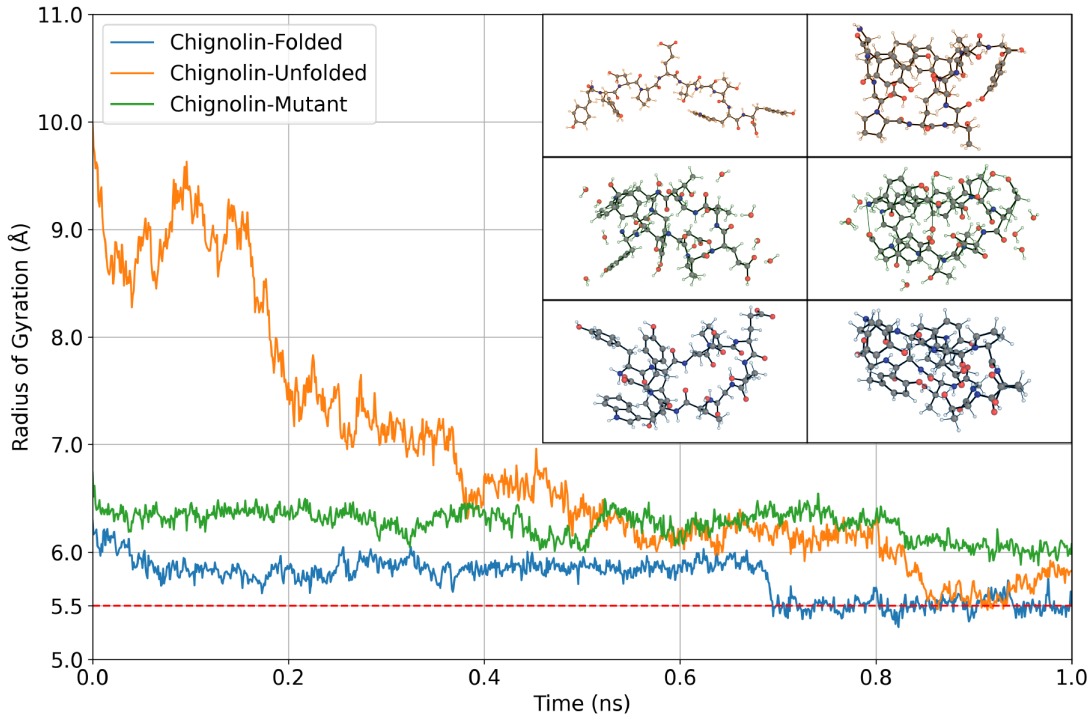


Figure 12: Plot of the radius of gyration (\AA) versus the time of simulation (ns) for the three simulations performed on Chignolin (PDB: 1UAO) and Chignolin mutant (PDB: 5AWL). In rectangular boxes initial structures (left boxes) and final structures (right boxes) of the 1 ns simulations are presented with and outline color corresponding to that of the lines of the plot. Orange is the simulation that starts from an unfolded structure of Chignolin, green corresponds to the simulation for the Chignolin mutant and blue corresponds to the simulation that starts from a partially folded structure of Chignolin. The red line corresponds to the computed radius of gyration for the PDB 1UAO structure.

Understanding the dynamics of proteins is crucial for deciphering their biological function, and remains a core challenge of computational chemistry. Machine learning potentials have the capability of modelling non-covalent interactions, which are key components of secondary and tertiary structures of proteins, due to the quantum mechanical data on which they are trained on. In this section we perform simulations on the well-known engineered Chignolin peptide (PDB: 1UAO), an artificial prototype for the protein folding phenomenon. This study diverges significantly from the majority of studies discussed in this manuscript as we are employing a machine-learning potential trained mainly on materials chemistry for a biological purpose.

We perform three separate simulations:

- A simulation starting from a partially folded structure of Chignolin.
- A simulation starting from an unfolded structure of Chignolin.
- A simulation of a mutant of Chignolin (PDB: 5AWL) starting from its PDB structure which contains 12 crystallographic waters.

Representative starting structures for the folded and unfolded Chignolin were obtained from Ref (171), specifically the first (folded) and last (unfolded) geometries from the 9543 conformations sampled by replica exchange molecular dynamics. We protonate negatively charged residues (1UAO: ASP3, GLU5, GLY10 | 5AWL: ASP3, GLU5, TYR10) and remove the proton on GLY1 for 1UAO and on TYR1 for 5AWL. We

are aware that the real stable state of Chignolin is non-neutral and solvated but this test is performed in a neutral environment as MACE-MP-0 was not trained with a charged based loss and testing stability of the simulation is our primary goal. Simulations were performed at 300K for 1 ns at 1 fs time-step and a sampling frequency of 1 ps in the NVT ensemble using the Atomic Simulation Environment (ASE) package. The Langevin thermostat was employed with a friction coefficient of 10 ps^{-1} . MACE-MP-0 with the D3 dispersion correction was used for all simulations.

From Figure 12 we can see that from its unfolded state, Chignolin is compacting throughout the course of the simulation (yellow line), while the folding state is maintained when starting from a partially folded state (blue line). The latter shows a sudden reduction in radius of gyration around 700 ps of simulation. This jump is related to the formation of a hydrogen bond between the OH of a phenolic residue and the oxygen of the backbone of Chignolin effectively making the compacting process converge and the radius of gyration closer to experiment. Both simulations of Chignolin converge to the radius of gyration computed for the crystal structures 1UAO (red line). Similarly, the Chignolin mutant shows stability across the simulation and maintains its folded structure (green line).

Figure 13 depicts some physical and chemical phenomena happening throughout the simulations. Specifically, we observe continuous proton transfer between the neutralised COOH and NH₂ functional groups of GLY1 and GLY10 of Chignolin (left) and many proton transfers between various residues of the Chignolin mutant and the crystallographic waters (right). This shows the remarkable capability of MACE-MP-0 in modelling non-covalent interactions but more importantly in modelling reactivity in molecular dynamics simulations. We point out that these observed processes of proton transfer are not possible to observe with classical force-fields as they are generally not parametrised for such effects.

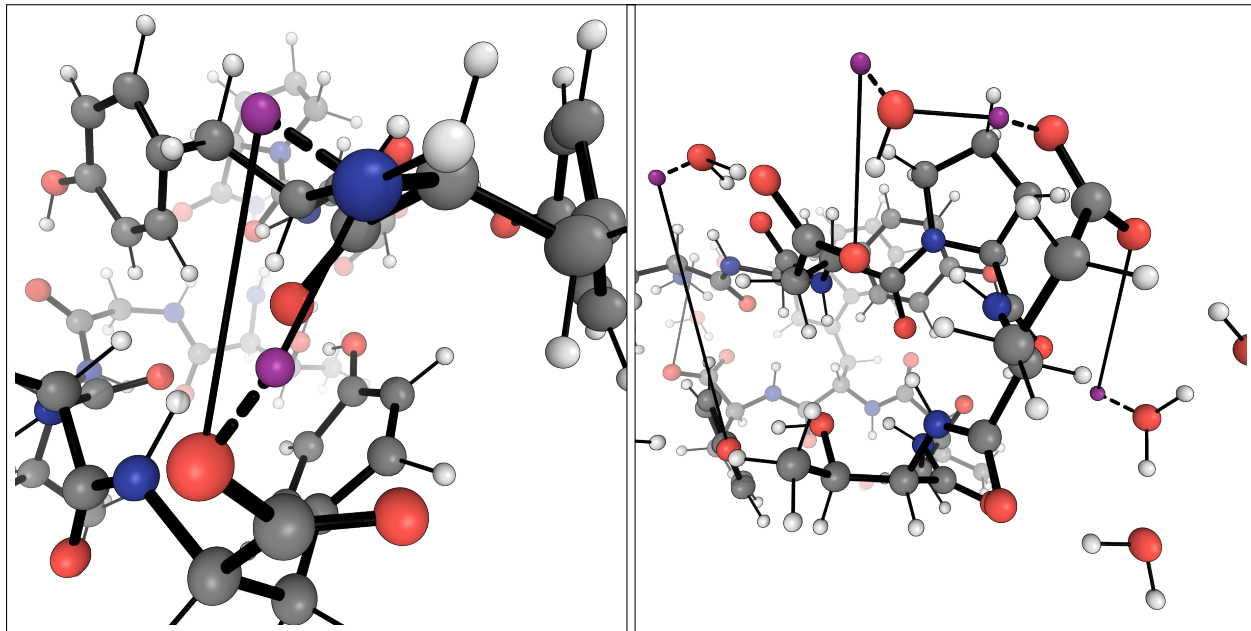


Figure 13: Depiction of representative proton transfers occurring during the 1 ns simulations. Hydrogens that are being transferred are highlighted in purple. The bond connectivity of the original starting structure is kept to highlight the transfer of a proton. The newly formed bonds are shown in dashed black cylinders. (Left) Proton transfer between COOH of GLY 10 and NH₂ of GLY 1 shown for the last frame of the simulation started from the partially folded Chignolin structure. (Right) Series of proton transfers between residues containing COOH, phenolic groups (-OH) and crystallographic H₂O for the last frame of the Chignolin mutant simulation.

Similarity statement

The MP dataset encompasses only 99 structures exclusively composed of the elements hydrogen (H), carbon (C), oxygen (O), and nitrogen (N). Based on the UMAP analysis, the atomic environments of Chignolin and Chignolin mutant are clustered similarly to those of the filtered 99 structures (see Figure 14), which could mean that the environments of the training set are fairly similar to those of the test structures . However, after manual inspection, we observe that the filtered structures only resemble the protein under study by some functional groups such as carboxylic acid (-COOH), amino groups (-NH₂), aromatic and amide groups. Some of the most similar structures are *e.g.* mp-998880, mp-1203308, mp-556151, mp-707289 and mp-1203544.

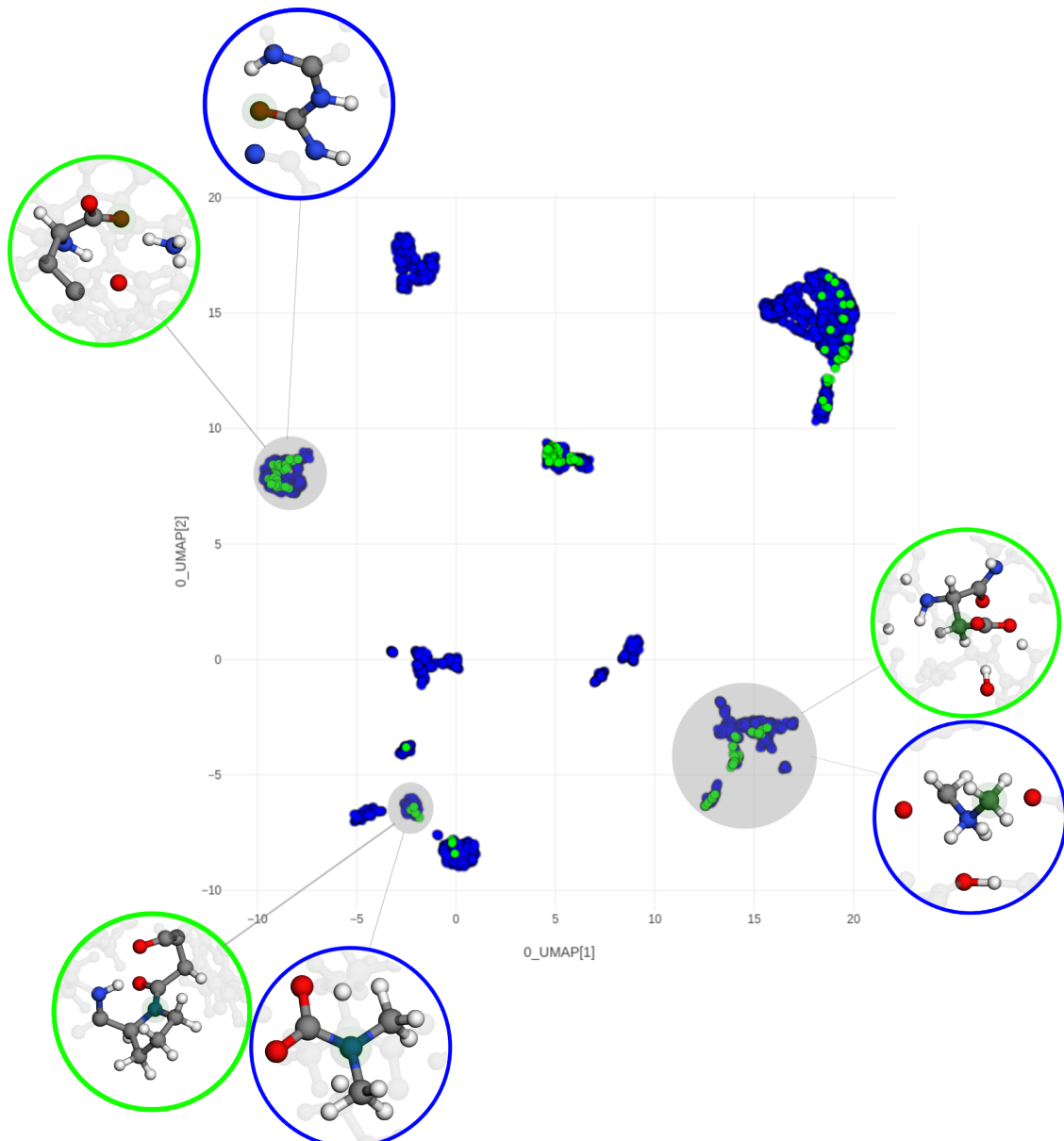


Figure 14: Comparison of the atomic environments in the 99 filtered structure of the training data (blue dots) and in the Chignolin mutant structure (green dots) in the form of a UMAP plot. Insets of some local environments are shown for a few key functional groups of the protein (green circles) with corresponding similar clustered environments from the training set (blue circles)

Performance summary

All three simulations performed showed no specific un-physical phenomena. Moreover, for all systems the radius of gyration is maintained or converges to the value computed from the PDB structures. However, we note that residues that were charged in the PDB structures were protonated, thus the experimental folding (i.e. formation of secondary structure) cannot be fully recovered in this context.

A.8 Hydrogen combustion

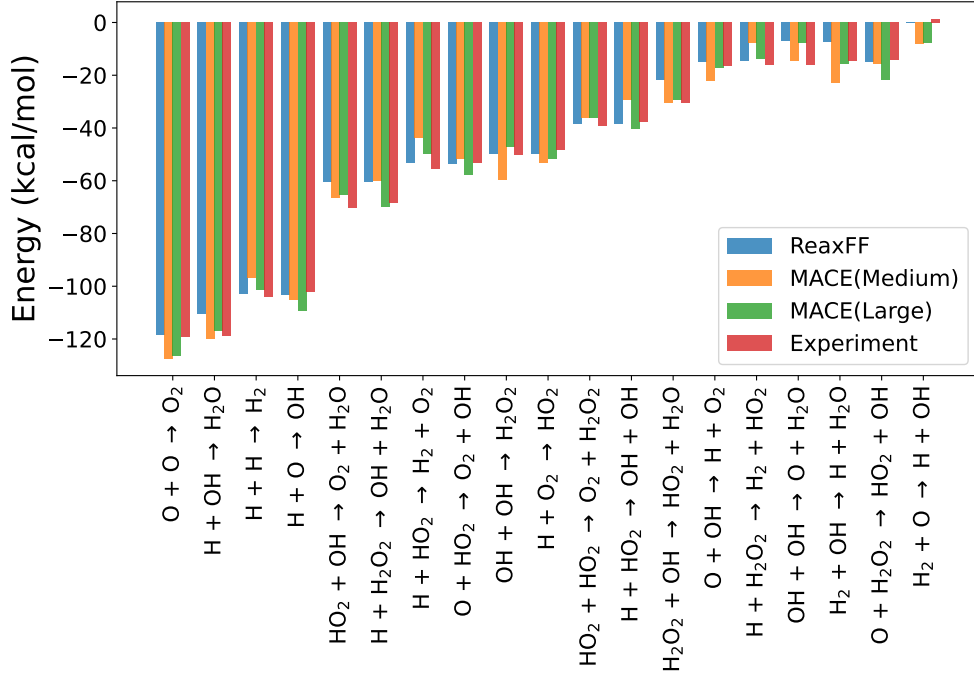


Figure 15: Comparison of Heats of Reaction of Key Hydrogen Combustion Reactions with ReaxFF and Literature

Describing the complex reactivity in hydrogen combustion systems is a challenging task, often approached through thermodynamics via quantum mechanical (QM) calculations. However, accurately capturing kinetics in molecular dynamics simulations is hindered by the lack of a suitable transferable empirical force field, a difficulty compounded by the challenge of collecting experimental data in high-pressure, extreme explosion conditions. In this context, we compare our machine learning force field, MACE-MP-0, against the reactive classical empirical force field ReaxFF (172). ReaxFF model was created by fitting to an extensive QM dataset. The creation involved the identification of key reactions and components, and the collection of data on formation heats, reaction heats, and energy barriers, as well as computing bond stretching energies and valence angle distortion energies for all combinations of hydrogen and oxygen. In our study, the performance of MACE-MP-0 in describing these reactions is evaluated and compared to both ReaxFF and experimental values. It is important to note that MACE-MP-0 has not been specifically trained for hydrogen combustion reactions as the training data primarily comprises periodic materials and a smaller fraction of molecular crystals; see appendix A.8.

As seen in Fig. 15, the ReaxFF and MACE-MP-0 models agree well with experimental values (173), yielding an RMSE of 4.82, 6.59 and 4.83 kcal/mol. In particular, the large MACE-MP-0 model performs on par with ReaxFF. This is a surprising feat, considering that ReaxFF parameters were tuned using the reaction energies and transition states of relevant hydrogen oxidation reactions.

Packmol (174) is employed to randomly arrange a 1:1 fuel mixture comprising 128 H₂ and 64 O₂ molecules within cubic cells (side length, $a = 25\text{--}42 \text{ \AA}$), yielding densities ranging from 0.05–0.25 kg/dm³. Employing NVT simulations for 100 ps with the MACE-MP-0 potential, we tracked the evolution of H₂/O₂ mixtures. Reactivity analysis focused on water formation, identified via pairwise cutoffs derived from the first minima of the radial distribution function. The relationship between temperature/density variations in the fuel mixture and the water formation rate is depicted in Fig. 16a and Fig. 16c. We find qualitative agreement with the water formation curves of Ref. (172), with a max conversion of approx. 80 %.

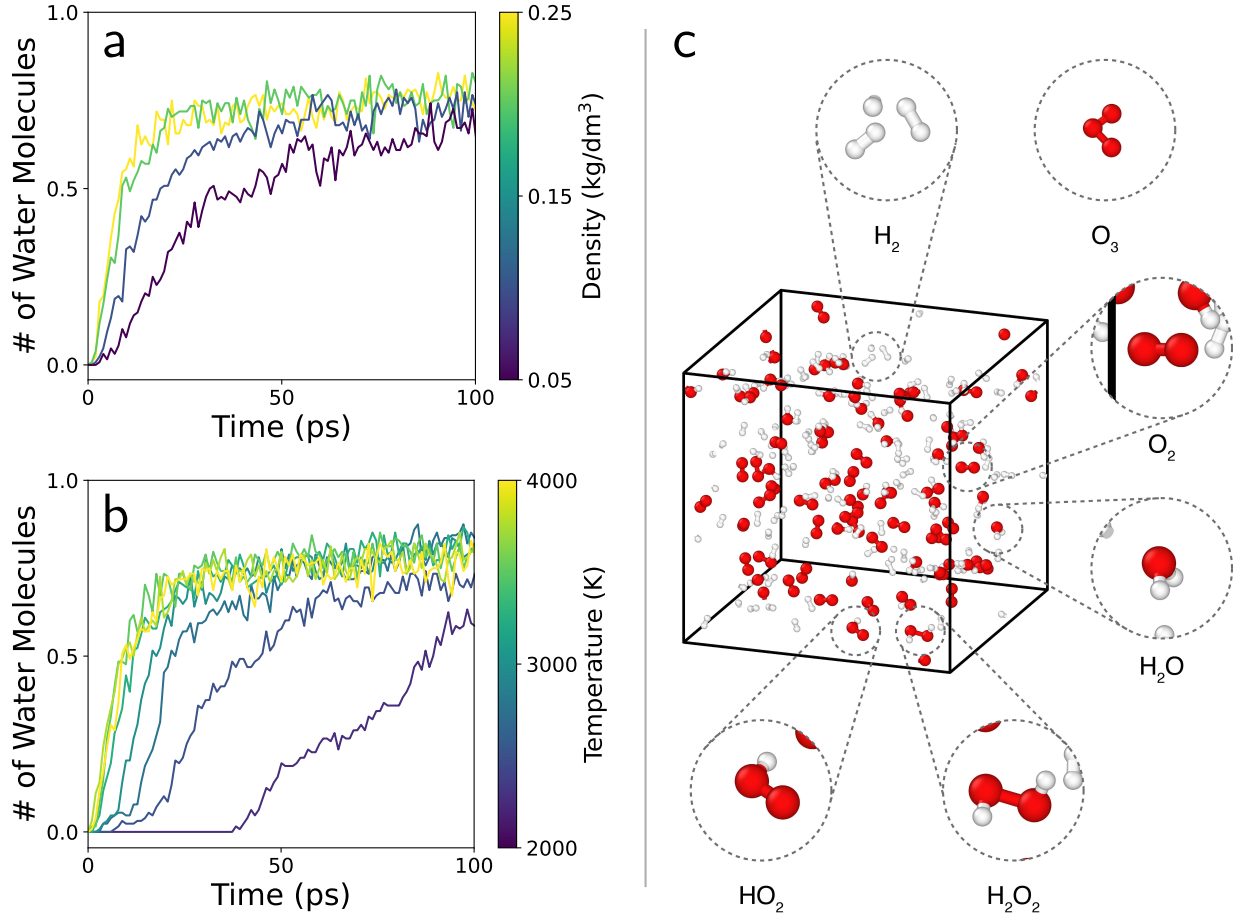


Figure 16: Analysis and visualization of hydrogen combustion in MD simulations. Water formation as a function of elapsed time for a range of (a) densities and (b) temperatures. (c) Representative snapshot during MD simulations, with key species highlighted. Note, although O₃ is not present in the particular simulation frame shown, it is occasionally observed in other simulations.

Similarity statement

We analyze the MPtrj training dataset for the key species in hydrogen combustion (O₂, H₂, H₂O, H₂O₂, HO₂, and OH). These species are present as minority units in other structures, appearing in 2277, 1310, 1342, 232, 21, and 0 structures, respectively. We find 21 molecular crystals composed exclusively of O₂, 17 for H₂, 11 for H₂O, 2 for H₂O₂. There are only eight structures made up of multiple key reaction species. UMAP analysis reveals only 2 MPtrj structures (mp-684678 and mp-1181087) with high similarity to frames within MD simulations.

Performance summary

Heats of reaction close to experimental values (typically within 5 kcal/mol) for 19 reactions. Chemically correct species produced during combustion, with final yield also consistent with reference methods.

A.9 Sulfur polymerisation

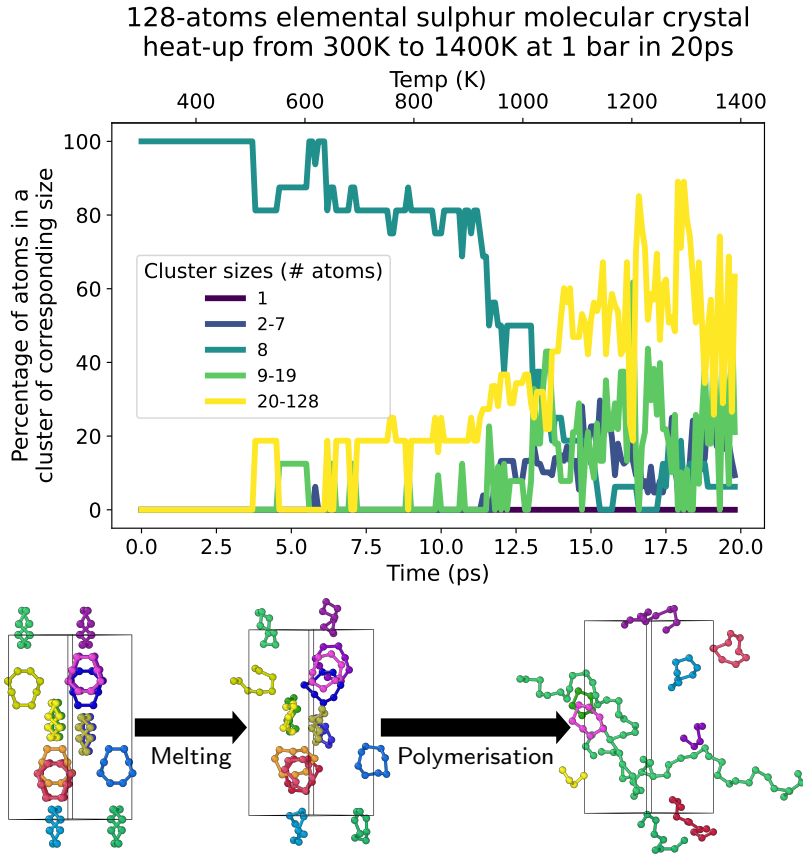


Figure 17: **Elemental sulfur.** Evolution of the cluster size as a function of temperature in a 20 ps heat-up simulation with a linear increase in temperature applied over time. The pictures below are representative snapshots from the simulation, visualised in OVITO (175).

We ran a 20 ps NPT heat-up of a 128-atom structural model of elemental sulfur from 300 to 1400 K at 1 bar. At ambient pressure, experiments show that the molecular crystal formed of S_8 rings melts at 392 K and starts polymerizing at 432 K (176), forming large chains that result in a 4-fold increase in viscosity of the liquid. We can qualitatively reproduce this melting and chain formation with MACE-MP-0+D3 correction (Fig. 17). The simulated melting temperature does not exactly match the experiment, as expected for a very fast run with only 128 atoms – however, the simulation does qualitatively reproduce the onset of depolymerisation with increasing temperature, where large chains break down into smaller ones. For these reasons, we can say that MACE-MP-0+D3 is at least qualitatively applicable to simulate the polymerisation of elemental sulfur starting from α -rhombohedral crystalline S_8 (with further work being required to test the quantitative agreement).

Similarity statement

The MP dataset contains 31 structures that only contain the element sulfur. Based on UMAP analysis, we see that a large part of the atomic environments in the example system are similar to environments in the training data. The database contains geometry optimizations of sulfur crystals formed of rings with various sizes: 6 (mp-7), 7 (mp-557559), 8 (mp-77), 9 (mp-556269), 10 (mp-557031), 11 (mp-561370), 12 (mp-558014), 13 (mp-583072), 14 (mp-561513), 10x6 (there exists a sulfur crystal form comprised of S_{10} and S_6 rings, 557031), 18 (mp-555915) and 20 (mp-558964). It also contains crystals with planar strands of sulfur (mp-1179643), trigonal polymeric sulfur (mp-555760), and so-called fibrous sulfur (quenched polymeric liquid sulfur, mp-1196831), as well as isolated

dimers (mp-1179639), trimers (mp-655141) and single atoms (mp-1063988). It does not contain melt or polymeric liquid structures. Based on the UMAP analysis, the closest (most relevant) structures in the training set are: mp-556269, mp-555915, mp-83, mp-557031, mp-557559, mp-666931. We provide `sulfur.json` to help visualize the interactive UMAP on chemiscope.org.

Performance summary

Qualitatively correct polymerisation, starting at a temperature that is estimated to be within 20% of the experimental value.

A.10 Zeolites

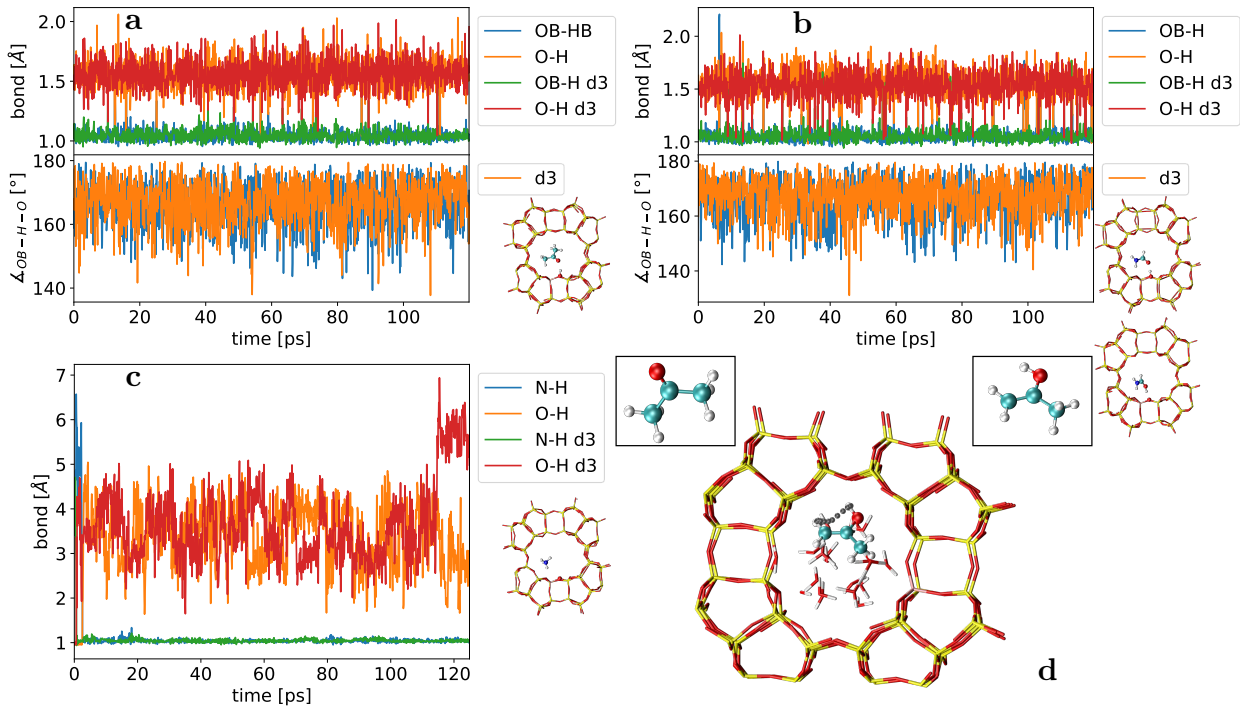


Figure 18: a) MOR-Al with acetone, instantaneous bond lengths between O@BAS, H@BAS and O@acetone and H@BAS upper panel and angles lower panel - for both MACE-MP-0 and D3 corrected a hydrogen bond is formed. b) same as a) but for formamide, one can see deprotonation events when O–H bond value approaches 1 Å, c) NH₃ case with bonds same as a) NH₃ quickly deprotonates the BAS to form NH₄⁺ d) NEB (177, 178) path for keto–enol tautomerism of acetone, the path is indicated by the H atom traces, only final position of the rest of the atoms is shown

Zeolites are mesoporous materials with an important role as heterogeneous catalysts in several industrial processes. In this section, we assess the suitability of MACE-MP-0 to model these materials. We chose two zeolites, Modernite and Zeolite Socony Mobil-5 - ZSM-5 or MOR and MFI by their International Zeolite Association names. We have investigated the dynamic stability of the zeolite frameworks themselves, MOR with NH₃, acetone and formamide inside one channel and MFI with water, cyclohexane and a mixture of N₂ in one channel and CO₂ in the other. Each zeolite was modified by adding a Brønstead acid site - BAS, Al, and the compensating H on the adjacent oxygen, see Fig. 18. Another set of simulations was carried out on MOR-Al, where in addition to acetone, we introduced 20 water molecules and 32 water molecules, and similarly for MFI-Al with cyclohexene instead of acetone. MACE-MP-0 correctly identified the adsorption sites, for ammonia, acetone and formamide and the structural motifs in agreement with DFT calculations from, (179) in NPT ensemble (180, 181) simulations carried at 300 K and 400 K for 125 ps each using ASE. Furthermore, in the case of ammonia MACE-MP-0 correctly predicts the formation of the NH₄⁺ and its stabilization around the BAS by the creation of hydrogen bonds with adjacent oxygen atoms, see Fig. 18 panel c. MACE-MP-0 also correctly reproduces the DFT findings that acetone does not deprotonate the BAS but forms hydrogen bonds, while formamide predominantly forms hydrogen bonds but deprotonates the BAS occasionally. Additionally, for the system MOR-Al with acetone and 20 water molecules, we have computed the barrier of the keto-acetone to enol-acetone conversion. MACE-MP-0 gave a barrier of 2.11 eV and with D3 correction, 2.20 eV, numbers are in good agreement with PBE calculations reported in (182). The code used to generate the trajectories is available in the repo (183).

Similarity statement

For the system MOR-Al the training set contains 145 structures that have Si, O, Al, and H elements on their own or along with other elements. Based on UMAP analysis, we see almost all atomic environments in the example system are similar to environments in the training data. Similar findings hold true for MFI-Al with 145 structures matches. One note, on the structures with adsorbates inside, they hold very low structure matches, for examples, acetone in MOR-Al, matches only three structures, and formamide only one, and none very close to the studied zeolites. Adsorbants on their own match 1029 structures for formamide, 1892 for acetone and 3139 for NH₃. If we consider only Si, O, Al, and H elements we have only 11 similar structures for both zeolites considered and none is an exact match but they offer good representability of the local environments.

The closest (most relevant) structures in the training set are CO₂ (mp-556034, mp-20066, mp-995224, mp-11725, mp-644607, mp-1102227, mp-1190685, mp-995198, mp-1190699, mp-1077906, mp-1077316, mp-729728). CO₂ alone matches 4896 structures with C, O and alongside other elements.

We provide

- MOR-Al_FilterType.exclusive_SiOAlH_chemiscope_input.json
- MFI-Al_FilterType.exclusive_SiOAlH_chemiscope_input.json
- MFI-Al-H2O_FilterType.exclusive_SiAlOH_chemiscope_input.json
- MFI-Al-H2O-cyclohexene_FilterType.exclusive_SiAlOCH_chemiscope_input.json
- MFI-Al-H2O_FilterType.exclusive_SiAlOH_chemiscope_input.json
- MFI-Al-cyclohexene_FilterType.exclusive_SiAlOCH_chemiscope_input.json
- MOR-Al_FilterType.inclusive_SiOAlH_chemiscope_input.json
- MFI-Al_FilterType.inclusive_SiOAlH_chemiscope_input.json

to help visualize the interactive UMAP on chemiscope.org.

Performance summary

Correct prediction of binding sites, and qualitatively correct reaction behaviour for a range of structures and ligands, including good agreement of predicted reaction barrier with DFT.

A.11 Open-circuit voltage of lithiated graphite

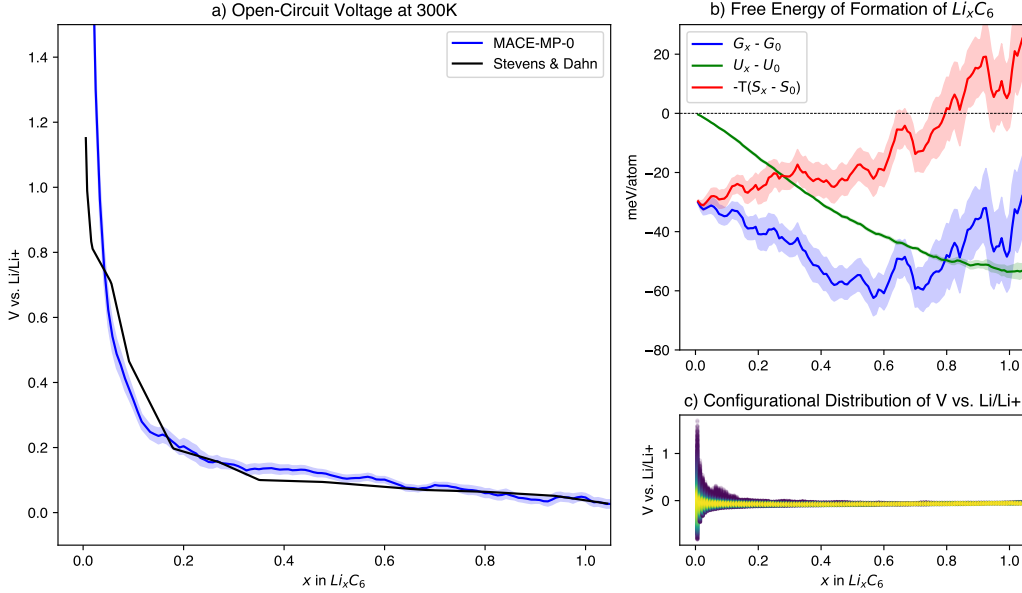


Figure 19: (a) The open-circuit voltage profile of lithium in graphite versus lithium metal, computed with MACE-MP-0 (blue) using a hybrid Grand Canonical Monte Carlo(GCMC)/Molecular Dynamics protocol, contrasted with an experimental reference (black) (184). The variance of the simulated voltage is estimated over 100 bootstrapped samples of GCMC/MD trajectories. Representative lithium-graphite configurations are shown at $x = 0.3, 0.5, 1.0$. (b) The contributions to the free energy of formation of sampled lithium-graphite phases. (c) The density plot of individual $\text{Li}/\text{graphite}$ structures sampled during a GCMC/MD simulation, showing the distribution of potential values over the configurational ensemble.

The open-circuit voltage profile of an electrode material is an example of a technologically relevant macroscopic observable that can be accessed through atomistic simulation. We apply MACE-MP-0 to model the thermodynamics of lithium-ion intercalation in graphite using hybrid grand canonical Monte Carlo/molecular dynamics (GCMC/MD).

Beginning from a 720-atom cell of pristine graphite containing 10 graphene layers, we generate 40 parallel simulation trajectories of 30,000 steps each at a system temperature of 300 K. In our GCMC/MD protocol, at every simulation step, we update the ionic positions according to Verlet dynamics. Every 5 steps, we generate a Monte Carlo proposal on the system volume, followed by a proposal on the system's composition. For the volume proposal, we sample a perturbation of the unit cell: this is a set of 3 Euclidean vectors sampled component-wise from a normal distribution with a mean of zero and variance of 0.01 Å. We add these random vectors to the existing lattice vectors and rescale the atomic positions to generate the proposed unit cell update. For the composition proposal, we randomly make one of three modifications to the population of lithium ions: insertion, deletion, or swapping. We choose one of these types of modification at random and then generate 5 candidate structures, each with either a single new lithium atom placed in a void in the host lattice (insertion), an existing lithium atom displaced into a void (swapping), or an existing lithium atom removed (deletion). As the lattice in our simulations is *not* fixed, but evolves under molecular dynamics, we use Voronoi triangulation to identify void sites in the atomic lattice, excluding all sites subject to steric overlap according to the atomic radii. Once the set of composition candidates is generated, their energy is evaluated, and the lowest-energy candidate is used as the composition proposal. If a composition proposal is accepted, before proceeding to the next simulation step, we relax the ionic positions and the unit cell for up to ten ionic steps with a force tolerance of 0.05 eV/Å using the FIRE algorithm.

After sampling configurations with this protocol, we compute the open-circuit voltage as a function of

lithium concentration over the sampled ensemble. Following previous work (185), the open-circuit voltage is estimated as the negative of the free energy of formation per atom of the phase with composition Li_xC_6 from reference states of graphite (C_6) and metallic BCC lithium, divided by the lithium concentration: $V(x) = -\Delta G_{f,\text{Li}_x\text{C}_6}/x$. The free energy per atom of the metallic lithium reference state is taken as the potential energy predicted by MACE-MP-0 of BCC lithium after structural optimization, neglecting entropy. To determine the free energies per atom of the C_6 and Li_xC_6 phases, we compute the internal energy U and Gibbs entropy S as Boltzmann averages over the sample distribution at concentration x : $G(x) = U(x) - TS(x)$, $U(x) = \sum_j (E_j \cdot p_j)$, $S(x) = -k_B \cdot \sum_j (p_j \cdot \ln(p_j))$, with probabilities $p_j = e^{-\frac{E_j}{k_B T}} / \sum_j e^{-\frac{E_j}{k_B T}}$, where E_j is the potential energy per atom predicted by MACE-MP-0 and j indexes the set of all simulation frames with composition Li_xC_6 .

MACE-MP-0 reproduces the experimentally known voltage profile of Li/graphite with good quantitative accuracy (Fig. 19a). In the regime of $x > 0.04$, the error is < 0.1 V, which reflects the combined error of the model as well as the limitations of the GCMC/MD protocol. This may be compared favorably with a recent purpose-developed model for lithium-graphite energetics (186), which reported < 0.1 V error for $x > 0.0833$ in an open-circuit voltage profile produced through GCMC; that model was trained on more than 8,000 system-specific DFT calculations, while MACE-MP-0 obtains comparable accuracy zero-shot. We note that at very low concentrations, our predicted voltage is higher than the experimental voltage by as much as a factor of 3, indicating overstabilization of dilute lithium. Since the lithium fraction appears in the denominator of the expression for the open-circuit voltage, very slight energetic deviations are magnified in this range; moreover, the free energy at low concentrations is dominated by the entropic contribution (Fig. 19b), for which the limited sample size introduces uncertainty. Beyond this lowest-concentration regime, MACE-MP-0 provides good agreement with experiment.

Similarity statement

There is a skew towards battery materials in MP. Given this, there are several Li–C structures that are relevant to this application: mp-1210743 (Li_2C), mp-976060 (Li_3C), mp-1223102 ($\text{Li}_7\text{C}_{120}$), mp-1378 (LiC), mp-1021323 (LiC_{12}), mp-1232339 (LiC_{12}), mp-1001581 (LiC_6). There also exist 62 pure carbon structures including graphite (mp-48).

Performance summary

Correct prediction of voltage as a function of Li concentration with reference to experimental curve.

A.12 Jahn-Teller Distortions in LiNiO₂

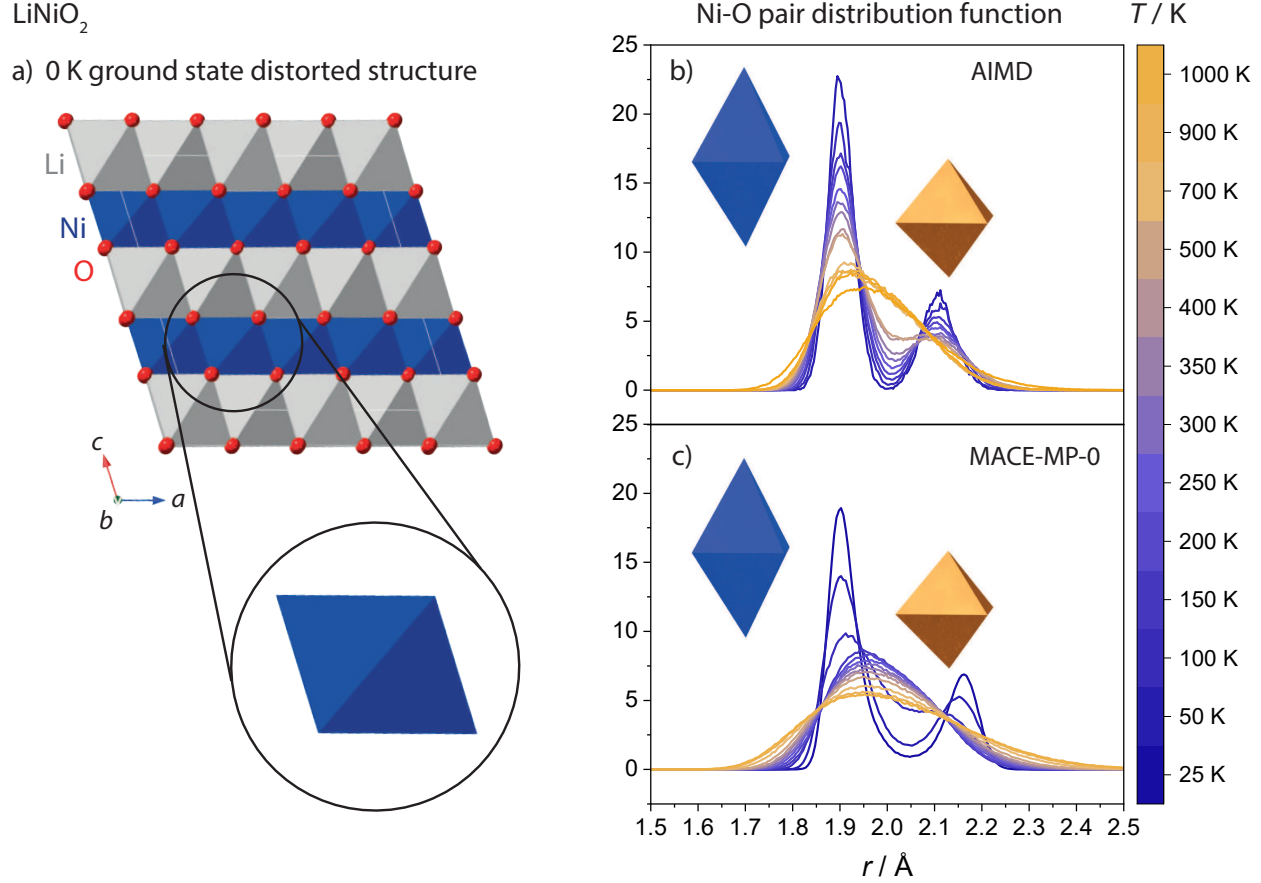


Figure 20: a) Ground state structure of LNO. b) Ni–O pair distribution functions (PDF) as a function of temperature computed by AIMD. (187) c) PDFs computed by MACE-MP-0. Insets indicate shapes of NiO₆ octahedra (blue: distorted, yellow: undistorted).

LiNiO₂ (LNO) is an important material in lithium-ion battery research, serving as a model for future high-performance cathode materials with reduced or no cobalt content. Structural and chemical degradation of these materials is a key challenge, so understanding their thermodynamic and dynamic properties is critical. In particular, ordered regions of Jahn-Teller distorted NiO₆ octahedra may influence electron and Li-ion transport. Recent computational and experimental efforts have proposed a phase transition from a low-temperature distorted to a high-temperature undistorted phase (187).

We have investigated the ability of MACE-MP-0 to reproduce these results. We used a 256-atom supercell, initialized from the established ground state structure with zigzag long-ranged ordering of the distorted long axes in NiO₆. We performed NPT-ensemble dynamics using MACE-MP-0 without a D3 correction, in line with the earlier AIMD simulations at the PBE+U level of theory.

Performance

The MACE-MP-0 model demonstrates stable dynamics during a heating trajectory from 0 K to 1000 K with temperature increments of 10 K/ps, time step 1 fs. Long simulations (at least 500 ps) could be run at 1000 K without significant energy drift or noticeably unphysical behavior.

Figure 20 shows that MACE-MP-0 correctly predicts a phase transition from Jahn-Teller-distorted octahedra (two PDF peaks) at very low temperatures to undistorted (one peak) at higher temperatures. MACE-MP-0 predicts the onset of the transition at around 150 K, compared with 250 K observed by AIMD

simulations and VT-XRD (187). This discrepancy is due either to deficiencies in the model or to very slight differences in the DFT methods being compared.

Similarity statement

Battery materials are well represented in the MP database. 1393 structures in the training set contain Li, Ni, or O atoms, 143 contain all three elements, and 23 have the exact formula LiNiO_2 representing different crystal structures. However, many of these structures are obtained from geometry optimization and hence neglect the temperature dependence of the equilibrium geometry. MACE-MP-0 is a useful tool to explore this temperature dependence.

Performance summary

Correctly captures emergence of Jahn-Teller distortions as a function of temperature, with an underestimation of the transition temperature compared with DFT.

A.13 Point and extended defects in BCC metals

	DFT	MACE-MP-0
W	3.185	3.188
Mo	3.163	3.170
Nb	3.322	3.313

Table 1: Lattice constants (in units of Å) for W, Mo and Nb computed by variable-cell minimisation. DFT reference data is from Ref. (188) for W, Ref. (189) for Mo and Ref. (190) for Nb.

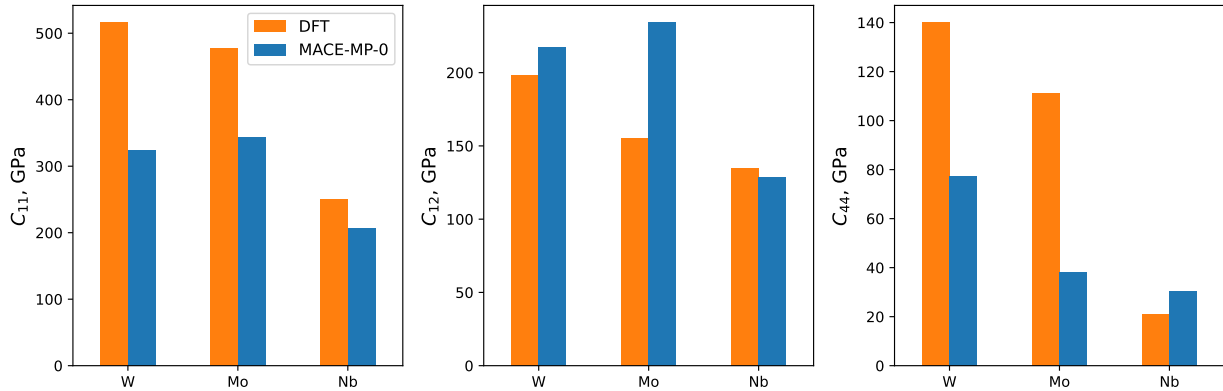


Figure 21: Cubic elastic constants for W, Mo and Nb computed with linear stress-strain fits for DFT (orange; from Ref. (188) for W, Ref. (189) for Mo and Ref. (190) for Nb) and the MACE-MP-0 (blue).

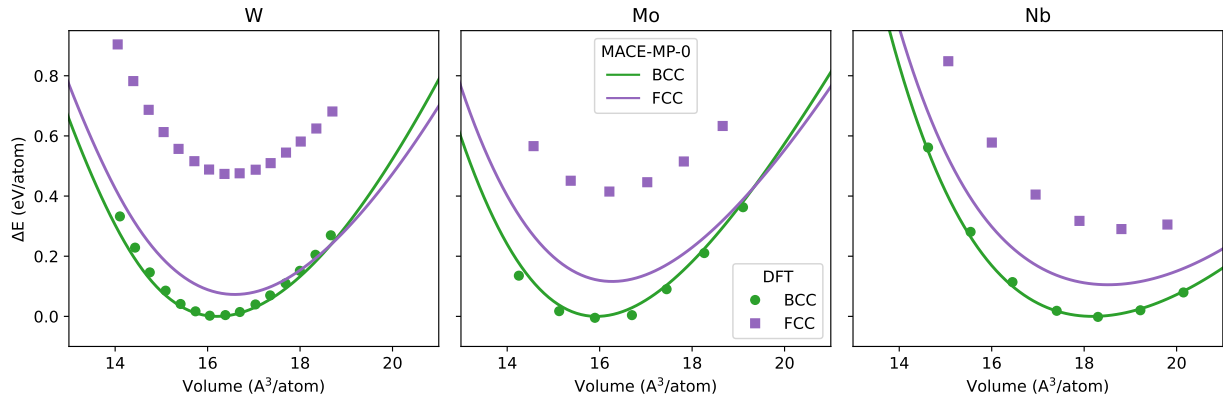


Figure 22: Energy vs volume curves for W, Mo and Nb computed with the medium MACE-MP-0 model for FCC (purple) and BCC (green) crystals. The DFT reference data shown with the circular (BCC) and square (FCC) points is from Ref. (191).

This test explores bulk and extended defect properties of three prototypical BCC metals: W, Mo and Nb. An accurate description of these properties is essential to enable predictive modelling of mechanical responses to applied loads such as dislocation glide (194), dislocation climb through interaction with point defects, grain boundary motion, and the competition between cleavage and dislocation emission that underpins the brittle to ductile transition in fracture. Across-the-board accuracy for bulk and defect properties in these systems is challenging even for bespoke machine learning potentials fit to carefully curated datasets (195).

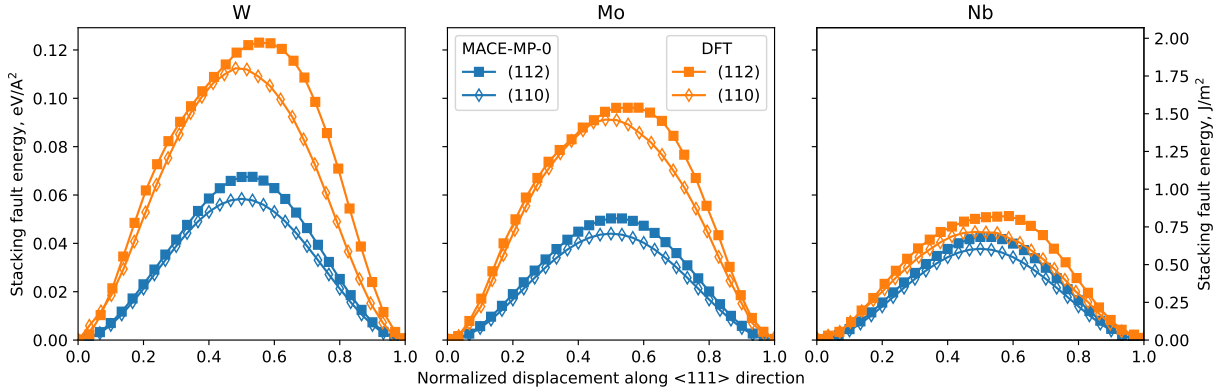


Figure 23: Generalised stacking fault profiles for (112)[111] and (110)[111] Γ -surfaces predicted by the MACE-MP-0 model, shown in blue. The DFT reference data, shown in orange, is from Ref. (192).

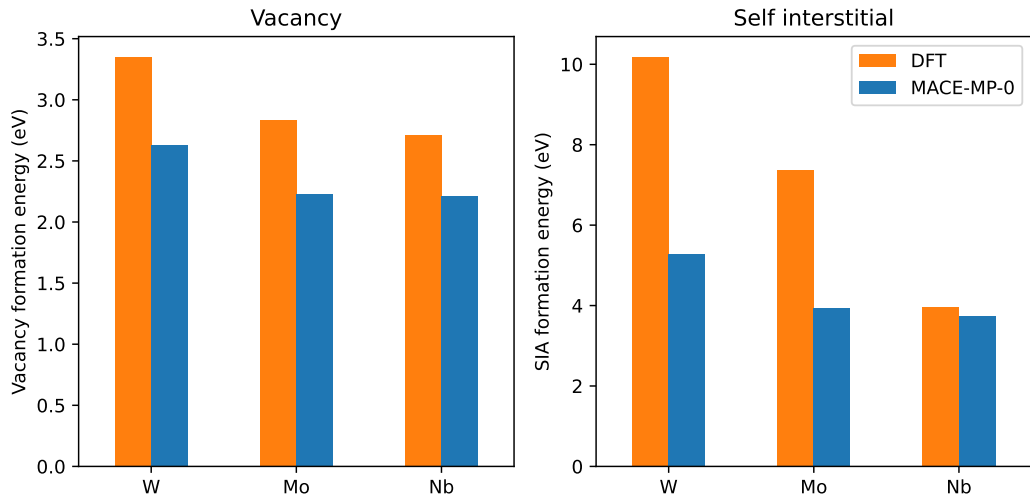


Figure 24: Vacancy and SIA formation energies for W, Mo and Nb computed with the MACE-MP-0 model (blue), and DFT reference data from Ref. (193) (orange).

Lattice and elastic constants are shown in Table 1 and Fig. 21, respectively. Lattice constants are generally well reproduced, but there is a general softening of the elastic response. In Fig. 22 we compare the energy-volume (E-V) curves predicted by the MACE-MP-0 model for BCC and FCC phases of the three metals with reference DFT data from Ref. (191). The BCC cases show generally good agreement, consistent with the inclusion of some BCC data in the training set. There is room for improvement in the curvature of the E-V curves (critical for the elastic properties) for W and Mo, while Nb is well described. FCC energies are underestimated, which is unsurprising as no FCC structures for any of these elements are present in the training set. The curvature is approximately correct, also for FCC, giving reasonable predictions of the elastic response.

We next investigated point defect formation energies, including vacancies and self-interstitial atoms (SIAs). Calculations were performed in a $5 \times 5 \times 5$ supercell and were relaxed to a force tolerance of 1×10^{-5} eV/Å. For the SIAs, a short MD run was performed to escape the initial metastable configuration. The results, illustrated in Fig. 24 show good agreement with reference DFT data is from (193): vacancy energies are predicted within ca. 20% of the DFT value and SIA energies within 50%. For all three elements the MACE-MP-0 predicts that the $\langle 111 \rangle$ dumbbell is the most stable SIA configuration, in agreement with DFT.

Subsequently, we looked at generalised stacking fault energy profiles for the (112) and (110) Γ -surfaces along the [111] direction as shown in Fig. 23. These results were obtained with constrained minimisation where atoms were allowed to move only in the direction perpendicular to the cut surface and with a force tolerance of 1×10^{-3} eV/ \AA . The details of the method are explained in Ref. (196). Nb is very well described by the MACE model, while there is an underestimate in the stacking fault energies in W and Mo by around a factor of two that explains the underestimates in the screw dislocation glide barriers discussed below.

Dislocations in BCC materials lie predominantly in the $\langle 111 \rangle\{110\}$ and $\langle 100 \rangle\{010\}$ slip systems. We investigated the characteristics of $\langle 111 \rangle$ screw and $\langle 100 \rangle$ edge dislocations by calculating the transition pathways and Peierls barriers using the nudged elastic band (NEB) method and the MACE-MP-0 potential comparing against DFT (197) and hybrid QM/MM calculations (198, 199) where the data is available.

The cells contained ≈ 1400 atoms for the [111] screw dislocation and ≈ 2200 for the [100] edge dislocation. Geometry optimisations to obtain starting configurations used the FIRE algorithm (200) with a force tolerance of 1×10^{-6} eV/ \AA . To create and analyze atomistic dislocation configurations we employed the `matscipy.dislocation` module (155). The transition path calculation is performed with an adaptive ODE solver (178) following the approach of Refs. (198, 201), using fifteen intermediate images with stopping force tolerance of 0.025 eV/ \AA . Starting positions for the NEB relaxation were obtained by linear interpolation between initial and final configurations.

Figs. 25 and 26 illustrate the NEB minimum energy path depicting the Peierls barriers for $\langle 111 \rangle$ screw and $\langle 100 \rangle$ edge dislocations in W, Mo and Nb. We compare to DFT results where they are available. Insets within Fig. 25 illustrate the dislocation core structures at the initial, intermediate, and final positions along the MACE-MP-0 minimum energy path. Screw dislocations are known to be a sensitive probe of potentials, since the accuracy required is on the meV/atom level. For Nb the dislocation core structure is correctly predicted as the easy core seen in DFT (197), while for W and Mo the degenerate core is incorrectly predicted. Moreover, for W the MACE-MP-0 predicts the hard-core structure at the saddle point rather than the split core seen in DFT. The observed agreement with the DFT glide barrier is therefore somewhat fortuitous. The barrier height is underestimated for Mo and Nb and overestimated for W compared to reference DFT results (197). For the edge dislocation, where energy differences are larger, we find that the barrier height aligns well with QM/ML results in W (198), while it is an overestimate in comparison with QM/MM results for Mo (199). However, the presence of a minimum along the transition path results in a spurious stable dislocation configuration. In Mo the barrier is overestimated.

We anticipate the performance of MACE-MP-0 for all properties considered here would be substantially improved by enhanced accuracy in stress and a more precise agreement on the elastic constants, followed by fine-tuning on defect configurations where necessary.

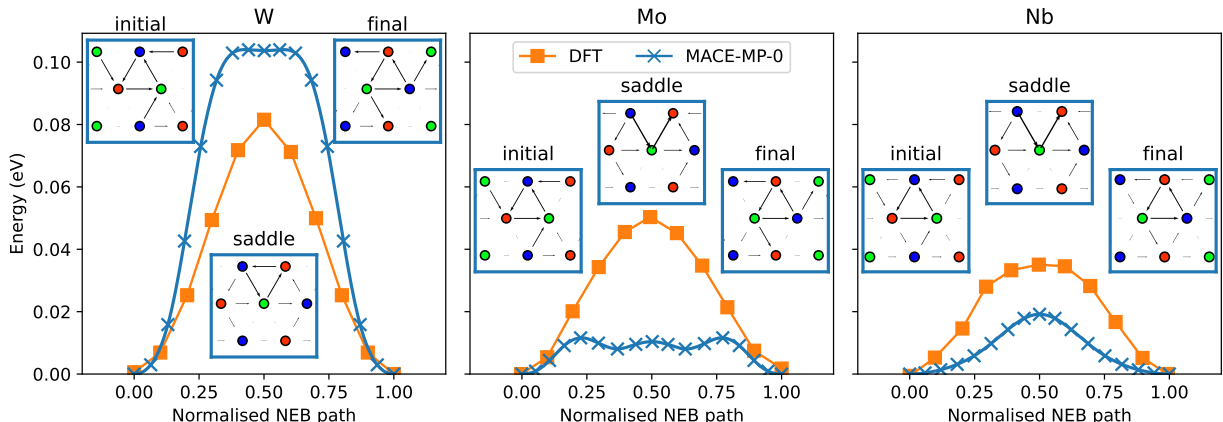


Figure 25: Screw dislocation glide barriers for W, Mo and Nb. DFT data from (197)

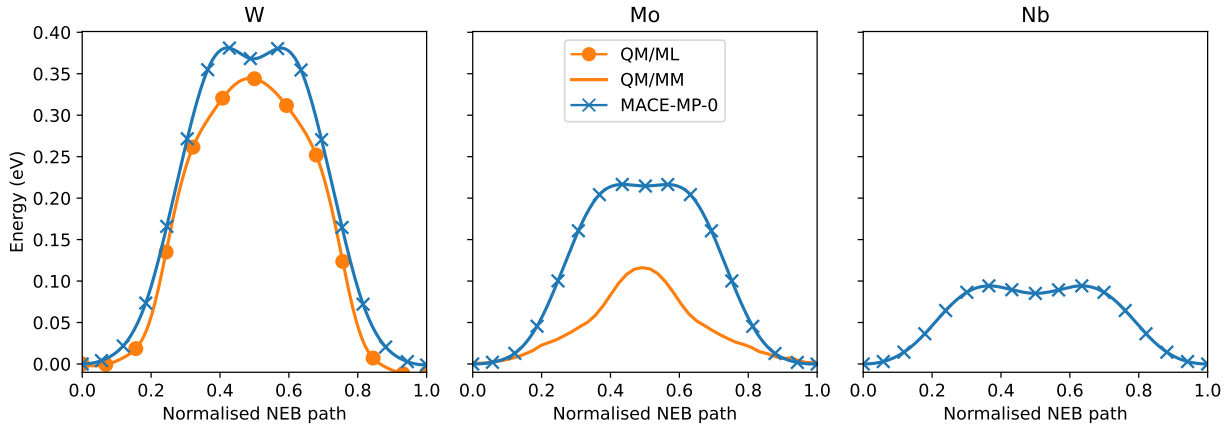


Figure 26: Edge $\langle 100 \rangle$ dislocation glide barriers for W, Mo and Nb. QM/ML data for W from Ref. (198), QM/MM data for Mo from Ref. (199)

Similarity statement

The MP dataset includes 3 elemental tungsten, 2 elemental molybdenum, and 2 elemental niobium structures. They are all crystalline without any defects. Based on UMAP analysis, we find that the closest structures in the training set are mp-8641 for tungsten, mp-8637 for molybdenum and mp-8636 for niobium. We provide `W_input.json`, `Mo_input.json` and `Nb_input.json` to help visualize the interactive UMAP on chemiscope.org.

Performance summary

Energy-volume curves for BCC are well reproduced, while for FCC structures they show a ca. 0.5 eV/atom shift in energy. Stacking fault profile energies for Nb are well reproduced, while for W and Mo they are underestimated by a factor of around two with respect to DFT. Relaxed point defect structures are reasonable in all cases, with formation energies within 50% of reference DFT values. Peierls energy barrier profiles for dislocation glide are qualitatively correct, with the barrier correct for the edge- underestimating for the screw-dislocation. There is a small spurious local minimum near the top of the barrier for the edge dislocation.

A.14 Alumina defects and bulk diffusion

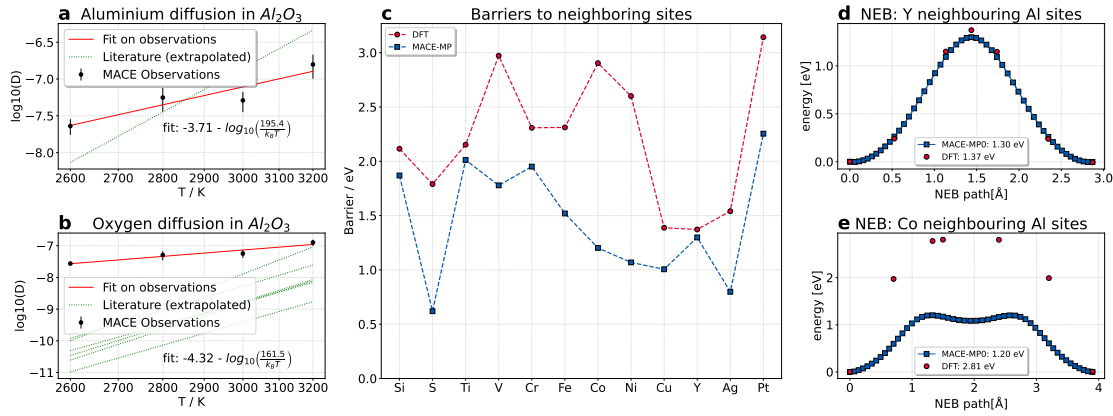


Figure 27: **a–b:** Arrhenius plot of elemental diffusion in Al_2O_3 compared with experimental results from (202); **c:** Comparison of MACE-MP-0 NEB barrier paths (blue) and PBE single point evaluation of the MACE-MP-0 transition state (red) for elements in Al or O sites in Al_2O_3 moving to neighboring sites (dashed lines are just guide to the eye); **d–e:** lowest energy NEB path for Y (where MACE-MP-0 is accurate) and Co (where there is a substantial discrepancy), with single point PBE evaluations indicated by red circles.

A.14.1 Bulk diffusion

One Al and one O vacancy were introduced into a 270-atom alumina supercell, and over 2 ns (at 2.5 fs) MD was used at temperatures between 2800–3200 K to measure diffusivities of the two elements. Diffusivities agree within one order of magnitude for Al, and activation energies are underestimated for both compared to extrapolated experimental values (202). This demonstrates the long-timescale stability of the model, even at high temperatures and for long MD trajectories, but highlighting a shortcoming of the model for quantitative prediction of macroscopic observables.

A.14.2 Elemental defects

Elemental defects in Al_2O_3 were investigated by substituting Si, S, Ti, V, Cr, Fe, Co, Ni, Cu, Y, Ag, and Pt into lattice sites in a $2 \times 2 \times 1$ (120 atom) supercell and minimal energy paths to neighboring sites were obtained using NEB (203, 204) starting from a linear interpolation. Paths were converged (max 50 steps, 0.3 eV/ \AA tolerance on projected forces) and the lowest energy one was tested with PBE single point evaluations using CASTEP (205). Comparing MACE-MP-0 and PBE on Fig. 27c–e there are large discrepancies, with a total force component RMSE of 0.33 eV/ \AA across 139 structures evaluated.

A few NEB calculations failed catastrophically, this was found to be due to lack of sufficient repulsion between Al-Ag for distances under 0.8 \AA , and could be prevented by using an initial guess path with atoms not so close to each other.

Similarity statement

There are 109 structures in the MP dataset containing exclusively Al & O, pure Al_2O_3 appears as mp-1143 (used to generate supercells). There is a total of 243 structures in the training set with Al & O and exactly one of Si, S, Ti, V, Cr, Fe, Co, Ni, Cu, Y, Ag or Pt.

Performance summary

Activation energies for self-diffusivity are underestimated compared to experimental values (extrapolated from lower temperatures). Dopant atom migration minimum energy paths are all stable, and are sometimes accurate (e.g. Yb) and sometimes only qualitative (e.g. Co) with respect to DFT single point reevaluations.

A.15 Random structure search: Arsenic

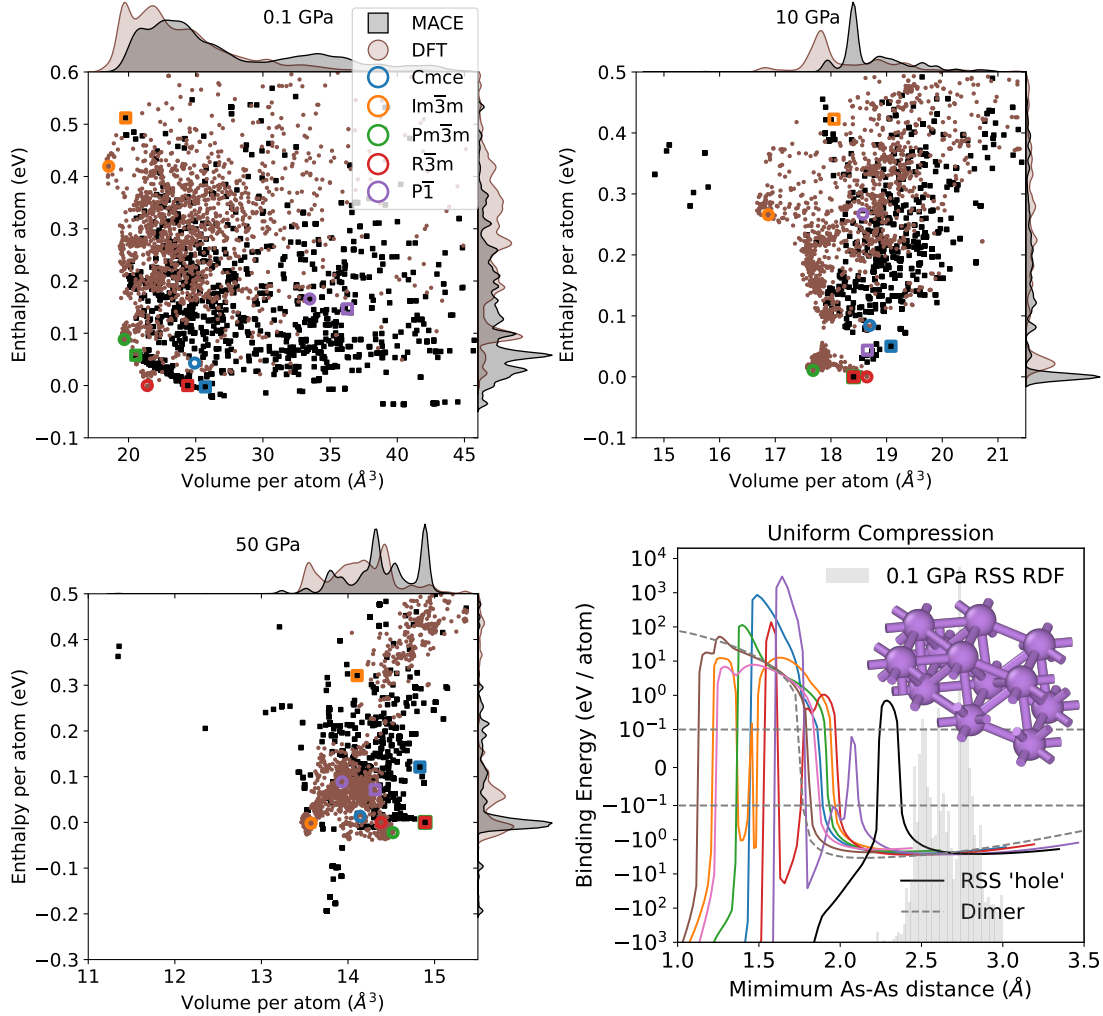


Figure 28: Densities of states of random structure search (RSS) minima for As at 0.1, 10 and 50 GPa obtained using MACE-MP-0 (black, squares) and DFT (brown, circles), with known As structures outlined in various colors (see legend). The bottom right panel shows how the binding energy of 7 (unrelaxed) randomly generated structures (colored lines), and one pathological structure found during RSS (black line and inset) vary as the structures are compressed uniformly with fixed fractional atomic coordinates. The As–As dimer energy and the RDF for the 0.1 GPa As RSS structures are shown for comparison.

Ab initio Random Structure Searching (AIRSS) (206) is a simple, yet highly successful, approach for discovering new materials computationally. Multiple candidate structures are generated randomly, subject to physically motivated constraints, and then relaxed to local enthalpy minima using ab-initio methods such as DFT. There is great interest in accelerating structure prediction by using surrogate models (28, 207–209), such as ML potentials, to perform the initial structural relaxations. Here we test the suitability of MACE-MP-0 (without the D3 correction) for this task by searching for structures of Arsenic at 0.1, 10 and 50 GPa. The exceptional structural variety encountered during RSS probes the robustness of the model in an extremely extrapolative regime; there are only six As structures and no high-pressure data in the training set.

At each pressure, 2000 ($\times 100 n$) random structures were generated using $n = 2\text{--}6$ atoms per primitive unit cell, 2–4 randomly chosen symmetry operations, minimum distance constraints of 2 \AA and a volume per atom of 15–40 \AA^3 . The structures were then relaxed with MACE-MP-0 (ASE, force tolerance of $1 \times 10^{-3} \text{ eV}/\text{\AA}$)

and CASTEP (205); PBE exchange-correlation functional (22), 400 eV cutoff energy, k-point spacing of $2\pi \times 0.05 \text{ \AA}^{-1}$ and Vanderbilt ultrasoft pseudopotentials (210) with a force tolerance of 0.05 eV/ \AA and stress tolerance of 0.1 GPa. With these settings 96% and 99% (at 0.1 and 10 GPa) of structural relaxations were successful with DFT and MACE-MP-0 respectively. The distributions of relaxed structures are depicted in Fig. 28 and the known structures listed in table 2 are highlighted with colored symbols. At 0.1 and 10 GPa the energy and volume distributions are visually similar (note the systematic shift in volume distribution) with the relative energy differences between the highlighted structures, particularly the low-energy ones, generally being small compared to the overall range. Inspection of the structures at 0.1 GPa reveals that similar 3-fold coordinated 3D, layered, and 1D structures are found with both MACE-MP-0 and DFT. Furthermore, we note that the known structures listed in table 2 were all found using MACE-MP-0, including a simplified packing of the As_4 tetrahedra found in yellow As. The lowest energy structures found at 0.1 GPa contain As_8 cubes. The cluster of dense structures found about 0.3 eV/atom above the minimum at 10 GPa contain 6-fold coordinated As in a 3D kagome-like lattice. Relaxing these structures with DFT preserves this connectivity but causes the the volume to increase to about $19 \text{ \AA}^3/\text{atom}$.

At 50 GPa, the similarity between the DFT and MACE-MP-0 results decreases markedly, with 7% of relaxations failing, compared to 1% at 0.1 and 10 GPa. These failures are caused by “holes” in the MACE-MP-0 potential energy surface, where exceptionally dense, highly coordinated structures are predicted to be overly stable. An example of such a structure is shown in the inset of the bottom right of Fig. 28. The repulsion seen in the As–As dimer curve indicates that these holes are caused by higher body-order terms in an extrapolative regime - holes occurs at shorter As–As distances than occur in the radial distribution function of the 0.1 GPa RSS results. We note that such holes are not typically an issue during ambient pressure MD, due to the large energy barriers seen in Fig. 28, and can likely be fixed by including some high pressure data in the training set.

Table 2: Summary of known Arsenic structures. The white P structure type is used as a proxy for yellow As as the structure is unknown (211).

Structure	Pressure	In training set?	Space Group	Z	Found with 0.1 GPa MACE-MP-0?
A7, grey As (212)	ambient	yes	$R\bar{3}m$	2	yes
black P (213)	ambient	yes	$Cmce$	4	yes
white P	ambient	no	$P\bar{1}$	24	As ₄ tetrahedra found
simple cubic (214)	27–57 GPa	yes	$Pm\bar{3}m$	1	yes
bcc (214)	$\geq 110 \text{ GPa}$	no	$I\bar{m}\bar{3}m$	1	yes

Similarity statement

The MP dataset set contains only six pure As structures. Of these, grey arsenic ($R\bar{3}m$) (212) and the orthorhombic allotrope ($Cmce$, isostructural with black phosphorus) (213) have both been observed at ambient conditions whilst the simple cubic structure ($Pm\bar{3}m$) (214) is stable at moderate pressure between 27–57 GPa. The remaining three structures are >0.4 eV/atom above grey arsenic. There are an additional 3857 unique structures that contain As and other elements. Within these optimised structures there are a total of 22047 As environments of which 1606, 1537, 534 and 12 are 1, 2, 3 and 4-fold coordinated by neighbouring As respectively (2.7 \AA cutoff). Many of the 3-fold As environments are found in AsX compounds where X is a group I or II element and the As atoms are arranged in local clusters. There is one As atom which is bonded to 4 neighboring As atoms ($\text{Cs}_7(\text{InAs}_2)_3$, mp-1203378), one structure containing isolated As_4 tetrahedra (AsO_3 , mp-1215144) and two structures containing connected As_4 tetrahedra ($\text{Re}_4\text{As}_5\text{S}_4$ mp-1209063 and $\text{Re}_4\text{As}_6\text{S}_3$ mp-1219545).

Performance summary

All expected low enthalpy stable structures found. Unphysically low energy structures uncovered at high pressures and small internuclear distances.

A.16 Properties of bulk and nanoconfined water

See main text section 2.1 for results and discussion.

Similarity statement

The MP dataset contains 21 structures composed of O and H elements and 7769 structures that have O and H elements alone or together with other elements. Based on UMAP analysis, we see that some atomic environments in the example system are similar to environments in the training data. For instance, bulk water and ice comprise typical molecular environments (*e.g.*, the environment of atom 20 in structure 13 of `water_exclusive_OH_chemiscope_input.csv`) but also environments of hydrogen peroxide (*e.g.*, the environment of atom 1 in structure 14 of `ice_exclusive_OH_chemiscope_input.csv`). Despite being two dimensional, the superionic phase also comprises distinct environments mimicking those of water molecules (*e.g.*, the environment of atom 3 in structure 20 of `superionic_exclusive_OH_chemiscope_input.csv`) and dissociated environments mimicking those of hydrogen peroxide (the environment of atom 12 structure 12 of `superionic_exclusive_OH_chemiscope_input.csv`). The environments farthest from the MP dataset are the monolayer oxygen environments surrounded by a (flat) hexagon of 6 other oxygen atoms.

Performance summary

The MACE-MP-0 model demonstrates stability and reliable performance in conducting simulations across diverse conditions for both bulk and confined water. It maintains stability in NVT simulations at experimental densities and temperatures for bulk water, ice Ih, and reactive proton defects (OH^- and H_3O^+). The model describes extensive proton transfer in nanoconfined water at 4 GPa and 600 K, in good agreement with reference methods.

A.17 Ethanol-water density-composition curves

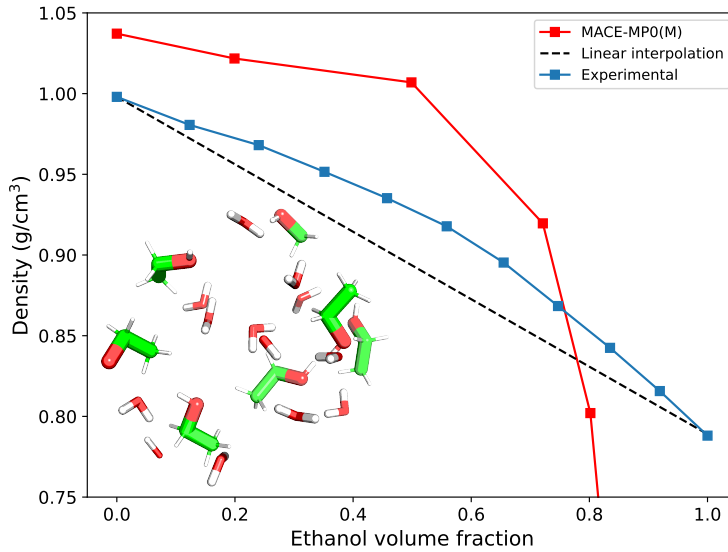


Figure 29: Ethanol–water density curves obtained by NPT MD using MACE-MP-0 in double precision, compared to experimental data taken from Ref. (215).

In this section, we investigate the ability of the MACE-MP-0 model to describe mixtures of molecular liquids. In particular, we study the density-composition curve for a range of volume fractions of ethanol in water. Initial configurations were generated with Packmol (174), with 120 molecules per box, and the initial box vectors were set to be slightly below the experimental density for each composition. Initial structures were minimised to a tolerance of 0.1 eV/Å with the L-BFGS algorithm. Trajectories were generated in the NPT ensemble using ASE, including a D3 dispersion correction with the Becke-Johnson damping function. Final densities were computed as the averaged of the final 1000 snapshots from the simulation, once the density had converged.

Similarity statement

The MP dataset contains 37 structures that contain only the elements C, H, and O. Based on UMAP analysis, we observe that almost all atomic environments in the example system are similar to environments in the training set. On closer inspection, we find that the most similar environments to the majority of the example configurations are clusters primarily containing water, hydroxide and atomic hydrogen and oxygen, with a few examples containing small hydrocarbon-type fragments.

Performance summary

For low ethanol volume fractions, MACE-MP-0 predicts the density deviation from the linear behaviour (with a 4% error in the absolute density, not uncommon for a GGA DFT functional for molecular fluids), however simulations of pure ethanol result in the boiling off of the liquid at ambient conditions, resulting from the underestimation of the boiling point.

A.18 Solvent mixtures

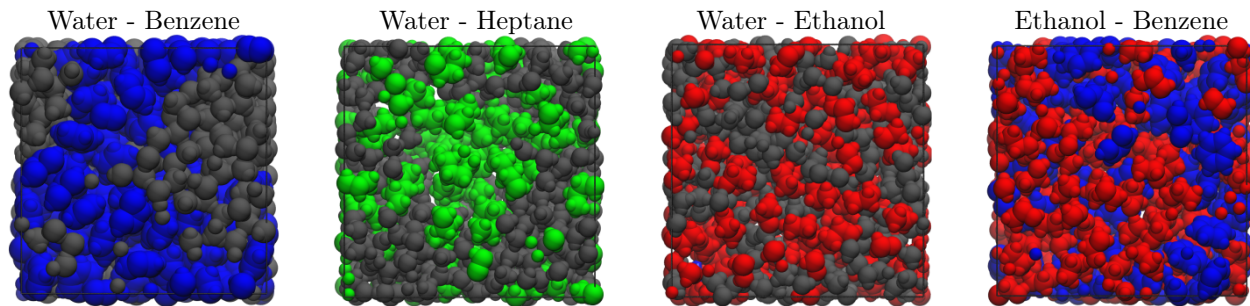


Figure 30: Snapshots of solvent mixtures after 1 ns of NVT MD. The solvents shown are benzene (blue), heptane (green), ethanol (red), and water (grey). Axis orientations in the figures were chosen to highlight the phase separation in these systems.

Modeling solvent mixtures requires an accurate description of intermolecular forces within highly disordered systems. To investigate the performance of MACE-MP-0 in this setting, MD simulations were performed for four mixtures of solvents of varying polarity. The investigated systems are water-benzene, water-heptane, water-ethanol, and benzene-ethanol. Simulations were performed at 300 K in the NVT ensemble via the ASE interface. A time step of 1 fs and a friction constant of 0.001 fs^{-1} were used. In the case of immiscible solvents, a mixture of equal volumes of both solvents with their corresponding densities was assumed. In the case of miscible solvents, the experimental density of the mixtures was used. All systems were initialized with a uniform random mixture of both solvents using the `packmol` code. (174)

Figure 30 shows the states of all systems after 1 ns. Notably, mixtures of water with apolar solvents (heptane and benzene) quickly form separate phases, whereas the ethanol-water system remains mixed on the timescale of the simulation. This is in good agreement with experiment. However, the mixture of ethanol and benzene (which are fully miscible at 300 K) also shows phase separation.

Similarity statement

The MP dataset contains 37 structures composed exclusively of C, H, and O, and 1902 structures that contain C, H, and O along with other elements. Regarding the specific molecules, several ice structures but none of the other molecules are included as pure compounds. The closest to benzene (with the ratio of C:H 1:1) is mp-995197 containing chains of dimethylbenzenes with methyl-methyl bridges. The UMAP analysis shows that many atomic environments from our structures have similar environments in the training data. However, no liquid configurations are included in the MP. We provide two files to visualize the interactive UMAP on chemiscope.org. `solvents_mixtures_CHO.json` contains structures exclusively containing C,H, and O. `solvents_mixtures_CHOplus.json` includes structures containing C, H, and O along with other elements.

Performance summary

Miscibility of three out of four mixtures correctly predicted, ethanol and benzene incorrectly showed phase separation.

A.19 Aqueous interfaces

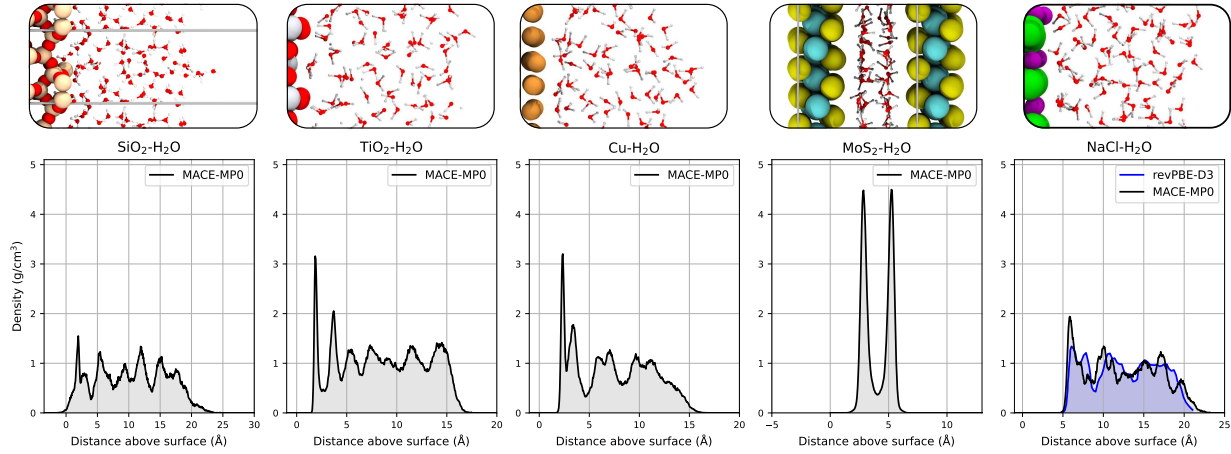


Figure 31: Water structure and density at various interfaces. Representative sections of the simulation cells with the equilibrium water density profile below them. The system depicted are water on silicon dioxide (SiO_2), titanium dioxide (TiO_2), copper (Cu), between two layers of molybdenum disulfide (MoS_2), and on sodium chloride (NaCl).

Simulating complex systems, such as solid-liquid interfaces, is a difficult endeavor, as the potential must simultaneously describe the two materials and their interface. We tested the effectiveness of MACE-MP-0 on a wide range of aqueous interfaces, from oxides and metals to confinement.

NVT MD simulations were performed on a variety of surfaces at a temperature of 330 K. The average density of water above the surface is shown in Fig. 31.

SiO_2 and TiO_2 were two notable oxide systems in which dissociative and molecular adsorption was observed, respectively. Deprotonation of water was expected on the surface of silicon dioxide, which is evidenced by the shoulder in the water density plot. These figures show that the interfacial water property is accurately reproduced; however, the liquid phase is overstructured, which is a common characteristic of the PBE functional (50) used in the Materials Project.

Water in confinement was also investigated within MoS_2 slit pores. The simulation captures the pronounced stratification characteristic of the aqueous phase perpendicular to the two-dimensional layers. This was also observed for water confined between graphene sheets and boron nitride nanotube. In particular, in Fig. 31 we show sharply defined interfacial water layers between the MoS_2 sheets. Upon the addition of interlayer spacing (not shown), we also capture additionally smoother intermediate layers, noting that with more layers, we lose the sharp peaks at the surfaces.

Finally, the NaCl (001) surface in contact with water was simulated. The system comprised a (3×4) $\text{NaCl}(001)$ supercell containing 24 atoms, with 3 NaCl layers and a unit cell lattice constant of 5.72\AA on top of which were 89 water molecules. A subsequent 25\AA of vacuum was added between the adsorbed water layer and the lower layer of the surface. The layered structure of the water as previously observed in *ab initio* PBE simulations in Ref. (216) is captured by the MACE-MP-0 model, with the positions of the density minima and maxima qualitatively agreeing with the PBE simulations.

Simulation of dissolution processes is another challenge for the MACE-MP-0 model. It must be able to describe the very different chemical environments of the bulk crystal surrounded by water going through the stages of ions detaching from the crystal to fully solvated ions in solution. In Fig. 32, we compare the MACE-MP-0 model in NVT simulations of the pristine NaCl (001) interface in contact with water and a NaCl nanocrystal surrounded by water at 400 K. The nanocrystal system simulated comprised a $4 \times 4 \times 4$ NaCl nanocrystal comprising 32 ions, with lattice constant 5.72\AA surrounded by 625 water molecules, giving a final concentration when dissolved of 2.84 mol/kg .

As expected, for a pristine NaCl surface, the model predicts no dissolution events on the time scale of the simulation. Meanwhile, for the nanocrystal surrounded by water, the model captures a dissolution

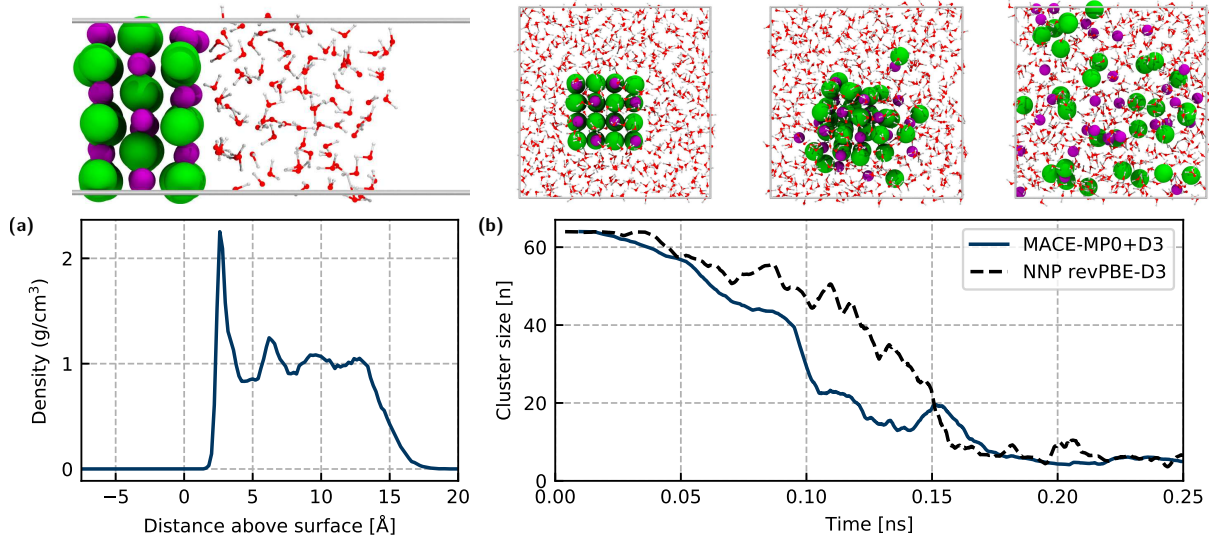


Figure 32: Dissolution of NaCl in water. (a) Density profile of water in contact with NaCl(001) surface, with a representative snapshot from the simulation showing no dissolution events from the pristine surface. (b) Evolution of crystal size of $4 \times 4 \times 4$ NaCl nanocrystal in water over time, comparing the MACE-MP0 (blue line) with an ML model explicitly trained to capture NaCl dissolution (black dashes) (49). Representative snapshots showing the dissolution progress of the crystal are shown above the plot.

mechanism similar to that reported by Ref. (49) with an ML model trained specifically to capture NaCl dissolution at revPBE-D3 level of theory. The dissolution proceeds via a crumbling mechanism, where an initial steady loss of ions precedes rapid disintegration of the crystal. The resulting solution of ions in water also displays correct expected orientation of the water molecules with respect to the ions.

Similarity statement

The MP dataset contains 460, 100, 112, 13 and 29 structures composed exclusively of [H, O, Si], [H, O, Ti], [H, O, Cu], [H, O, Mo, S] and [H, O, Na, Cl], respectively. The corresponding number of structures inclusive of the given atoms along with other elements is 477, 215, 435, 260 and 190. Based on UMAP analysis, the closest atomic environments for each of these systems are mp-626085, mp-626550, mp-697660, mp-990086 and mp-504600. Two files are provided for each of the systems for visualising using chemiscope, one for inclusive and one for exclusive matches in the training set.

Performance summary

All interface structures correctly predicted, including dissociative adsorption on SiO₂ and molecular adsorption on TiO₂. At the salt/water interface correctly predicted dissolution from nanocrystal and no dissolution from flat surface on nanosecond time scale.

A.20 Molten salts

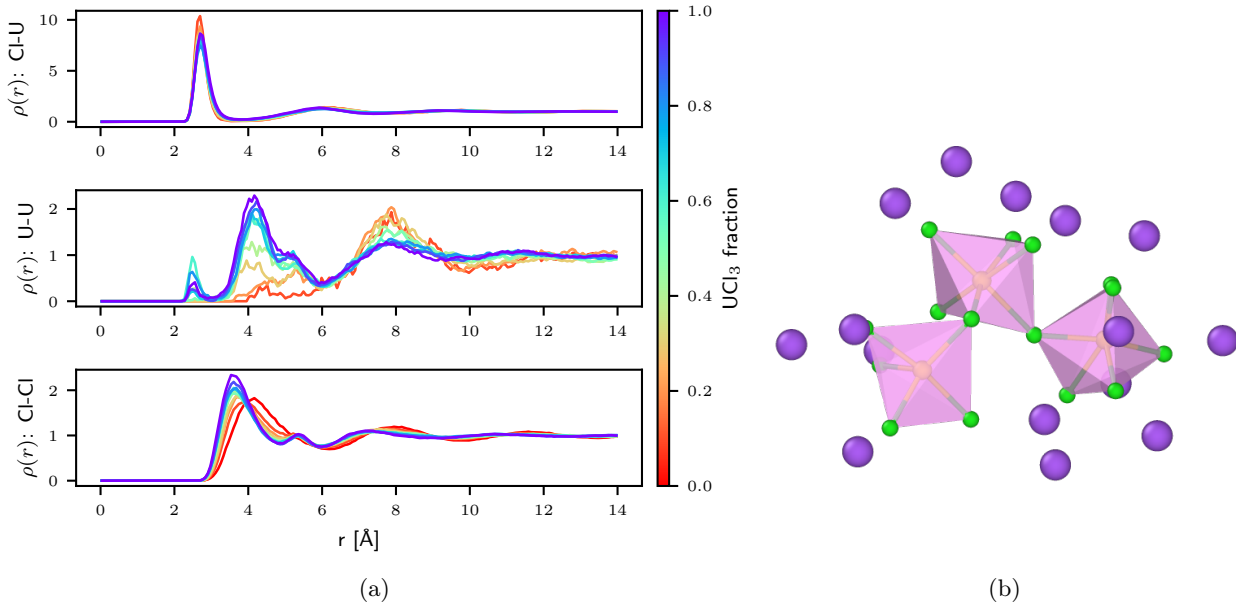


Figure 33: NaCl–UCl₃ molten salt mixtures at 1100K. (a) Pair correlation function of NaCl–UCl₃ mixtures at 1100 K. (b) Example U–Cl oligomers forming vertex sharing coordination polyhedra (U: yellow, Cl: green, Na: purple).

With increasing interests in molten-salt energy technologies, we have simulated binary NaCl–UCl₃ salt mixtures (NaCl)_(1-x)(UCl₃)_x at different compositions using MACE-MP-0. The initial structures were randomized using Packmol in a cubic cell at the density estimated by the linear interpolation of the densities of constituent solid-state salt at 0 K divided by a constant factor of 1.05. (174, 217). We then implemented geometric optimization using Lennard-Jones potential and further relaxed structures using MACE-MP-0 with a three-step process: geometric optimization, NVT relaxation through annealing at 1.2× target temperature, and NPT relaxation at 1100 K and ambient pressure. Figure 33a presents the pair correlation functions between Cl–U, U–U, Cl–Cl in salt mixtures. The characteristic peaks and transitions are consistent with previous polarizable ion models (218) and AIMD simulations (219), except for a noticeable shift of U–U peak from 4.5 to 4 Å. The shift could be explained by the lack of Hubbard U correction for rare earth elements in MP, leading to unrealistic ionic radii and solvation shell in the mixture. We also note that there is a small U–U peak around 2.5 Å. This peak is absent in previous molten salt studies at high temperature (219), but as it is close to the equilibrium distance between U as demonstrated by the homonuclear diatomic curve (Fig. 56), its appearance indicates the formation of a few U–U bonds at a high fraction of molten UCl₃ salt.

Similarity statement

The MP dataset contains 573 structures composed of at least one Na, U, or Cl atom, 14 elemental Na crystals, 14 elemental U crystals, and 3 Cl₂ molecular crystal structures. Based on UMAP analysis, we see that all atomic environments in the example system are similar to environments in the training data. We found that Cl₂ molecular crystals are close to the molten salts but most of the pure U metals are found separated from the molten salt in terms of MACE descriptors. We provide

- T_1100-P_0-seed_3-npt-5_chemiscope_input.json

to help visualize the interactive UMAP of molten Cl₆₄Na₂₈U₁₂ on chemiscope.org.

Performance summary

Correct pair distribution peaks and variation of peak positions as a function of concentration, with a notable shift in the first U-U peak position, due to absence of Hubbard- U correction.

A.21 Room temperature ionic liquids

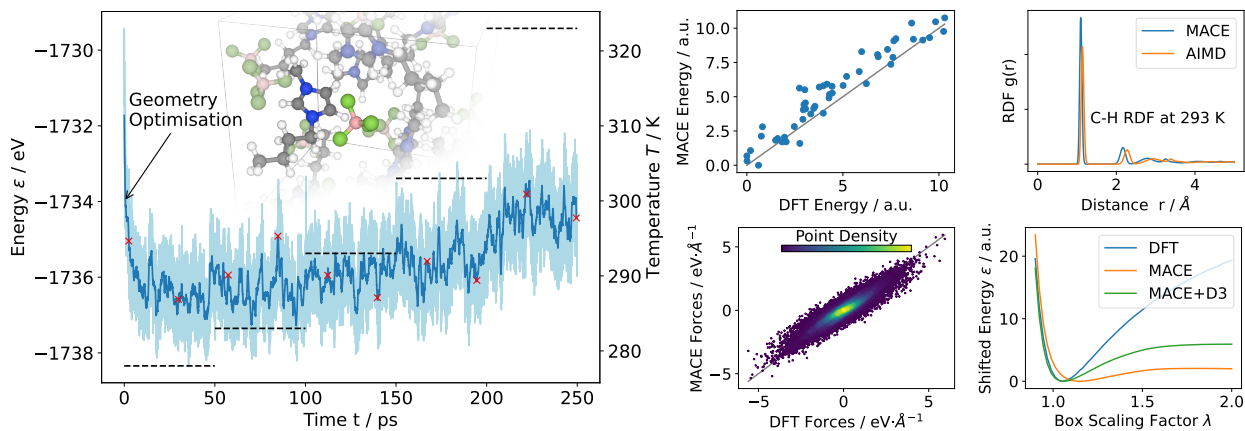


Figure 34: MD simulation of the BMIM BF₄ room temperature ionic liquid. The left panel shows energy as a function of the trajectory, starting from an energy minimization, followed by MD simulation in an NVT ensemble with a step-wise increase in temperature (dashed lines, right axis). The middle column of panels shows energy and force parity plots for configurations from the trajectory (red markers). The right top panel compares RDF to AIMD, and the right bottom panel shows a rigid-molecule volume-scan test (120).

Room temperature ionic liquids provide a class of organic solvents with desirable properties such as low melting and high boiling points, chemical inertness, and good ionic conductivity, making them applicable to different chemical and physical applications. Furthermore, these properties can be tuned by changing substituents on the anion or cations. The vast availability of substituents makes simulations at quantum mechanical accuracy to optimize these *in silico* a very interesting approach.

For the given example, the class of imidazolium-based ionic liquids was chosen. The introduced MACE model struggles with running simulations that are only composed of a single chlorine anion, resulting in a Cl bonded to the aromatic ring. Therefore, simulations using the more commonly used BF₄ anion with the 1-butyl-3-methylimidazolium (BMIM) cation were conducted. A single MD simulation was performed starting at the experimental density (220) of BMIM BF₄ at 273 K. The temperature was stepwise increased from 273 K to 323 K. Between each increase, the cell was adjusted to the new density and equilibrated over 500 fs. All simulations are conducted using the MACE-MP-0 with additional D3(BJ) corrections.

At each temperature, an NVT simulation using a Langevin thermostat was conducted for 50 ps with a time step of 0.5 fs. From the final trajectory spanning 250 ps over 5 different temperatures, data points were uniformly selected, and energies and forces were compared to DFT (221). Additionally, the radial distribution function was compared to an AIMD simulation, indicating a shift in the hydrogen positions compared to DFT. Furthermore, the interatomic interactions are probed using a volume scan, showcasing the importance of the additional D3(BJ) correction to stabilize the correct volume (see Figure 34). Finally, a MD simulation in an NPT ensemble at 1 atm and 300 K showed that the model reproduces the experimental density within 5%.

Similarity statement

There are 52 structures in the MP dataset that explicitly include the BF₄ anion. Although there are organic nitrogen-containing molecules as well as heterocyclic systems, there are no alkyl-substituted imidazolium derivatives like BMIM in the training dataset. We provide BMIM_BF4.json for a comparison of snapshots from the MD trajectory to the training dataset on chemiscope.org.

Performance summary

Stable MD for BF₄ anion, but Cl anion bonded to imidazolium. Intermolecular distance distribution shows small peak shift, and intermolecular attraction underestimated.

A.22 High-pressure hydrogen

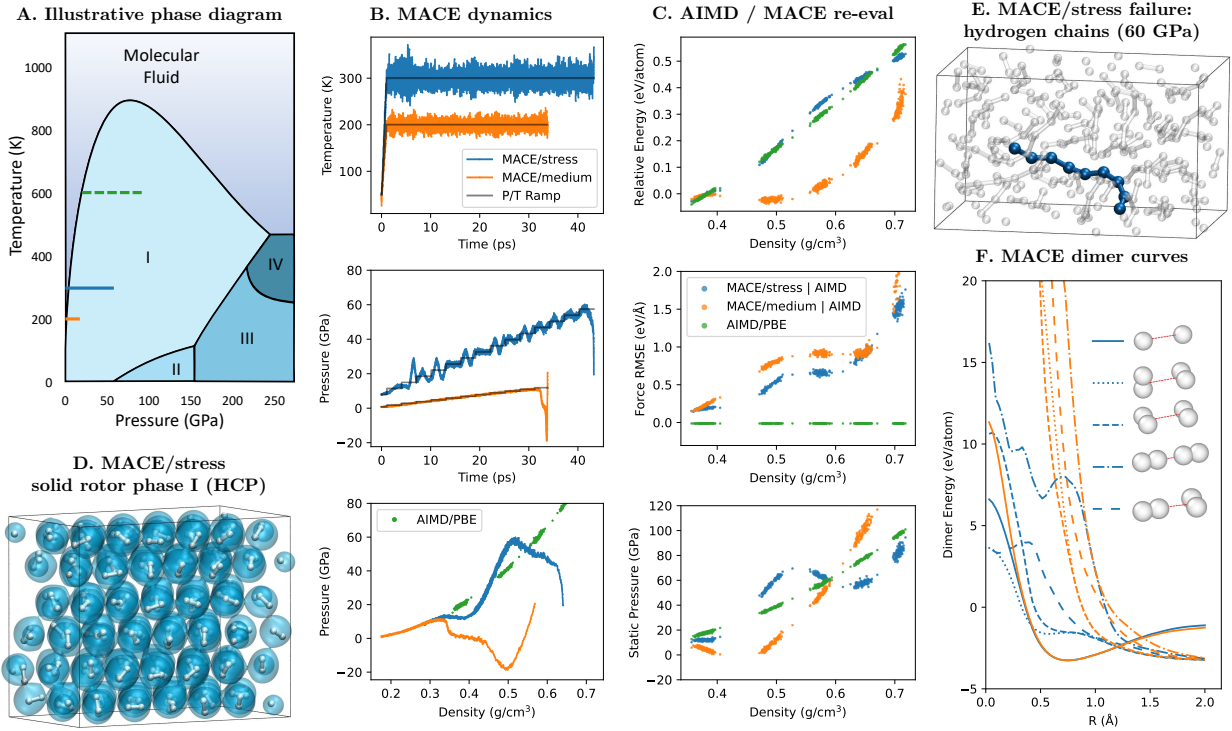


Figure 35: (A) Illustrative phase diagram of high-pressure hydrogen (222, 223). Horizontal lines show the NPT-MD simulations: MACE-MP-0 (orange), MACE/stress (blue) (see text) and AIMD/PBE (green) (224). (B) Temperature and pressure during MACE-MD, and those externally applied by the thermostat/barostat. The bottom panel shows the pressure/density dependence in MACE-MD compared to AIMD. (C) MACE properties (energy, forces, pressure) reevaluated on the AIMD trajectory and compared to the original PBE result. (D) At low pressure MACE reproduces solid hydrogen phase I as a hexagonal-close-packing (HCP) lattice of free rotors. (E) At higher pressure (60 GPa) the potential fails and forms unphysical hydrogen chains before exploding. (F) MACE energy curves computed for different orientation of the H₂-H₂ dimers. The distance is measured between the centers of mass of the two molecules.

Condensed-phase hydrogen is an exotic state of matter that forms at extreme conditions in the core of larger planets and in specially-designed laboratory diamond anvil cells. Despite the simplicity of the hydrogen atom and molecule, the condensed phase exhibits fascinating phenomena such as entropy-driven phase transitions (225, 226), phonon localization (227, 228), quantum rotor solid phases (229), and an insulator-to-metal transition (230, 231). AIMD has been used extensively to study the molecular mechanisms underlying these phenomena, however, simulations are often affected by finite-size effects. Bespoke ML potentials, fitted to reproduce the interaction of hydrogen molecules with ab initio accuracy, have demonstrated simulations at an unprecedented level of detail, unlocking new scientific observations (230). Being so different from other materials in the MP database, solid hydrogen is a uniquely challenging test for MACE-MP-0.

The stability of the potential on this system was tested by running MD simulations at high pressure and by investigating the H-H and H₂-H₂ dimer curves for molecules in different orientations. The MD simulation started from a thermalized crystal structure with P6₃/m symmetry and pressure was slowly ramped up at constant temperature. MACE-MP-0 becomes unstable and explodes at pressures around 10 GPa. Attempting a simple remedy, we fitted a new model called “MACE/stress” which differs from MACE-MP-0 by having a larger weight on the stress error (by a factor of 10) in the loss function. This potential is more robust and remains stable up to 60 GPa. At low pressures, both potentials reproduce the correct behaviour of hydrogen phase I: HCP crystal of freely rotating hydrogen molecules. The accuracy

of the potential was also quantified by re-evaluating the energy, forces and pressure on an existing AIMD trajectory (224). MACE-MP-0 reproduces the PBE energy on the AIMD trajectory up to surprisingly high pressures (100 GPa), however, during dynamics it forms unphysical hydrogen chains well below that pressure (60 GPa). The energy–separation curves for H₂-H₂ dimers are generally smooth, with a few exceptions in MACE/stress, where the lower repulsion between H₂ molecules results in chain formation, but also explains why this simulation is stable up to higher pressures.

Similarity statement

The MP dataset contains 17 structures crystal structure composed exclusively of H. From these, only 2 structures are above the 0.2 g/cm³ density value: mp-1096977 (hexagonal P4/mmm 0.24 g/cm³) and mp-754417 (hexagonal P6/mmm 0.24 g/cm³), yet MACE-MP-0 was found to extrapolate well up to around 0.30–0.35 g/cm³ where the potential starts to break down. We provide `hydrogen_exclusive.json` for visualization on chemiscope.org.

Performance summary

Correct solid hydrogen structure reproduced at low to moderate pressures. At pressures above 10 GPa, the potential failed and resulted in unphysical structure. A refitted potential with higher weight on stress errors failed at 60 GPa.

A.23 Ammonia and borane thermal decomposition

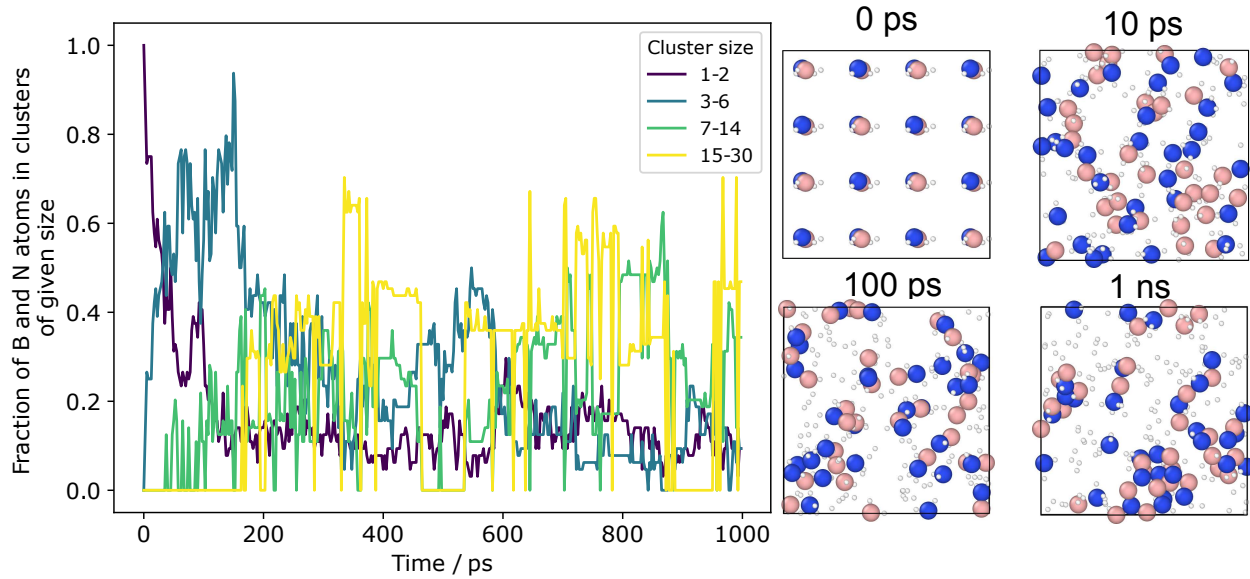


Figure 36: Decomposition of ammonia and borane at 1600 K. The plot shows the time evolution of cluster size in terms of the fraction of heavier atoms (B and N) found in each cluster size group. Snapshots of the system at different times show the growth of BN clusters and evolution of H₂ molecules.

Ammonia and borane form an adduct NH₃BH₃. At high temperatures, these molecules lose hydrogen gas to give increasingly heavier B- and N-containing molecules, ultimately resulting in the growth of hexagonal boron nitride (232). We simulated this process with MACE-MP-0 by running NVT molecular dynamics simulation of 32 ammonia and 32 borane molecules in a cubic box of length 16 Å, at a temperature of 1600 K for 1 ns with 0.5 fs time step. We analysed the time evolution of the system in terms of the sizes of heavier atom clusters (excluding hydrogen), illustrated in Fig. 36. Initially, the formation of ammonia borane adduct and small borane clusters is seen, while in 100 ps timescales B and N atoms are increasingly more clustered, exhibiting B-N bonds in chains and six-membered rings as found in borazine and hexagonal boron nitride.

Similarity statement

The training set contains 67 structures composed of H, B, N elements. The training set contains various structures encountered during the simulation including ammonia, borane, and HBN compounds of various stoichiometries, for example borazine (B₃N₃H₆) and (BNH₂)_n chains. We performed UMAP analysis for 100 frames taken from the 1 nanosecond simulation against training data containing at least one of the HBC elements and any other elements. Based on the UMAP values, most of the simulation environments are clustered near the training data, with exceptions being species with unusual valency (e.g. BH₂). The closest structures in the training set are mp-1197795, mp-1203334 (both containing B and N, among other elements) and mp-1214811 (B₆N₆H₁₀ bicyclic aromatic compound). We provide `ammonia-borane.json` for visualization on chemiscope.org.

Performance summary

Model correctly predicts hydrogen production and BN cluster formation from thermal decomposition of NH₃BH₃.

A.24 Heterogeneous Catalysis

Computational heterogeneous catalysis evolves around the exploration of *operando* catalyst stability and catalytic reaction mechanisms to provide information about the nature of the active site that defines a catalyst's performance. This information provides a basis for screening applications to find efficient and ideally non-precious and non-toxic catalysts. To this end, a variety of atom-scale properties are investigated, including bulk and surface energies to evaluate catalyst stability in (surface) phase- or Pourbaix diagrams, as well as adsorption energies, reaction thermodynamics, and reaction barriers that are key to elucidating mechanisms and catalytic activity (71). Local geometry optimizations and transition state searches via *e.g.* NEB calculations (203, 204) that yield target properties are usually conducted on slab models that exemplify the catalyst surface. By expanding the usual surface science approaches via thermodynamic referencing of protons and electrons to pH and applied potential on basis of the computational hydrogen electrode (CHE) (81), concepts in thermal catalysis can be extended to electrocatalysis. This approach provides fairly robust results even though the simulation of the electrolyte, charged species or an applied potential and thus the direct influence of the electrified solid/liquid interface is omitted. The computationally involved methodology is fully transferable to MACE-MP-0 and we included all mentioned aspects in the examples presented in the main text and below.

A.24.1 Pourbaix diagrams

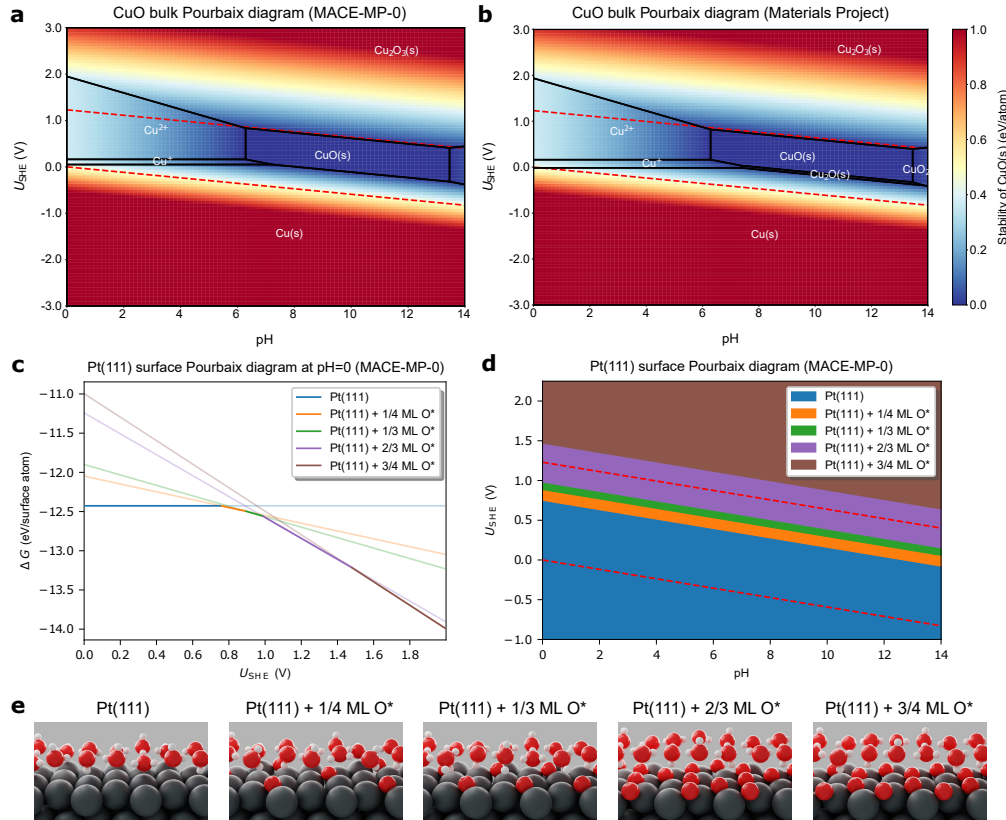


Figure 37: Pourbaix diagrams of CuO bulk systems with energies of relevant solid compounds taken from (a) the MACE-MP-0 calculations and (b) the MP reference. (c) and (d) shows the MACE-MP-0-calculated Pt(111) surface Pourbaix diagrams at pH = 0 and at various pH, respectively, which are in good agreement with (58). Different stable surface structures are represented in different colors. (e) shows the stable Pt(111) surface structures from low to high applied potentials. The red dashed lines indicate the stable window of water ranging from $U_{\text{RHE}} = 0 \text{ V}$ to $U_{\text{RHE}} = 1.23 \text{ V}$ ($U_{\text{RHE}} \approx U_{\text{SHE}} + 0.059 \cdot \text{pH}$).

In Fig. 37 we show the Pourbaix diagrams, calculated by the MACE-MP-0 with D3 corrections, which

illustrate the aqueous stability for a CuO bulk and a Pt(111) surface in dependence of applied potential and pH as referenced by the CHE. Structures for bulk CuO and all other related oxide and peroxide compounds are taken from MP and are subsequently optimized (both atomic positions and cell parameters) using MACE-MP-0. The energy corrections for oxides and peroxides, as well as the free energies for aqueous ions, are consistent with the values used in MP. As shown in Fig. 37a and b, the overall trend of the CuO stability predicted by MACE-MP-0 is well-aligned with the result given by MP, except for the narrow region of the Cu_2O phase that is not reproduced by MACE-MP-0. For the Pt(111) surface, MACE-MP-0 is used to optimize the surface geometry with different coverages of O^*/OH^* adsorbates together with an ice-like water layer. As depicted in Fig. 37c–e, MACE-MP-0 predicts that the Pt(111) surface starts to oxidize at $U_{\text{SHE}} = 0.77$ V (pH=0), followed by a step-wise increasing O^* surface coverage with more positive electrode potential. This is in good agreement with the Pt(111) surface Pourbaix diagram reported previously (58), except that in our study the 0.5 ML O^* coverage is not found to be stable at any electrode potential.

A.24.2 Linear Scaling Relationships (LSR)

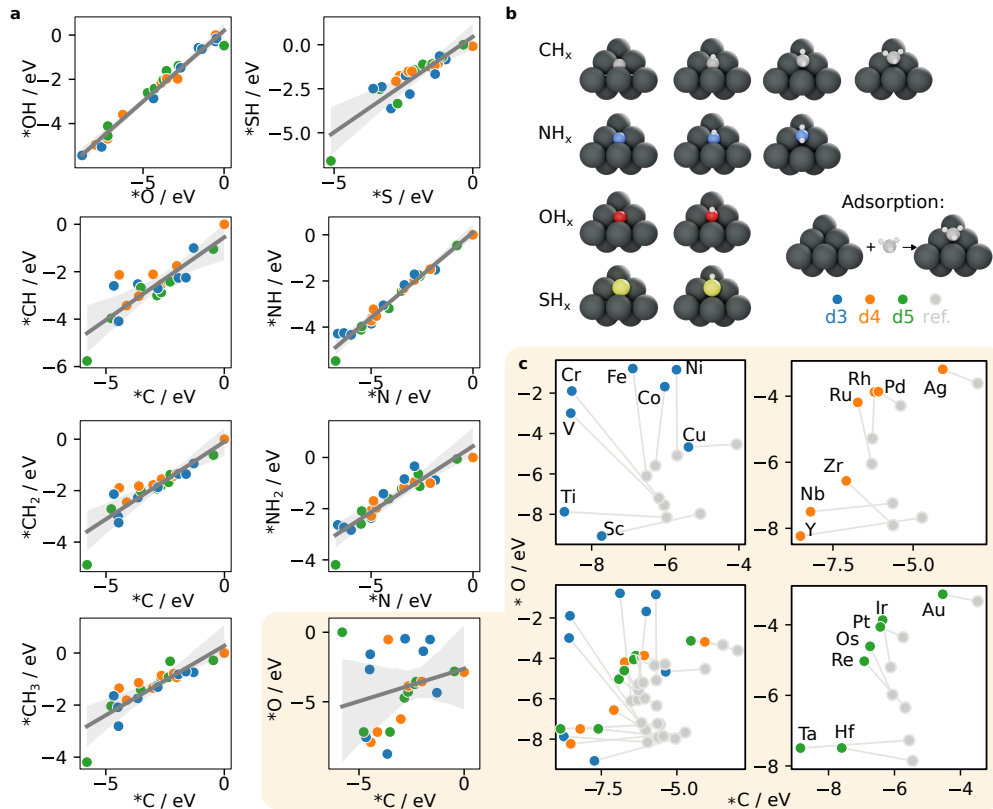


Figure 38: Correlation plots (a) between the adsorption energies of two intermediates at the same (hollow site) of tightly packed metal surfaces (b). The correlation between $*\text{O}$ and $*\text{C}$ (c) is not linear (in agreement with the literature).

Adsorption energies of molecules and intermediaries are indicative of catalyst reactivity and often used as descriptors in screening studies for catalyst materials. The adsorption energies are governed by electronic and geometric factors. Provided a consistent geometric environment (*e.g.* a hollow site of a tightly packed metallic lattice) across different metal surfaces, the trend in adsorbate binding energies resulting primarily due to electronic effects can be observed. A well-known property of catalytic surfaces (*e.g.* transition metals) is that binding energies of individual intermediates are not independent of each other, as a consequence of the varying degree of occupation of the metallic d-band (59, 84). Linear scaling relationships (LSR) were found for a range of metallic surfaces and molecules that bind to this surface through the same atom (*e.g.*

E scales with EH_x , where $E = C, O, N, S$ and $x = 1, 2, 3$), however, this scaling is not linear when comparing adsorbates that bind through different atoms (*e.g.* C versus O).

In Fig. 38 we show the correlation between the adsorption energies of EH_x , where $E = C, O, N, S$, and $x = 0, 1, 2, 3$. The structures (Fig. 38b) were relaxed with the MACE-MP-0 model with D3 correction (cutoff = 4 nm), and the adsorption energy was computed as $\Delta E_{\text{ads}} = E(a*) - E(*) - E(a)$, with a as the adsorbate and $*$ as the surface slab. The observed correlations are linear in all cases except for the correlation between O and C. In Fig. 38, the mace computed adsorption energies (blue/green/orange circles) are compared to the corresponding DFT values (connected with faint gray lines to faint gray circles) as reported by Norskov (59). In this plot, although the absolute error of the obtained adsorption energies in comparison to the DFT values is high (which is not surprising as the model is extrapolating in this example), the trend of grouping metals into passive (noble, *e.g.* Au) catalytic (so-called Pt group) and non-reducible (*e.g.* Zr) is correctly captured and the essence of the LSR relationships was reproduced with the MACE-MP-0+D3 model.

A.24.3 CO (electro-)oxidation on Cu

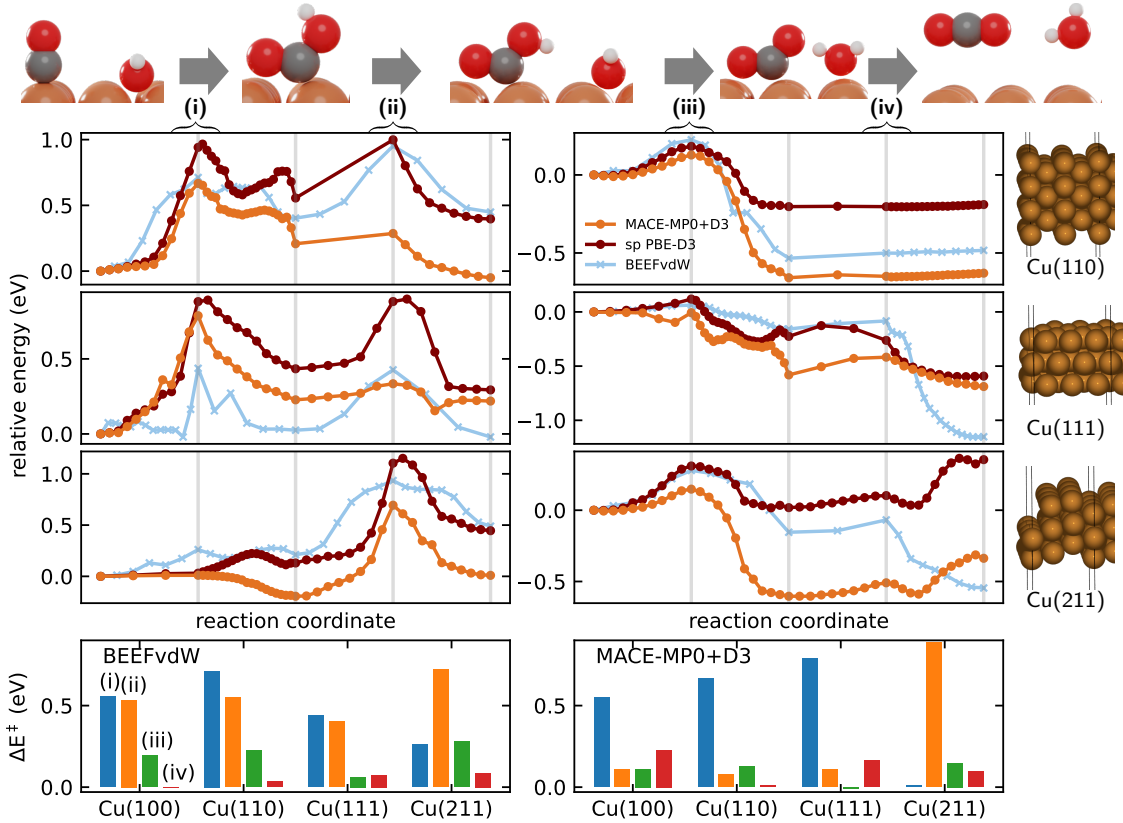


Figure 39: NEB profiles (top) and extracted barriers (bottom) of reactions (i-iv) computed for the non-potential dependent steps in the multistep reaction mechanism of CO electro-oxidation on the low index Cu facets (110), (111), and (211) (for profile of Cu(100) see main text). The reaction mechanism and the original BEEF-vdW NEB data without implicit solvent (light-blue) is adapted from (60). The NEB calculations were repeated via MACE-MP-0 (orange) with an additional D3 correction and single point PBE+D3 calculations (dark-red) were performed for the MACE-MP-0+D3 NEB-path.

We test the ability of MACE-MP-0 to predict the catalytic reaction mechanisms for the oxidation of CO on different facets of Cu which was previously explored via DFT (60). The evaluated reaction barriers present the potential-independent reaction steps of the CO oxidation via electrochemically adsorbed OH* groups. The electrochemical OH* adsorption (not included here) can be described via the CHE (81). We

recompute the reaction pathways using MACE-MP-0+D3 via NEB calculations in lattice-parameter-adjusted simulation cells. In Fig. 39 we show the MACE-MP-0+D3 reaction pathways and barriers together with corresponding PBE+D3 single points and the original BEEF-vdW NEB calculations for two Cu terraces (111) and (100) and two step-sites (110) and (211). MACE-MP-0+D3 displays a mixed performance for the various reaction steps i-iv. The coupling (i) and dehydrogenation (iii) barriers are reproduced within 10 % of the original BEEF-vdW data (60). An exception is the coupling barrier on Cu(111) which is overestimated by 100 %. For this latter transition state we, however, find good agreement with the single point PBE-D3 data which indicates divergence due to the DFT functional (PBE+D3 vs. BEEF-vdW). A throughout gross and moderate underestimation of the torsional rearrangement of COOH (ii) and desorption of CO₂ (iv) is found. We believe that this shortcoming is likely due to missing training data which is suggested by large deviations from the PBE+D3 single point calculations. Despite the quantitative differences in reaction barriers, we find MACE-MP-0+D3 to mostly preserve the qualitative trends between the reaction steps i, iii, and vi (ii is inaccurately described) and facets as well as the overall reaction mechanism.

A.24.4 In₂O₃

As a final test system we investigate a key step (CH₂O₂ → CH₂ + O) in carbon dioxide hydrogenation to methanol over indium oxide via an NEB transition state search. This reaction has been extensively studied with *ab initio* methods due to indium oxide's promising selectivity compared to conventional modified copper catalysts (61, 87). First, we perform a global geometry optimization of the reactant near an oxygen vacancy. MACE-MP-0 correctly identifies the three-oxygen-coordinated indium as the active site (61). Following a NEB calculation MACE-MP-0 predicts the reaction barrier within 10% of that investigated with DFT (1.30 eV vs. 1.16 eV), as visible in Fig. 3.

Similarity statement

With the exception of the CuO bulk Pourbaix diagram, which is based on structures from the Materials Project, all presented examples treat surface slab models (with and without reacting adsorbates) which are a strong extrapolation of MACE-MP-0's dataset. The dataset does not include any such slab models but only related bulk structures. These bulk structures include 6 bulk structures that contain Pt, O, H and 15 bulk structures that contain Pt and O for the Pt Pourbaix diagram and the corresponding LSR example (similar number for other metals in the LSR), 8 different Cu-bulk phases and 111 structures composed of Cu, O, Cu, and H along with other elements for the example of CO oxidation on different Cu facets, and 9 structures that contain In, O, H and C and a 825 bulk structures that contain indium and oxygen for the In₂O₃ example. The most similar configurations for the CO oxidation example are Cu₂H₄C₄N₃O with the Materials Project ID mp-686268 and for the In₂O₃ example (NH₄)In(OH)PO₄ with the ID mp-764968. We provide Pt_LSR.json and COoxCu_closest_training_points.csv for the LSR and CO oxidation example to help visualize the interactive UMAP on chemiscope.org.

Performance summary

Solid energies accurately predicted leading to correct Pourbaix diagrams. Adsorption energies overestimated, but linear scaling relationships between different surface/adsorbate pairs preserved. Minimum energy paths for reactive steps qualitatively correct, in some cases small (0.2 eV) in other larger (0.5 eV) energy errors.

A.25 Carborane rearrangement

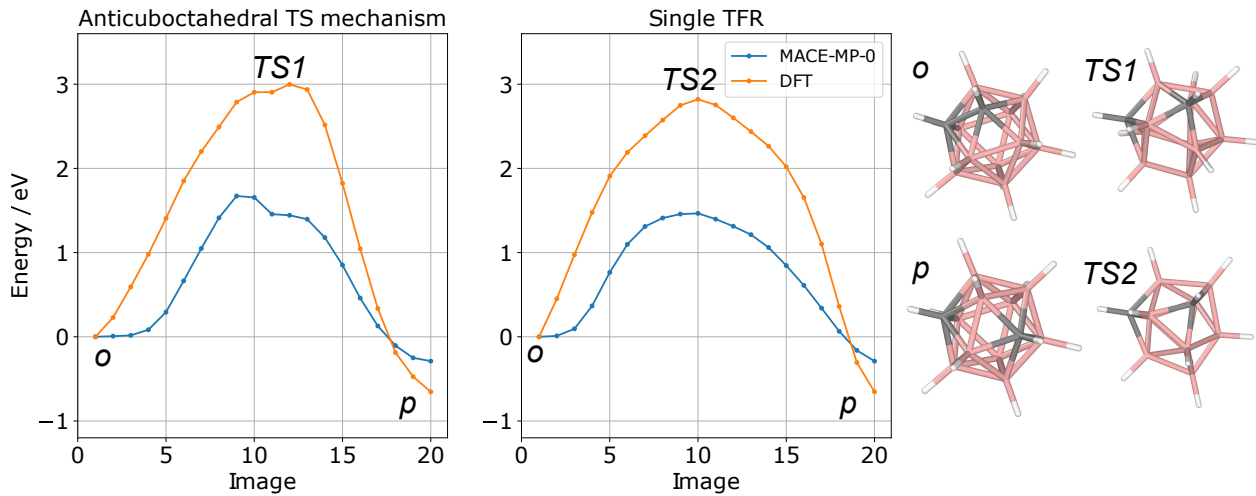


Figure 40: DFT NEB pathways for the isomerization reaction of *ortho*-carborane to *meta*-carborane. MACE-MP-0 energies, evaluated on the same pathways, are shown. All energies are shown relative to the *ortho* isomer energy. On the right, end point and transition state structures are illustrated.

Carborane ($C_2H_{12}B_{10}$) is an organoboron compound with uses in drug discovery (233) and organometallic chemistry (234). It adopts icosahedral cluster structures, with three isomers based on different relative positions of carbon atoms: *ortho* (*o*), *meta* (*m*), and *para* (*p*). The thermally activated rearrangements between these isomers have been thoroughly studied (235), with several mechanisms proposed involving triangular face rotation (TFR). We used MACE-MP-0 to study two pathways from the *ortho* isomer to the *meta* isomer: one involving an anticuboctahedral transition state (by mutual rotation of two opposite faces), the other involving the rotation of a single triangular face.

We used MACE-MP-0 to provide preliminary rearrangement pathways for each mechanism to be refined with DFT using the NEB method. For each mechanism, a pair of endpoint structures was built, with the atom labels consistent with the mechanism. The endpoint structures were relaxed with force tolerance of $0.01\text{ eV}/\text{\AA}$ at PBE/def2-TZVPPD level of theory using ORCA 5.0.1 (236). The initial NEB pathways with 20 images and a spring constant $2\text{ eV}/\text{\AA}^2$, were relaxed using MACE-MP-0 and then further relaxed at PBE/def2-TZVP level of theory. Figure 40 shows the rearrangement energy profiles with their endpoint and transition state structures. MACE-MP-0 qualitatively captures the structural details of each rearrangement while underestimating the barrier height of the rearrangement.

Similarity statement

The training set contains 5 structures composed of H, B, C elements, and 21837 structures that have H or B or C along with any other elements. The dataset contains 2 structures or containing icosahedral $C_2H_{11}B_{10}$ clusters linked by a C-C bond to form a dimer, 1 icosahedral borane $B_{12}H_{12}$ cluster and 18 other borane clusters containing trigonal B_3 faces. Along these, the dataset contains several hundred structures involving derivatives of borane and carborane clusters such as salts, metal complexes, and halogenated species. The closest structures in the training set are mp-1194548 ($C_4H_{22}B_{20}$ containing two icosahedral carborane clusters joined with a C-C bond), and metal complexes containing carborane ligands: mp-759303, 705569, 1199795, 1198024.

Performance summary

Carborane rearrangement minimum energy paths geometrically correct, with the energy barrier underestimated.

A.26 Transition Metal Dichalcogenides

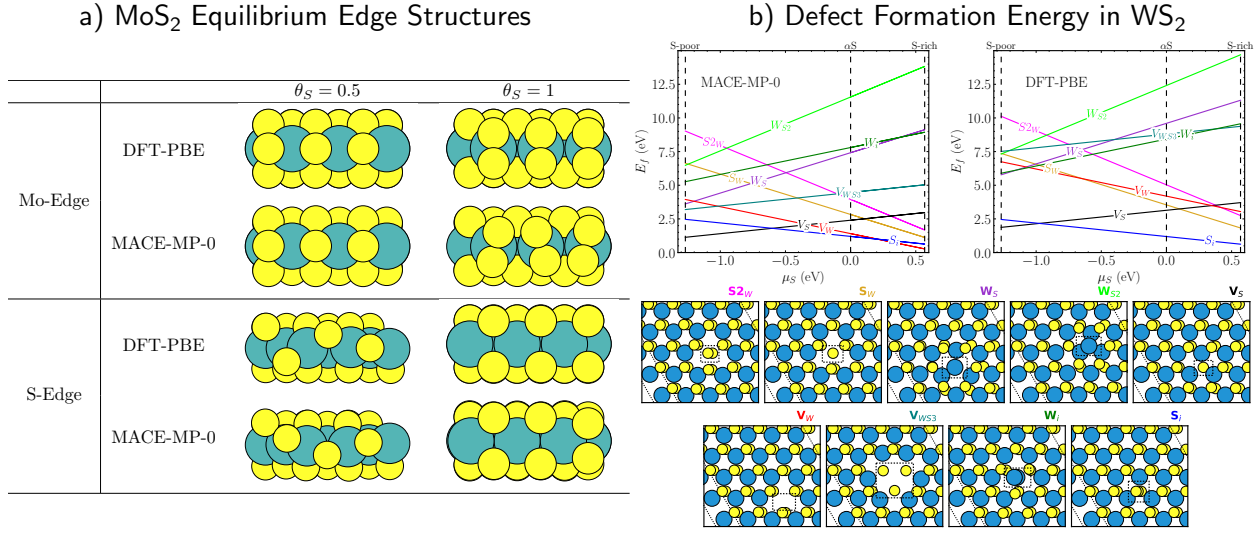


Figure 41: (a) shows four MoS₂ edge models of different type and sulfur coverage (θ_S). DFT-predicted structures are obtained from (237). MACE-MP-0 structures are the result of 100 ps of MD at 300 K followed by a geometry optimization. (b) compares the defect formation energies predicted by MACE-MP-0 and DFT-PBE results from (238). Geometries of defects considered here as relaxed using MACE-MP-0 are also shown in (b).

Edges in MoS₂ and TMDs more broadly are known to be sites of high reactivity with much relevance to TMD-catalyzed reactions and material aging studies. Studies have recently addressed the structure of MoS₂ edges under various conditions using DFT (237). Here, we examine stable Mo-edge and S-edge configurations with sulfur coverage $\theta_S = 0.5$ and $\theta_S = 1$ from (237). The edge models are multi-layer models, i.e stacked infinite stripes. We assess the MD stability of MACE-MP-0 + D3 dispersion on these structures by running 100 ps of MD (NVT ensemble) at 300 K. Final structures are geometry optimized and taken as equilibrium geometries. Figure 41a shows the MoS₂ edge structures considered. All configurations exhibited stable MD for 100 ps. The Mo-edge and S-edge configurations largely retain the structural features predicted by DFT. The $\theta_S = 1$ S-edge is seen to have a sulfur dimer forming which is a favorable reconstruction in monolayer and not multi-layer models (237).

Defects have a significant impact on the optical and electronic properties of 2D TMDs and come in various types including vacancies. We assess the ability of MACE-MP-0 to describe defect formation energies (E_f) of various defects in WS₂ as compared to PBE from (238). The formation energy is calculated using the formula:

$$E_f = E_{\text{defect}} - E_{\text{pristine}} - \sum \Delta n_i \mu_i \quad (2)$$

where E_{defect} and E_{pristine} are energies of the WS₂ with and without defects, n_i and μ_i are the number of atoms and chemical potential of element i . The chemical potential of S obeys the equilibrium condition $\mu_{WS_2} = \mu_W + 2\mu_S$, and is bounded by predefined S-poor and S-rich conditions: $\mu_S^{\text{bulkW}} \leq \mu_S \leq \frac{1}{2}\mu_S^{\text{S}_2}$. It is calculated with respect to the α-S as the reference state (238). Figure 41b shows E_f values predicted by MACE-MP-0 and DFT are in qualitative agreement. Large deviations can be observed in some of the high-energy defects such as V_{WS_3} and V_W with a consistent underestimation of energies and forces by MACE-MP-0.

Similarity statement

Majority of the Mo–S or W–S containing structures in the database include primitive units of layers of MoS₂ or WS₂. However, clusters of Mo–S and W–S were found as well. Edge models for MoS₂ are rare,

with three structures identified (mp-990083, mp-989179 and mp-990086). These include a variant of the $\theta_S = 1$ S-edge and the $\theta_S = 0$ Mo-edge. No defect models of WS₂ were found in the dataset.

Performance summary

Geometric reconstruction of nanoribbon edges mostly correct, apart from small deviations. Ordering of defect formation energies qualitatively correct with an overall tendency to underestimate precise values.

A.27 Electrode-electrolyte interface / Battery system

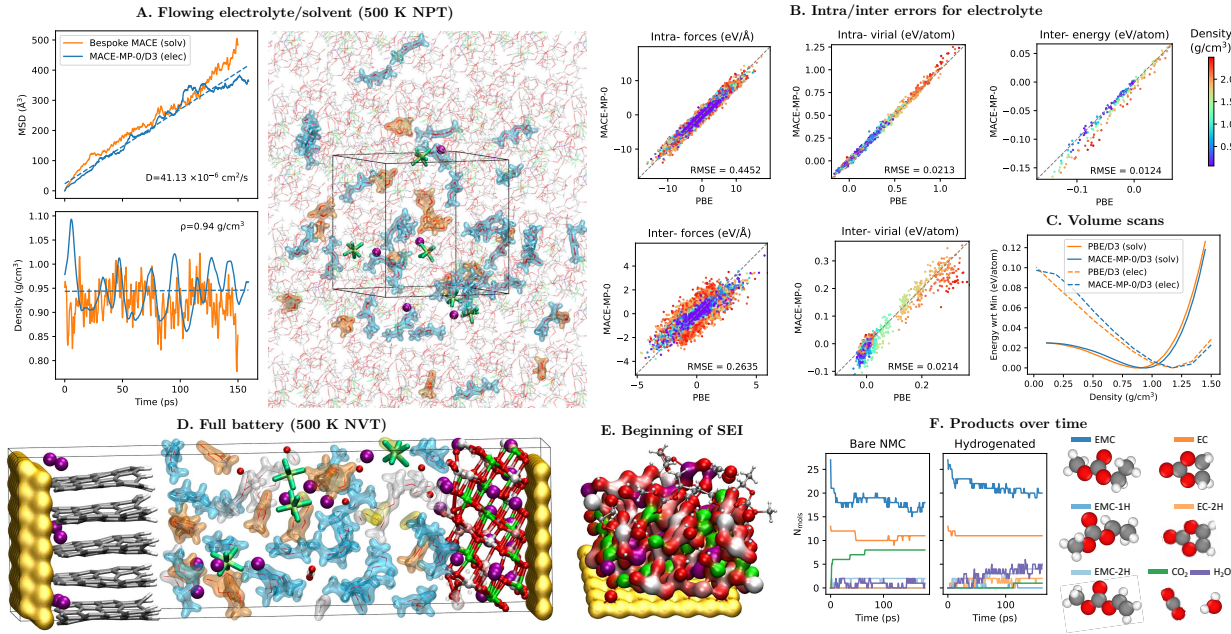


Figure 42: (A) Flowing EC/EMC LiPF₆ electrolyte with stable density and intact molecules at 500 K MACE-MP-0+D3 NPT MD. Comparison with a bespoke MACE model trained and tested exclusively on PBE/D2 EC/EMC solvent mixture, which will be published elsewhere. Final simulation snapshot, repeated across PBC (unwrapped) highlighting the diffusion of the simulated molecules ‘outside’ the simulation box. (B) Intra-/Inter-molecular energy / forces / virial evaluated on independent PBE test set spanning all possible compositions of EC/EMC LiPF₆ electrolyte at densities between 0.1–2.5 g/cm³. (C) Rigid-molecule volume-scan test (120) for both charge-neutral solvent and full electrolyte, compared to PBE. (D) Full battery simulation (Cu | H-capped graphite+Li | EC/EMC+LiPF₆ | NMC+Li (239)), final snapshot of 500 K MACE-MP-0+D3 NVT-MD, showing degraded solvent (grey iso-surface molecules), new CO₂ and H₂O, oxygen atoms originating from the cathode floating in the electrolyte. (E) Close-up of cathode-electrolyte interface showing solvent molecules chemisorbed to surface. (F) Time progression of the predominant molecular species in the electrolyte for the two NVT simulation settings (1. neat NMC, 2. H-capped NMC (H on exposed O atoms)).

Atomic-level interactions between the electrodes and electrolyte play a crucial role in determining the performance of electrochemical devices, including batteries, fuel cells, and electrocatalysts. Understanding these interactions is essential for optimizing the energy storage, conversion, and catalytic properties of these devices and to this end molecular modelling plays a crucial role. The remaining challenge is that processes underpinning transport and degradation in these devices take place on a long time scale, inaccessible to ab initio simulations. MLIPs are ideally suited to bridge this gap, bearing in mind that these complex materials and heterogeneous interfaces cover an extensive chemical space which poses a big challenge to ML models. Here we test the performance of MACE-MP-0 on three separate systems – pure (EC/EMC LiPF₆) electrolyte, the electrolyte-graphite anode interface, and the complete battery including the copper interface, anode, electrolyte and NMC cathode (totalling 9 chemical elements). We performed MD simulations at 500 K using MACE-MP-0+D3 to stress-test the qualitative robustness of the potential. Further, we quantitatively assessed the potential on a separate PBE test set in order to establish the accuracy of describing intra- and intermolecular interactions.

Previous work (120) has shown that modelling even the neat solvent is a challenge to MLIPs owing to the weak, but crucially important, inter-molecular interactions. Here we find that MACE-MP-0 is stable in the NPT ensemble at 500 K, the density is preserved while the electrolyte (solvent+salt) remains liquid and all molecules remain intact for the entire duration of the simulation (approx. 150 ps). A similar NPT

simulation was performed for the pure solvent with a bespoke MACE model trained exclusively for EC/EMC solvent mixtures at PBE/D2 level (will be published elsewhere). Both the densities and diffusivities of the two simulations closely agree with each other, demonstrating that the out-of-the-box MACE-MP-0 can reproduce the performance of the custom trained model. The accuracy of the model was also tested on a diverse PBE test set of electrolytes spanning all physical compositions and densities (will be published elsewhere). MACE-MP-0 reproduces both intra- and inter-molecular interactions and performs surprisingly well on rigid-molecule Volume scans (120) which test the inter-molecular PES. The potential capture the $1/r$ scaling of the energy in the charged system to surprisingly large volume (low density) values.

The electrolyte-anode interface, as well as the full battery were simulated in the NVT ensemble, since the volume of the entire system was not stable in NPT simulations (possibly the result of large compressibility differences along the x-direction normal to the liquid electrolyte layer vs the y/z-directions along the solid electrode slabs). All NVT simulation were stable at 500 K for the entire simulation time (100-200 ps). The electrolyte Li-ions were found to deintercalate from both the graphite anode and NMC cathode and the electrolyte was mobile. The H-capped graphite was found to be inert, whereas the cathode-electrolyte interface exhibited pronounced reactivity. Evident from the start of the simulation was the extensive proton transfer from the carbonate solvent (EMC in particular) to the oxygen atoms in NMC. This in turn led to continuous breakdown of solvent molecule (which became a radical) and chemisorption onto the cathode surface, possibly demonstrating the initial steps of SEI formation. Notably, substantial amounts of CO₂ and H₂O were generated in the process, and oxygen atoms were easily extracted from the cathode leaving behind binding sites for the oxygen-rich carbonate molecules. A separate simulation setting was tested where the exposed oxygen atoms of the cathode were hydrogenated before the simulation. Similar reactivity was observed albeit with different outcomes, notably more water molecules and less carbon dioxide was generated in the process. These early simulations demonstrate MACE-MP-0 is robust for battery interfaces and showcase the initial steps in modelling the SEI formation with ab initio accuracy – which has been a long-held dream of the scientific community.

Similarity statement

To perform the similarity analysis, 100 representative (decorrelated) structures were taken from the previously described simulations. While the MP dataset does not contain liquids, for all three simulations the UMAP analysis showed that all atomic environments were well represented in the MP dataset. More specifically, the pure electrolyte was found to contain environments close to mp-995234 and mp-995218 which correspond to HCO and H₄C₅O₂, respectively. These configurations were also found to be similar for the snapshots obtained by running the electrolyte-anode interface, and also notably included mp-707412 corresponding to H₂₂C₁₀O₃. For the entire battery system configurations such as mp-1194779 and mp-698267 were found to be similar which correspond to CuH₃C₃O₄ and CoHCO₃ respectively. We provide:

- `interface_chemiscope_input.json`
- `battery_chemiscope_input.json`
- `electrolyte_chemiscope_input.json`

to help visualize the atomic environments against the MP dataset at chemiscope.org.

Performance summary

Solvent and electrolyte properties (density, diffusivity) well captured compared with custom-trained model. Full battery simulation stable at fixed volume but unstable with variable volume, and shows electrolyte breakdown at unpassivated electrode.

A.28 Metal–organic frameworks

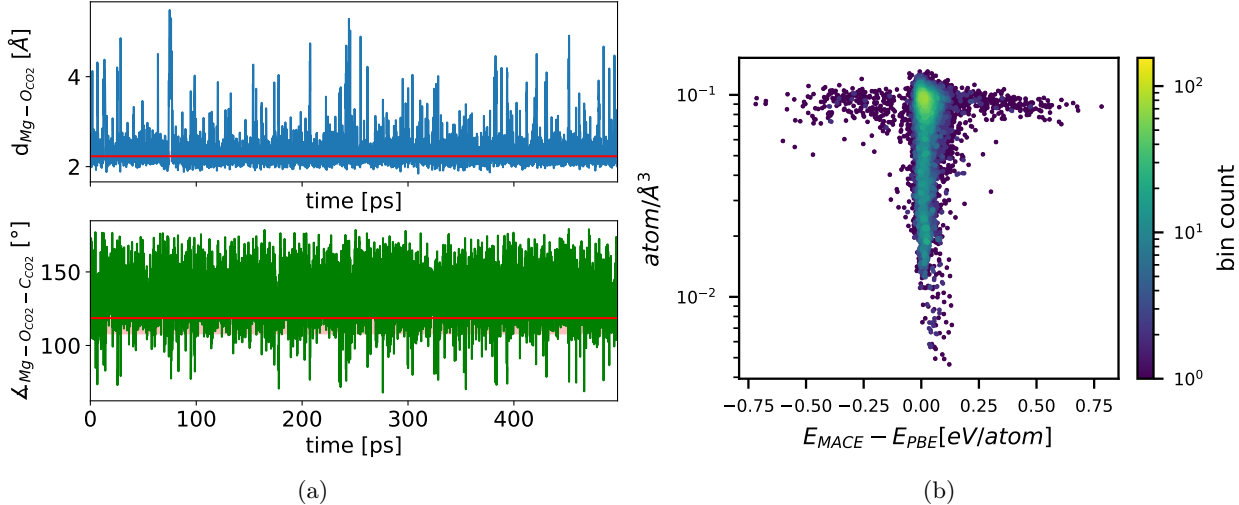


Figure 43: (a) Top panel: instantaneous distance between the Mg center and the closest oxygen from CO_2 in Mg-MOF-74, the red line shows the predicted average value from previous work. (90) Bottom panel: instantaneous angle between Mg center, closest oxygen and carbon in the CO_2 , red line indicates an average value from previous work from Ref. (90) (b) Figure 4a inset. Error between MACE-MP-0 predicted and PBE energies on 20,375 relaxed structures taken from the QMOF database, Refs. (88, 89). High-error, sparsely-populated region structures are mainly high density entries with elemental dependence shown in Figure 4b.

A.28.1 QMOF

Given that MACE-MP-0 is pretrained against PBE, whereas QMOF was constructed from PBE-D3(BJ) calculations to account for dispersion corrections (48, 140), in the comparison with QMOF, we compare MACE-MP-0 predicted energies with QMOF PBE energies by subtracting dispersion correction from total QMOF energies.

We noted that most of the high-energy error MOF structures are high in atomic density (Figure 43b), and that the errors cannot be canceled by adding dispersion correction. Thus, we further analyze the element-wise energy error per atom by distributing the absolute energy error per atom to the constituent elements by the corresponding composition in each MOF structure. As presented in Figure 4b, there is a strong elemental dependence of energy error per atom. Most of high error elements can be attributed to the difference of chosen pseudopotentials used by MP and QMOF databases (in particular the choices of which electrons are treated as valence states), see Table 3.

MPtrj	Be	Bi	Cr_pv	Eu	Fe_pv	Gd	Li_sv	Mg_pv	Mo_pv	Nb_pv	Ni_pv	Os_pv	Re_pv	Ti_pv	V_pv	W_pv	Yb_2
QMOF	Be_v	Bi_d	Cu	Eu_3	Fe	Gd_3	Li	Mg	Mo_sv	Nb_sv	Ni	Os	Re	Ti_sv	V_sv	W_sv	Yb_3

Table 3: Difference in VASP POTCARs used by MPtrj and QMOF

A.28.2 CO_2 adsorption

All the calculations for the CO_2 dynamics with MOFs were performed with MACE-MP-0 by adding the D3 dispersion correction (48) to the MACE-MP-0 potential. The simulations were carried out with ASE (240) on a cell containing 165 atoms with one CO_2 molecule, initialised at the centre of the pore, using NVT Langevin dynamics (241) with a friction factor of $5 \times 10^{-3} \text{ fs}^{-1}$. The temperature was set to 600 K with a time step of 1 fs. Twenty-four 1 ns trajectories were generated using different initial velocities, and all quantities presented were averaged over all of them, discarding the first 2 ps from each to account for equilibration. All structures

had their cells and positions optimised at start using `FrechetCellFilter` from ASE. The code used to generate the trajectories is available in the repo (183).

Similarity statement

The MP dataset does not contain MOFs. There are 8 structures containing all MgOCH elements, and 62 structures that have MgOHC elements on their own or along with other elements. Based on UMAP analysis, we see that most atomic environments, both MgO and linkers, in the example system, are similar to environments in the training data but none is Mg-MOF-74 specific.

The closest (most relevant) structures in the training set are CO₂ (mp-556034 mp-20066 mp-995224 mp-11725 mp-644607 mp-1102227 mp-1190685 mp-995198 mp-1190699 mp-1077906 mp-1077316 mp-729728). CO₂ alone matches 4896 structures with C, O and alongside other elements.

We provide

- `co2_FilterType.exclusive_OC_chemiscope_input.json`
- `mg-mof-74-co2_FilterType.exclusive_MgOCH_chemiscope_input.json`
- `mg-mof-74-co2_FilterType.exclusive_MgOCH_chemiscope_input.json`

that contain exact matches of Mg, O, C and H and the inclusive versions

- `mg-mof-74-co2_FilterType.exclusive_MgOCH_chemiscope_input.json`
- `mg-mof-74-co2_FilterType.inclusive_MgOCH_chemiscope_input.json`
- `mg-mof-74_FilterType.inclusive_MgOCH_chemiscope_input.json`

to help visualize the interactive UMAP on chemiscope.org.

Performance summary

Excellent energy prediction for large database of MOFs. Correct prediction of binding structure and free energy of CO₂ in Mg-MOF-74.

A.29 Combinatorial Materials Discovery

A.29.1 Formation energy of hypothetical materials

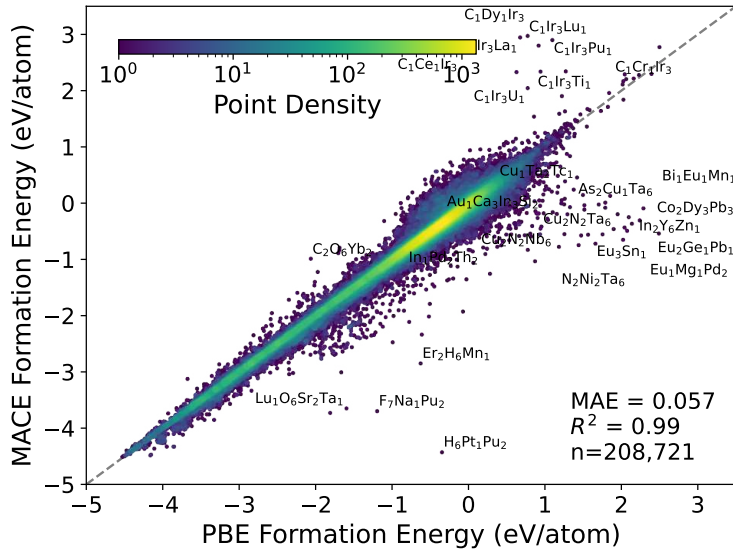


Figure 44: Formation energy parity plot showing the difference between the DFT-relaxed energy and the MACE-MP-0-relaxed energy starting from WBM initial structures.

MACE-MP-0 trained on the MPtrj dataset generalizes to out-of-distribution (OOD) chemistries as shown by its performance on the WBM dataset (242) which was generated using elemental substitutions drawn according to a data-mined chemical similarity measure (243). The initial set of 9,524 structures for substitution were taken from the Materials Project convex hull. The substituted structures were relaxed using the `MPRelaxSet` PBE DFT workflow. After this, the convex hull was recalculated using the new structures and then subsequent rounds of substitution were carried out on the new structures that ended up on the combined MP plus growing WBM convex hull. In total, 5 rounds of substitutions were carried out yielding a dataset of 257,487 inorganic crystals that are OOD with respect to MP and therefore well suited to benchmarking. For this investigation, we use the cleaned version of the WBM dataset released in Matbench Discovery (MBD) (244), which first discards 524 crystals with unphysical or missing labels. Subsequently, all structures in WBM with composition+prototype matching a structure in MP are removed. Within WBM composition+prototype, duplicates are dropped leaving only the lowest energy structure. The final test set consists of 215 488 materials, and of these we obtained MACE-MP-0 relaxed structures for 208 750.

Following the MBD protocol, we use MACE-MP-0 to relax the initial substituted structures and compare these predictions against the ground truth formation energy calculated with DFT. Before calculating metrics, we drop 29 structures predicted to have formation formation enthalpies < -5 eV/atom. The most prevalent elements in these dropped materials are H (36.4%), Mn (11.7%), Fe (10.5%), Pu (10.1%), and Cr (5.7%), suggesting the existence of holes in the MACE-MP-0 PES for transition metal and f-block hydrides. The predictions on the MACE-MP-0 self-relaxed structures result in an MAE of 57 meV/atom as shown in Fig. 44. The OOD nature of the WBM dataset can be seen in the increase in MAE between WBM batches from 48 meV/atom for the first batch to 78 meV/atom for the final batch as the structures become increasingly dissimilar to MP due to accumulated substitutions. When these predictions are used to attempt to classify whether the structure lies above or below the MP convex hull training set, MACE-MP-0 achieves an F1 score of 0.67 and a discovery acceleration factor (DAF) of 3.76. The DAF is the ratio of the precision (TP/PP) to the prevalence (P/N) of the test set. Here, TP = True Positives, PP = Predicted Positives, P = Total Positives and N is the test set size. These results show that MACE-MP-0 can extrapolate to novel chemistries and is well-suited to high-throughput materials discovery.

Similarity statement

By construction there is no overlap in terms of both composition and prototype together between MP and the WBM test set studied here. However there is overlap for both compositions and prototypes separately. MP contains 105 583 unique reduced formulae, whilst the WBM test set contains 160 055. Of these 15 782 overlap MP albeit with all instances being examples of different prototype structures. MP contains 32 933 different isopointal prototypes, whilst the WBM test set contains just 2816. Of the prototypes found in WBM 1813 are also found in MP. Of the isopointal prototypes not seen in MP the 5 most common are (occurrences in parentheses): ABC2_oI8_71_a_b_f (323), ABC2_hP12_181_c_d_i (215), AB2_hP9_189_f_adg (156), ABC2_oI8_44_a_b_c (117), AB4C6_mC22_8_a_2ab_2a2b (106). These arise due to changes in symmetry during the relaxation of the substituted structures.

A.29.2 Stoichiometric substitutions

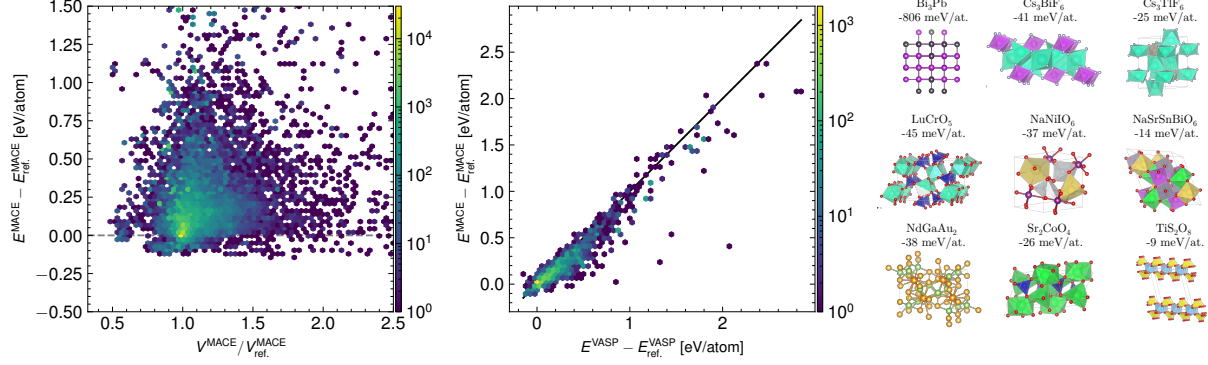


Figure 45: Left: Relative energies vs. volumes of ca. 150k relaxed structures generated via exhaustive element substitutions for 100 MP compositions. Center: Correlation between relative energies calculated with DFT and MACE-MP-0 for 6909 randomly drawn structures from the left plot. Right: DFT validated examples of newly discovered stable phases, along with their energies relative to the MP convex hull.

To test the interpolative and extrapolative capabilities of the model within MP chemistry, exhaustive element substitutions for 100 randomly selected compositions were performed. Specifically, MP was first filtered to remove all compositions with more than 16 atoms in the reduced formula, to ensure that a sufficient number of possible substitutions. This set was randomly split into host and target compositions with a 60:40 ratio. 100 compositions were randomly drawn from the target split and substituted into each stoichiometrically matching host, yielding 154,685 substituted structures. These were optimized with MACE-MP-0 using full unit cell relaxations (without the D3 correction). In Fig. 45, the results are shown in terms of energies and volumes relative to the most stable structure of that composition within the MP. The distribution is sharply peaked at $\frac{V}{V_{\text{ref}}} = 1$ and $E - E_{\text{ref}} = 0$, indicating that the substituted cells often relax back to the known ground state structure from MP. This makes MACE-MP-0 potentially suitable for predicting the crystal structures of unknown materials. For a random sample of 6909 structures, the MACE-MP-0 relative energies were validated with MP-compatible PBE DFT calculations, yielding an RMSE of 0.097 eV/atom.

Beyond recovering the MP ground state, the wide range of substitutions tested also yields a large number of alternative structures for each composition. 2518 of these have relative energies of zero or lower and are thus predicted to be more stable than the MP reference. To validate these predictions, DFT relaxations were performed for all structures with negative relative energies. The results confirm that 2120 of them are indeed more stable than the corresponding MP reference. Importantly, not each of these is a new stable phase, as some relaxations converged to the same minimum and multiple lower energy structures are found for some compositions. Nonetheless, for nine of the 100 compositions considered here, new structures with energies below the current MP hull were discovered (for Bi₃Pb, Cs₃BiF₆, Cs₃TlF₆, LuCrO₅, NaNiIO₆, NaSrSnBiO₆, NdGaAu₂, Sr₂CoO₄, and TiS₂O₈). These constitute genuine predictions of new, thermodynamically stable phases relative to the MP convex hull. These phases were also not reported in the recent GNoME effort (which focused on compositions not included in MP). However, the WBM dataset does report slightly more stable structures for NaNiIO₆ and NdGaAu₂. It also includes structures for Cs₃BiF₆ and Cs₃TlF₆, which are less stable than the ones reported herein.

Similarity statement

The MP contains at least one (*e.g.* NaNiIO₆, NaSrSnBiO₆) and at most 423 (Sr₂CoO₄) structures that contain all elements in the discovered stable phases. These matches are similar to the discovered structures, as host and reference structures are present in the MP. Yet, the discovered phases are unique and by definition not part of the training set. For each discovery, the closest structures in the training set are: mp-1106139

(Bi_3Pb), mp-559695 (Cs_3BiF_6), mp-561827 (Cs_3TlF_6), mp-1211553 (LuCrO_5), mp-545399 (NaNiIO_6), mp-1522253 (NaSrSnBiO_6), mp-1220399 (NdGaAu_2), mp-1100068 (Sr_2CoO_4), mp-775149 (TiS_2O_8). We provide json files to visualize interactive UMAPs on chemiscope.org.

A.29.3 Analysis of highly-coordinated theoretical structures

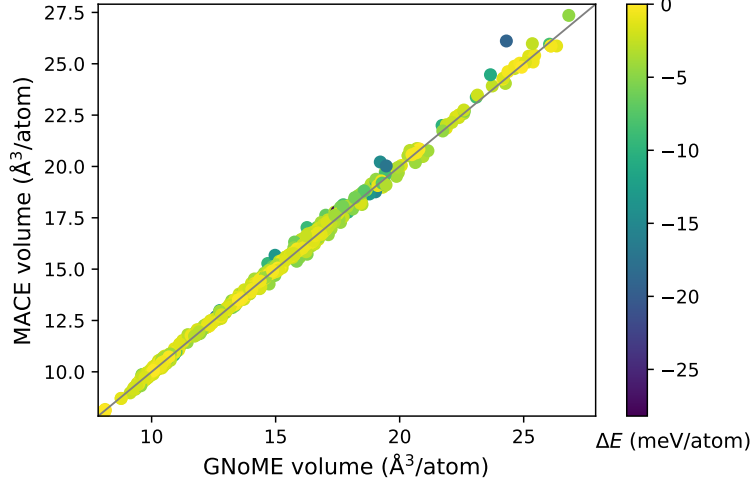


Figure 46: Comparison of the volume of the highly-coordinated structures in the GNoME database (28) (horizontal axis) against the same structures relaxed with the MACE-MP-0 UIP (vertical axis). The line of perfect agreement is plotted as the solid black line. The points are colored by the difference in the total MACE-MP-0 potential energy (in meV/atom) after relaxation and prior to relaxation. The line of best fit is $V_{\text{MACE-MP-0}} \approx 1.009 \times V_{\text{GNoME}} - 0.102$, with $R^2 \approx 0.998$. +

The recent GNoME database (28) published approximately 381,000 stable materials which could not be matched to any experimental structure in the Inorganic Crystal Structure Database (ICSD) (245), nor any public repository of theoretical structures such as the Open Quantum Materials Database (OQMD) or Materials Project. An analysis of the local coordination environment of these structures using the CrystalNN algorithm (246) reveals 21,300 structures with maximum coordination number greater than 16.

To evaluate the performance of MACE-MP-0 against the GNoME UIP which generated these structures, we have re-relaxed 1,199 structures with a predicted maximum coordination number greater than 20. The `FrechetCellFilter` class in the Atomic Simulation Environment (ASE) (240) was used to relax structures until the maximum (absolute) Cartesian component of any MACE-MP-0 inter-atomic force was less than 10^{-5} eV/Å. No dispersion correction was used to augment MACE, consistent with the lack of a dispersion correction in GNoME. All relaxations were successful, however two boron-dominated structures (GNoME identifiers 00edc694b5 and fc5cb3e024) took significantly longer than the other structures to reach this tolerance.

The MACE-relaxed structures are highly similar to the GNoME ones. Figure 46 plots the volumes of these structures from the GNoME database before and after relaxation with MACE. In virtually all cases, MACE relaxes structures to an indistinguishable configuration. Only 19 structures (1.6%) undergo an energy lowering of greater than 10 meV/atom during relaxation. 22 structures underwent a change of space group during relaxation, in all cases an increase in symmetry. After relaxation, the maximum predicted coordination number changed for 135 structures (11%), and decreased in all cases.

These observations cumulatively suggest that MACE-MP-0 performs comparably to the GNoME UIP for these highly-coordinated structures, and yields equilibrated structures of equal or higher symmetry than the GNoME UIP.

Similarity statement

By construction, the materials in the GNoME set do not exist in the MP dataset. The GNoME set was constructed in part by substituting elements on structures that originated in the Materials Project. However, some of the GNoME materials exist in the same chemical space as those in MP. For the 1,199 GNoME materials considered here, 131 (10.9%) contain exactly the same elements as structures in MP. The chem-

ical space of maximum overlap, Cu-La-Zn, contains four GNoME (7ee54b7a37, 3422b9acb0, f36439bb45 and 68a5e7535f) and two MPtrj (mp-1223296 and mp-1093834) materials. We provide two JSON-format dictionaries, `MPtraj_chem_env.json.gz`, and `GNoME_chem_env_w_ovlp.json.gz`, which tabulate the chemical environments spanned by MP and the GNoME subset, respectively. The GNoME subset is further categorized by overlap with MP.

Performance summary

Excellent energy prediction of WBM and GNoME hypothetical materials, and able to newly discover stable materials as validated by DFT.

A.30 Alanine Tripeptide free energy surface

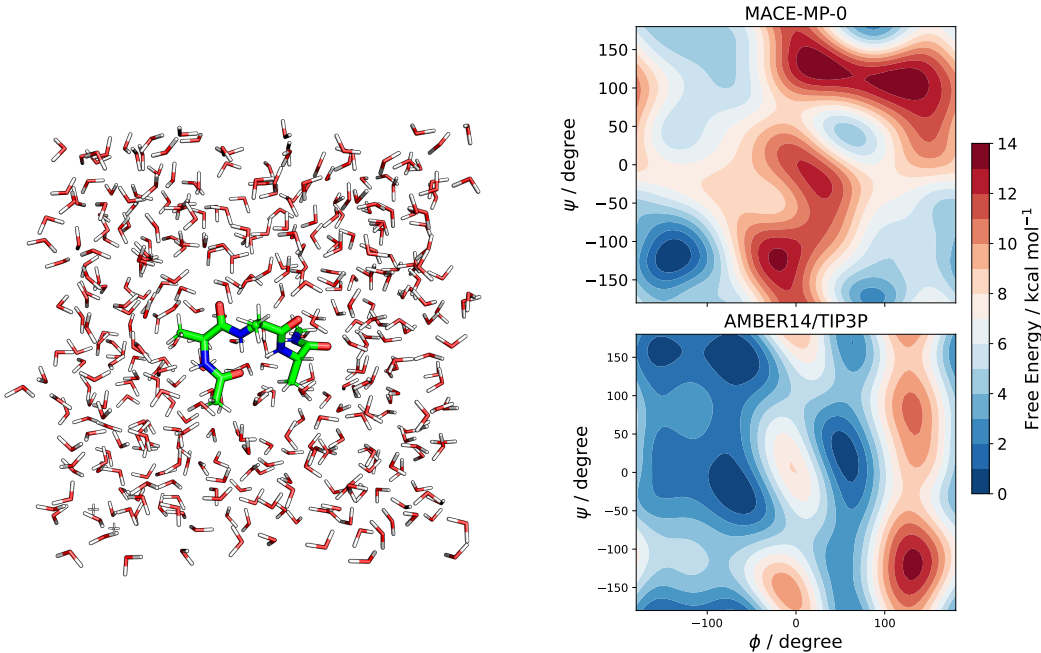


Figure 47: Left: Alanine tripeptide solvated in explicit water. Right: Free energy surface calculated from 300 ps of biased sampling with MACE-MP-0 (Top) and the classical empirical forcefield AMBER14/TIP3P (Bottom)

In this section, we investigate the ability of MACE-MP-0 to construct the free energy surface of a simple peptide. We simulate a periodic box containing an alanine tripeptide solvated with explicit water for 300 ps without D3 correction. Sampling of the central backbone torsions was accelerated by metadynamics, as implemented in OpenMM, using an initial Gaussian height of 1 kJ/mol and a temperature scaling factor of 10. Whilst we find that the dynamics appear physically reasonable, MACE-MP-0 fails to accurately identify the correct minima. Gaussian fits to experimental NMR J-coupling indicate the secondary structure is predominantly a polyproline II conformation ($\phi = 75^\circ$, $\psi = 150^\circ$), whereas this region shows little population with MACE-MP-0 (247).

Similarity statement

The MP dataset contains 99 structures containing exclusively the elements H, C, O and N. Based on UMAP analysis, we observe that all atomic environments in the example system are similar to environments in the training set. On closer inspection, we find that the most similar environments to the majority of the example configurations are clusters of water, ammonia and NO₂ molecules. Several examples contain oxygen-bearing molecules near water molecules, allowing for sampling of hydrogen bonding. We also find configurations containing clusters of large aromatic compounds containing carbon, nitrogen, oxygen and hydrogen. Interestingly, we also find a large cluster containing diverse configurations of small C,H,N,O-containing fragments, including carboxyl and amide fragments, *e.g.* mp-997182.

Performance summary

Stable MD at ambient conditions, but incorrect free energy of conformers.

A.31 Molecule-Surface Interactions

A.31.1 Adsorption energies - S24 dataset

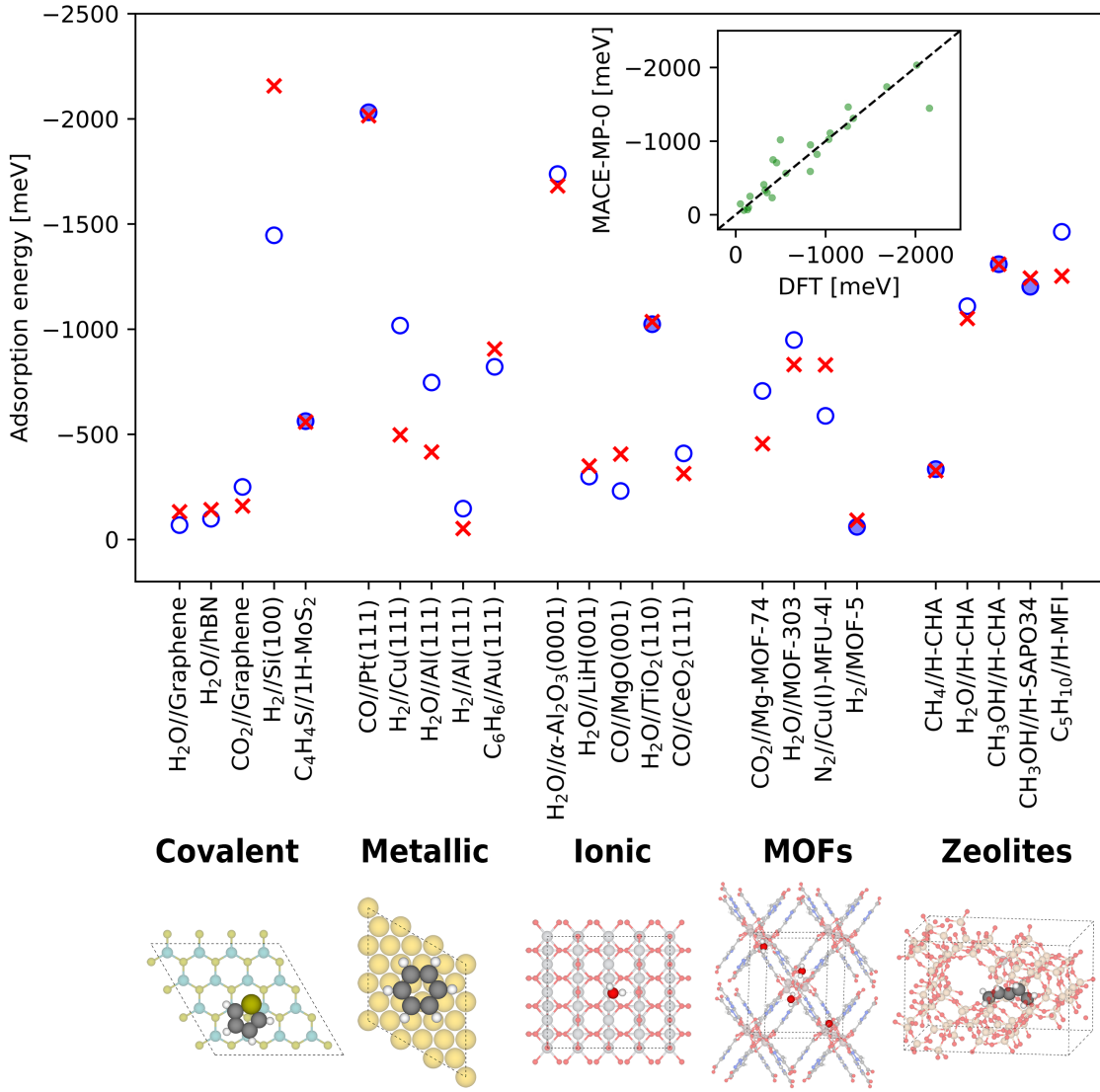


Figure 48: Comparison between DFT (PBE-D3(BJ), red crosses) and MACE-MP-0 (blue circles) adsorption energies calculated for a diverse set of surfaces consisting of covalent, metallic, and ionic bonds as well as the porous material classes: MOFs and zeolites. Filled circles indicate surfaces where MACE-MP-0 reaches chemical accuracy (43 meV) agreement to DFT. The inset shows that there is a strong correlation between DFT and MACE-MP-0 adsorption energies (Pearson correlation coefficient of 0.93).

Describing the interaction between a molecule and a surface with first-principles accuracy is central towards designing new and improved materials for heterogeneous catalysis, gas storage and separation, and many more (248). Here, we test the accuracy of MACE-MP-0 (with Becke-Johnson D3 dispersion correction) for a set of prototypical systems found in surface chemistry, encompassing metallic, covalent and ionic-bonded surfaces, together with porous metal-organic frameworks (MOFs) and zeolites. The structures used within this work - dubbed the S24 dataset - were taken from an amalgamation of published (249–259) and unpublished works. Fig. 48 summarizes the computed PBE-D3(BJ) energies using PYMATGEN to generate VASP (4, 260, 261) inputs with the MPRelaxSet settings. We observe excellent performance of MACE-MP-0

across the range of surfaces, with a mean absolute deviation (MAD) of 138 meV. Performance is particularly excellent for the ionic surfaces (with an MAD of 78 meV) and zeolites (with an MAD of 63 meV), with many systems reaching within chemical accuracy (\sim 43 meV) against the DFT reference. Performance is worse for the surfaces with metallic and covalent character, where the systems with the highest errors appear to be for H₂ adsorption onto Si(100) and Cu(111) surfaces with (absolute) differences of 710 and 519 meV to the DFT reference, respectively. Rather than simple (molecular) physisorption, H₂ dissociates onto both of these surfaces and this appears to represent a challenging case for MACE-MP-0 to handle.

Similarity statement

The S24 dataset contains 72 structures comprising 24 adsorbates, surfaces, and adsorbate-surface combinations. Based on the UMAP analysis, the elemental compositions of the adsorbates occur 6 to 27 times, the surfaces 0 to 9043 times and the adsorbate-surface combinations 0 to 4896 times on their own or along with other elements. Importantly, the training dataset does not contain any gas-phase molecules, surface-truncated models, or MOFs. For bare surfaces, on average, similar element compositions occur in the training data as follows: 3997 covalent, 5805 metallic, 2859 ionic, 46 MOFs, and 88 zeolites. For adsorbate-surface combinations, on average, the number of similar element compositions occurring in the training data are lowered to: 1492 covalent, 340 metallic, 499 ionic, 46 MOFs, and 59 zeolites. There is no clear correlation between the number of similar training data for a surface type and the accuracy of MACE-MP-0, with zeolites performing far better than metallic or covalent systems.

Performance summary

Good agreement is generally achieved for adsorption energies, with excellent performance (close to chemical accuracy) for adsorption onto ionic surfaces and porous materials. Performance appears to become poorer with dissociative chemisorption of H₂, albeit still reproducing the adsorption energy to the correct order of magnitude.

A.31.2 Relative energies - OC157 dataset

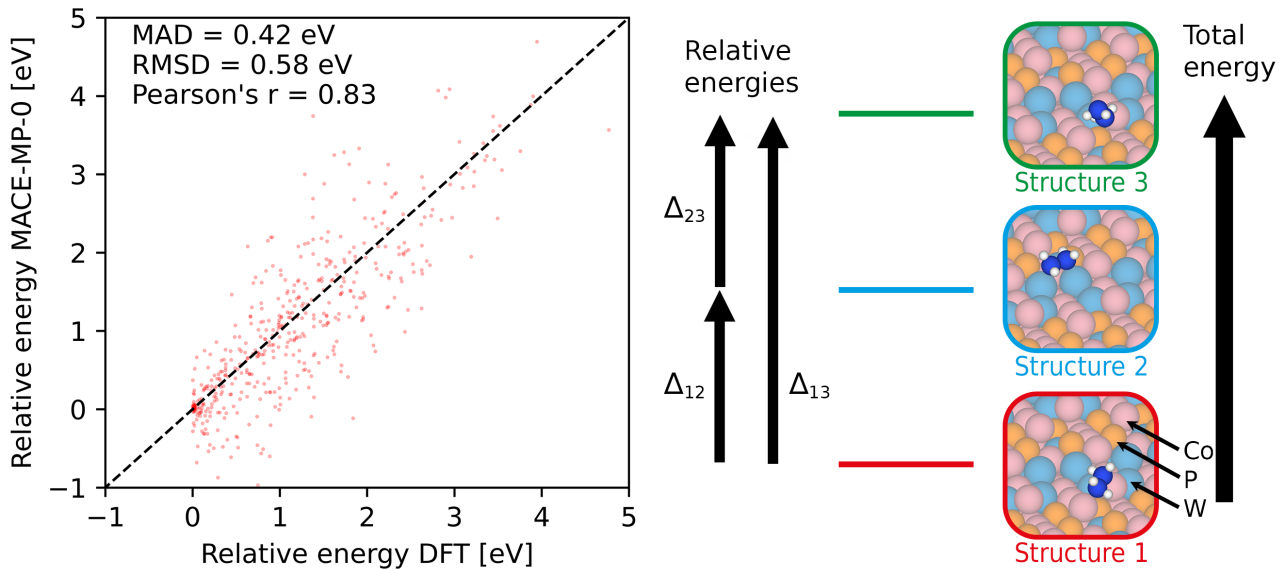


Figure 49: Comparison between the MACE-MP-0 and DFT (PBE-D3(BJ)) in predicting the relative energies between three structures across 157 molecule-surface combinations. This contains a highly diverse set of molecule-surface combinations which span 54 elements of the periodic table involving up to three elements per surface.

Identifying the most stable structures for a molecule-surface system is pivotal towards predicting the activity and selectivity of a catalyst, facilitating rational design of new catalyst materials (262). We compare MACE-MP-0 against MPRelaxSet DFT, both with Becke-Johnson damped D3 dispersion added, at predicting the relative energies between 3 structures for 157 molecule-surface combinations. These surfaces were taken from the Open Catalyst Challenge 2023 (263, 264), using structures generated by the baseline EquiformerV2 model trained on the OC20-S2EF-2M dataset. While 200 molecule-surface combinations were originally provided, we have excluded those containing oxygen (O) in combination with several transition metals (Co, Cr, Fe, Mn, Mo, Ni, V and W) as this leads to complications with the Hubbard U correction (see main text) with MPRelaxSet settings. Fig. 49 shows the 471 relative energies (Δ_{12} , Δ_{13} and Δ_{23}) for each of the remaining 157 molecule-surface systems, where Δ_{XY} is the relative energy between structure X and Y, predicted with MACE-MP-0 and calculated with DFT. Overall, we observe a moderately strong correlation between MACE-MP-0 and DFT on the relative energies, providing a Pearson correlation coefficient of 0.83 and an MAD of 0.42 eV. In particular, out of the 157 molecule-surface combinations, the lowest DFT energy configuration was correctly identified by MACE-MP-0 for 121 of the surfaces.

Similarity statement

The molecule-surface combinations in the OC157 dataset cover all elements up to and including Bi (atomic number 83), except He, Li, Be, B, F, Ne, Mg, Cl, Ar, Br, Kr, I, Xe, Ba and all lanthanoids. The UMAP analysis shows that 126 of the 157 molecule-surface combinations have no similarity to the training dataset, with a further 20 having less than 10 and only 3 having more than 20 similar compositions.

Performance summary

Moderate performance at predicting the absolute value of the relative energies between various molecule-surface configurations. Lowest energy (DFT) structure correctly predicted in 77% of the cases.

A.32 Computational efficiency (twenty-element alloy)

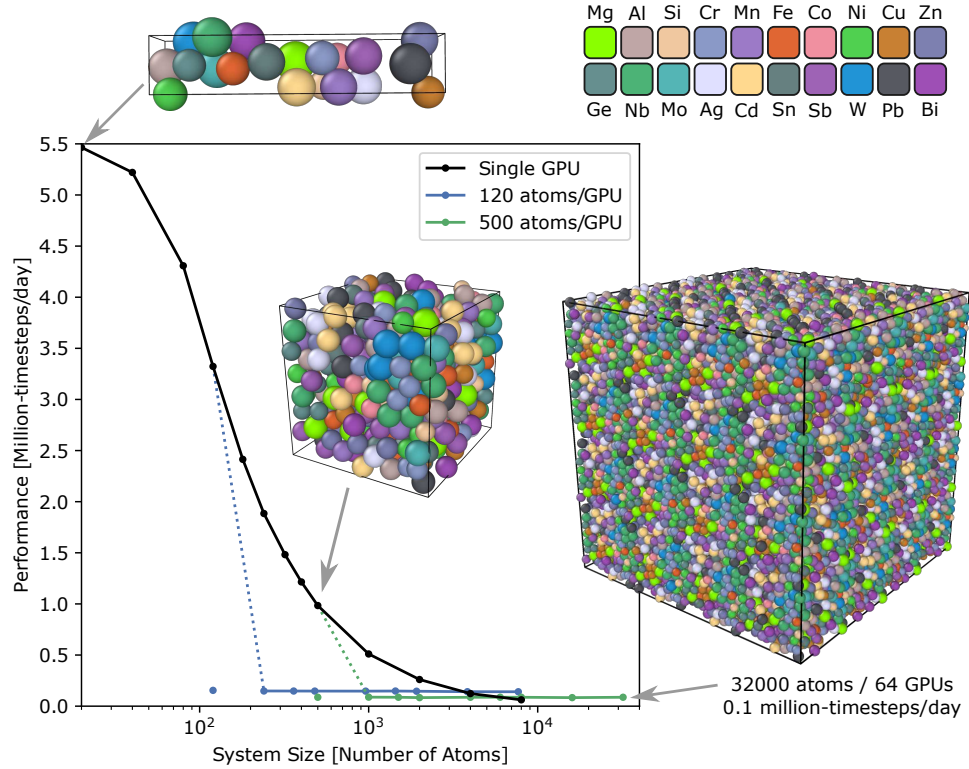


Figure 50: Computational performance for NPT dynamics in LAMMPS, measured for the 20-element Cantor alloy at ambient pressure and 300 K. The black curve indicates the performance on a single GPU, without domain decomposition, where the full structure is passed from LAMMPS to MACE as a periodic graph. The colored curves demonstrate weak scaling for 120 or 500 atoms per GPU; the dashed parts of those curves signify a transition to domain decomposition. The latter requires a different MACE evaluation strategy which (at present) incurs significant additional cost; the isolated colored dots show the performance when this strategy is used with a single GPU.

This section demonstrates the current computational performance of the medium MACE-MP-0 (without dispersion correction), while also illustrating stable dynamics for a large, diverse system. High entropy alloys are multicomponent mixtures with at least four or five distinct elements, where each component appears in non-trace proportions. Here, we consider the 20-component alloy investigated by Cantor (265), which contains equal amounts of Mn, Cr, Fe, Co, Ni, Cu, Ag, W, Mo, Nb, Al, Cd, Sn, Pb, Bi, Zn, Ge, Si, Sb, and Mg. [See also recent computational work by Ceriotti and co-workers (38, 266).] Our simulations were performed with LAMMPS (267), utilizing its Kokkos extensions (268), on NVIDIA A100 GPUs. For these tests we used the “medium” sized model (as for other applications) and 64-bit floating point operations. The “small” model is about a factor of two faster.

Figure 50 shows the computational results. For the single-GPU simulations (black curve), we began with supercells of a 20-atom FCC primitive cell, then performed a short melt-quench procedure over 20 ps at ambient pressure (which involved heating to 4000 K, holding at 4000 K, cooling to 300 K, and holding at 300 K). We then measured the computational throughput over 5 ps of NPT dynamics at ambient pressure and 300 K. The colored curves demonstrate multi-GPU performance with domain decomposition (weak scaling). At present, this mode incurs significant additional cost, only becoming favorable for very large systems. These 3 ps simulations were initialized by replicating 120- or 500-atom cells. In all cases, the primary aim was to measure performance for a reasonably well-mixed system, and we did not attempt to reach full equilibration. Moreover, the performance quoted here is provisional: substantial improvements

are expected when using, for example, custom CUDA kernels for expensive operations, which are under development.

Similarity statement

Of the 150k MP structures, roughly 100k have at least one of the 20 elements used in this example, but only 3461 have compositions drawn exclusively from that set. Of this latter group, 193 are single-component structures, 2079 are binaries, 1155 are ternaries, and 34 are quaternaries. Moreover, no structure in the entire database has five or more of the 20 elements considered here. While it is encouraging that the dynamics appear stable for such a diverse, out-of-sample composition, we expect that incorporating dedicated datasets like that reported in (38) could enhance quantitative predictions.

Performance summary

Stable molecular dynamics for solid and liquid. In parallelisation, perfect weak scaling up to 32,000 atoms and 64 GPUs.

B Benchmarks

B.1 Phonons

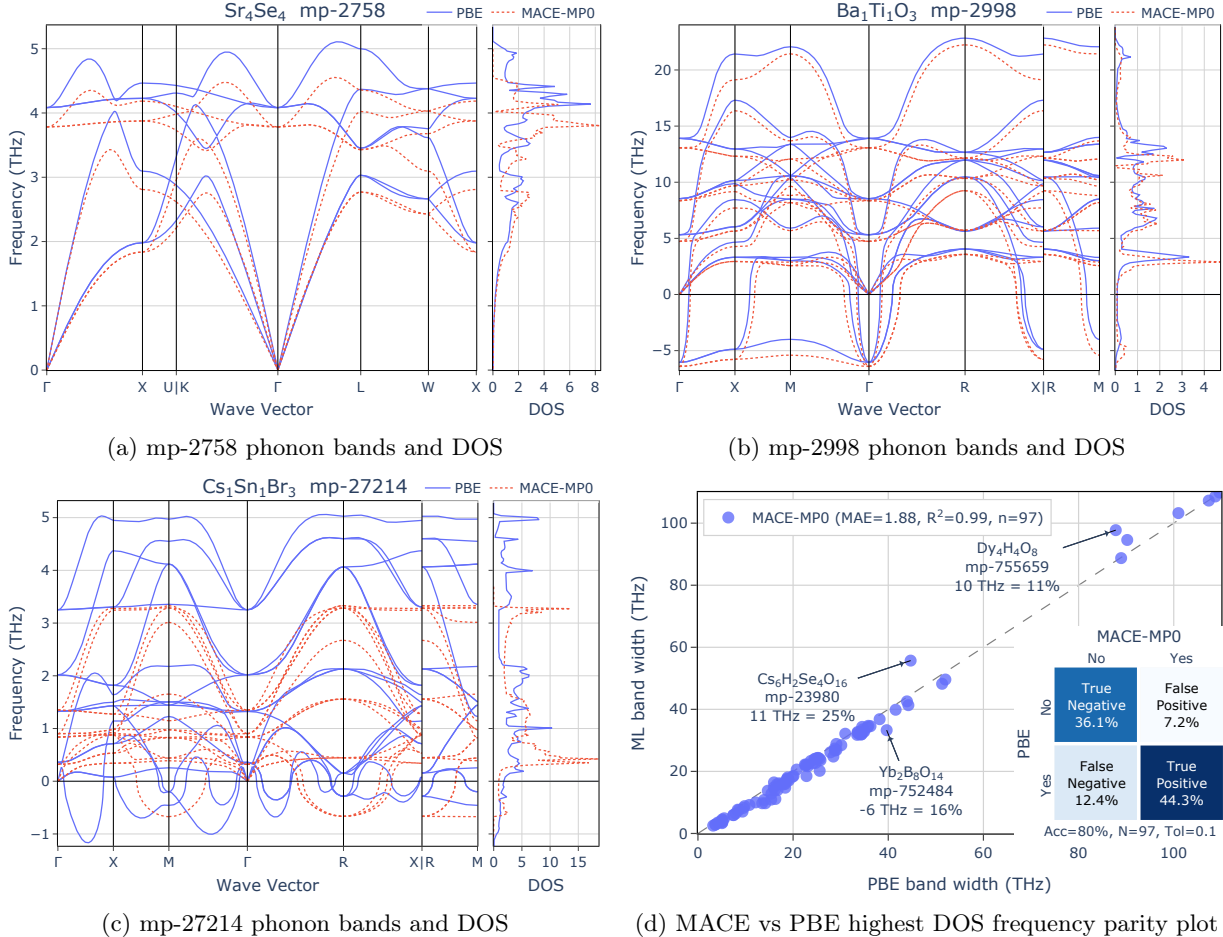


Figure 51: Comparison of PBE and MACE-MP-0 phonon band structures (BS) and density of states (DOS). PBE reference data was taken from PhononDB (269, 270). a) and b) show examples of particularly good phonon bands while c) is a particularly bad example. d) Parity plot of MACE vs PBE highest band frequency showing excellent agreement across diverse materials. The inset shows the confusion matrix for MACE-MP-0 vs PBE presence of imaginary modes (at any k -point). MACE-MP-0 achieves dynamic stability classification accuracy of 80% on our dataset of 97 materials of which 56.7% are PBE-unstable.

Accurate modeling of phonons is essential for determining dynamic stability of crystals, as well as entropic contributions to the free energy (271, 272). Both are important factors in the discovery of new materials. Harmonic phonons are typically calculated from the restoring force on atomic displacements and require highly accurate force predictions to be physical. An ML potential trained on PBE forces should be able to reproduce PBE lattice vibrations (122, 273). To assess the accuracy of MACE-MP-0 restoring forces, we compare phonon modes predicted via the finite-displacement method as implemented in Phonopy (269, 270) and atomate2 (274) with the PhononDB phonon database (269, 270). We restrict our analysis to materials in which magnetism and U-correction do not play a role, since the phonon reference database was calculated at PBE level of theory without consideration of magnetism nor U-corrections. Additional inaccuracies in the comparison may stem from not-fully-converged kinetic energy cutoffs of the plane-wave expansion or insufficient k -point density. Based on our analysis, the phonon reference calculations used the VASP-recommended and at the same time sufficiently high kinetic energy cutoff (1.3*ENMAX of the highest

ENMAX indicated in the pseudopotential files for the PAW method for each compound). In most cases, the reciprocal k -point density used matches that in MPRelaxSet for structure optimization and force calculations. However, there are some cases where the maximum distance between adjacent points along a reciprocal axis used is slightly lower compared to MPRelaxSet by an average 14 ± 13 and 19 ± 16 % for structure optimization and force calculations, respectively. As these are small deviations, the PhononDB results can be used as reasonable high-throughput reference data. To minimize the discrepancy between MACE-MP-0 and Togo results, we simulate identical supercells as found in the phonon database. In addition, we remove the non-analytic corrections derived from Born charges which are unavailable from electronic structure-less ML potentials. While MP also computed phonons for several thousand compounds, we do not use it as reference data due to MP using PBEsol, a functional incompatible with the MPtrj training set.

As examples, we show two compounds out of our set of 97 materials where DFT and MACE-MP-0 agree well (Figs. 51a and 51b), and one of the compounds of largest qualitative disagreement (Fig. 51c). The parity plot of MACE-MP-0 vs PBE highest-frequency phonon modes in Fig. 51d reveals that MACE-MP-0 typically slightly underestimates the highest overall frequency in the phonon band structure (henceforth referred to as band width, which correlates with the stiffness of the material's strongest bond) by 1–2 THz in comparison to DFT. MACE-MP-0 band widths have excellent predictive power of $R^2 = 0.99$. The largest absolute discrepancy between PBE vs MACE-MP-0 band width is around 11 THz (25%) for Cs_3HSeO_8 (mp-23980).

Highly specialised models for one element can achieve much lower errors of 0.1–0.2 THz over the whole band structure (273). MACE-MP-0 is far from achieving such accuracy. However, the deviations are close to results from models that specifically train only on the highest phonon peak on MatBench (275). Here, the best models arrive at mean absolute errors of 0.8–1 THz for the last phonon DOS peak, which is a similar but *not* identical quantity to the band width. We emphasize that neither MACE-MP-0 nor its training data was tailored in any way for phonon predictions. Yet still, MACE-MP-0 band structures achieve at least qualitative agreement with PBE for most materials, which can be sufficient for many practical applications (*e.g.* models that screen for low or high thermal conductivity (276)).

As shown in the confusion matrix inset to Fig. 51d, the model also provides useful signal on the presence of imaginary modes. The presence of such lattice vibrations indicates that the structure is dynamically unstable, meaning it can transform into a lower-energy structure by displacing atoms along the corresponding vibrational eigenvector. MACE-MP-0 achieves 80% accuracy on binary dynamic stability classification with a PBE unstable rate of 56.7% (a nearly balanced data set). While this clearly outperforms dummy accuracy of 50%, it also leaves room for significant improvement. The parameter $\text{Tol}=0.1$ in the inset caption determines how far below zero a band frequency (in THz) must reach to count as imaginary. For example, a mode at -0.09 THz would not be considered dynamically unstable while -0.11 THz would. A caveat to the above analysis is that the PBE unstable labels we use as ground truth may themselves contain false positives. That is, any un converged values of ENCUT and k -point density may result in incorrect dynamically unstable PBE labels that would stabilize by reaching numerical convergence. As is, MACE-MP-0 can already serve as a useful pre-screening filter for dynamically unstable materials, especially given the lower false positive (7.2%) than false negative rate (12.4%). This means MACE-MP-0 is less likely to predict materials as unstable that are stable than vice versa and hence is biased towards keeping materials in the candidate pool. We also emphasize the low computational cost of these predictions. Generating a complete phonon band structure on an Apple M2 Max CPU takes approximately 30 s. Running MACE-MP-0 on a supercomputer could easily generate approximate phonon bands for every material in MP or other large databases. However, the accuracy of MACE-MP-0 harmonic phonons is still insufficient to be a reliable substitute for DFT.

We share all code and data for this phonon analysis at <https://github.com/janosh/ffonons>. The code was written in a model-agnostic way. Subjecting other ML models that conform to the ASE calculator API to the same analysis should be straightforward.

Similarity statement

The structures whose phonon predictions we analyzed are all part of the training set. However, the supercells, including single-atom perturbations performed by the finite-displacement method are not.

B.2 Bulk and Shear Moduli

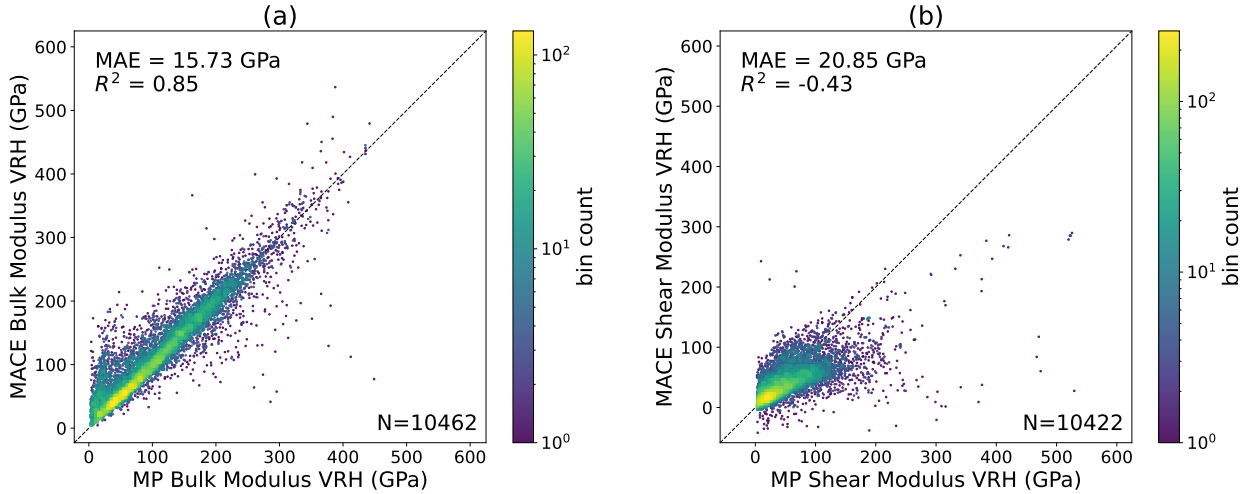


Figure 52: Comparison between MACE-MP-0- and MP-calculated (a) bulk moduli and (b) shear moduli for approximately 10,000 materials stored in the MP Database. The dashed line is a parity line (*i.e.* the target distribution of data). For bulk moduli, note that a single point for mp-721759 (face-centered cubic nitrogen) was excluded, as MACE-MP-0 predicted an unphysical high bulk modulus (≥ 600 GPa). For shear moduli, note that 26 points were excluded from this plot, as MACE-MP-0 predicted an unphysically high (≥ 600 GPa) or low (≤ -50 GPa) shear modulus; this includes mp-{1002105, 1002117, 1002165, 1002206, 1002207, 10030, 1008669, 1009019, 1009485, 1009731, 1077353, 13174, 1428312, 14549, 2458, 30083, 570354, 631377, 631475, 631524, 972442, 976419, 980204, 989573, 999086, 999263}.

MACE-MP-0 was benchmarked against the elastic properties of over 10,000 materials stored in the MP database. Being able to capture elastic properties such as bulk and shear modulus - which depend on the second derivatives of the energy with respect to strain - demonstrates a more precise ability to capture the potential energy surface.

Specifically, MACE-MP-0 was used to calculate the Voigt-Reuss-Hill average (277–279) bulk modulus and shear modulus as derived from stress-strain relations. The initial structures used for these calculations were the relaxed PBE (22) structures from MP; these structures were then re-relaxed using the MACE-MP-0 model, and then deformed. Specifically, a total of 4 strain magnitudes were used along 6 independent strain modes (in Voigt notation): $\epsilon \in [\epsilon_{11}, \epsilon_{22}, \epsilon_{33}, \epsilon_{44}, \epsilon_{55}, \epsilon_{66}]$. For ϵ_{11} , ϵ_{22} , and ϵ_{33} , the strain magnitudes were ± 0.01 and ± 0.005 . For ϵ_{44} , ϵ_{55} , and ϵ_{66} , the strain magnitudes were ± 0.06 and ± 0.03 . These calculations were performed using the `elasticity` module from the `MatCalc` package (280). Hence, all of these predictions are based on equilibrium, bulk crystals alone. Moreover, to filter out likely unphysical DFT predictions, elastic properties from MP were excluded from this analysis if the DFT VRH average bulk or shear modulus are less than -50 GPa or greater than 600 GPa. Note that the data excluded due to unphysical DFT-based properties are distinct from the data not plotted in Fig. 52 due to poor MACE-MP-0 predictions.

Results comparing MP and MACE-MP-0 bulk moduli with MAE of 15.73 GPa and R^2 of 0.85 are shown in Fig. 52(a). This compares favorably to the R^2 value of 0.757 reported for M3GNet (23). Similarly, results for shear moduli are shown in Fig. 52(b). MACE-MP-0 struggles to predict shear properties, likely due to a lack of sheared structures in MP.

Similarity statement

None of the DFT deformation calculations contained in MP are present in the MPtrj training set used for MACE-MP-0.

B.3 Cohesive energies

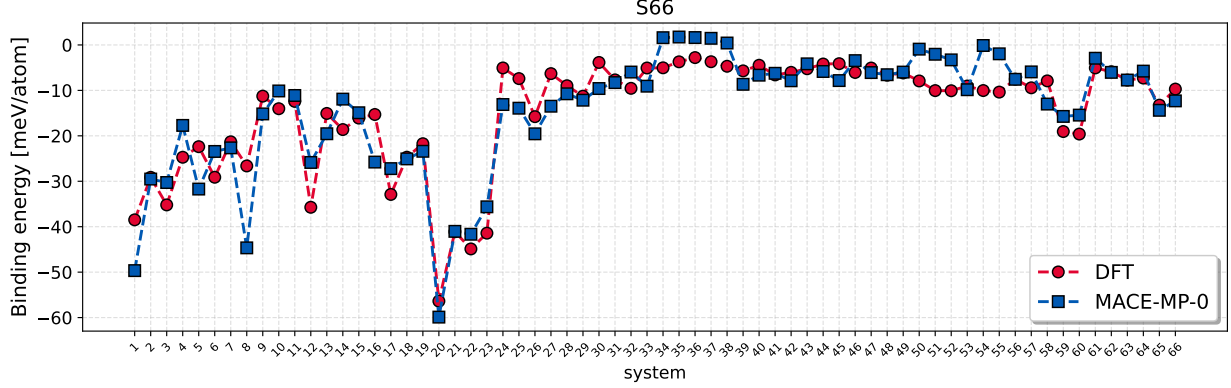


Figure 53: Comparison between DFT (red circles) and MACE-MP-0 (blue squares) calculated binding energies of the S66 dimers. The binding energies are divided by the number of atoms in each dimer. The lines are guides for the eye.

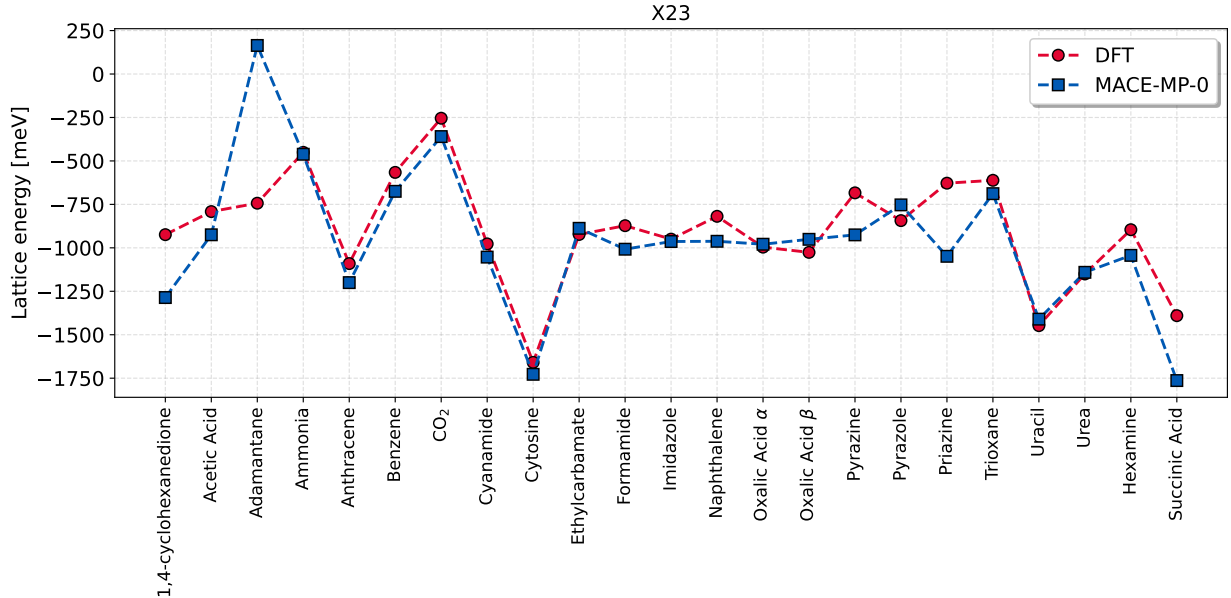


Figure 54: Comparison between DFT (red circles) and MACE-MP-0-calculated (blue squares) lattice energies of the X23 dataset. The lines are guides for the eye.

In this section, we benchmark MACE-MP-0 against the cohesive energies of widely used data sets of molecules and molecular crystals, S66 (107) and X23 (108). S66 is a dataset comprising 66 molecular complexes at their reference equilibrium geometries, designed to cover the most common types of noncovalent interactions in biomolecules while keeping a balanced representation of dispersion and electrostatic contributions. X23 is a dataset of 23 organic molecular crystals. Furthermore, we analyze the relative stabilities of the ice polymorphs in DMC-ICE13 (54). The DFT calculations were performed using VASP (4, 260, 261) with the PBE functional and D3 dispersion correction with Becke-Johnson damping. The energy cutoff is 520 eV. Gas phase calculations were performed at the Γ point in a 25 Å cubic box. Solid phase calculations were performed with a $4 \times 4 \times 4$ k-point grid. The results comparing MACE-MP-0 and DFT binding energies of the S66 dimers, and the lattice energies of X23 and DMC-ICE13 are shown in Fig. 53, Fig. 54, and Fig. 55.

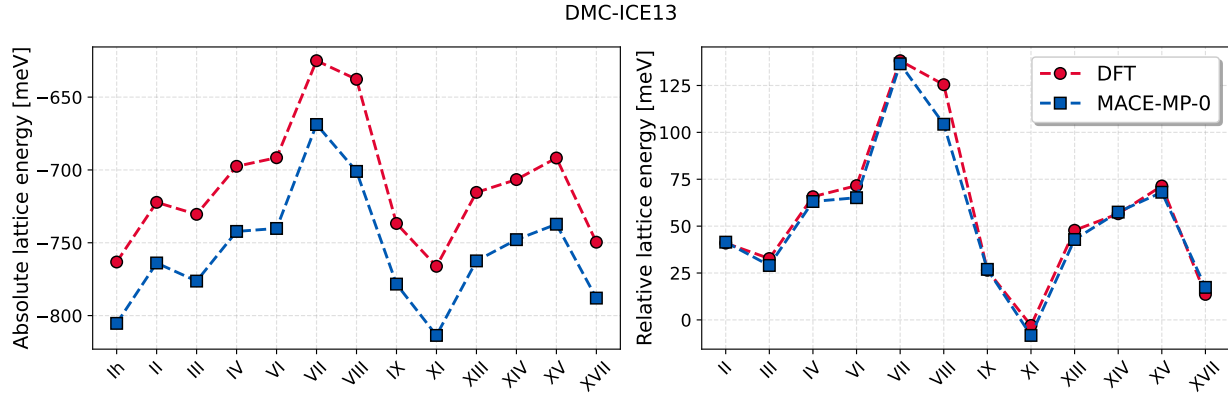


Figure 55: Comparison between DFT (red circles) and MACE-MP-0 -calculated (blue squares) lattice energies of the DMC-ICE13 dataset. We report both the absolute lattice energies (left), *i.e.* the energy per molecule of each crystalline phase with respect to the gas phase, and the relative lattice energies (right), *i.e.* the lattice energy relative to ice Ih.

The MAE is approximately 4 meV/atom for S66, 160 meV for X23, and 46 meV for the DMC-ICE13 absolute lattice energies. The relative stabilities of the ice polymorphs are correctly captured with an MAE of 4 meV on the relative lattice energies.

Similarity statement

S66 and X23 comprise dimers and molecular crystals containing C, H, N, or O atoms. Ice polymorphs contain H and O atoms. The MP database contains 73799 structures with O atoms, 10312 structures with H atoms, 11356 structures with N atoms, and 9043 structures with C atoms. The database contains 6 structures matching an exact chemical formula in S66; these are H_4O_2 , $\text{C}_4\text{HO}_8\text{O}_4$, C_8H_8 and C_4H_4 . 16 structures match an exact chemical formula in X23; these are $\text{C}_8\text{H}_{16}\text{O}_8$, $\text{C}_{20}\text{H}_{32}$, H_{12}N_4 , C_4O_8 , $\text{C}_8\text{H}_{16}\text{N}_{16}$ and $\text{C}_2\text{H}_8\text{N}_4\text{O}_2$. 9 structures match an exact chemical formula in DMC-ICE13; these are $\text{H}_{24}\text{O}_{12}$ and H_{16}O_8 . Overall, the database contains 630 structures with organic molecules and 1342 structures with water molecules. We provide `s66_chemiscope_input.json`, `x23_chemiscope_input.json`, and `dmcice13_chemiscope_input.json` to help visualize the interactive UMAP on chemiscope.org.

B.4 Atomization energies and lattice constants of solids

In the following section, we benchmark MACE-MP-0 against the atomization energies and lattice constants of a set of solids. The details of the DFT calculations are the same as in appendix B.3. Solid phase DFT total energies were computed with a $16 \times 16 \times 16$ k-point grid. MACE-MP-0 and DFT atomization energies (in eV/atom) are reported in table 4. The MAE is 0.732 eV/atom. Significant errors in the atomization energies of solids arise from the lack of isolated atom energies in the training set. For this reason, we also report the values of the atomization energies obtained by using the MACE-MP-0 energy of the solid and the DFT energies of the isolated atoms. We refer to these values as ‘corrected MACE-MP-0’. The MAE for the corrected values is approximately 0.055 eV/atom. Lattice constants are computed on equilibrium structures obtained by geometry relaxation with a force convergence threshold of 0.03 eV/Å. MACE-MP-0 and DFT lattice constants (in Å) are reported in table 5. The MAE is 0.03 Å.

Similarity statement

All the tested solids are contained in the database, with an exact matching chemical formula for 71 structures. We provide `solids_chemiscope_input.json` to help visualize the interactive UMAP on chemiscope.org.

Atomization energies of solids

	DFT	MACE-MP-0	Δ	$\Delta/\text{DFT} \%$	corrected	MACE-MP-0	Δ	$\Delta/\text{DFT} \%$
Ag	3.098	2.823	0.275	9		3.205	-0.107	3.5
Pd	4.398	4.120	0.278	6		4.356	0.042	1.0
Rh	6.404	5.853	0.551	9		6.405	-0.001	0.02
Li	1.782	1.157	0.625	35		1.784	-0.002	0.1
Na	1.244	0.947	0.297	24		1.240	0.004	0.3
K	0.987	0.437	0.550	56		1.002	-0.015	1.5
Rb	0.881	0.231	0.650	74		0.855	0.026	3.0
Cs	0.808	0.098	0.710	88		0.793	0.015	1.9
Ca	2.138	2.041	0.097	5		2.219	-0.081	3.8
Sr	1.810	1.751	0.059	3		1.841	-0.031	1.7
Ba	2.079	1.871	0.208	10		2.034	0.045	2.2
Al	3.891	3.373	0.518	13		3.862	0.029	0.7
Cu	4.075	3.749	0.326	8		4.435	-0.359	9
Si	4.922	4.366	0.556	11		4.840	0.082	1.7
Ge	4.036	3.696	0.340	8		4.041	-0.005	0.1
C	8.033	7.574	0.459	6		8.015	0.018	0.2
LiF	4.267	1.800	2.467	58		4.283	-0.016	0.4
NaF	3.798	1.676	2.122	56		3.825	-0.027	0.7
NaCl	3.129	1.799	1.330	43		3.122	0.007	0.2
MgO	4.710	4.196	0.514	11		4.726	-0.016	0.3
SiC	5.762	4.847	0.915	16		5.761	0.001	0.02
GaAs	2.548	2.247	0.301	12		2.572	-0.024	0.9
LiCl	3.377	1.716	1.661	49		3.374	0.003	0.1
			MAE			MAE		
			0.687			0.041		

Table 4: Comparison between DFT and MACE-MP-0-calculated atomization energies of solids. The column Δ reports the difference between DFT and MACE-MP-0 values. Energies are reported in eV/atom.

Lattice constants of solids				
	DFT	MACE-MP-0	Δ	$\Delta/\%$
Ag	4.082	4.093	-0.011	0.27
Pd	3.891	3.907	-0.016	0.41
Rh	3.76	3.812	-0.052	1.38
Li	3.352	3.302	0.05	1.49
Na	4.107	4.068	0.039	0.95
K	5.191	5.145	0.046	0.89
Rb	5.572	5.463	0.109	1.96
Cs	6.106	6.07	0.036	0.59
Ca	5.463	5.421	0.042	0.77
Sr	5.908	5.948	-0.04	0.68
Ba	4.976	4.938	0.038	0.76
Al	4.002	3.993	0.009	0.22
LiF	3.995	4.017	-0.022	0.55
NaF	4.619	4.628	-0.009	0.19
NaCl	5.585	5.575	0.01	0.18
MgO	4.203	4.208	-0.005	0.12
Si	5.434	5.399	0.035	0.64
Ge	5.719	5.703	0.016	0.28
GaAs	5.69	5.66	0.03	0.53
Cu	3.568	3.561	0.007	0.20
C	3.562	3.556	0.006	0.17
LiCl	5.056	5.019	0.037	0.73
SiC (a)	3.072	3.075	-0.003	0.10
SiC (c)	5.029	5.025	0.004	0.08
				MAE
				0.03

Table 5: Comparison between DFT and MACE-MP-0-calculated lattice constants of solids. The column Δ reports the difference between DFT and MACE-MP-0 values. Lattice constants are in Å.

Barrier heights of CRBH20

	DFT	MACE-MP-0	Δ	$\Delta/\text{DFT} \%$
1	1.7194	2.0593	-0.3399	20
2	1.9241	2.5655	-0.6414	33
3	1.7499	2.2417	-0.4918	28
4	1.8238	2.0893	-0.2655	15
5	1.7237	2.2944	-0.5707	33
6	1.5653	1.1929	0.3724	24
7	1.0911	1.5189	-0.4278	39
8	1.8983	1.5607	0.3376	18
9	1.5477	2.0802	-0.5325	34
10	1.7115	1.7171	-0.0056	0
11	1.7379	1.8844	-0.1465	8
12	2.0361	2.0365	-0.0004	0
13	1.8739	1.7503	0.1236	7
14	1.976	1.6933	0.2827	14
15	1.8865	1.8492	0.0373	2
16	1.5741	0.9392	0.6349	40
17	1.2587	1.0375	0.2212	18
18	1.7497	1.3102	0.4395	25
19	1.6989	1.6871	0.0118	1
20	1.7654	1.2114	0.5540	31
MAE				
0.3				

Table 6: Comparison between DFT and MACE-MP-0-calculated barrier heights for CRBH20. The column Δ reports the difference between DFT and MACE-MP-0 values. Energies are in eV.

B.5 Reaction barrier heights

In the following section, we benchmark MACE-MP-0 against the reaction barrier heights of the CRBH20 dataset (109), comprising 20 barrier heights for the cycloreversion of heterocyclic rings. The set-up of the DFT calculations is the same as in appendix B.3. MACE-MP-0 and DFT barrier heights (in eV) are reported in table 6. The MAE is approximately 0.3 eV.

Similarity statement

The CRBH20 dataset comprises barrier heights of organic molecules, containing H, O, C, N, S, and F atoms. We report the list of atoms with the number of structures in which they are contained in parentheses: O (73799), S (11972), H (10312), N (11356), F (11277), C (9043). Overall, the database contains no structures matching an exact chemical formula in CRBH20. We provide `crbh20_chemiscope_input.json` to help visualize the interactive UMAP on chemiscope.org.

B.6 Homonuclear diatomics

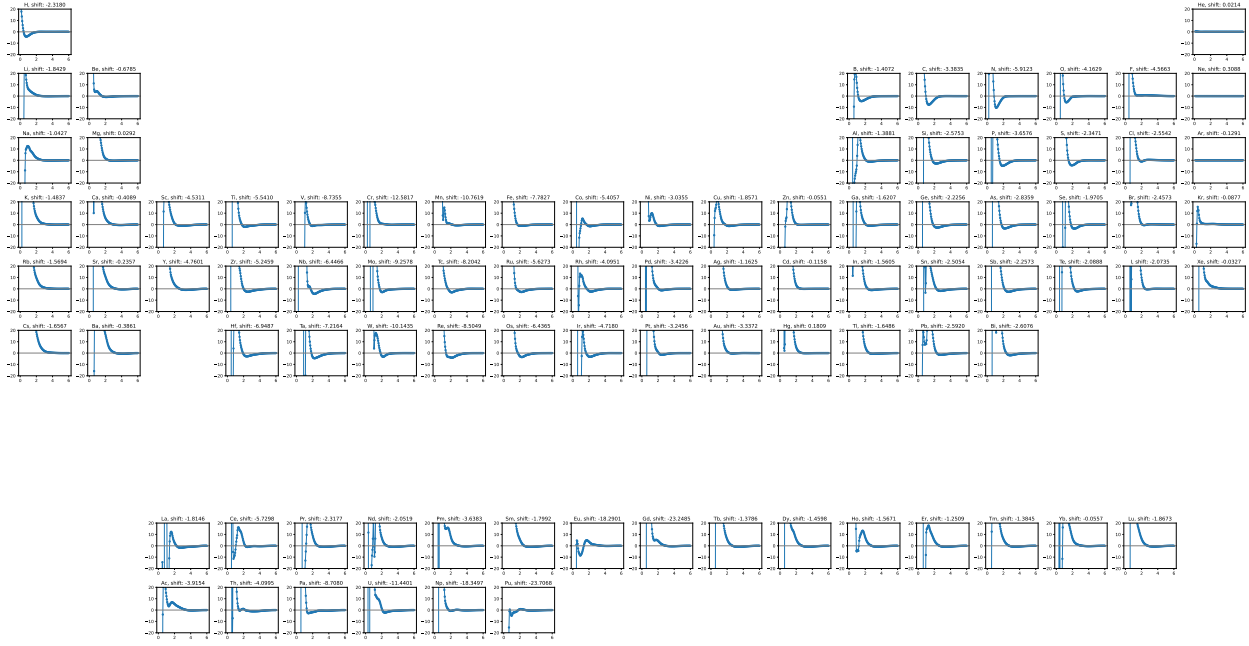


Figure 56: Energies of homonuclear diatomics in vacuum. For the majority of the periodic table there is clear repulsion at small distances, except for some elements.

Core repulsion is essential for stable modeling of atomic interactions, so atoms are prevented from coming too close together, especially when modeling high temperatures and pressures. Energies of all pairs of atoms have been evaluated with the model in vacuum, to test the 2-body interaction. The resultant curves for homonuclear diatomics are plotted in Fig. 56. Some elements have non-repulsive potential at small distances, and the noble gases He, Ne, Ar – which had negligible presence in the training set (Fig. 58) – are flat.

C Training Methods and Data Exploration

C.1 Training protocol

The pretrained MACE-MP-0 interatomic potentials consists of multi-body message passing (interaction) layers. In each layer, the message is encoded in the irreducible representation basis with C channels up to an angular frequency of order L . This is specified as (128x0e+128x1o+128x2e) for 128 channels and $L = 2$.

In each batch updating step, the weighted sum of Huber losses (281) of energy, forces, and stress incurred by all structures in a batch are averaged and back-propagated into the neural networks:

$$\begin{aligned} \mathcal{L} &= \frac{\lambda_E}{N_b} \sum_{b=1}^{N_b} \mathcal{L}_{\text{Huber}} \left(\frac{\hat{E}_b}{N_a}, \frac{E_b}{N_a}, \delta_E \right) + \frac{\lambda_F}{3 \sum_{b=1}^{N_b} N_a} \sum_{b=1}^{N_b} \sum_{a=1}^{N_a} \sum_{i=1}^3 \mathcal{L}_{\text{Huber}}^* \left(\frac{\partial \hat{E}_b}{\partial r_{b,a,i}}, F_{b,a,i}, \delta_F \right) \\ &\quad + \frac{\lambda_\sigma}{9N_b} \sum_{b=1}^{N_b} \sum_{i=1}^3 \sum_{j=1}^3 \mathcal{L}_{\text{Huber}} \left(\frac{1}{V_b} \frac{\partial \hat{E}_b}{\partial \varepsilon_{b,i,j}}, \sigma_{b,i,j}, \delta_\sigma \right), \end{aligned} \quad (3)$$

where $\lambda_E, \lambda_F, \lambda_\sigma$ are predetermined weights of energy, forces, and stress losses. $(\lambda_E, \lambda_F, \lambda_\sigma) = (1, 10, 100)$ is adopted. The energy fine-tuned small model (“small-energy”) is trained for additional 50 epochs with $(\lambda_E, \lambda_F, \lambda_\sigma) = (10, 1, 100)$. N_b and N_a are batch size and the number of atoms in each structure. Huber deltas $\delta_E = \delta_F = \delta_\sigma = 0.01$ are used. In particular, we use conditional Huber loss $\mathcal{L}_{\text{Huber}}^*$ for forces, where the Huber delta δ_F is adaptive to the force magnitude on each atom. To be specific, the Huber delta δ_F decreases step-wise by a factor from 1.0 to 0.1 as the atomic force increases from 0 to 300 eV/Å/atom. The Huber loss for forces can therefore be equivalently represented as:

$$\mathcal{L}_{\text{Huber}}^* \left(\frac{\partial \hat{E}_b}{\partial r_{b,a,i}}, F_{b,a,i}, \delta_F \right) = \begin{cases} \mathcal{L}_{\text{Huber}}(\dots, \delta_F), & F_{b,a,i} < 100 \\ \mathcal{L}_{\text{Huber}}(\dots, 0.7\delta_F), & 100 \leq F_{b,a,i} < 200 \\ \mathcal{L}_{\text{Huber}}(\dots, 0.4\delta_F), & 200 \leq F_{b,a,i} < 300 \\ \mathcal{L}_{\text{Huber}}(\dots, 0.1\delta_F), & F_{b,a,i} \geq 300 \end{cases} \quad (4)$$

Standardization of target variables (here energies, forces and stresses) with different scales has been proven to be important for weight initialization and training stability (282), in that a large spread of input or output will result in large and uneven weight values and cause model instability. After each message passing layer k , the node energies ϵ_a are scaled and shifted before sum pooling. The energy prediction of each structure therefore reads:

$$\hat{E} = \sum_{a=1}^N \left[\sigma \left(\sum_{k=1}^K \epsilon_a^{(k)} \right) + \mu_Z \right], \quad (5)$$

where K denotes the total number of message passing layers and $\epsilon_a^{(k)}$ is the node energy of atom a at k -th layer. μ_Z and σ are the mean of atomic energies and the root mean square of the atomic forces computed over the training dataset. The predicted forces and stress are computed through PyTorch’s automatic differentiation `torch.autograd` of total energy with respect to atomic positions and lattice strain tensor.

The pretrained MACE-MP-0 models are trained for 200 epochs with 40–80 NVIDIA A100 GPUs across 10–20 nodes on HPE (Hewlett Packard Enterprise) Cray EX supercomputer Perlmutter, maintained by National Energy Research Scientific Computing Center (NERSC), a U.S. Department of Energy Office of Science User Facility located at Lawrence Berkeley National Laboratory (LBNL).

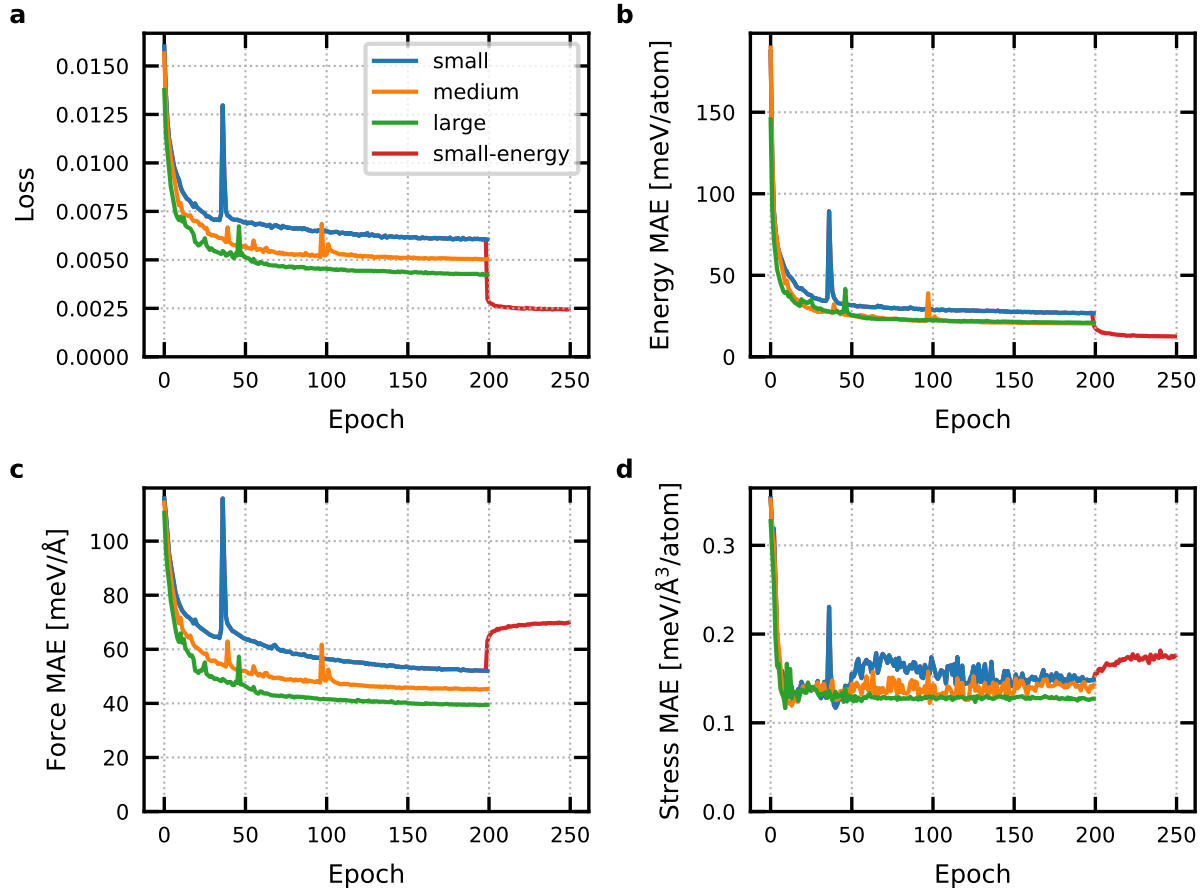
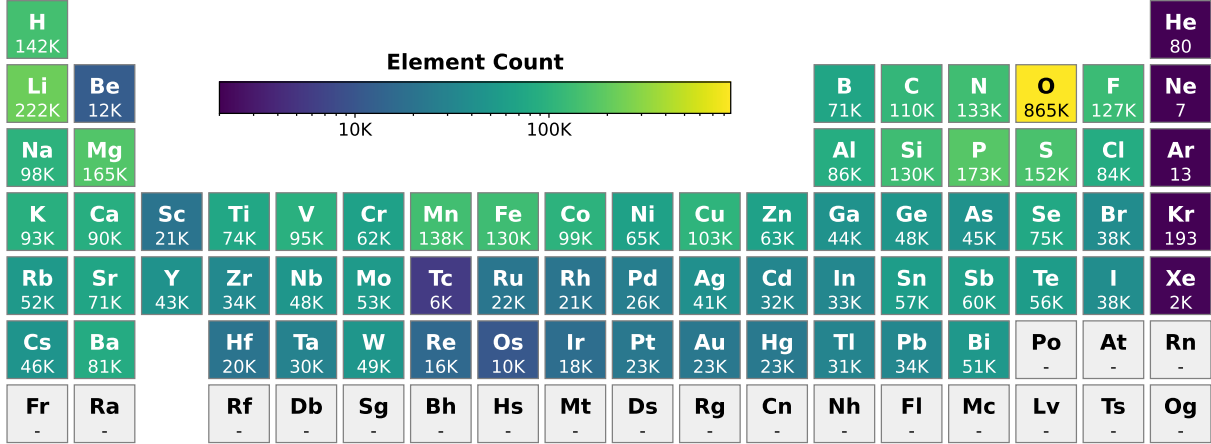
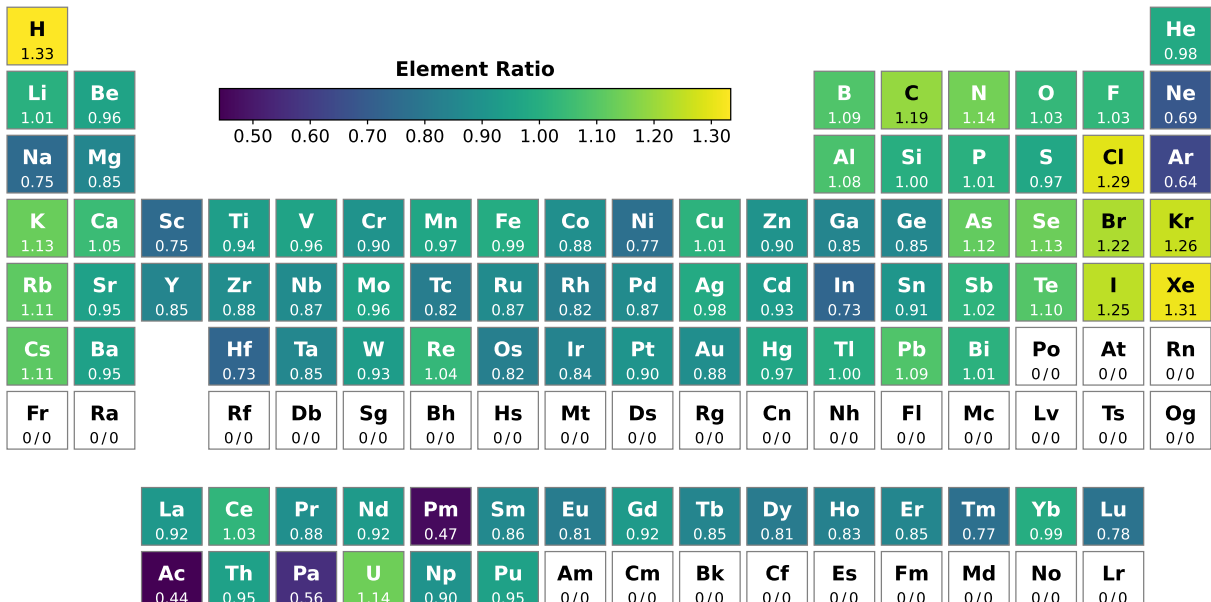


Figure 57: Training curves of MACE-MP-0 models fitted to MPtrj data. (a) Loss (eq. (1)). (b-d) Mean absolute error (MAE) of (b) energy per atom, (c) force, and (d) stress per atom. All curves are evaluated on the validation set.

C.2 Exploration of the training data



(a) MPtrj training set element occurrence



(b) Normalized ratio of elements in MPtrj to MP, $\frac{\text{MPtrj} / \text{len(MPtrj)}}{\text{MP} / \text{len(MP)}}$

Figure 58: The number of structures containing a given element in the MPtrj training set (24). MPtrj consists of multiple configurations from every relaxation trajectory in MP. Some elements can require more ionic steps to relax than others. To visualize this, b shows the overabundance of elements relative to the number of structures containing a given element in MP ground states (after normalizing by dividing each dataset by its number of structures). That is, the factor 1.33 for hydrogen in b indicates that structures containing hydrogen were selected 33% more frequently than the base prevalence of hydrogen in MP ground states.

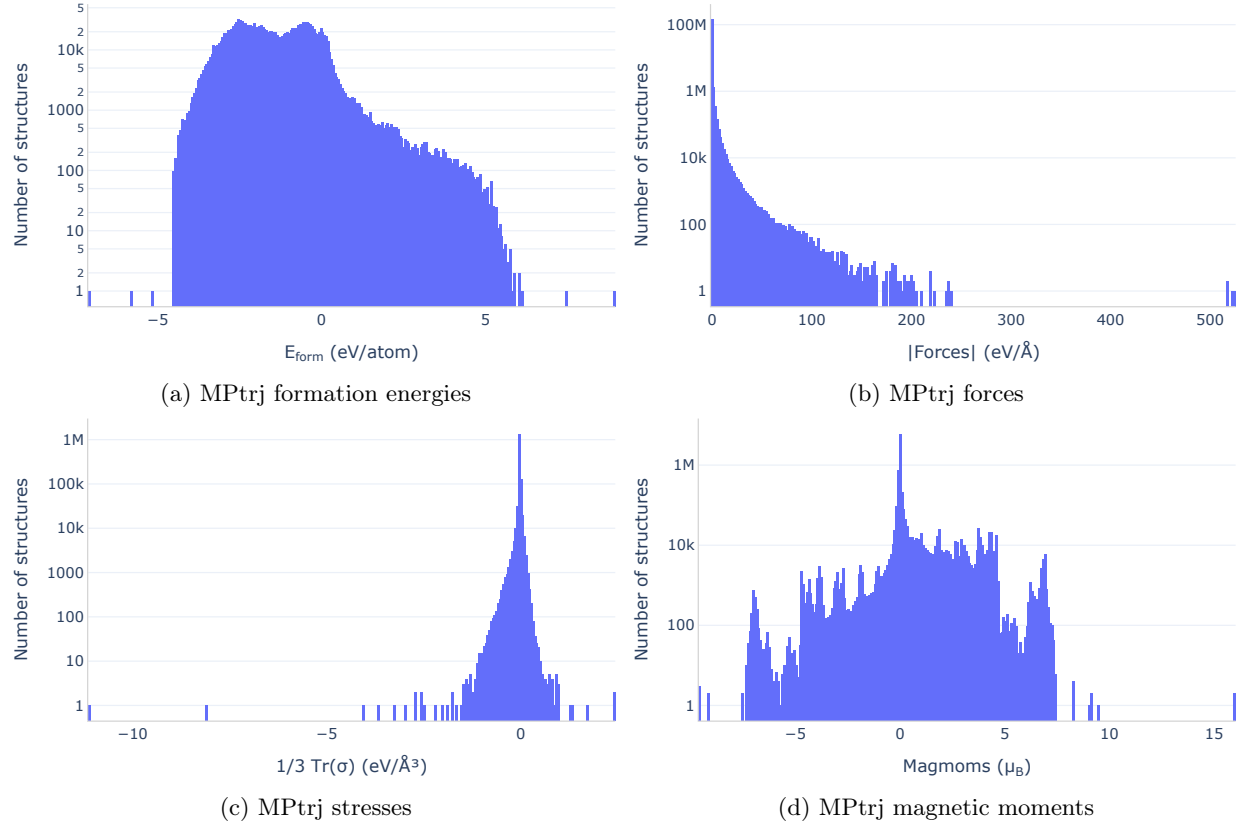


Figure 59: Distribution of energies, forces, stresses and magnetic moments in the MPtrj dataset (24, 244). The bimodality in the formation energy distribution is due to the MP anion correction scheme (283, 284) which significantly lowers oxide formation energies.

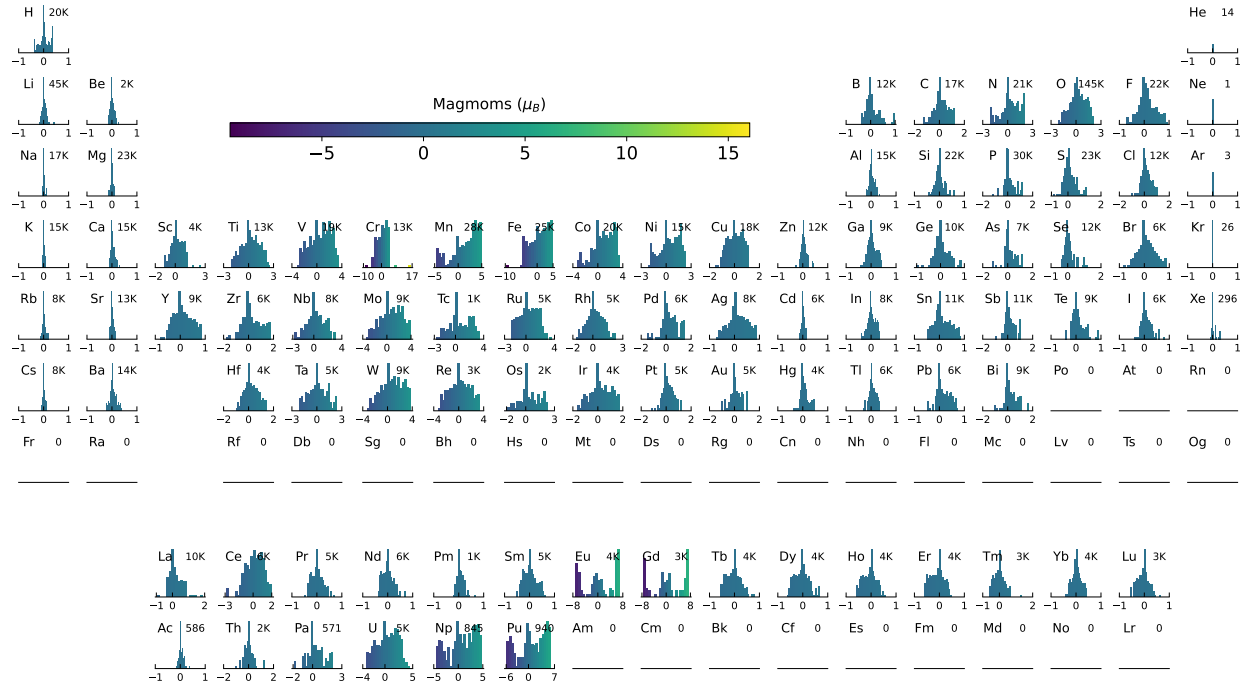


Figure 60: Distribution of magnetic moments for each element in the MPTrj dataset (24, 244, 285). The y-axis is log-scaled to allow visualization of the tail of high magnetic moments in some elements with a sharp peak at 0. The number in the top right corner of each element tile counts magnetic moments for that element in the MPTrj dataset. This plot reveals rare erroneous data points in MPTrj. For instance, Cr has a single-point calculation with a highly unphysical magnetic moment of $17\mu_B$.

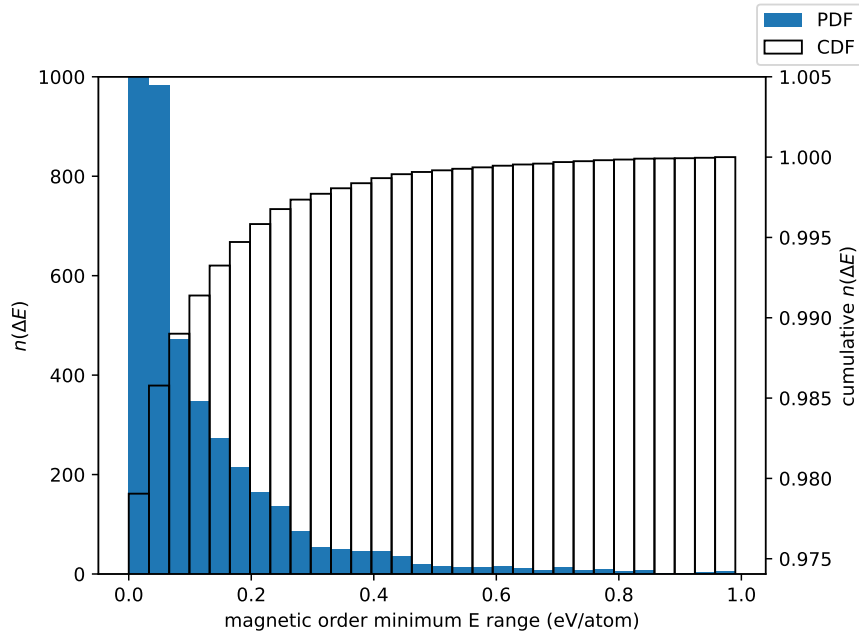


Figure 61: Distribution (PDF) of approximate deviation of energy within each material due to variation in magnetic order (non-magnetic calculation, calculation converges to moment zero, ferromagnetic, and other magnetic orders), with cumulative distribution (CDF) on right axis. The vast majority of materials have very small variation (y axis range does not show full extent of first PDF bar), but a few hundred include different magnetic orders with energies that vary by more than 0.1 eV/atoms

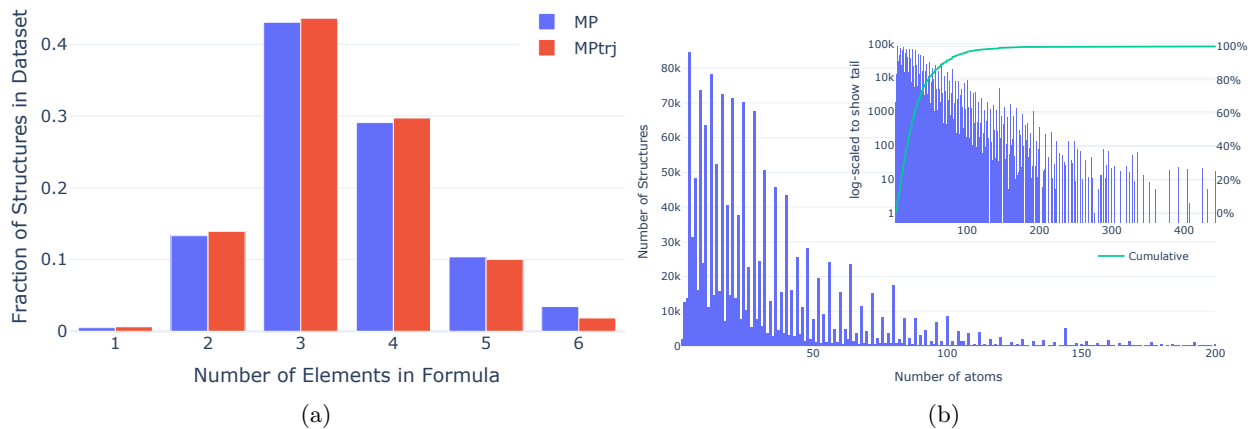


Figure 62: a) Distribution of the number of elements in the compositions of MP structures compared to MPtrj. We observe a slight overabundance of small numbers of elements in MPtrj relative to MP. b) Distribution of a number of sites in MPtrj. The inset shows the same distribution log-scaled to visualize the tail of high site counts. The green cumulative line in the inset shows that 82% have less than 50 sites and 97% of structures in MPtrj have less than 100 atoms.

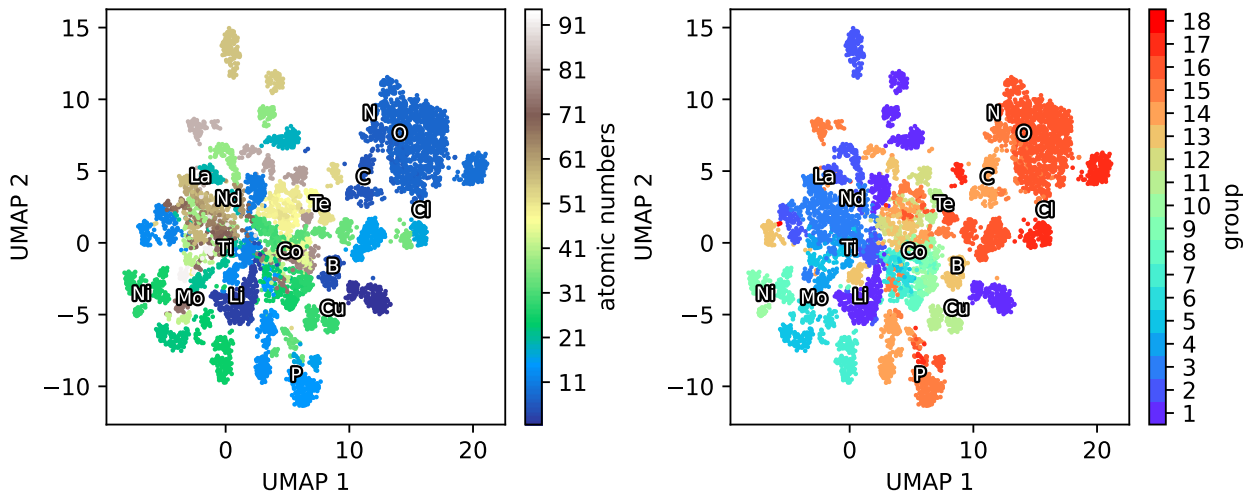


Figure 63: UMAP projection of MACE descriptors for atoms in MPtrj. Each point represents the averaged feature vector of a single element in one structure and is colored by atomic number (left) and group (right) in the periodic table. The features of MACE-MP-0 model are 256-dimensional vectors (concatenation from both first and second layer of 128 channels). Manhattan distance is used for the construction of a high-dimensional UMAP manifold.

C.3 Similarity analysis

In the examples above, we have shown that MACE-MP-0 is capable of surprising degrees of extrapolation. The use of semi-local features (as a result of message passing) (43) and element mixing (44) within the MACE architecture are key components underlying MACE-MP-0's capabilities. These components allow MACE-MP-0 to extrapolate to systems that globally seem completely different from the training data but have close matches locally.

To quantify the similarity, we compare atomic environments from test systems to filtered portions of the training data using the following procedure:

1. Filter training data to a subset with elemental compositions similar or exactly matching the test system.
2. Use MACE-MP-0 to extract invariant descriptors for all atoms in both the test system and the filtered training subset.
3. Calculate the cosine similarity between the atoms in the test system and each filtered training structure. For each atom, we use the maximum cosine similarity found this way. This is essentially a best-match structure kernel (286) that allows many-to-one mappings.
4. Average these maximum atomic similarities by element and then combine them by averaging again, yielding an element-stratified similarity.

Through this procedure, we identify training set structures that contain the most similar local environments to those in any given test system. In addition, we create `chemiscope` (287) (<https://chemiscope.org/>) input files containing UMAP (288) projections of the atomic descriptors (fitted only on the training environments), allowing a more granular and interactive inspection of the environments in the test and training data.

The code for analysing the data and generating `chemiscope` inputs is available as a Python package (63).